

Using Large Layered Intrusions as Analogues for Understanding Subduction Zone
Hydrothermal Systems

by

Erin Kay Benson

Department of Earth and Climate Sciences
Duke University

Date: _____

Approved:

Emily Klein, Supervisor

Alan Boudreau

Paul Baker

Drew Coleman

Dissertation submitted in partial fulfillment of
the requirements for the degree of Doctor
of Philosophy in the Department of
Earth and Climate Sciences in the
Graduate School of Duke University

2022

ABSTRACT

Using Large Layered Intrusions as Analogues for Understanding Subduction Zone
Hydrothermal Systems

by

Erin Kay Benson

Department of Earth and Climate Sciences
Duke University

Date: _____

Approved:

Emily Klein, Supervisor

Alan Boudreau

Paul Baker

Drew Coleman

An abstract of a dissertation submitted in partial
fulfillment of the requirements for the degree
of Doctor of Philosophy in the Department of
Earth and Climate Science in the
Graduate School of Duke University

2022

Copyright by
Erin Kay Benson
2022

Abstract

The genesis of layered intrusions has been the focus of countless studies. Layered intrusions have historically been viewed as natural laboratories to understand the evolution of a single large magma chamber. Many contain platinum- and palladium-rich reef-type deposits, making layered intrusions particularly important economically. Further, layered intrusions may be a useful analogue for understanding subduction zone hydrothermal systems.

This dissertation investigates layered intrusion genesis, specifically in relation to the suggested hydrothermal model of layered intrusion formation, which suggests migrating fluids may have remobilized economically important elements, creating the deposits observed in these intrusions today. The work is divided into eight chapters that explore three layered intrusions: the Bushveld Complex, South Africa, the Stillwater Complex, Montana, and the Skaergaard Intrusion, Greenland. New samples collected from the Stillwater Complex were analyzed for major and trace element compositions and radiogenic and stable isotopes. Investigations into the Bushveld Complex and Skaergaard Intrusion were based on previously published data.

The second chapter examines evidence for fluid circulation in the Bushveld Complex, South Africa, as responsible for some of the geochemical and isotopic signatures present in the complex. Previous isotopic studies of Bushveld are combined with numerical modeling of footwall dehydration to suggest that diapir-like structures

injected fluids into the Main Zone of the intrusion. This chapter further details the similarities between diapiric structures in the Bushveld Complex and those that have been modeled in subduction zone hydrothermal systems. The third chapter expands upon the Bushveld model, specifically in relation to the formation of iron-rich ultramafic pegmatoids and dunite pipes, which the work presented here suggests to be fluid-related.

In the fourth chapter, strontium, neodymium, and lead isotopes are analyzed for rocks from the Stillwater Complex, Montana, to compare with the isotopic mixing model results of the Bushveld Complex. Initial isotopic ratios are used to explore various proposed models of complex formation. Results suggest isotopic heterogeneity during complex formation, whether due to heterogeneous source regions or crustal/fluid contamination.

In the fifth chapter, stable isotope analyses (oxygen, hydrogen, and lithium) are used to better understand the formation of the pegmatoidal bodies thought to be related to fluids at Stillwater. Some evidence of fluid circulation may be observed in hydrogen and lithium isotopes. Geothermometry using oxygen isotopes is suggestive of lower cooling temperatures in the pegmatoids, and may provide evidence of mineral-scale disequilibrium attributable to fluid circulation.

The sixth and seventh chapters utilize the thermodynamic modeling program MELTS to explore problems of layered intrusion evolution. Understanding the evolution

of the liquids that formed various layered intrusions, and identifying magmas parental to layered intrusions, can pose a challenge. Using MELTS, bulk rocks can be synthetically remelted, and the evolution of the complex can be examined through analysis of estimated trapped liquid contents. The sixth chapter applies this method to the Stillwater Complex, while the seventh chapter extends this work to the Skaergaard intrusion in East Greenland. These investigations allow for examination of the magmatic processes operating alongside hydromagmatic processes in layered intrusions.

Dedication

To my husband, Ryan.

Contents

Abstract	iv
Dedication	vii
List of Tables	xiii
List of Figures	xiv
Acknowledgements	xvii
1. Introduction	1
2. Crustal Fluid Contamination in the Bushveld Complex, South Africa: An Analogue for Subduction Zone Fluid Migration	7
2.1 Chapter Summary	7
2.2 Introduction.....	8
2.3 Geology of the Bushveld Complex and Associated Rocks	11
2.3.1 Stratigraphy of the Bushveld Complex	11
2.3.2 Bushveld Country Rocks and the Metamorphic Aureole.....	15
2.3.3 Basement Diapirs.....	17
2.4 Field Evidence for External Fluid Flow into the Bushveld Complex.....	20
2.4.1 Geologic Evidence of External Fluids.....	20
2.4.2 Isotopic Evidence of Country Fluid Intrusion into the Bushveld Complex.....	23
2.5 Footwall Dehydration and Fluid Overpressure.....	26
2.6 Isotopic Consequences of Fluid Injection into the Bushveld Magma Chamber	29
2.6.1 Mixing Model Assumptions	30
2.6.2 Discussion of Model Results	38

2.7 Modeling Fluid Migration Associated with the Footwall Metamorphic Aureole	41
2.7.1 A Quantitative Model of Fluid Flow During Dehydration of the Floor Rocks	41
2.7.2 A Qualitative Model	46
2.8 The Subduction Zone Connection.....	51
2.8.1 Subduction Zone Fluids and Mantle Diapirs	51
2.8.2 The Bushveld Complex as an Analogue for Subduction Zone Hydrothermal Systems	56
2.9 Conclusions	58
3. Reply to Discussion of ‘Crustal Fluid Contamination in the Bushveld Complex, South Africa: An Analogue for Subduction Zone Fluid Migration’ by Roger Scoon and Andrew Mitchell (2020)	60
3.1 Chapter Summary	60
3.2 Introduction.....	60
3.3 Iron-Rich Ultramafic Pegmatite (IRUP) Formation	65
3.4 Dunite Pipes	69
3.5 Conclusions	71
4. Radiogenic Isotopes at the Stillwater Complex: Sr, Nd, and Pb as Isotopic Tracers.....	73
4.1 Introduction.....	73
4.2 Geology of the Stillwater Complex	76
4.2.1 Geologic Context and Country Rocks	76
4.2.2 Stillwater Complex Stratigraphy	78
4.2.3 Pegmatoids	81
4.2.4 Previous Isotopic Investigations	83
4.3 Methods	86

4.4 Results	88
4.5 Discussion.....	98
4.5.1 Disturbance of Stillwater Complex Isotope Systematics	98
4.5.2 Isotopic Heterogeneity in the Stillwater Complex.....	103
4.5.3 Crustal Contamination of Stillwater Parental Magma.....	109
4.6 Conclusions	113
5. Stable Isotope Constraints on the Formation of Stillwater Complex Pegmatoids.....	115
5.1 Introduction.....	115
5.2 Pegmatoid Petrography.....	117
5.3 Methods	118
5.4 Results	124
5.5 Discussion.....	125
5.5.1 Oxygen Isotope Geothermometry and Re-Equilibration.....	125
5.5.2 Models for Pegmatoid Formation	134
5.6 Conclusions	140
6. Using Synthetic Remelting to Identify Evolving Magma Compositions in Layered Intrusions I: Theory and Formation Models at the Stillwater Complex, Montana	142
6.1 Introduction.....	142
6.2 Synthetic Melt Modeling in a Closed System.....	146
6.3 Synthetic Melting in an Open System: The Effects of Late Liquid Loss	151
6.4 Application to the Stillwater Complex.....	158
6.4.1 Stillwater Complex Geochemical Analyses	158
6.4.2 Trapped Liquid Estimates.....	160

6.5 Synthetic Melting Results.....	162
6.6 Discussion.....	173
6.6.1 The Effect of Trapped Liquid on Stillwater Mineral Compositions.....	173
6.6.2 Models for Stillwater Complex Formation.....	174
6.7 Conclusions.....	181
7. Using Synthetic Remelting to Identify Evolving Magma Compositions in Layered Intrusions II: Application to the Skaergaard Intrusion, East Greenland.....	183
7.1 Introduction.....	183
7.2 Application to the Skaergaard Intrusion.....	185
7.3 Synthetic Melting Results.....	187
7.3.1 Modeling the Skaergaard Liquid Line of Descent.....	187
7.3.2 Fractional Crystallization Models.....	194
7.3.3 Mineral Compositions and the Trapped Liquid Shift Effect.....	197
7.3.4 Miscellaneous Results.....	200
7.4 Discussion.....	203
7.4.1 Comparison with Other Models.....	205
7.5 Conclusions.....	206
8. Conclusions.....	208
Appendix A: Sample Locations.....	210
Appendix B: Geochemical Data, Pegmatoid.....	211
Appendix C: Geochemical Data, Host Rock and Hornfels.....	214
Appendix D: Replicate H Isotope Analyses.....	222
References.....	224

Biography255

List of Tables

Table 1: Effect of 1% fluid addition in modification of B1 isotopic composition.....	39
Table 2: Rb-Sr isotope analyses	91
Table 3: Sm-Nd isotopic analyses	93
Table 4: Pb-Pb isotopic analyses	96
Table 5: Stable isotope analyses of mineral separates and bulk rock	126
Table 6: Oxygen isotope geothermometry	131
Table 7: Composition of model parent and model samples during synthetic melting...	147
Table 8: Major and selected trace element concentrations of host rock samples	163
Table 9: Trapped Melt Fraction (TMF) estimates for Stillwater	168
Table 10: Synthetic Melting of Skaergaard Samples, Modal Mineralogy (wt. %)... ..	191

List of Figures

Figure 1: Location map of the Bushveld Complex	9
Figure 2: Main stratigraphic units of the Bushveld Complex and its underlying metamorphic aureole.....	13
Figure 3: Detail of the geology of the part of the Eastern Bushveld Complex (top) and schematic structure cross-section across the Steelpoort pericline (bottom)	18
Figure 4: Diatreme (breccia pipe) from the Upper Critical Zone of the Eastern Bushveld Complex.	21
Figure 5: Sedimentary structures formed by fluid overpressures	22
Figure 6: Progressive loss of H ₂ O in a typical pelite undergoing prograde metamorphism	27
Figure 7: Schematic example of the generation of overpressured fluid by degassing and compaction.....	28
Figure 8: A fluid-magma Sr-Nd isotope mixing model for the Main Zone rocks	32
Figure 9: Examples of fluid-magma mixing models.....	35
Figure 10: Numerical model of footwall dehydration and volatile plume formation.	42
Figure 11: Semi-quantitative model of the thermal evolution of the Bushveld Complex and surrounding country rock.....	47
Figure 12: Examples of modeled mantle diapirs	53
Figure 13: Geology of the Stillwater Complex, with approximate sample traverses marked in red.	76
Figure 14: Stratigraphy of the Stillwater Complex with major mineral modes and major mineral compositional trends.....	79
Figure 15: Outcrop showing field relationship between pegmatoid bodies and spatially associated host rock.	83
Figure 16: Results of Rb-Sr isotopic analysis, for both Stillwater and hornfels samples. .	90

Figure 17: Results of Sm-Nd isotopic analysis, for both Stillwater Complex and hornfels samples.	94
Figure 18: Results of Pb-Pb isotopic analysis, for both Stillwater Complex and hornfels samples.	97
Figure 19: Stratigraphic section of radiogenic isotopes from Stillwater Complex and hornfels samples analyzed in this study.....	98
Figure 20: Sm-Nd isotopic analysis results from this study, alongside the Sm-Nd isotopic results of DePaolo and Wasserburg (1979) and Lambert et al. (1994).	102
Figure 21: ϵ_{Nd} at 2700 Ma for samples from this study, DePaolo and Wasserburg (1979) and Lambert et al. (1994) plotted against their chondrite-normalized Nd/Sm ratios	105
Figure 22: Three plots showing variance of initial isotopic ratios against one another..	111
Figure 23: Thin sections of Ultramafic series host rock and pegmatoid.	119
Figure 24: Thin sections of Lower Banded series host rock and pegmatoid.	120
Figure 25: Thin sections of altered pegmatoid samples.	121
Figure 26: Oxygen isotope analyses varying by stratigraphic height.....	127
Figure 27: Stratigraphic variation in hydrogen isotopes with height.....	128
Figure 28: Stratigraphic variability in bulk rock lithium isotopes with height.....	130
Figure 29: Plot of the $\delta^{18}O$ value of plagioclase vs the $\delta^{18}O$ value of pyroxene for pegmatoid (this study) and host rock (Dunn, 1986) pairs.....	132
Figure 30: Hydrogen isotope composition vs H ₂ O contents for analyzed whole rock and mineral separates, by unit and rock type.	138
Figure 31: Lithium isotope composition vs whole rock Li contents for hornfels and Stillwater Complex samples.	140
Figure 32: The synthetic melting model.....	149
Figure 33: Synthetic melting model for rocks with open-system behavior	154

Figure 34: The effect of open-system behavior on parental liquid evolution during fractional crystallization.....	156
Figure 35: The effect of open-system behavior on crystallized pyroxene composition. .	158
Figure 36: Stratigraphy of the Stillwater Complex.....	159
Figure 37: Synthetic melting curves for analyzed Stillwater samples in each of the three major units explored.....	169
Figure 38: Variability in compositions of plagioclase and orthopyroxene moving up-section.	170
Figure 39: Physical properties of the modeled Stillwater trapped liquid fraction moving up-section.	171
Figure 40: Modeled evolution of trapped liquid trace element concentrations as compared to measured bulk rock trace element composition.....	172
Figure 41: Trace element ratios in the modeled liquid and bulk rock.....	178
Figure 42: Stratigraphic lithological subdivisions of the Skaergaard intrusion.....	186
Figure 43: AFM diagram showing example Skaergaard sample synthetic remelting curves.....	189
Figure 44: SiO ₂ /FeO(t) plot of the evolution of the modeled trapped liquid composition based on trapped liquid estimates by Tegner et al. (2009).....	193
Figure 45: SiO ₂ /FeO(t) plots of modeled trapped liquid evolutions at varying trapped liquid proportions.	195
Figure 46: SiO ₂ /FeO(t) plots showing different parent evolution trends modeled in MELTS.	196
Figure 47: AFM plot showing the LLDs of Nielsen et al (2009) and Thy et al (2009) along with the MELTS modeled parent evolution at three different oxygen fugacities	198
Figure 48: A comparison of modeled and measured mineral compositions.....	199
Figure 49: Modeled physical properties of the system.....	201

Acknowledgements

This work would not have been possible without my family, friends, and the mentors and colleagues who have supported me. I would like to first thank my advisor, Dr. Alan Boudreau, for his support and guidance over the course of my Ph.D. at Duke. My thanks also go to my committee members, Dr. Emily Klein, Dr. Drew Coleman, and Dr. Paul Baker, for their support and advice. Dr. Gary Dwyer dedicated much of his time to assisting me with analytical procedures. Dr. Ryan Mills at the University of North Carolina – Chapel Hill provided similarly invaluable support in collection of radiogenic isotopes. I acknowledge support for this dissertation from NSF (EAR 1647727 to Dr. Alan Boudreau) and from the Society for Economic Geology (Hugh McKinstry Student Research Grant).

I would also like to thank my colleagues, both at Duke University and at the University of North Carolina – Chapel Hill. At Duke, my thanks go to Alex Niebergall, Dr. Benjamin Wernette, Dr. Rachel Coyte, Dr. Enrico Zorzetto, Zhen Wang, Dr. Kimberly Drouin, Gordon Williams, Connor Lester, Ariana Desouza, Ningjie Hu, and other members of ECS. At UNC, support from Allison Murrie and Evelyn Coleman was invaluable. My thanks also go to Kyle Krajewski, Dr. Joshua Rosera, and Ami Ward for assistance in lab procedures and other support. Jenn Marsh and Peishu Li provided invaluable assistance during field work at the Stillwater Complex in 2018.

Finally, I would like to thank my family for their continuous love and support. My mother Andrea Benson and father Eric Benson have always been willing to listen and support my research work, in addition to providing support in trip planning and technical troubleshooting. Support from my brother, grandmother, and extended family was invaluable in navigating graduate school. Last, I would like to thank my incredible husband, Ryan Andersen, who married me during graduate school and whose love and support has carried me through four degrees.

1. Introduction

Layered intrusions are large igneous bodies that exhibit layering, compositionally and by modal mineralogy (e.g., Wager and Brown, 1968; Cawthorn, 1996; O'Driscoll and VanTongeren, 2017). Although silicic examples exist, layered intrusions are typically mafic/ultramafic in composition (e.g., the Stillwater Complex, Montana; the Rustenburg Layered Suite of the Bushveld Complex, South Africa, and the Skaergaard intrusion, East Greenland). Layered intrusions provide valuable insight into magmatic crystallization, particularly of mafic and ultramafic magmas. In theory, layered intrusions record the evolution of the magma chamber, or at least the parental magma, from which it crystallized at a large scale (O'Driscoll and VanTongeren, 2017).

While many layered intrusions have been heavily studied, generalized formation models for many intrusions, and in particular the economically significant ore deposits, remain a matter of some debate. Orthomagmatic models envision layered intrusions and the economic deposits they contain as forming through traditional magmatic processes; PGE are collected by an immiscible sulfide liquid (Campbell and Naldrett, 1979), which often is suggested to form due to the mixing of multiple magmas. In contrast, hydromagmatic models call upon a fluid migrating upward through the crystal mush, scavenging ore elements from the mush (e.g., Kanitpanyachoen and Boudreau, 2013). Formation models for layered intrusions have been further complicated by the suggestion that these bodies were emplaced as a stack of out-of-

order sills rather than a single magma body (e.g., Mungall et al., 2016; Wall et al., 2018), although this model remains disputed (e.g., Latypov and Chistyakova, 2021).

During the formation of these large layered intrusions, contact metamorphism results in the dehydration of nearby country rock, creating metamorphic aureoles around the intrusion (e.g., Vaniman et al., 1980; Schiffries and Skinner, 1987; Labotka and Kath, 2001; Gleason et al., 2011). The layered intrusion thus preserves a system in which hot mafic and ultramafic rock overlies cold dehydrating crustal rock. The geometry of a layered intrusion is thus similar to that of a subduction zone, where the cold crustal rock (the subducting slab) moves beneath the hot ultramafic rock (the mantle wedge).

Subduction plays a key role in the dynamics of the deep earth. Subduction and the associated recycling of oceanic crust is linked to the origin and growth of continental crust (Rapp and Watson, 1995), and signatures from subducted materials have been identified in fresh oceanic crust (Ben Othman et al., 1989). Further, the mantle is a major reservoir for H₂O, with subduction delivering much of this water into the mantle (Thompson, 1992). The subducting slab carries water into the mantle both in sediments and in hydrous mineral phases such as serpentine (Schmidt and Poli, 1998; Rupke, 2004). Progressive metamorphism of hydrous phases releases fluids into the mantle wedge (e.g., Schmidt and Poli, 1998), likely following a model of continuous dehydration. Fluid release in subduction zones is responsible for generating the melts that form arc

volcanoes, as fluid flux in the mantle generates melting. Geochemical analysis of volcanic arc magmas have identified fluid signatures worldwide (e.g., Kent and Elliott, 2002; Kimura and Yoshida, 2006; Bouvier et al., 2008), and numerical modeling suggests that fluid is required to generate melting even in arcs with minimal identified fluid signature (Ayers, 1998).

While the importance of slab dehydration in generating melt at volcanic arcs is clear, there are major gaps in knowledge of the physical process of fluid migration into and out of the mantle wedge. This is primarily because it is very difficult to observe directly the processes by which slab components enter the mantle wedge and interact with the peridotite (Spandler and Pirard, 2013). Additionally, indirect observations, such as of exhumed subducted and mantle material, are complicated by retrograde metamorphism that may overwrite evidence of fluid flow at depth (Cartwright and Buick, 2000). Layered intrusions may present the closest observable analogue for fluid flow from cold crustal rock into hot ultramafic rock in a direct field setting. By tracing fluid circulation in layered intrusions, it may be possible to understand fluid migration in subduction zones.

This dissertation examines layered intrusions to identify regions of fluid flow in layered intrusions and demonstrate the impact that fluid may have had on the intrusion during formation. The second and third chapters focus on fluid flow at the Bushveld Complex. The Bushveld Complex was emplaced into previously-unmetamorphosed

sediments with a great deal of fluid available for dehydration. Interpretation of previously published isotopic data at the Bushveld Complex demonstrates that country fluid contamination can more realistically produce observed Bushveld isotopic variations than simple crustal contamination, which requires a very high degree of crustal assimilation. Further, numerical modeling conducted by collaborator James Connolly demonstrates the development of pipe-like channels that focus the fluid flow

The fourth and fifth chapters extend this work to the Stillwater Complex. While the isotopic composition of the Bushveld Complex is well-characterized, substantially less isotopic work has been conducted at the Stillwater Complex, in part due to a view that later regional metamorphism had largely reset some isotopic systems (such as Rb-Sr) (e.g., DePaolo and Wasserburg, 1979; Lambert et al., 1994; McCallum et al., 1999). The Stillwater Complex was emplaced into previously metamorphosed volcanoclastic rocks (Lobotka and Kath, 2001), and as a result less fluid was available for release during dehydration (e.g., Benson et al., 2020a). As a result, the studies of the Stillwater Complex here focus on pegmatoidal bodies found sporadically throughout the intrusion, which are thought to be fluid related (Braun et al., 1994; McIlveen, 1996; Hanley et al., 2008). Comparison of the pegmatoids to spatially associated host rock and to the underlying hornfels country rock is used to detect evidence of fluid circulation using radiogenic and stable isotopes. Analysis of multiple isotopic systems in the hornfels, and of radiogenic isotopes in a broader swath of Late Archean country rock in the Beartooth Mountains

(Wooden and Mueller, 1988; Wooden et al., 1991), suggests the country rock was isotopically very similar to the Stillwater Complex. Observed isotopic similarity between host rock and pegmatoid samples is thus expected in the case of crustal contamination. Isotopic variability in bulk rock samples is suggested to be the result of source heterogeneity; similarity of preexisting country rock to intruding Stillwater magmas may suggest a similar source region for the suite of Late Archean Beartooth Mountain rocks.

Finally, the sixth and seventh chapters use the thermodynamic modeling software MELTS (Ghiorso and Sack, 1995; Asimow and Ghiorso, 1998; Gualda et al., 2012; Ghiorso and Gualda, 2015) to better understand the evolution of parent magma and compaction processes occurring in layered intrusions. These chapters use trapped liquid to examine compaction in the Stillwater Complex, and the evolution of the parent liquid at the Skaergaard intrusion. Using the MELTS program, analyzed rocks are 'synthetically remelted.' To the extent that the original proportions of solid and liquid can be determined, remelting the rock should retrieve the original liquid that was in equilibrium with the original solid. This approach can recover the major and trace element composition of the liquid, and can identify how the liquid is changing as the intrusion crystallizes. Understanding the many processes operating in layered intrusions is key to separating out the effects of fluids from typical magmatic processes. Modeling results suggest that open-system processes such as compaction and possibly migration

of lost late-stage liquid upward into crystallizing magma were ongoing at the Stillwater Complex, as many samples display evidence of open-system behavior. Results at the Skaergaard intrusion suggest closed-system behavior, and indicate the parental melt evolved to become Si-enriched rather than Fe-enriched, which has been at the center of an ongoing debate among Skaergaard workers (e.g., Hunter and Sparks, 1987; McBirney and Naslund, 1990; Thy et al., 2009; Nielsen et al., 2019) .

In whole, the work presented here addresses issues of layered intrusion formation. Isotopic evidence supportive of fluid migration through the Bushveld and Stillwater Complexes also supports the hydromagmatic model of layered intrusion and ore deposit formation. Further, layered intrusions where evidence of fluid circulation is found may be used as analogues for subduction zone fluid migration, to better understand the pathways fluids follow when released from the subducting slab. While layered intrusions are not a perfect subduction zone analogue, this work suggests they are one of the best available locations to observe migration of fluids from cold rock into overlying hotter rock, and as such present an excellent opportunity to more broadly examine fluid migration in subduction zones.

2. Crustal Fluid Contamination in the Bushveld Complex, South Africa: An Analogue for Subduction Zone Fluid Migration

Published as: Benson, E., Connolly, J.A.D., and Boudreau, A.E., 2020, Crustal fluid contamination in the Bushveld Complex, South Africa: An analogue for subduction zone fluid migration: *International Geology Review*, doi: 10.1080/00206814.2020.1795734

2.1 Chapter Summary

Crystallization of the 2.06 Ga Bushveld magma formed a 9 km (maximum) sequence of ultramafic and mafic rocks that generated a large volume of country fluid as it thermally metamorphosed a 3+ km section of previously unaltered underlying sedimentary rocks of the Transvaal sequence – a geometry similar to that seen as subducting lithospheric slabs are heated by overlying mantle rocks. The presence of a diatreme (breccia pipe) and other large, pipe-like features in the Bushveld Complex located proximal to diapiric upwelling of the basement rocks suggest that overpressured fluids generated during dehydration of the footwall sediments are focused by the diapiric structures such that the country fluids rapidly penetrate the Bushveld rock. A re-examination of existing stable and radiogenic isotopic evidence is consistent with contamination of Main Zone magmas by 1–2% country fluid. Numeric modelling of the footwall dehydration similarly shows that most of the country fluids will be confined to pipe-like channels as it percolates into the Bushveld sill. Modelling also suggests that the maximum extent of the metamorphic aureole was reached at about the same time that the Main Zone began to crystallize. It is proposed that rapid inflation of the Bushveld sill

induced the sudden and catastrophic expulsion of overpressured country fluids to both generate the diatreme and contaminate the Main Zone magma, resulting in the Main Zone enrichment in crustal stable and radiogenic isotopic signatures (Sr, Nd, O and others). By analogy, it is also suggested that hydration melting in the mantle wedge is episodically driven by similar sudden influxes of slab fluids that are able to retain their geochemical and isotopic character by rapid channeled influx. This can be aided by flow focusing at diapirs structures at the upper slab-mantle contact.

2.2 Introduction

The 2.06 Ga (Walraven, 1988) Rustenburg Layered Series of the Bushveld Complex of the Republic of South Africa (hereafter simply referred to as the Bushveld Complex) is the world's largest layered intrusion, with area estimated to be >90,000 km² and a volume exceeding 450,000 km³ (e.g., Finn et al., 2015; Figure 1). In part because the intrusion is economically significant (hosting significant platinum-group element, chrome, and vanadium deposits), many studies have been undertaken of Bushveld formation. The Bushveld Complex exhibits a broad stratigraphic trend upwards to more fractionated rock compositions (e.g., Eales and Cawthorn, 1996; Maier et al., 2000; Figure 2). Early studies of Bushveld formation primarily relied on these compositional trends and considered the Bushveld to have formed by the continuous recharge and fractional crystallization of a single parent magma. Since then, observations of stratigraphic isotopic changes have led to a number of more complex models, including partial

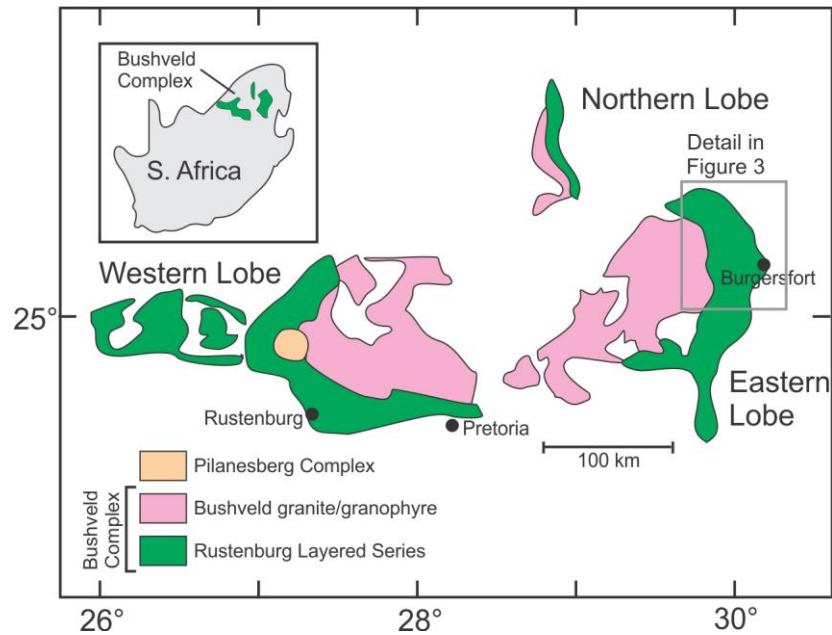


Figure 1: Location map of the Bushveld Complex, Republic of South Africa, showing the three major parts of the Bushveld, the Western, Eastern, and Northern lobes. The location of the detail of the Eastern lobe shown in Figure 3 is also noted.

melting of enriched mantle or assimilation of lower and/or upper crustal rocks during emplacement, some of which resultant magma may have different liquid lines of descent (e.g. Irvine, 1977; Von Gruenewaldt et al., 1985; Hatton and Sharpe, 1989; Harmer et al., 1995; McCandless et al., 1999; Maier et al., 2000; Harris et al., 2005; VanTongeren, 2018). For example, it is envisioned that the Sr isotopic change observed between the Main Zone and underlying rocks was the result of the introduction of a large volume of extensively contaminated Main Zone magma and a significant expansion of the Bushveld chamber (Kruger, 2005).

Although a number of studies have called upon contamination by upper crustal/roof rocks (e.g., Harris et al., 2005; Kruger, 2005), the possibility that at least some

of the large-scale isotopic variation is the result of in situ contamination of the Bushveld magma by crustal fluids has not been seriously explored outside of local contamination or late-stage modification of the original mineral assemblage. However, other areas of study have explored the impact of crustal fluid contamination of magma or its source rock. For instance, evidence from subduction zone magmas illustrates that crustal fluids can clearly affect the isotopic character of a mantle magma (e.g., Nohda and Wasserburg, 1981; Ito and Stern, 1986; Shaw et al., 2008; Woodhead et al., 2012). Furthermore, investigations into fluid contamination at various intrusions often rely heavily on isotopic compositions to differentiate between fluid alteration and crustal assimilation (e.g., Leeman and Hawkesworth, 1986; Hildreth et al., 1991).

This paper reviews the evidence that significant amounts of fluid were generated during metamorphism and deformation of the underlying country rock as the Bushveld magma cooled and crystallized. It is here proposed that the formation of footwall diapirs led to focused flow of country fluid, resulting in the rapid influx of fluid, the formation of breccia pipes in the lower portion of the Bushveld section, and mixed with the resident magma. Irrespective of other conventional contamination events, it is shown that the introduction of 1–2% crustal fluid can significantly shift the observed Sr, Nd, and stable isotopic compositions of a Main Zone magma from presumed Main Zone parent magma compositions. A numerical model of fluid generation in the footwall metamorphic aureole illustrates how country fluids develop spontaneous channels,

generating diapiric activity and can be largely isolated from affecting the surrounding igneous rocks.

Finally, the results suggest that the Bushveld Complex and other large layered intrusions can be excellent analogues to understand subduction zone hydrothermal systems. Because subduction processes occur at depth and cannot be observed directly, one must rely on geophysical observations, exhumed rock (generally from shallower parts of the subduction complex), experimental methods, and numerical models understand the subduction process. The Bushveld hydrothermal system, where hot ultramafic rocks overlie dehydrating country rocks, is a natural analogue to subduction zones without the complications of faulting and a later metamorphic overprint, and can provide insights into mantle processes. Several studies analyzing diapiric structures at Bushveld have drawn this connection to possible subduction zone diapirism as well (Gerya and Yuen, 2003; Ireland and Penniston-Dorland, 2015). Using the example of the Bushveld Complex, it is shown that metamorphic fluids can be effectively channeled by these diapirs structures and allow rapid influx of large volumes of fluid well ahead of the diapir itself for both the Bushveld and subduction systems.

2.3 Geology of the Bushveld Complex and Associated Rocks

2.3.1 Stratigraphy of the Bushveld Complex

The layered ultramafic to mafic rocks of the Bushveld Complex has been described as a lopolithic intrusion with a maximum thickness of about 9 km and

cropping out in three main regions; the western, eastern and northern lobes. However, with an aspect ratio >30:1 and locally extensive rheomorphic folding and diapirism of the floor rocks, it may be considered a variably thick sill. Palaeomagnetic evidence (e.g., Wilson et al., 2000; Letts et al., 2009) suggests that the Bushveld magma initially intruded as a horizontal sill but developed a modest dip during the emplacement of the Lebowa (Bushveld) Granite Suite soon after the formation of the Rustenburg Layered Suite. Its general geology and igneous stratigraphy have been well described and are only briefly summarized here. For a more complete discussion see Eales and Cawthorn (1996) and references therein.

The stratigraphy of the Bushveld Complex has been subdivided into five zones: a basal Marginal Zone, overlain sequentially by the Lower Zone, Critical Zone, Main Zone and finally Upper Zone (Figure 2). Evidence of a possible Basal Ultramafic Zone underlying the Marginal Zone has been found by drilling (Wilson, 2015), but has not been heavily explored. The Marginal Zone is comprised of sills of locally quenched textured pyroxenites and micropyroxenites whose compositions have been interpreted as parental to the main Bushveld magmas (Sharpe, 1985). The most common of these have been termed the B1 (parent to Lower Zone), B2 (Upper Critical Zone) and B3 (Main Zone) magmas (e.g., Harmer and Sharpe, 1985; Maier et al., 2000). The Lower Zone is approximately 800–1000 meters thick and consists primarily of layers of pyroxenite, dunite, and harzburgite with some chromite with small amounts of

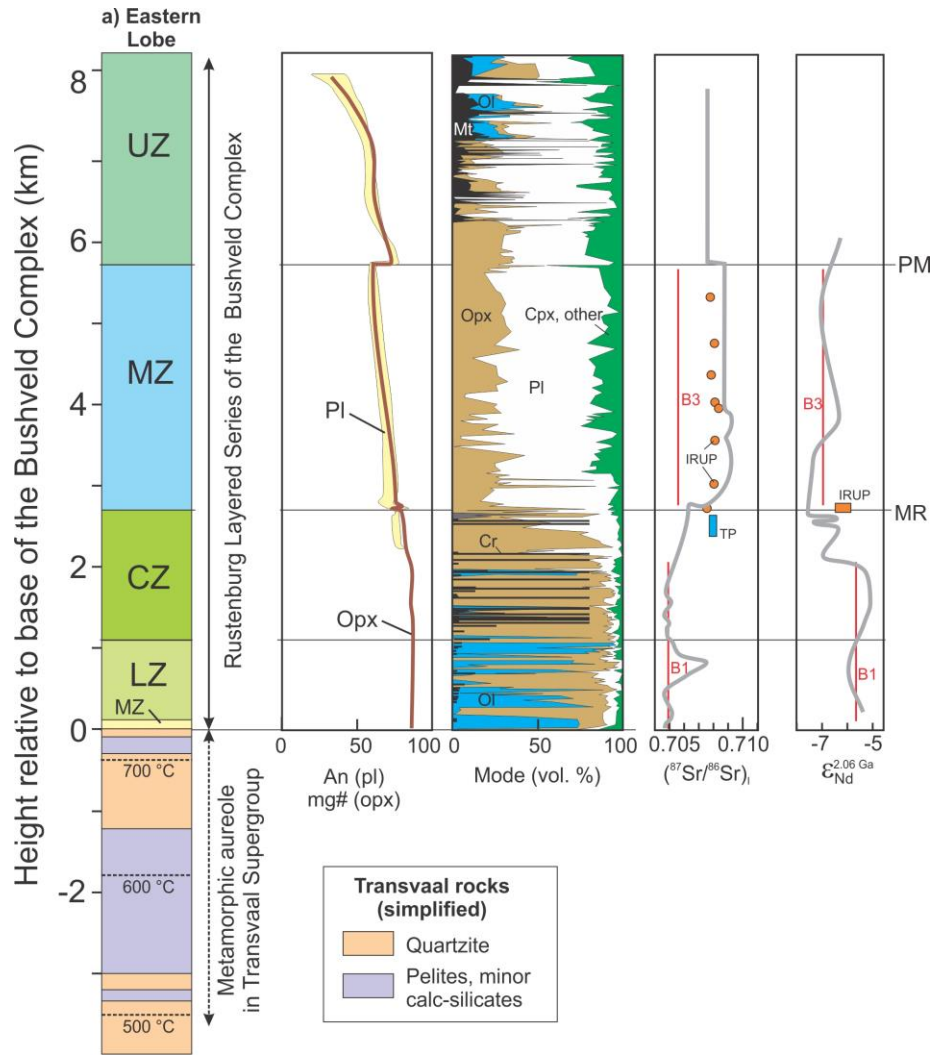


Figure 2: Main stratigraphic units of the Bushveld Complex and its underlying metamorphic aureole, as well as the Sr and Nd isotopic variations and pyroxene and plagioclase compositional variation. Maximum thermal isograds in the aureole are labeled. The labeled vertical grey lines in the plots of initial $^{87}\text{Sr}/^{86}\text{Sr}$ and ϵ_{Nd} isotopic trends are the isotopic compositions of the B1 and B2 sill/chilled margin rocks thought to be parental to the Lower/Lower Critical Zones and Main Zone, respectively. Orange dots indicate IRUP locations. Abbreviations: LZ, CZ, MZ, and UZ: Lower, Critical, Main, and Upper Zones of the Bushveld Complex, respectively; MR = Merensky Reef; PM = Pyroxenite marker near top of the Main Zone; TP = Tweefonein pipe and approximate location of breccia pipe shown in Figure 4; IRUP = ultramafic iron-rich pegmatoid associated with the Merensky Reef. After Kruger (1990, Cawthorn et al. (2000), Maier et al. (2000), Reid and Basson (2002), and Harris et al. (2003).

interstitial plagioclase, biotite, and clinopyroxene. The boundary between the Lower Zone and the Critical Zone has been defined in two ways: either a rather modest increase from about 2% to about 6% in the modal abundance of interstitial plagioclase (Cameron, 1978) or by a decrease in olivine abundance (Teigler and Eales, 1996). The Critical Zone is subdivided into the Upper Critical and Lower Critical Zones, with the boundary between the two occurring where plagioclase changes from an interstitial mineral to an abundant, euhedral phase. Thirteen major chromitite seams have been identified in the Critical Zone, namely, the Lower Group (LG) seams 1–7, four middle group (MG1-4) seams, and two upper group (UG) seams. The boundary between the Critical Zone and the Main Zone is usually taken to be the top of the Giant Mottled Anorthosite layer, an anorthosite with large oikocrysts of pyroxene. The Main Zone consists of a thick succession of norites and gabbronorites devoid of olivine or chromium spinel. The base of the Upper Zone is generally taken as occurring at the Pyroxenite Marker horizon (Kruger, 1990) and is also marked by the appearance of euhedral magnetite (Eales and Cawthorn, 1996). This zone is characterized by generally well-defined modal layering, with particularly well-developed magnetite and anorthosite layers.

These major zones are characterized by distinct variations in isotopic compositions, both radiogenic (e.g., Sr, Nd and Os) and stable (e.g., S, O and H). For instance, Nd and Sr ratios show non-monotonic and locally abrupt change moving up

throughout the stratigraphic section (Figure 2). Isotopic differences can show small-scale variations between zones as well; below the Upper Zone, isotopic disequilibrium is common both within grain (core-rim) and between different minerals (e.g., Roelofse and Ashwal, 2012). In contrast, Sr isotopes are constant at the mineral scale and for bulk rock in the Upper Zone (e.g., Chutas et al., 2012; Schannor et al., 2018). Furthermore, except for a modest jump to more primitive mineral compositions at the base of the Upper Zone, stratigraphic changes in isotopic composition are not strongly mirrored by mineral compositional trends. This problem of mineral-scale isotopic disequilibrium (e.g., Prevec et al., 2005; Chutas et al., 2012; Roelofse and Ashwal, 2012; Yang et al., 2013; Roelofse et al., 2015) despite only modest changes in mineral composition from expected fraction trends is a long-ongoing problem. These isotopic changes are conventionally explained by variable contamination by assimilation of crustal rocks either prior to introduction into the magma chamber (e.g., Harmer et al., 1995; Maier et al., 2000; Harris et al., 2005) or by assimilation of roof rock (e.g., Kinnaird et al., 2002). Additionally, some isotope studies of Bushveld samples have been used as evidence of circulation by crustal fluids (e.g., Schannor et al., 2018).

2.3.2 Bushveld Country Rocks and the Metamorphic Aureole

The Bushveld magma intruded the Transvaal Supergroup of the Proterozoic Pretoria Group sedimentary rocks composed dominantly of shale, quartzite, evaporites, and lava filling the Transvaal paleobasin (to 2.5 Ga in age) (Eriksson et al., 1993, 1995).

These rocks underwent very little deformation or thermal metamorphism before the emplacement of the Bushveld magmas. The Bushveld Complex formed a metamorphic aureole that extends at least 3.5 km (to the 500°C isotherm) beneath the base of the Bushveld sill (Figure 2). Heating of the country rock was intense enough to produce localized melting near the base of the Bushveld (Harris et al., 2003).

The rocks immediately below the Bushveld Complex that were thermally metamorphosed include quartzites and psammities of the Lakenvalei and Magaliesberg formations and argillaceous metasediments and minor calcsilicates of the Vermont and Silverton formations, all part of the Early Proterozoic Pretoria Group of the Transvaal Supergroup (Harris et al., 2003). While the country rocks immediately beneath the Bushveld Complex include the Magaliesberg quartzite which would not generate volatiles other than loss of pore fluids, the shales, carbonates and evaporates can serve as a source of volatile components in addition to H₂O.

Geologic and isotopic evidence for hydrothermal circulation related to the intrusion of the Bushveld Complex (including the Bushveld Granite) has been summarized by Gleason et al. (2011). Evidence includes veins in Bushveld rocks derived from Transvaal fluids (detailed more below), marginal hydrothermal ore deposits including a number of Bushveld-age Mississippi Valley-Type (MVT) mineral deposits in the Transvaal Sequence, and ~2.0 Ga palaeomagnetic overprinting of the Transvaal

sediments. They suggest that a regional-scale Bushveld-age hydrothermal system circulated as far as 700 km outward from the present margins of the Bushveld.

2.3.3 Basement Diapirs

A series of footwall upwarped dome- and trough-like structures were first mapped at the Bushveld Complex in the 1960s and 1970s. These structures locally intrude up into the Upper Zone (e.g., the Phepane diapir of Figure 3). The domes are important because they can channel both igneous and country fluids into the upwarped regions. Button (1978) suggested these structures were diapiric, as the density difference between the mafic complex and the underlying sedimentary layers could easily give rise to diapirs. Since then, a number of authors have also discussed the occurrence of these features as related to syn-magmatic deformation and diapiric upwelling (Uken and Watkeys, 1997; Gerya and Yuen, 2003; Clarke et al., 2005). Bushveld diapirism differs in some ways from typical models of diapirism. Typical diapirism involves heated, low-density floor rock material rising into the overlying cooling magma. However, the floor rock domes at Bushveld never reach the temperatures of the overlying rock (Clarke et al., 2005), which is why they have been termed 'cold diapirs' (Gerya and Yuen, 2003; Gerya et al., 2004; Clarke et al., 2005).

Uken and Watkeys (1997) investigated the internal structure of the domes and suggested that emplacement of the northeastern Bushveld Complex was initiated by a series of finger-shaped intrusions. Folds developed between them, which provided

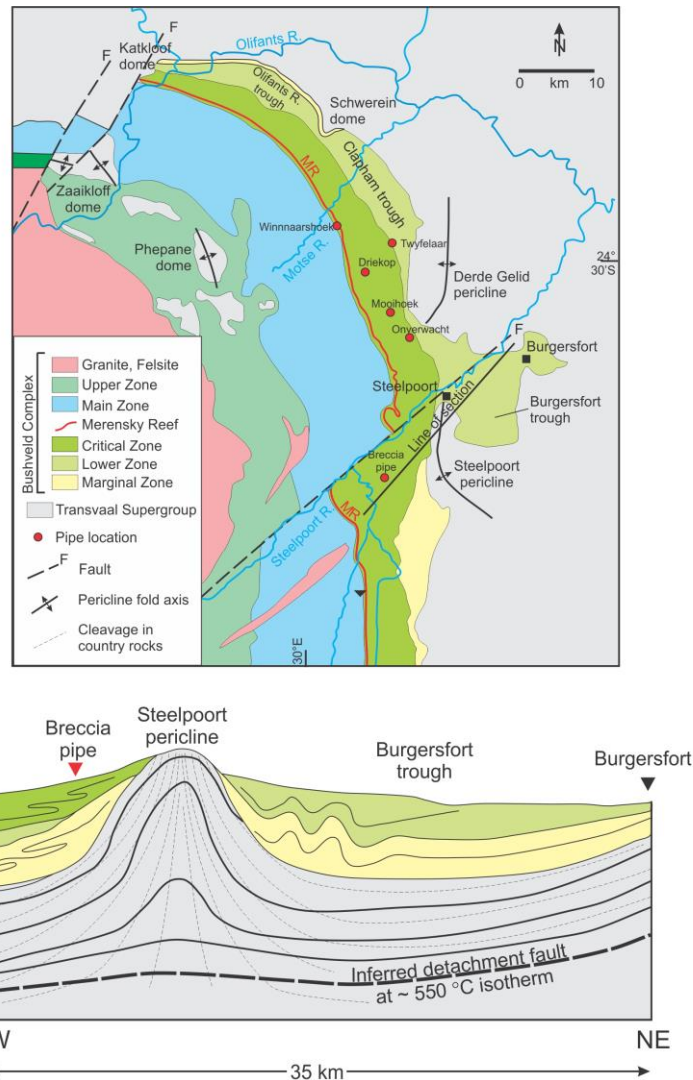


Figure 3: Detail of the geology of the part of the Eastern Bushveld Complex (top) and schematic structure cross-section across the Steelport pericline (bottom) (no vertical scale). Location of some of the discordant pipes and the breccia pipe shown in Figure 4 are also noted. The Phepane diapir is present in the northern portion of the Upper Zone. The cross-section is along the labeled “Line of Section” and illustrates the locally extensive degree of deformation in the country rock below the Bushveld as well as deformation and local thickening in the lowermost lithologic units of the Bushveld Complex. The detachment level corresponds roughly with the 550°C peak metamorphic isotherm (Uken and Watkeys, 1997). Top: after Scoon and Costin (2018). Bottom: Adapted from Clarke et al. (2005) and published with permission from the Geological Society of South Africa.

focus for initiation of diapirism within the intrusion. Clarke et al. (2005) investigated deformation in the Bushveld rocks adjacent to the Steelpoort pericline. They found decreasing intensity of deformation both upwards and laterally in the intrusion and suggested country- rock diapirism as the most likely cause, as the folds would have formed due to drag and radial expansion as the diapir rose.

The petrology of the Phepane diapir was investigated by Johnson et al. (2004). They found evidence of spinel-cordierite symplectites replacing andalusite that they interpreted as a result of decompression, which would have occurred during the thermal peak as the diapir rose into the Bushveld rocks. Ireland and Penniston-Dorland (2015) analyzed oxygen and lithium isotopes across the contact of the Phepane Dome and the Bushveld Complex host rocks itself. Their results suggest that diffusional exchange occurred for less than 5 Myr, which fits within the crystallization time predicted for the Bushveld Complex.

Numerical modelling by Gerya et al. (2004) utilized a Rayleigh–Taylor instability model driven by the density contrast between intrusion and sediments for subduction zones that were used by Gerya and Yuen (2003) and showed the Bushveld diapir model to be geophysically feasible. The modelled diapir growth rate of 0.8 cm/yr is consistent with that estimated by Uken and Watkeys (1997) of 0.6 cm/yr. They suggest that, while these types of diapirs have been observed only at the base of the Bushveld Complex, other layered mafic intrusions may have formed similar structures. However, Bushveld

diapiric structures are only common in the thickest sections of eastern Bushveld where they intruded a sedimentary sequence that had not previously been heated. This situation is not likely to be common at other intrusions, which may limit the prevalence of similar structures elsewhere. A possible exception is seen in the Archaean-age Stillwater Complex in Montana where variations in the thickness of the Ultramafic Zone occur on about the same scale as the Bushveld structures. It has been suggested that the thicker eastern part of the Stillwater Complex formed in a subsiding basin (Raedeke and McCallum, 1984); a Stillwater diapiric model would appear to be equally viable but has not yet been tested.

2.4 Field Evidence for External Fluid Flow into the Bushveld Complex

2.4.1 Geologic Evidence of External Fluids

A number of features of the Bushveld Complex are suggestive of the influence external fluids may have had on the intrusion. Schiffries and Skinner (1987) and Schiffries and Rye (1990) noted the presence of high temperature (maximum temperature about 700°C) saline hydrothermal veining that cut both the intrusion and the underlying contact aureole. Schiffries and Skinner (1987) also noted the presence of fluid inclusions with highly saline, high-temperature fluid inclusions with high Cl concentrations. More recent work has shown that these are widespread throughout the Bushveld stratigraphy (Buick et al., 2001; Pronost et al., 2008; Roelofse and Ashwal, 2012).

Associated with the diapiric structures in the Eastern Bushveld are a number of pipe-like features. One spectacular feature of the Bushveld Complex is the diatreme (breccia pipe) proximal to the Steelpoort pericline, that brings Bushveld rocks from at least the Lower Zone up into the Critical Zone (Figure 4, Ferguson and McCarthy, 1970; Boorman et al., 2003). The breccia pipe shows features typical of rapid fluid-driven emplacement: 1) the larger blocks are concentrated on the central part of the diatreme where fluid velocities are expected to be highest; 2) elongated blocks are aligned parallel to the axis of the pipe and parallel to the inferred fluid flow direction; and 3) blocks from the deeper Lower Zone are smaller than those from the Critical Zone. Although

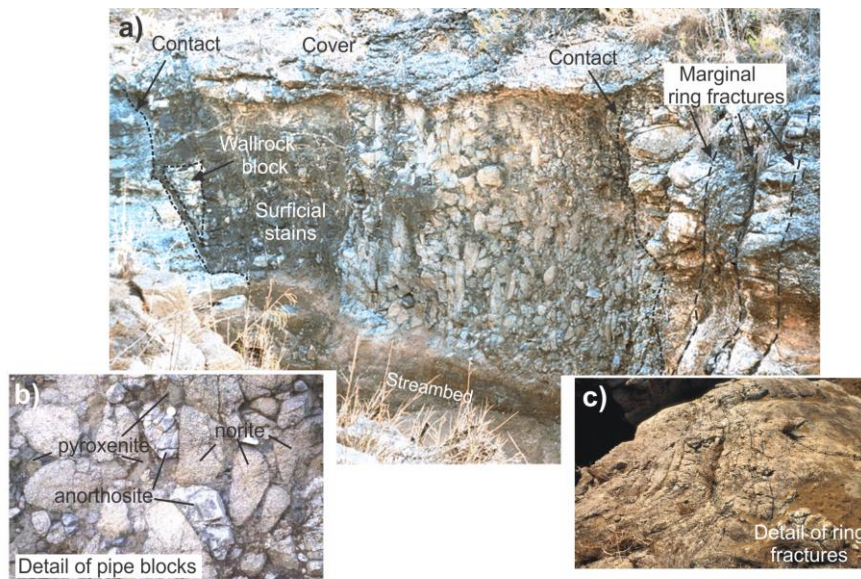


Figure 4: Diatreme (breccia pipe) from the Upper Critical Zone of the Eastern Bushveld Complex. A) Overview of the pipe, interpreted to have formed by the rapid upward movement of overpressured fluid. B) Detail of the blocks from the Lower Critical Zone and the Lower Zone of the Bushveld included in the pipe. C) Ring fractures developed in the host Critical Zone rocks that surround the pipe. From Boorman et al. (2003), reproduced with permission.

kimberlite diatremes are an obvious analogue, it is suggested that the km-long gas blowout pipes that can occur in sedimentary basins are a more apt comparison (e.g., Løseth et al., 2011; Figure 5). The pipe illustrates that transport of large volumes of fluid can be sharply localized as it moves through the lower parts of the Bushveld Complex.

It has been previously suggested that the diatreme formed by igneous fluids generated entirely within the Bushveld mush (e.g., Boorman et al., 2003). This was based on the lack of country rock in the breccia pipe. However, the lithologies present in the diatreme that came from the deeper parts of the Bushveld stratigraphy are the smallest.



Figure 5: Sedimentary structures formed by fluid overpressures as analogues for the Bushveld breccia pipe of Figure 4. A) and B) Example of pockmark at the core of a blowout pipe developed in mudrocks (after Løseth et al., 2011, reproduced with permission). C) Seismic sections of km-scale sedimentary blowout pipes (redrawn after Løseth et al., 2011).

Thus, it is possible that country blocks did not make it up to the level of the exposure. Furthermore, brecciation might only have occurred within the crystal pile and did not reach into the footwall for reasons discussed below. While this isotopic character of the

diatreme has not been studied, it does have an interstitial ultramafic component between the blocks that is similar to the iron-rich ultramafic pegmatoids (IRUP) seen elsewhere in the Bushveld Complex. Bushveld IRUP has enriched (crustal) isotopic signatures, distinct from Critical Zone rocks (Reid and Basson, 2002) (the Merensky IRUP Sr and Nd isotopic compositions are shown in Figure 2).

Besides the breccia pipe, a number of discordant Mg- to Fe-rich pipes, some PGE-bearing, that occur in the lower sections of the Eastern Bushveld and have a more controversial origin (c.f. Scoon and Mitchell, 2004 for a more detailed review). They appear to be concentrated near faults and the floor diapirs, similar as for the diatreme (Viljoen and Scoon, 1985). The presence of relic chromitite layers that crosscut some of these pipes is one piece of evidence that they formed by replacement of the original lithology. While some have interpreted the metasomatic agent to be a silicate liquid (e.g., Cawthorn et al., 2000; Günther et al., 2018) others have suggested that the iron enrichment seen in the core of the pipes are the result of metasomatic reaction involving Fe-, PGE- and Cl-rich fluids (e.g., Schiffries, 1982).

2.4.2 Isotopic Evidence of Country Fluid Intrusion into the Bushveld Complex

A number of isotopic studies have suggested that very little country fluid made it into the Bushveld Complex. For example, it has been suggested that $\delta^{18}\text{O}$ in the Platreef, which occurs near the floor of the eastern Bushveld Complex, was mostly magmatic, with perhaps some interaction with calcsilicate footwall rocks resulting in

lower $\delta^{18}\text{O}$ (Harris and Chaumba, 2001). Harris et al. (2005) similarly found that elevated $\delta^{18}\text{O}$ at Bushveld was likely due to contamination at depth, in a magma 'staging' chamber. Sulfur isotope analyses have been used to suggest magmatic fluid backflow into the country rock, rather than from the country rock into the intrusion, occurred at Bushveld (Penniston-Dorland et al., 2008). Ireland and Penniston-Dorland, (2015) measured lithium isotope variations at the base of the Bushveld Complex. They find deeper penetration of Li country-rock signatures (~60 m) compared to oxygen signatures (~4 m) but suggest that this is due to the higher diffusivity of Li rather than country fluid contamination. Chlorine isotopes suggest that Bushveld Cl is isotopically distinct from the country rocks (Willmore et al., 2002).

In contrast with this evidence are isotopic signatures consistent with a deeper penetration of country fluids into the Bushveld Complex. For example, Schiffries and Rye (1990) noted that although the $\delta^{18}\text{O}$ of the late-stage veins that cut the Bushveld was controlled by isotopic exchange with the Bushveld intrusive rocks, the $\delta^{13}\text{C}$ and δD was inherited from the Transvaal rocks. Buick et al. (2000) had a similar interpretation. In addition, Mathez and Waight (2003) noted Pb isotopic disequilibrium between plagioclase and sulfide of the Upper Critical Zone. They suggested that some of the Pb originated from the isotopically distinct country rocks and was introduced at temperatures at which the composition of sulfide but not plagioclase could be modified. Chutas et al. (2012) suggested much of that same thing to explain Sr disequilibrium

between plagioclase and orthopyroxene of the Critical Zone. They proposed that orthopyroxene was more likely to be affected by an infiltrating metasomatic agent as it underwent exsolution on cooling. Magalhães et al. (2018) found evidence of laterally homogeneous but stratigraphically variable crustal S signatures throughout the Bushveld Complex. The variations they observed were correlated to variations in $^{87}\text{Sr}/^{86}\text{Sr}$ and ϵ_{Nd} , although not systematically, which suggests the involvement of multiple contaminants. Although Magalhães et al. (2018) do not consider fluids due to lack of textural evidence, variations in S isotopes corresponding to Sr and Nd variations may indicate that these variations are also fluid-related. More recently, Schannor et al. (2018) suggested that higher initial $^{87}\text{Sr}/^{86}\text{Sr}$ of plagioclase in the UG2 chromitite and the footwall pyroxenite reflects infiltration of fluid derived from dehydrating country rocks beneath the Bushveld Complex. Zeh et al. (2020) analyzed Hf isotopes in zircon grains and found overlapping ϵ_{Hf} values in the RLS and the contact aureole which they suggested could have been achieved by aqueous fluid infiltration from the contact aureole.

In short, while a number of studies have examined variations in isotopic ratios throughout the Bushveld Complex, many have been limited in the scope they have considered. The majority examine isotopic alteration of the solid assemblage; in some cases, alterations that occurred during flux melting. While a number of studies note that isotopic variations throughout the Bushveld are likely related to country-rock

contamination, most do not look seriously at the possibility that fluids contaminated the magma. As this study will demonstrate, fluids have great potential to explain a large number of observed isotopic variations. In addition, this fluid ingress may have been distinctly channeled, as seen in the breccia pipes and other features; numerical models presented here highlight this fluid channeling.

2.5 Footwall Dehydration and Fluid Overpressure

The breccia pipe noted above points to the development of considerable fluid volumes and overpressure to drive pipe formation. Typical crustal rocks can lose 3–6% of their mass to dehydration during metamorphism (Connolly, 2010). This is equivalent to a body of water roughly 90–180 meters deep for each kilometer of rock dehydrated, and it is the release of this water that likely weakens the host rock and promotes diapir formation. Furthermore, the intrusion of the Bushveld magmas into previously unmetamorphosed sediments is rather unique; many other (large) intrusions are hosted by high grade metamorphic or granitic rocks. A comparison between the Bushveld and the Stillwater Complex in south-central Montana illustrates this difference. Comparing the H₂O contents of pelite as a function of temperature (Figure 6), the biotite schist that hosts the Stillwater Complex would have but a fraction of the H₂O content of a lower temperature shale or slate intruded by the Bushveld magma.

Furthermore, crystallization and thermal modelling of the Bushveld Complex show that a considerable thickness of crystal pile can accumulate prior to reaching the

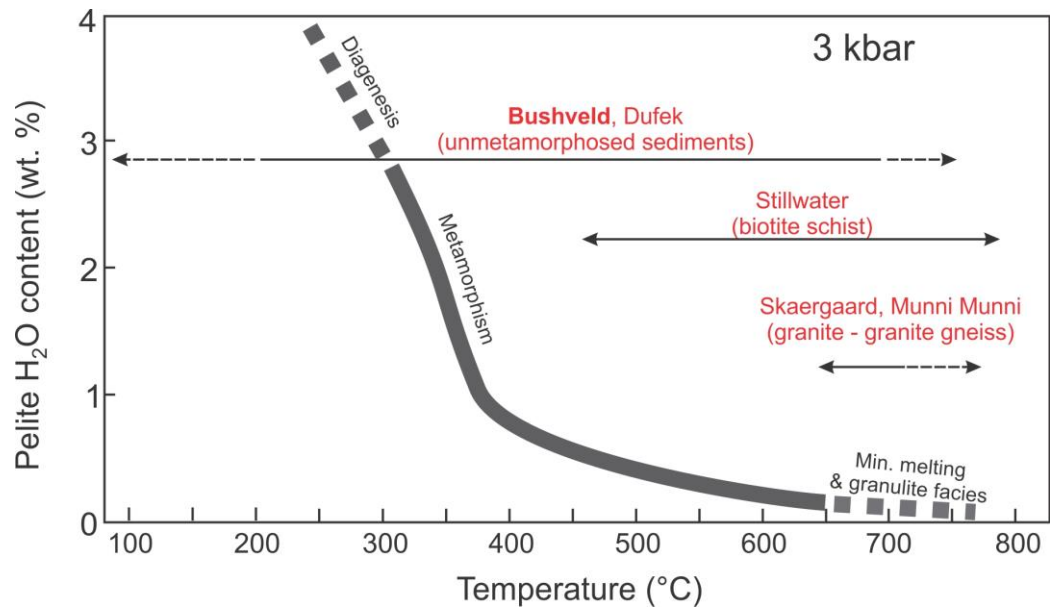


Figure 6: Progressive loss of H₂O in a typical pelite undergoing prograde metamorphism as a function of temperature at 3 kbar total pressure (after Connolly, 2010). Calculation assumes pure H₂O, and reactions involving CO₂ are ignored. Also noted are the approximate metamorphic temperatures seen in host rock prior to emplacement of some selected intrusions, as discussed in the text.

thermal maximum in the basement rock (e.g., Cawthorn and Webb (2013)). Near the base of the Layered series, temperatures of the igneous rocks and immediately underlying country rocks are similar and fluids moving from a pyroxene hornfels into a Bushveld pyroxenite can be in roughly chemical equilibrium. The influx of fluid may not be clearly evident in any obvious mineral reactions in the rock, in what one might term cryptic flow.

A first-order model for the understanding of how breccia pipes can develop during dehydration of the underlying country rock is shown in Figure 7 (after Connolly,

2010; Connolly and Podladchikov, 2013). In this figure, fluid is generated at the base of the sill by dehydration of the country rock; fluid generated within the intrusion is ignored. If the rocks are also undergoing compaction, then the lithostatic load pressing on the fluid at the base of the fluid generation zone will be transferred upwards by the fluid. Compaction at the base squeezes fluid upwards to the upper portion, producing a high porosity region where it is accommodated by dilational deformation. This process has the effect of propagating the reaction-generated porosity upwards and into the lower part of the sill. As long as fluid transport can keep up with the developing fracture

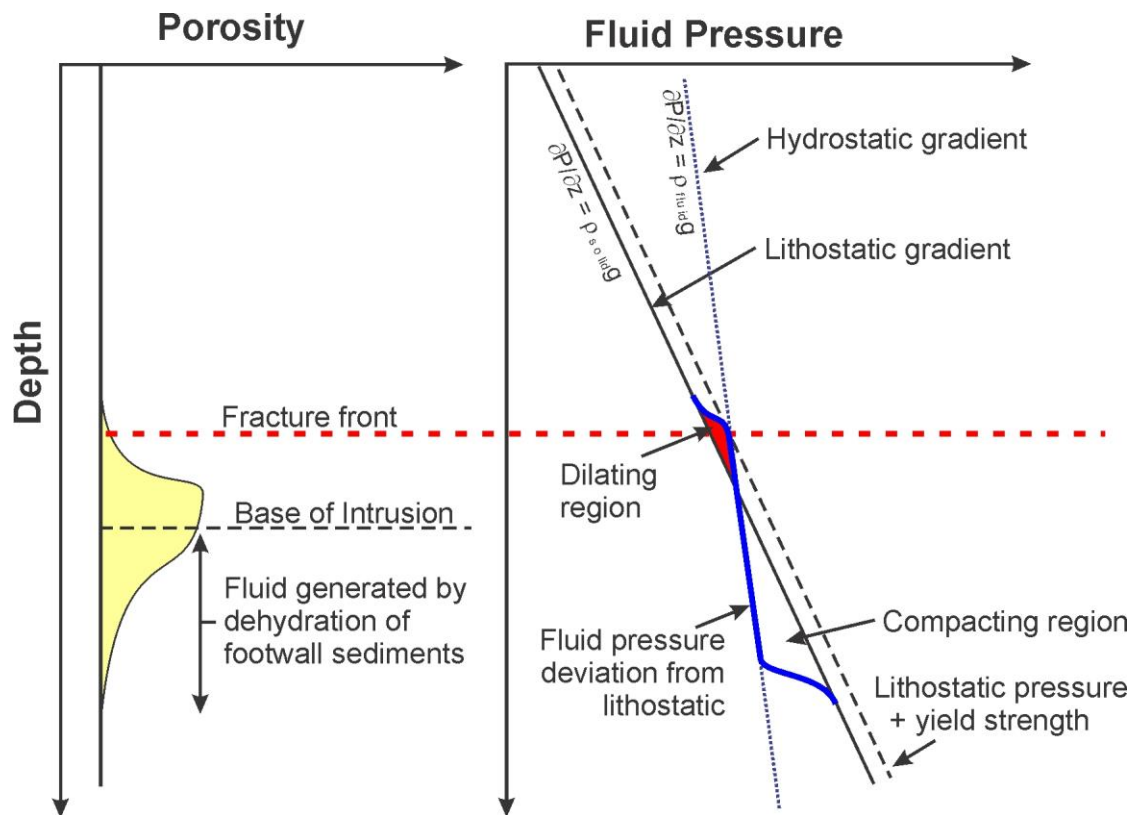


Figure 7: Schematic example of the generation of overpressured fluid by degassing and compaction of the lower portions of the Bushveld Complex and footwall sedimentary rocks (after Connolly, 2010; Connolly and Podladchikov, 2013). The

absence of footwall rocks in the diatrema suggests the overpressured fracture and brecciation began within the Lower Zone of the Bushveld Complex. Because the absolute pressure is depth-dependent, the overpressure is scaled relative to the difference between a lithostatic gradient for the rock and a hydrostatic gradient for the connected pore fluid. Compaction occurs where the lithostatic pressure exceeds the hydrostatic pressure, and dilation where the hydrostatic pressure exceeds the lithostatic pressure. The net effect is the upward movement of a high porosity (fluid-rich) region into the sill. See text for additional discussion.

network and if fluid flow is rapid enough, the result is brecciation and explosive injection of country fluid into the magma chamber. However, as shown in the numerical modelling below, the high porosity region can detach from the source when the compaction rate at the base becomes comparable to the fluid production rate, giving rise to solitary waves that propagate upwards independently of its source (Connolly and Podladchikov, 2013).

2.6 Isotopic Consequences of Fluid Injection into the Bushveld Magma Chamber

The possibility of country fluid contamination of the Bushveld magma adds an additional degree of freedom to Bushveld isotope geochemistry. Currently, isotopic variation between zones has made it challenging to fully understand the origin and development of the Bushveld Complex. Conventional contamination models have often relied heavily on high amounts of crustal contamination (30–40%, Maier et al., 2000; Harris et al., 2005) and/or magma mixing to explain isotope compositional variations in the Bushveld. For example, Maier et al. (2000) noted the Lower and Lower Critical Zone samples have similar Sr and Nd isotopic compositions compared to their assumed

parental magmas, the B1 sill and chilled margin. The B1 and the Lower and Lower Critical Zones also have similar incompatible trace-element ratios (e.g., Sm/La and Th/La). The Main Zone also has similar incompatible element ratios and Nd isotopes to its assumed parental magma, the B3 sill/chilled margin. However, the Main Zone rocks have distinctly more radiogenic Sr (0.708 vs. 0.7055) than does the B3 sill/chilled margin sample. These isotopic variations are illustrated in Figure 2. To explain these variations, conventional models of crustal contamination or magma mixing require some contortions, which can be relaxed under an assumption of country fluid contamination.

2.6.1 Mixing Model Assumptions

To illustrate the effect of vapor addition to the Main Zone magma, a number of simple mixing models are shown. A wide variety of isotopic studies have been conducted at Bushveld; some have been discussed above. These mixing calculations include Sr, Nd, O, H, S and Pb. For these calculations, the complication of isotopic disequilibrium, noted previously, is ignored. The composition of a fluid derived from Bushveld country rocks is not well-constrained. Thus, fluid concentrations of the isotopes in question are based on fluid inclusion studies from other locations, such as Sudbury. Parental magma compositions are limited by available data. Where possible, isotopic signatures of Marginal Zone rocks, particularly B3 samples generally considered to represent Main Zone parental magmas, are used in the calculation. Although these Marginal Zone samples may already be contaminated by assimilation of

Transvaal materials or deeper crustal rocks, the isotopic and trace-element ratio similarity between B1 and much of the Lower and Critical Zones suggests that the B3 is the best candidate for the original Main Zone magma. Furthermore, fluid contamination need not be the only source of crustal contamination in the intrusion; this work means only to highlight that it can contribute to contamination of the Bushveld. For isotope systems where Marginal Zone data are not available (S, Hf), parental magmas are assumed to be mantle-derived; assumptions for these isotopic systems are discussed in more detail below. All mixing models are shown in Figures 8 and 9. Details of the mixing models are as follows:

A Sr-Nd mixing calculation (Figure 8) is based on a parental magma of the B3 isotopic composition (Maier et al., 2000) and a poorly constrained fluid. The Sr content of the vapor (4400 ppm) is that reported for average Sudbury brine inclusions (Hanley et al., 2005) and is assumed to have an initial Sr isotopic composition of a Bushveld footwall schist ($Sr_i = 0.722$; Maier et al., 2000). For Nd, fluid concentrations of 10, 20 and 30 ppm are shown; 10 ppm is a high value also from Sudbury fluid inclusions (again, from Hanley et al.). A typical upper crustal ϵ_{Nd} of -17 is used for Nd (also from Maier et al.). Nd and Sr data for the Bushveld Complex Main Zone are taken from Maier et al. (2000) as well.

In mixing $\delta^{18}O$ and δD , the parental magma was assumed to approximate the lowest $\delta^{18}O$ and δD of Marginal Zone samples. Also shown on this mixing diagram are

the isotopic compositions of several potential magmatic source regions for the Bushveld, including MORB ($\delta^{18}\text{O} = 5.7\text{‰}$; Ito et al., 1983; Kyser and O'Neil, 1984; Eiler, 2001, $\delta\text{D} = -80\text{‰}$; Kyser and O'Neil, 1984), boninite ($\delta^{18}\text{O} = 6.5\text{‰}$; Kyser et al., 1986, $\delta\text{D} = -55\text{‰}$; Dobson and O'Neil, 1987), and komatiite ($\delta^{18}\text{O} = 5.2\text{‰}$, Lahaye and Arndt, 1996; $\delta\text{D} = -140\text{‰}$, Stone et al., 2003). The 'true' parental magma(s) of the Bushveld Complex are a matter of some debate (e.g., Barnes, 1989). We suggest the Marginal Zone values of $\sim 6.8\text{‰}$ used as parental compositions have experienced assimilation of dry crustal

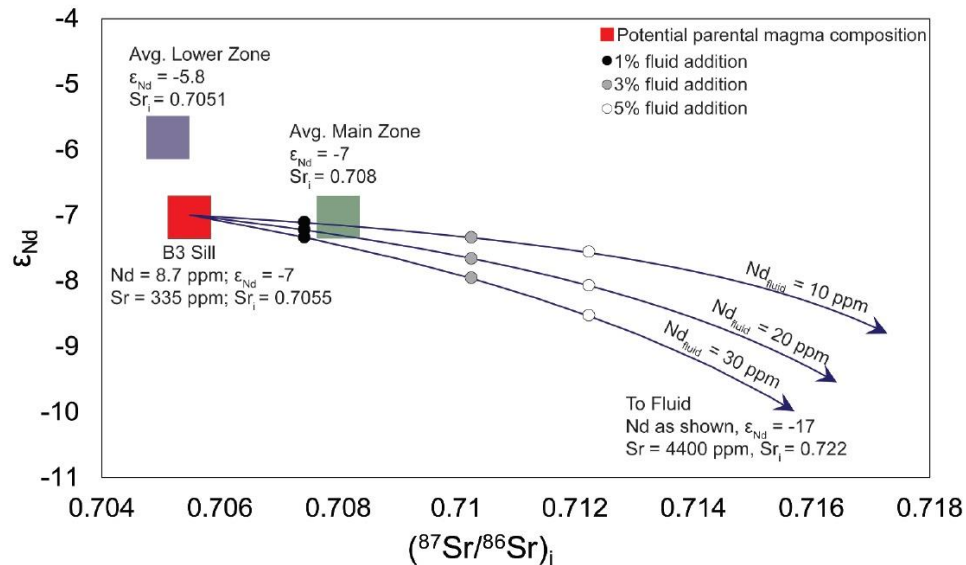


Figure 8: A fluid-magma Sr-Nd isotope mixing model for the Main Zone rocks (relative to the presumed initial Main Zone magma, denoted 'B3') of the Bushveld Complex. Endmember mixing components are as listed, and the points on the mixing line indicate 1% (black), 3% (grey), and 5% (white) weight fraction of vapor in the mixed composition. The three mixing lines are for different Nd concentrations in the endmember vapor as labeled. The compositions of the B3 magma, the Lower Zone, and the Main Zone are shown by the colored boxes labeled 'B3 Sill', 'Avg. Lower Zone', and 'Avg. Main Zone', respectively.

material that substantially altered $\delta^{18}\text{O}$ but not δD . Concentrations of O are calculated from the total O contents of average B3 samples (Sharpe, 1981). H contents of a typical mantle magma are calculated at approximately 300 ppm, based on H_2O contents of a typical MORB (0.17–0.51 wt. %, Sobolev and Chaussidon, 1996). Country fluid isotopic compositions were estimated based on country-rock measurements as well as analyses of fluid inclusions. $\delta^{18}\text{O}$ in the metamorphosed hornfels of the Transvaal Supergroup range from 9‰ to 15‰ (Schiffries and Rye, 1989); fluid fractionation has the potential to raise this by a few per mille (Shieh and Taylor, 1969), bringing $\delta^{18}\text{O}$ to 20‰. δD values from a number of sources suggest a wide range of possible values for country-rock hydrogen isotopes. Schiffries and Rye (1990) identified a δD range of –71‰ to –29‰ from fluid inclusions. The hydrogen concentration in a dehydrated fluid is poorly constrained; we use 11% H concentration as a maximum estimate. Also shown are $\delta^{18}\text{O}$ (Schiffries and Rye, 1989, 1990; Harris et al., 2005) and δD (Mathez et al., 1994; Willmore et al., 2002; Harris et al., 2005) from the Bushveld Complex itself.

Several authors have noted distinct Pb isotopic disequilibrium between minerals in Bushveld samples (e.g., Mathez and Waight, 2003; Mathez and Kent, 2007; Chutas et al., 2012). This has been suggested to be the result of alterations to Pb isotopic composition of some minerals (such as sulfides) around the time of crystallization, but after certain minerals (such as plagioclase) had closed to isotopic alteration. The low U contents of relevant minerals suggest no radiogenic in-growth to impact initial Pb

isotopic compositions, although the mobility of U means this is not a guarantee (Harmer et al., 1995; Mathez and Waight, 2003); Bushveld Pb isotopic ratios are assumed to represent true initial ratios. Pb typically shows evidence of substantial alteration during cooling, while plagioclase shows less evidence of this due to an earlier closure. Pb contents in an initial Bushveld parental magma would be low; because Pb is mobile, a fluid can be highly Pb-enriched relative to the parental magma. B3 compositions suggest a parental magma for the Bushveld may have contained roughly 1.5 ppm Pb (Harmer et al., 1995). Fluid inclusions from Sudbury have Pb concentrations of 1.03 wt. % (10,300 ppm); reducing this by a factor of 10 in the event of low Pb concentrations in Transvaal sediments brings this value to 1,030 ppm for the fluid. B3 magmas contain $^{206}\text{Pb}/^{204}\text{Pb}$ of 16 and $^{207}\text{Pb}/^{204}\text{Pb}$ of 15.4 (Harmer et al. 1995). The question of the Pb isotopic ratios in Transvaal sediments is complicated by the issue of Pb and U mobility as well as radiogenic ingrowth. While Pb isotopic ratios have been measured in a number of Transvaal sedimentary groups (dolomites, Jahn et al., 1990; Campbellrand Supergroup, Sumner and Bowring, 1996; Black Reef pyrites; Barton and Hallbauer, 1996), radiogenic ingrowth and subsequent Pb loss have made reliable calculation of initial Pb compositions challenging. For this reason, the mixing plot for Pb shows mixing for several possible initial isotopic compositions, based in part on standard upper crust Pb ratios and in part on discussions of measured Pb ratios and calculated μ values in Transvaal sediments. Because the $\text{Pb}_{\text{fluid}}/\text{Pb}_{\text{magma}}$ ratio would have been high, the

unconstrained initial Pb ratios of the sediments are the largest source of error in this calculation. However, Figure 9b shows that alteration of magmatic Pb isotope ratios can occur with little fluid addition.

S isotopes have two common isotopic signatures that are analyzed; $\delta^{34}\text{S}$ tracks mass-dependent fractionation while $\Delta^{33}\text{S}$ is a measure of mass-independent fractionation caused by Archaean atmospheric conditions (Farquhar and Wing, 2003). Analyses of both S isotopic measurements have been made throughout different limbs of the Bushveld Complex (e.g., Sharman-Harris et al., 2005; Penniston-Dorland et al., 2012).

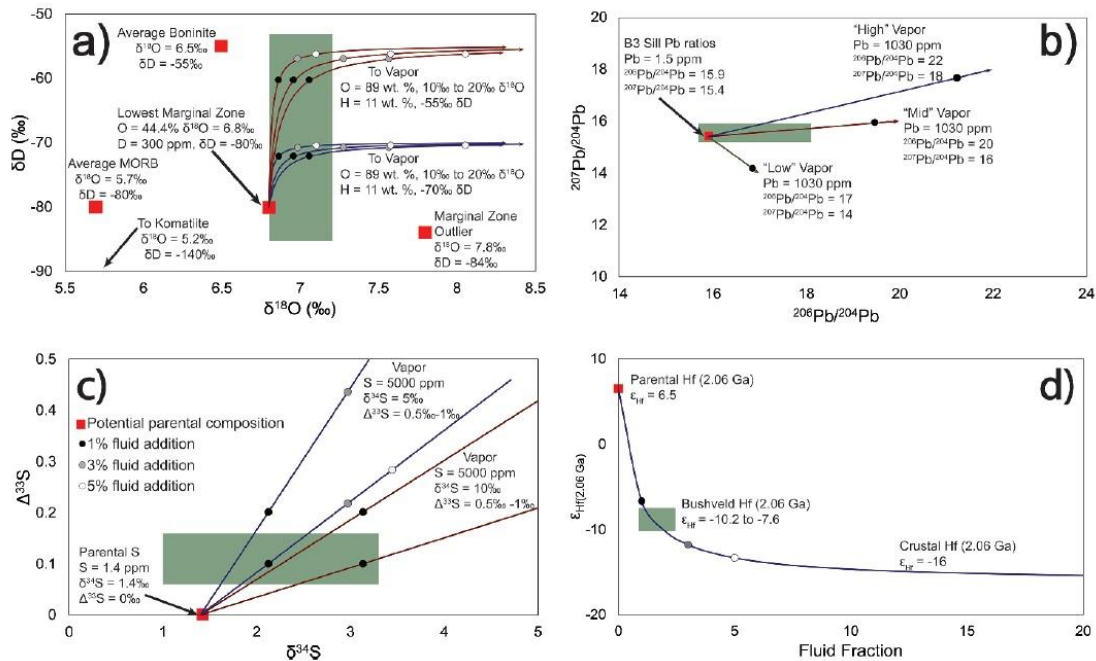


Figure 9: Examples of fluid-magma mixing models. In all mixing models, the red boxes highlight potential parental magma compositions. Black, grey, and white points on mixing curves indicate 1%, 3%, and 5% fluid addition, respectively. A) A fluid-magma mixing model explaining alteration in $\delta^{18}\text{O}$ and δD compositions throughout the Bushveld Complex relative to a parental magma resembling the lowest Marginal Zone sample. Endmember mixing components are listed. The labelled lines show

differing fluid $\delta^{18}\text{O}$ compositions. Due to relative lack of variation in isotopic ranges for $\delta^{18}\text{O}$ and δD throughout the Bushveld Complex, the Bushveld as a whole is displayed as one region on the plot. B) A fluid-magma mixing model for $^{207}\text{Pb}/^{204}\text{Pb}$ and $^{206}\text{Pb}/^{204}\text{Pb}$ variation in the Bushveld Complex. Due to the high Pb contents of the fluid relative to the magma, mixing is strongly dominated by potential country-rock fluid Pb sources. Each mixing lines indicates a different potential source. D) A fluid-magma mixing model for S isotopes, showcasing both $\delta^{34}\text{S}$ and $\Delta^{33}\text{S}$ variation. Blue lines use vapor $\delta^{34}\text{S}$ of 5‰ while red lines use vapor $\delta^{34}\text{S}$ of 10‰. $\Delta^{33}\text{S}$ for the vapor is either 0.5‰ (lower mixing line) or 1.0‰ (upper mixing line). D) A fluid-magma mixing model for ϵ_{HF} variation, plotted against fluid fraction. Green box at shows Bushveld composition at the time of emplacement.

Multiple sulfur isotope studies of the eastern and western limbs of the Bushveld found $\Delta^{33}\text{S} = 0.06\text{--}0.16\text{‰}$ and $\delta^{34}\text{S} = 1.0\text{--}3.6\text{‰}$ (Penniston-Dorland et al., 2012a; Magalhães et al., 2018). Two samples measured by Magalhães et al. (2018) were found to have much lower $\delta^{34}\text{S}$ of 0.58‰ and -1.19‰ . These samples were outliers compared most other samples and may reflect less contamination or assimilation of country-rock sulfur from a different source (e.g., Transvaal pyrite with negative $\delta^{34}\text{S}$; Strauss and Beukes 1996). Mantle $\delta^{34}\text{S}$ and $\Delta^{33}\text{S}$ are well established at $0 \pm 2\text{‰}$ and $0 \pm 0.03\text{‰}$, respectively (e.g., Ripley et al., 1999; Farquhar et al., 2002). Labidi et al. (2012), using a different extraction technique, found a more narrow range of -1.8‰ to 0.02‰ for $\delta^{34}\text{S}$ originating from the DM (depleted mantle) reservoir; modelling isotope mixing with their average DM $\delta^{34}\text{S}$ of 0.91‰ resulted in mixing lines shifted somewhat towards lighter $\delta^{34}\text{S}$ values and carrying most mixing lines out of the range of Bushveld S isotope values. However, Sharman-Harris et al. (2005) suggest a $\delta^{34}\text{S}$ value of 1.4‰ as the original parental composition based on sulfide inclusions from beneath the craton; this is the value used

in S isotope modelling shown in Figure 9c. 0‰ is used as the $\Delta^{33}\text{S}$ parental value for S isotope mixing calculations. Unaltered mantle is thought to contain ~200 ppm S (Nielsen et al., 2014). S contents of a hydrothermal vapor or fluid phase are poorly quantified due to the difficulty in detecting sulfur-bearing species in fluid inclusions (Pokrovski et al., 2005). A fluid concentration value of 5000 ppm is chosen for S as a conservative, rough estimate of S alone. Transvaal sediments exhibit a wide range of $\delta^{34}\text{S}$ values; Penniston-Dorland et al. (2012) use -0.4‰ to 5‰ for $\Delta^{33}\text{S}$ and Strauss and Beukes (1996) find a $\delta^{34}\text{S}$ range of ~3-20‰. Because high values of S isotopes are not common, mixing calculations for S isotopes utilize mid- to low-range values of $\delta^{34}\text{S} = 10‰$ and $5‰$ and $\Delta^{33}\text{S} = 1‰$ and $0.5‰$, respectively.

The Bushveld Complex has observed Hf isotopic compositions that differ substantially from those that would be found in a theoretical komatiite parental magma. Zirakparvar et al. (2014), VanTongeren et al. (2016), and Zeh et al. (2020) have explored Hf isotopes in zircons at Bushveld and associated sediments. Zirakparvar et al. and VanTongeren et al. found relatively uniform Bushveld $\epsilon_{\text{Hf}}(2.06 \text{ Ga})$ values of $-8.6 (\pm 2.6)$, Zirakparvar et al.; ± 1.2 , VanTongeren et al.) for 2.06 Ga (Bushveld emplacement). Zeh et al. (2020) found a range in $\epsilon_{\text{Hf}}(2.06 \text{ Ga})$ in Bushveld Complex mafic floor rocks of -10.2 to -7.6 . In lieu of more specific Hf constraints on a parental magma for Bushveld, a komatiite parent is assumed (Barnes, 1989; Zirakparvar et al., 2014). A komatiite magma would have $\epsilon_{\text{Hf}}(2.06 \text{ Ga})$ of $+6.5$ (Zirakparvar et al., 2014). Komatiite magmas have Hf

concentrations of ~0.715 ppm (again from Zirakparvar et al., 2014). Transvaal sediments exhibit a range in $\epsilon_{\text{Hf}}^{(2.06 \text{ Ga})}$ values; the Hf mixing model here utilizes $\epsilon_{\text{Hf}}^{(2.06 \text{ Ga})} = -16$ (Zeh et al., 2020). Fluid incorporation of Hf is a complicating factor. As a HFSE, Hf typically experiences low mobility in aqueous fluids, instead migrating during partial melting (e.g., Barry et al., 2006). However, there is evidence that fluid Hf enrichment of a few hundred ppm can occur under certain circumstances (e.g., Zeh et al., 2010; Zeh and Gerdes, 2014). For this reason, the Hf mixing model uses a fluid Hf concentration of 200 ppm.

2.6.2 Discussion of Model Results

Taken together, these mixing calculations demonstrate that the addition of roughly 1 wt. % of a country fluid can pull the B3 composition towards the more typical Main Zone isotopic composition. Assuming that the 3.5 km thick Bushveld aureole (to 500°C isotherm) generated 3–6 wt.% H₂O, the addition of 1–2 wt.% vapor to the 2–3 km enriched section of the Main Zone would require about a third to half of vapor generated from footwall dehydration was injected into the Main Zone. Table 1 provides a summary of the impact of this amount of fluid on the various isotopic systems for which there are sufficient data at the Bushveld Complex. Some isotopes are more strongly impacted than others. For example, δD and Sr are relatively sensitive to the addition of vapor, while $\delta^{18}\text{O}$ and Nd are less sensitive. This is likely due to relative concentrations of these elements between the vapor and the parental magma; higher

concentrations of an element in the parental magma leads to the vapor having a less noticeable comparative impact. Table 1 includes the expected isotopic shifts of several isotopic systems not shown in Figure 9. These include chlorine, carbon, and lithium. Few studies have been conducted on these isotopic systems at Bushveld (Cl, Willmore et al., 2002; C, Pronost et al., 2008; Li, Ireland and Penniston-Dorland, 2015). However, these isotopic ratios can also experience substantial alteration from a small amount of fluid; further investigations into these systems are required to better identify large-scale alterations from expected magmatic values.

Table 1: Effect of 1% fluid addition in modification of B1 isotopic composition. The effect on B3 magma is similar.

System	Parental Magma		Sediment-Derived Fluid		Effect of 1% fluid addition
	Conc (ppm)	Int. Value (2.06 Ga)	Conc (ppm)	Int. Value (2.06 Ga)	
Radiogenic Isotopes					
⁸⁷ Sr/ ⁸⁶ Sr	158	0.705	4,400	0.722	+0.002
¹⁴³ Nd/ ¹⁴⁴ Nd	20	$\epsilon_{Nd} = -5.8$	20	$\epsilon_{Nd} = -17$	$\Delta\epsilon_{Nd} = -0.2$
¹⁷⁶ Hf/ ¹⁷⁷ Hf	0.715	$\epsilon_{Hf} = 6.5$	200	$\epsilon_{Hf} = -16$	$\Delta\epsilon_{Hf} = -1.2$
²⁰⁶ Pb/ ²⁰⁴ Pb	1.5	15.9	1030	17 to 22	+1 to +5
²⁰⁷ Pb/ ²⁰⁴ Pb	1.5	15.4	1030	14 to 18	-1 to +2
Stable Isotopes					
¹⁸ O/ ¹⁶ O	440,000	$\delta^{18}O = 5.7\text{‰}$	890,000	$\delta^{18}O = 10 \text{ to } 20\text{‰}$	+0.2‰
D/H	600	$\delta D = -80\text{‰}$	110,000	$\delta D = -70 \text{ to } -50\text{‰}$	+10 to 20‰
³⁷ Cl/ ³⁵ Cl	500	$\delta^{37}Cl = 3.0\text{‰}$	50,000	$\delta^{37}Cl = 1.0\text{‰}$	-1‰
¹³ C/ ¹² C	200	$\delta^{13}C = -5.0\text{‰}$	10,000	$\delta^{13}C = -2.5\text{‰}$	+1‰
³⁴ S/ ³² S	200	$\delta^{34}S = 1.4\text{‰}$	5000	$\delta^{34}S = 5 \text{ to } 10\text{‰}$	+1.7‰
$\Delta^{33}S$	200	$\Delta^{33}S = 0\text{‰}$	5000	$\Delta^{33}S = 0.5 \text{ to } 1\text{‰}$	+0.1 to 0.2‰
⁷ Li/ ⁶ Li	1.5	$\delta^7Li = 3.0\text{‰}$	200	$\delta^7Li = 20\text{‰}$	+9‰

Theoretically, the fluid could also be contaminated by the Lower Zone rocks it passes through. However, the fluid is relatively insensitive to this potential contaminate. This is again due to relative concentrations; typical Lower Zone concentration of Sr and Nd is about 20–40 ppm and 1–2 ppm, respectively (Maier et al., 2000). These values are largely controlled by the amount of trapped liquid. While fluid contamination by Lower Zone rocks is possible and would tend to pull the fluid towards a higher ϵ_{Nd} , this would require equilibration with a substantial mass of Bushveld rock.

In comparison to the results of other contamination models (e.g., Maier et al., 2000; Harris et al., 2005; Penniston-Dorland et al., 2012; Zirakparvar et al., 2014), our results demonstrate a need for substantially less contamination. Maier et al. (2000), analyzing Nd and Sr isotopes, found that pulling Bushveld parental magmas to the modern measured isotope signatures required that as much as 40 to 50 wt. % of the Main Zone be crustal in origin. Harris et al. (2005) suggested that mixing $\delta^{18}O$ between crust and parental magma would require 38% contamination. Similarly, Zirakparvar et al. (2014) suggested that producing the observed $^{176}Hf/^{177}Hf$ shifts would require incorporation of 80% Hf from the crust. Because a fluid will preferentially incorporate and become enriched in some elements, a crustal fluid source for this same contamination requires much less addition of the contaminant. As shown in Table 1 and Figures 8 and 9, 1–2 wt. % of a fluid (which can realistically be generated by Bushveld emplacement) can be responsible for observed shifts in isotopic ratio. Because

incorporation of 30% or more crustal material would have additional resulting complications, we suggest that Main Zone equilibration with a smaller amount of fluid is reasonable.

2.7 Modeling Fluid Migration Associated with the Footwall Metamorphic Aureole

2.7.1 A Quantitative Model of Fluid Flow During Dehydration of the Floor Rocks

To illustrate the pattern of metamorphic fluid flow that might have arisen beneath the Bushveld Complex, a 2-dimensional thermomechanical finite-difference model was used to simulate metamorphic devolatilization and compaction-driven fluid expulsion beneath the sill (Connolly and Podladchikov, 2007; Connolly, 2010; Figure 10). The spatial domain is a 1 km wide section that extends from the surface to 20 km depth and is resolved with a nodal spacing of 20 m. The sill is 8 km thick and emplaced instantaneously at 6 km depth in crustal rocks with a geothermal gradient of 30 K/km. Only part of this spatial domain is shown in Figure 10, which is centered on the lower contact of the sill. The initial temperature of the sill is its assumed liquidus (1500 K). The solidus temperature is taken to be 1200 K, and the latent heat of crystallization (0.3 MJ/kg) is released as a linear function of temperature. For simplicity, a single muscovite dehydration reaction is considered with kinetic and thermodynamic parameters after Connolly (1997a). The equilibrium dehydration temperature immediately below the sill is ~850 K (and increases with depth by ~36 K/km) and is thus roughly 370 K below the

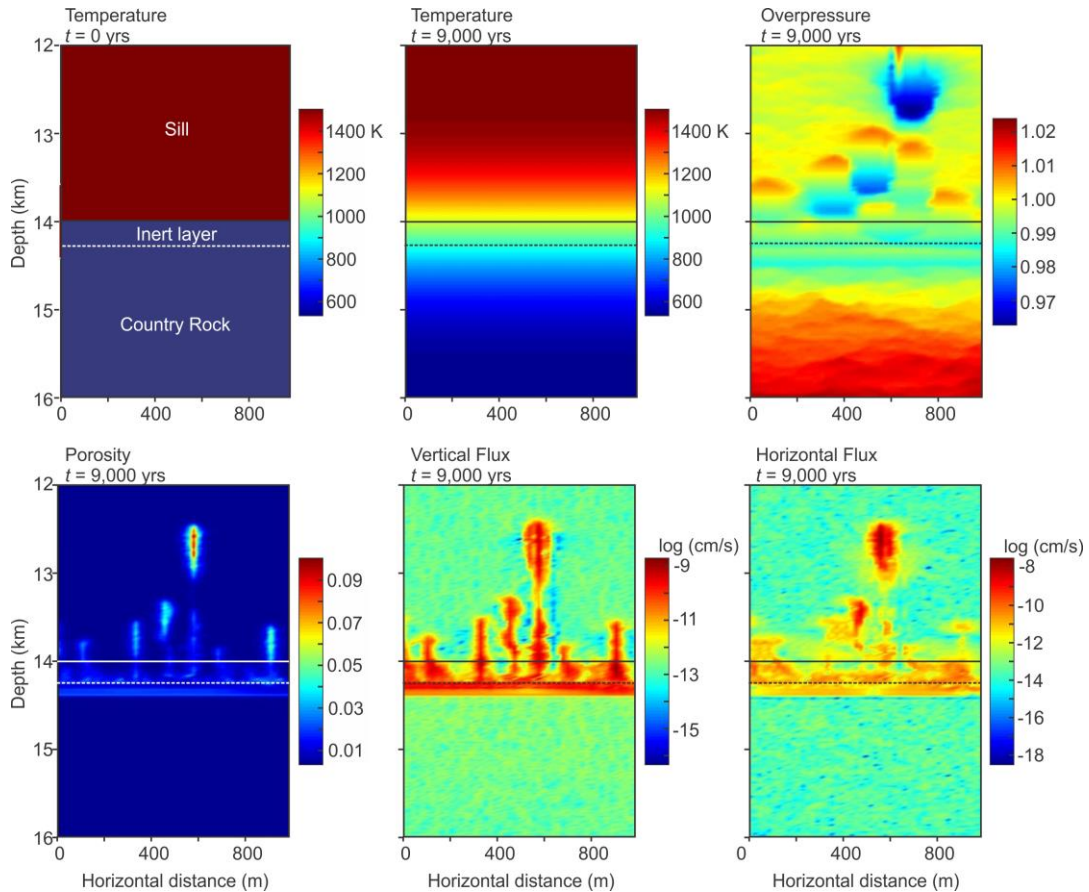


Figure 10: Numerical model of footwall dehydration and volatile plume formation. Upper left shows the initial condition of a hot sill intruded into sediments with a geothermal gradient ranging from 573 K at the bottom to 1473 K at the top at $t = 0.0$. A 200 m thick inert layer is included at the top of the country rock to mimic the Magaliesberg quartzite and to improve numerical stability. All other figures show the system after $t = 9,000$ years. Upper center and upper left shows the thermal profile and overpressure. The bottom three figures show the porosity, vertical, and horizontal flux, respectively. The steep front of vapor flux at the base of the metamorphic aureole mimics the steep fluid generation front (not shown). A video of the numerical model is available as part of the on-line supplemental material. See text for additional discussion.

initial temperature of the footwall rock. A 200 m thick inert layer is included at the top of the country rock to mimic the Magaliesberg quartzite and to improve numerical stability.

Fluid expulsion is assumed to be initially controlled by the rate at which viscous compaction collapses the fluid-filled porosity generated by the dehydration process. Once a wave has nucleated its properties are independent of what happens in the source, that rate of wave propagation depends on rock and fluid viscosities and densities. Furthermore, it is assumed that embrittlement caused by the generation of high fluid pressures by dehydration and/or compaction can be characterized by a reduced effective viscosity. The governing equations are for the flow of a low viscosity fluid through a viscous solid with finite porosity. In applying this model to the lower portion of the Bushveld Sill, the assumption is made that the crystal mush can be approximated as a porous low viscosity solid. In reality, the true three-phase system (silicate-liquid, water-rich fluid, and solid) is likely to be substantially more complex. In particular, water released by dehydration of the footwall rocks will both dissolve in the silicate liquid and lower the solidus of the silicate liquid. In view of these simplifications, the viscous rheology of both the country rocks and crystal mush is taken to follow a single power-law constitutive relation based on the properties of quartz (Paterson and Luan, 1990), likewise the permeability (k) of both mush and country rock is characterized by a single power law relation with porosity (Φ). Both the country rocks and sill are assigned a small initial porosity randomly distributed in the range 0.05–0.15%.

Previous work (Connolly and Podladchikov, 2007) has shown that fluid flow in this scenario is channeled into pipe-like structures with a characteristic spacing comparable to the viscous compaction length (δ) and that the width of the channels varies inversely with the weakening caused by high fluid pressure. Because the channels have radial symmetry in 3-dimensions, the 2-D geometry of the model does not accurately capture the relation between metamorphic fluid production and channelized fluid flux. Aside from the fluid flux itself, this deficiency has the consequence that heat advection by the fluid; a cooling effect in the lower portion of the sill is not accurate. In the model, this effect is insignificant and earlier work (Connolly, 1997b) suggests it would likewise be insignificant in 3-dimensional models.

The viscous compaction mechanism by power-law creep is thermally activated such that the effective solid viscosity, and therefore the viscous compaction length within the mush and the underlying rocks, can be expected to vary by at least six orders of magnitude due to temperature effects alone. After solid rheology, the initial porosity is the most important factor controlling the compaction length and time (τ) scales, specifically, $\delta \propto \sqrt{\phi}$ and $\tau \propto \delta \phi^2 \propto 1/\phi^{3/2}$ (Connolly and Podladchikov, 2015). Given that the Bushveld Sill was emplaced in shallow unmetamorphosed sediment, the initial porosity used here may underestimate the true porosity of the unmetamorphosed sediments by an order of magnitude. Such an underestimate would increase the length

scale for compaction-generated processes by roughly a factor of three, while reducing their timescale by a factor of 0.03.

The present numerical simulation differs from previous models of channelized metamorphic fluid flow induced by decompression weakening (Connolly, 2010), in that the viscous mechanism is power-law rather than linear creep and that it accounts for the temperature dependence of the viscous mechanism. The latter detail has the consequence that the model has no intrinsic compaction length, although it is possible to evaluate the local compaction length. The numerical results of Figure 10 show that despite these differences, channelization does develop and, in the specific case considered, develops with a characteristic spacing of ~125 m. This characteristic spacing is likely influenced by a number of factors that have not been investigated individually, but variations that increase the local compaction length and/or decrease the rate of devolatilization likely will increase the characteristic spacing. Because the channel-forming mechanism results in compaction of the surrounding rocks (Connolly and Podladchikov, 2007), once the initial set of channels form then all subsequent fluid flow exploits the existing channels and, because the local compaction length decreases upwards due to the inverted thermal gradient, there is no tendency for the channels to coalesce. These generalizations assume a homogeneous metamorphic source. Strong source heterogeneity (i.e., floor diapirs) would likely lead to flow events with larger spatial variability.

Likewise, this simulation differs from previous numerical models of diapirism in the Bushveld Complex (e.g., Gerya and Yuen, 2003). Their model relied on diapir nucleation at the site of a pre-existing anticlinal fold on the intrusion floor. Reducing the size of the fold reduced the size of the diapir or eliminated it altogether. Gerya and Yuen's (2003) modeling of cold diapirism in layered intrusions thus suggest that without specific floor geometries (i.e., high initial anticlines formed during initial magma intrusion), diapirism cannot develop. It is here suggested that the channelized flow of fluids released during dehydration melting or otherwise induce localized weakening of the floor rocks.

2.7.2 A Qualitative Model

A semi-quantitative model that combines the fluid transport numerical model and field observations noted here with the quantitative model of the thermal evolution of the Bushveld Complex and surrounding country rock by Cawthorn and Webb (2013) as well as the floor diapir formation model of Gerya et al. (2004) is shown in time sequence diagrams of Figure 11. Over time, this sill is allowed to both crystallize owing to heat loss out the bottom and top (forming a growing crystal pile at the base of the sill) and inflate to a final thickness of 8 km. The model is illustrated in four major steps (a-d in Figure 11). Figure 11a presents the initial condition of a 2 km thick sill injected 2 km below the surface. Following Gerya et al., it is assumed the floor has topographical irregularities that form the sites of eventual dome/diapir formation. In Figure 11b, after

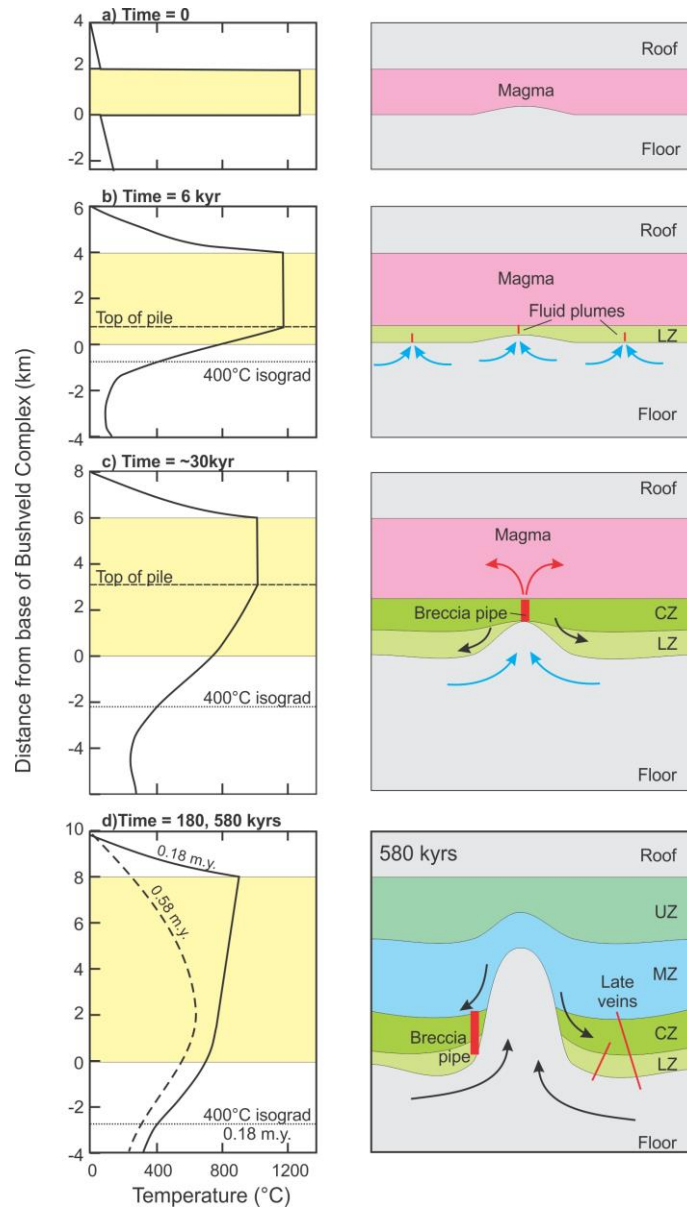


Figure 11: Semi-quantitative model of the thermal evolution of the Bushveld Complex and surrounding country rock, floor diapir formation, and breccia pipe emplacement at different times after initial emplacement as shown. Thermal evolution, inflation, and crystallization model is after Cawthorn and Webb (2013), diapir development is broadly after Gerya et al. (2004), and the quantitative model of fluid generation and transport of this study. Note that the maximum extent of the floor heating (and hence dehydration) occurs at about the same time the Main Zone begins to crystallize, and stays hot for at least a half million years.

6,000 years, the sill has grown the 4 km thick and formed much of the Lower Zone.

Heating and dehydration of the floor rocks lead to numerous fluid plumes percolating into the Lower Zone section (blue arrows). Injection of these fluids could give rise to the minor excursion in Sr and other isotopes seen in the Lower and Critical Zones.

After about 30,000 years Figure 11c, the sill has grown to 6 km thick. It is about this time that the maximum heating and dehydration of the floor rock occurs. Growth of the diapir leads to a preferential flow of fluid focused into the diapir and into the sill, resulting in the formation of a breccia pipe and injection of large volumes of fluid into the magma chamber above the crystal pile. Deformation of the crystal pile in response to the intrusion of the diapir starts to speed up (black arrow). Although not shown, it is assumed that fluid injection into the Bushveld chamber is minimal once the maximum extent of thermal heating and dehydration of the country rock is reached during crystallization of the Main Zone. New injections of magma during the crystallization of the Upper Zone pull the isotopic compositions back towards mantle compositions with only minimal country fluid contamination at this point.

After 180,000 years Figure 11d, growth of the sill is to 8 km and crystallization is complete (solid temperature profile). The intrusion continues to cool, however, and even after 580,000 years (dashed temperature profile) the floor rocks remain hot, allowing diapir growth to continue, but very little additional dehydration fluid is generated after about 30,000 years. Over time, the earlier formed pipes are pushed to the flanks of the

diapir as the domes continue to intrude and deform the Bushveld Layered Series. As the system eventually cools, fractures and veins can form in the increasingly brittle rocks as temperatures fall below 700°C (Schiffries and Rye, 1990).

In summary, heating of the Transvaal sediments resulted in a) generation of diapiric upwelling and b) generation of large volumes of fluid. The combined effect is that inflow of country fluids is focused by the developing domes, leading to continued fluid inflow into the growing dome even as the rocks themselves dehydrate. This inflow enhances both local melting of the country rock and the growth of the dome itself.

There are numerous caveats to the above model. For example, the filling of the magma chamber could be a continuous or aperiodic process. Aperiodic infilling and inflation of the Bushveld magma chamber can lead to relatively abrupt increases in the pressure in the underlying Transvaal sequence. The marked changes in isotopic composition of the Bushveld rocks noted in Figure 2 have been attributed to major periods of chamber growth (e.g., Kruger, 1990). However, the added weight of the Main Zone magma during rapid inflation of the Bushveld chamber could have triggered the sudden loss of over-pressured gas, in what one might consider to be the world's largest whoopee cushion effect.

The brecciation seen in the diatreme implies the top of the pipe had a free surface in which to expel the blocks. This is most readily accomplished by allowing the country fluids to reach the top of the crystal pile and enter the magma chamber. Evidence of

melting of existing mush on the floor of the magma chamber suggested by Eales et al. (1988) might be one result of a lower liquidus temperature resulting from fluid-magma mixing. The formation of chromite as a restite mineral is another possible result of an incongruent hydration-induced partial melting event (e.g., Schannor et al., 2018). Deeper in the pile, infiltrating country fluids may be affected by the inherently anisotropic nature of layered intrusions and locally move laterally along more permeable layers.

For the country fluid, the main pathways into the chamber are primarily by channeled pipe-like porous flow that can be rapid enough to induce brecciation of the more solidified parts of the crystal pile at high temperatures where fluids are focused by floor structures such as the developing diapirs. Away from the channeled inflow of country fluids into the Bushveld Complex, the igneous rocks near the base of the intrusions may show little evidence of this fluid influx; the rock would preserve their initial isotopic signature, for example.

Finally, the fluid flow model shown in Figure 10 illustrates that the country fluid incursion produces highly permeable pipes that can have a horizontal flow component that can drain interstitial igneous fluids generated during the crystallization of the surrounding mush. This is supported by the work of Peyerl (1982), who noted that the PGE mineralogy in the surrounding host rock, particularly the distal chromitite layers, has been affected out to 1–2 km beyond the margins of the PGE-enriched pipes. This would suggest that the secondary dunite pipes and their associated PGE mineralization

developed by the inflow of mineralizing fluid from the surrounding crystal pile largely as envisioned by Schiffries (1982).

2.8 The Subduction Zone Connection

2.8.1 Subduction Zone Fluids and Mantle Diapirs

Subduction zones play a key role in the dynamics of the Earth, generating high-magnitude deep earthquakes and potentially transporting material to the mantle-core boundary. This system of recycling oceanic crust is linked to the origin and growth of continental crust (Rapp and Watson, 1995) and signatures from subducted materials have been identified in fresh oceanic crust (Ben Othman et al., 1989). Further, the mantle is a major reservoir for H₂O. Estimates suggest subduction zones deliver six times more H₂O into the mantle than is released back at the surface by arc volcanism, with this subducted H₂O likely stored, in part, as a free fluid phase above 200–300 km depth, and bound entirely in minerals below this depth (Thompson, 1992).

Subduction processes generate the melts that become arc volcanoes such as the 'Ring of Fire'. Study of the erupted materials at volcanic arcs provides much of the insight into slab dehydration and fluid circulation. Trace element and radiogenic isotope signatures both indicate a relatively large slab component, although trace-element measurements suggest a significantly higher amount of slab material than do isotopic signatures (Hawkesworth et al., 1993). Geochemistry of the NE Japan arc as well as numerical modelling of slab-fluid fluxed melting in the mantle wedge demonstrate

island arc volcanic activity is strongly driven by fluid-induced mantle melting (e.g., Kimura and Yoshida, 2006). The geochemical signatures of fluids released from subducted slabs have been identified in other volcanic arc magmas worldwide (e.g., Kent and Elliott, 2002; Bouvier et al., 2008). Additional numerical modelling suggests that even in arc materials that exhibit minimal to no trace element or isotopic slab signature, H₂O is required to generate island arc basalts (Ayers, 1998). Slab fluids are estimated to migrate relatively quickly through the mantle wedge, with typical transfer times of approximately 30,000 to 120,000 years indicated by ²³⁸U-²³⁰Th disequilibrium (Hawkesworth, 1997). While there is little doubt that the lithospheric slab dehydrates as it descends, it is uncertain as to how fluid escapes the subducted slab and migrates through the mantle wedge to generate melt. Several authors (e.g., Gerya and Yuen, 2003; Marschall and Schumacher, 2012) have suggested that the formation of buoyant mantle diapirs can allow for fluid addition into the mantle wedge, generating melt; it is suggested here that these diapirs are perhaps even more important in fluid focusing.

The conceptual model for diapirism in a subduction zone involves gravitational instabilities forming along a thin, buoyant layer at the surface of the subducting slab. These instabilities then detach and rise through the mantle wedge. This was modeled in two dimensions by Gerya and Yuen (2003); examples are shown in Figure 12. They model a scenario in which cold, less dense plumes emerge from the slab surface due to

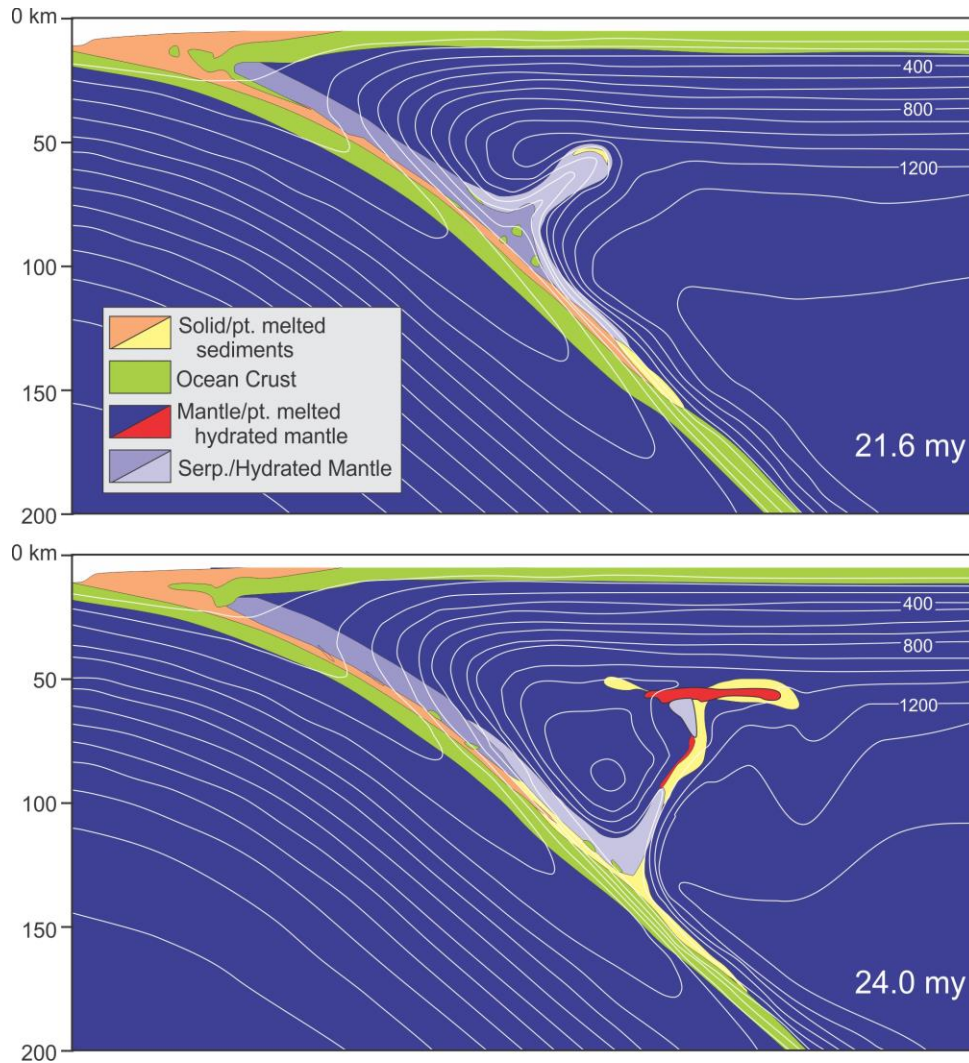


Figure 12: Examples of modeled mantle diapirs , showing the variation in morphology of 'cold plumes' for two variations of model parameters in numerical experiments with high initial buoyancy. Redrawn and simplified after Gerya and Yuen (2003)

Rayleigh–Taylor instabilities (the same process noted above which can produce diapirs at the Bushveld Complex; Gerya et al., 2004). The slab *mélange*, a mixture of hydrated peridotite, sedimentary rock, and altered oceanic crust, is less dense than the

asthenosphere (although temperature differences slightly offset density differences).

Their model finds like upwellings of cold, less dense material into hot, dense material

are geodynamically feasible. An expanded model (Gerya et al., 2006) incorporates the thermodynamic effects of slab dehydration, metamorphic reactions, and mantle melting. This model suggests that two types of plumes may form: mixed, which initiate from the slab and entrain both slab and mantle materials, and unmixed, which initiate from the mantle due to slab-derived fluid infiltration. This may explain the variations in volcanic arc magma signatures; arc magmas with crustal melt signatures may derive from mixed plumes, while those with fluid signatures originate from unmixed plumes. Gerya et al. (2006) also note the similarity to Bushveld Complex diapirs, although they discuss these diapirs in the context of heat rather than fluid transport. Their model was expanded to three dimensions (Zhu et al., 2009) and found great similarity to the distribution of volcanoes in the subduction zone of northeastern Japan. Zhu et al. note that plume shape and growth are strongly a function of mantle viscosity, a value which is not well constrained near the plate boundary.

More in-depth modelling is conducted on diapir formation in subduction zones by Marschall and Schumacher (2012). They explore in detail the possibility that *mélange* zones could be responsible for the combined altered oceanic crust, sedimentary, and depleted mantle signatures in erupted arc magmas. Using results from field investigations of exhumed *mélange* zones, numerical modelling, geophysics, and geochemistry, they produce a conceptual model for the formation of diapirs in subduction zones. In this model, *mélange* is formed; its low mechanical strength leads to

instabilities and the development of buoyant diapirs, which rise into the hot corner of the mantle wedge, dehydrate, melt, and generate fluid and melt compositions which are ultimately the source of plutons and surface volcanoes. This model suggests that the trajectories of plumes as they rise would not necessarily be vertical but may be impacted by corner flow and move obliquely away from the trench. This presents a solution to a number of questions raised by other models: it explains the location of the volcanic forearc as well as the source of the trace element signatures in erupted materials.

Investigations into diapir formation have utilized geochemistry in addition to the geophysical and numerical methods highlighted above. One major concern for the viability of the diapir model is the time it would take for a plume to rise. Based on ^{10}Be and U-Th isotope systematics, the timescale of a subduction cycle is well established. Hall and Kincaid (2001) experimentally simulated subduction-driven flow and buoyant mantle flow with two solutions of different densities to understand the growth of instabilities. Their results suggest the rapid transport times dictated by isotopic results would be feasible under the diapir model. Cruz-Urbe et al. (2018), drawing on the conceptual model of Marschall and Schumacher (2012), found that partially melted *mélange* materials injected as part of the diapir could account for the geochemical signatures of erupted arc materials. The conclusion that mantle wedge plumes could account for the petrology of arc melts is supported by other authors as well (e.g., Castro et al., 2010).

2.8.2 The Bushveld Complex as an Analogue for Subduction Zone Hydrothermal Systems

The stratigraphic sequence of a footwall of unmetamorphosed sediments overlain by an ultramafic sequence of olivine + pyroxene bearing rocks of the Lower Zone of the Bushveld Complex is broadly analogous to the mafic lithosphere slab ± sediments subducting beneath an ultramafic mantle wedge. In both instances, footwall rocks may rise as diapirs into overlying ultramafic rock. The Bushveld evidence noted above illustrates that fluid released by heating of the underlying rock can be effectively focused by the diapirs, allowing for rapid inflow into the growing crystal pile. This can allow for the fluid to retain its isotopic and composition signature of the descending slab (in the subduction case) or that of the underlying Transvaal sediments (in the case of the Bushveld Complex).

There are, of course, differences in the two environments. This includes the fact that subducting slabs has a pronounced dip as compared with the presumed initially sub-horizontal lower contact of the Bushveld with the country rock, which likely did not develop its modest dip until the generation by lower crustal melting and intrusion of the Bushveld Granite by the same thermal anomaly that produced the Bushveld magma. The model (Figure 10) demonstrates that even without this dip, the diapirs can channel fluids to move vertically. Furthermore, the rapid fluid influx into the Bushveld magma chamber allowed space for brecciation of the fluid channelway. Perhaps most significantly, slab fluids are largely incorporated into any mantle melt generated. The

eruption of this melt provides direct inference of the fluid composition. In contrast, the fluid addition and silicate melt produced by hydration melting in the Bushveld system can be diluted by mixing with large volumes of pre-existing magma, which then is only recorded by the later precipitated solid assemblage. Thus, country fluid signatures in Bushveld diapirs may be weaker than they would appear in a mantle melt generated by a subduction zone diapir.

With these caveats, however, large sills such as the Bushveld Complex can act as proxies for dehydration processes in subduction zones, allowing one to observe in the field how country fluids can migrate into hotter rocks and to identify how their geochemical and isotopic characteristics might be altered or not as it does so. The diapir model is not the only model for subduction zone fluid release and migration; identifying geochemical and isotopic alterations due to fluid influx at Bushveld may help to further understand how viable the diapir model is in subduction zones. Additionally, the diatreme and other pipe-like bodies of the Bushveld Complex suggest that fluid influx into the mantle wedge can be unusually voluminous and rapid, following an extended period of fluid overpressure build-up and its sudden release. This rapid fluid transport allows the slab fluids to retain much of their geochemical characteristics as they quickly move into the mantle wedge. A corresponding build-up of fluid overpressure and periodic release of vapor into the hotter parts of the mantle wedge would suggest that

hydration melting in subduction zones is periodic and not continuous. The periodic nature of arc magmatism may, in part, reflect this intermittent fluid influx.

A common objection to the idea that country fluids have contaminated the Bushveld magma is the presence of Mississippi Valley-type deposits in the Transvaal Supergroup and other evidence noted above imply that all of the country fluids migrated laterally and not up into the intrusion. However, it is noted that models of fluid flow in subduction zones show a combination of fluid flow both along the dipping subducting plate (where it may reach the forearc regions) as well as vertical and into the overlying mantle.

2.9 Conclusions

The Bushveld Complex is apparently unique in that it was intruded relatively rapidly as a thick sill into an unmetamorphosed sedimentary sequence, leading to the formation of a wide basal aureole and the generation of voluminous amounts of metamorphic fluids. The most pronounced expression of this is the formation of diapiric structures in the thicker parts of the Bushveld and evidence for fluid focusing in these structures by the presence of diatremes and other pipe-like bodies of a size and character unique to the Bushveld Complex. These bodies and numeric modelling results suggest that much of the country fluid influx is focused by the diapirs structures into pipe-like channels. Rapid influx of country fluid into the magma chamber can affect the crystallization behavior and isotopic character of the resident magma.

The thermal profile and lithologic sequence of the Bushveld Complex and the underlying country rock are similar to that seen in subduction zones. Understanding the degree that country fluids can retain their geochemical and isotopic character as they percolate through thick sequences of Bushveld ultramafic and mafic rock has implications for slab fluids. The results here suggest that fluids can retain their initial geochemical characteristics by periodic, rapid migration through overlying rock. In this regard, studies of the geochemical and isotopic character of late-crystallizing Bushveld minerals and comparisons with intrusions that intruded drier country rocks may prove enlightening. More broadly, the merger of two major fields of igneous petrology and geochemistry, layered intrusions and subduction zone magmatism, will be of benefit to both.

3. Reply to Discussion of ‘Crustal Fluid Contamination in the Bushveld Complex, South Africa: An Analogue for Subduction Zone Fluid Migration’ by Roger Scoon and Andrew Mitchell (2020)

Published as: Benson, E., Connolly, J.A.D., and Boudreau, A.E., 2020, Reply to discussion of ‘Crustal fluid contamination in the Bushveld Complex, South Africa: an analogue for subduction zone fluid migration’ by Roger Scoon and Andrew Mitchell (2020), *International Geology Review*: <https://doi.org/10.1080/00206814.2020.1830444>

3.1 Chapter Summary

In their discussion of our recent publication, Scoon and Mitchell (2020) put forward a number of arguments against the hydromagmatic model of Bushveld Complex formation that we present. Their criticisms of our model focus primarily on the formation mechanisms of the discordant bodies present at Bushveld, namely the iron-rich ultramafic pegmatites and the dunite pipes. While this was a minor portion of our paper, we here review evidence in favor of a fluid-related origin for these discordant bodies, in contrast to the primarily magmatic origin that Scoon and Mitchell present.

3.2 Introduction

In their discussion of our recent publication, Scoon and Mitchell (2020) (hereafter just Scoon and Mitchell) express a number of criticisms and reservations regarding some details of our model. We welcome the opportunity to discuss their concerns. Briefly, we suggested that extensive dehydration of the underlying country rock of the Bushveld Complex generated large volumes of volatile fluid that rapidly penetrated the lower section of the Bushveld stratigraphy, channeled both by rapid porous flow and local

formation of diatreme pipes and that this fluid contamination can account for some isotopic anomalies of the Main Zone. These country fluids were locally channeled by synchronous diapir formation of the floor rocks. More broadly, we suggested that the Bushveld system is an excellent analogue for understanding fluid migration in subduction zones. We also suggested that our results had consequences for other discordant, pipe-like bodies and iron-rich ultramafic pegmatite (IRUP) formation models, but did not elaborate as it was outside the scope of the paper. The comment by Scoon and Mitchell allows us to follow up on this aspect of our work: indeed, we think this is yet another area where the Bushveld system can enlighten on mantle processes and vice-versa.

Scoon and Mitchell pointed out a number of minor errors in our stratigraphic section and some imprecise terminology which we welcome. Without much comment on the main points of the paper noted above, they instead put forward a number of critiques focused on our suggestion that our results have implications for the formation of other discordant bodies in the Bushveld Complex. We recognize that the origin of the dunite pipes and IRUP are controversial; for this reason, our discussion of these features focused primarily on the importance of a breccia pipe, located in the eastern limb of the Bushveld Complex, as the stronger evidence for largescale fluid involvement. We called attention to its similarity with km-scale blowout pipes developed in sedimentary basins (recently, deep blowout pipes are now appearing in tundra regions of Siberia,

presumably driven by climate change and accelerated methane production in the permafrost and illustrating that gas blowouts can occur on land as well; Chuvilin et al., 2020). In their discussion of our paper, Scoon and Mitchell agree that this breccia pipe could have acted as a pathway for country fluid into the Bushveld but disagree on its potential importance.

Scoon and Mitchell suggest that, if the Bushveld was affected by country fluid infiltration, that there should be evidence in the Lower Zone and Critical Zone. We note that, except for the Upper Zone, the mineral assemblages of the Bushveld complex do indeed show extensive evidence for isotopic disequilibrium (e.g., Mathez and Waight, 2003; Prevec et al., 2005; Chutas et al., 2012; Roelofse and Ashwal, 2012; Yang et al., 2013; Roelofse et al., 2015). A more important question is if the fluid can retain its crustal signature as it traverses the lower portions of the complex. Our model for fluid migration draws on a channelized flow, whereby the fluid is able to 'skip' over the Lower and Critical Zones and directly invade the Main Zone magma. This is most evident in the rapid flow required to form a 10 m diameter breccia pipe.

In regards to porous flow, Boudreau (2019) discussed two mechanisms that can limit isotopic equilibration with the country fluids in the lower, cooler sections of the Bushveld Complex. First, grain-scale interaction of fluids based on isotopic re-equilibration is on the order of 10³–10⁵ years for amphibolite-granulite grade metamorphic rocks (e.g., van Haren et al., 1996; Graham et al., 1998), the longer times

approaching the cooling time for the Bushveld complex (e.g., Cawthorn and Webb, 2013). Le Roux et al. (2009) summarized slow diffusion rates in mantle minerals that imply that isotopic equilibration may not be reached during partial melting at hot mantle temperature and relatively slow melting rate of an isotopically heterogeneous assemblage. Second, some isotopes will not have high bulk rock abundances of the element in question to affect the isotopic character of the infiltrating fluid, particularly if the fluid is otherwise in chemical equilibrium with the host minerals. For example, both Sr and Nd are strongly incompatible in olivine and low-Ca pyroxene. Hence, the ultramafic rocks that make up the lower portions of the Bushveld and Stillwater complexes do not present a large reservoir of Sr and Nd to exchange with a rapidly moving fluid, a point made in our paper. As in a subduction system, it does appear that crustal fluids can traverse thick sections of hot ultramafic Bushveld rock and still retain a crustal isotopic signature. The observation that IRUP is found mainly above the Lower Critical Zone is consistent with the infiltrating fluids not becoming particularly reactive until they encountered hotter rocks above the Lower Zone.

Another implication noted in our paper is that the vertical pipe-like structures will channel both country fluid as it flows upward and also pulls in igneous fluids by horizontal flow component from the solidifying Bushveld host use the same channels to migrate out of the crystal pile. This has implications for ore components that some pipes

can contain, and can complicate the isotopic signature of the pipes as the two fluid sources mix and react in the fluid channels (see below).

Scoon and Mitchell also disagree with our initial magma thickness in our summary model, suggesting it is too thick. In our Figure 11, we had combined our modelled fluid migration results with that of Cawthorn and Webb (2013) for the crystallization history of the Bushveld magma and Gerya et al. (2003) for the footwall diapir formation. In terms of the thermal history of the complex, we note that crystallization of a sill is largely controlled by heat loss out the top by direct contact of the magma with the roof rock. In regard to how fast the crystal pile grows, the thickness of the magma chamber is not important as long as some magma is always present, either as a single fractionating thick sill or a continuously replenished inflating sill undergoing mixing and fractional crystallization. Another minor point could be made of the original Cawthorn and Webb model. It is not clear how one can form an 8 km thick intrusion that initially intruded only 2 km below the surface without forming a large blister on the surface of the earth. The shallow intrusion model of Cawthorn and Webb also leads to perhaps a too short cooling time and it does not reproduce the hotter footwall country-rock geotherms of Harris et al. (2003). These problems could be minimized by placing the intrusion deeper and are the focus of ongoing study.

3.3 Iron-Rich Ultramafic Pegmatite (IRUP) Formation

As for the IRUP and dunite pipe formation, there is debate if they represent a distinctive process as Scoon and Mitchell suggest or if the IRUP-dunite represent a continuum of replacement by a reactive fluid/melt or a fractionating intrusive magma crystallizing in eroded melt-filled channels. Strong evidence for replacement is seen in the relic chromitite layers in the host rock that continue through the dunite pipes (Scoon and Mitchell's Figure 2).

In regard to IRUP, there have been a number of models and contrasting interpretations. As noted by Scoon and Mitchell, the IRUP appears to have replaced the original lithology (ignoring those examples that may have a fault or fracture control); the debate is if this is a volume for volume metasomatic replacement or if the host rock was first removed (physically or by melting) prior to crystallization of a distinctive IRUP magma. In mantle sections of ophiolites, discordant bodies are common and are generally viewed as important for rapid flow of mantle partial melts. Most workers interpret these bodies as metasomatic replacement bodies that involve a focused reactive flow (e.g., Kelemen et al., 1995). For the Bushveld metasomatic replacement favored by Scoon and Mitchell, they suggest that the metasomatic agent was an Fe-rich silicate liquid derived from the Upper Zone that percolated downward through the Main Zone and into the Critical Zone, based on the Fe-rich mineralogy and Sr isotopic similarity between the two. Others have suggested that the metasomatic agent was a Fe-, PGE- and

Cl-rich fluid (e.g., Schiffries, 1982; Boudreau, 2019). In contrast, others have suggested that the IRUP formed by the intrusion of a mantle magma that first removed portions of the host rock before crystallizing (e.g., Cawthorn et al., 2000, 2018; Günther et al., 2018).

In regard to the Scoon and Mitchell interpretation, we note the following counter evidence for Upper Zone liquid involvement in IRUP formation, at least for those in the Critical Zone. Besides Fe-rich minerals, the Upper Zone magmas are also saturated in plagioclase and, in the more evolved liquids, apatite. As Scoon and Mitchell note, the IRUPs do not contain significant plagioclase and bulk rock IRUP compositions reported by Cawthorn et al. (2018) contain <0.05 wt. % P_2O_5 with one notable exception. As noted by Cawthorn et al. (2018) and Boudreau (2019) the IRUP clinopyroxene is enriched in the wollastonite (wo) component and lack exsolution lamellae as compared with typical Bushveld host rock clinopyroxene of similar mg#. This is again inconsistent with the clinopyroxene having precipitated from a UZ magma but it is consistent with a lower temperature (secondary) origin.

A point generally ignored is that the hydrous mineral assemblage of the Upper Zone rocks contains very little Cl, in contrast to the Lower Zone/Critical Zone rocks for which these minerals, particularly the apatite, are unusually Cl-rich as compared with other layered intrusions (Willmore et al., 2000). Although extensive study of the hydrous minerals of the IRUP and dunite pipes is lacking, Schiffries (1982) reports that they are also Cl-enriched. This is particularly important, as high-temperature Cl-rich fluids will

be solute-rich, particularly for Fe (e.g., Yardley, 2005), with obvious implications for the formation of Fe-rich pegmatite and Fe-rich hortonolite pipes. Finally, as is evident in their name, IRUPs have a very coarse-grained to pegmatoidal texture whereas the UZ rocks are not pegmatoidal. This and the abundance of biotite and amphibole suggests that they grew in a fluid-saturated system. In short, a connection between the IRUP and the Upper Zone is, in many ways, difficult to justify.

A broader point that Scoon and Mitchell and some other studies overlook is that the IRUPs tend to be associated with leucocratic to anorthositic host rocks (see Figure 1 of the Scoon and Mitchell comment, also Cawthorn et al., 2018). Analogous ultramafic/anorthosite segregations occur in other intrusions as well. For example, beneath the Basistoppen sill in the Skaergaard intrusion, Naslund (1986) noted podiform anorthosite-ultramafic segregations thought to be caused by the sill's intrusion into the hot Skaergaard ferrogabbros. Similar segregations are also found in the Lower Zone and Marginal Border Series of Skaergaard, where there is no source of reheating. Sonnenthal (1992) suggested these segregations were due to reaction with a Cl-rich fluid, although they did not present details of the mechanism involved. Discordant troctolite-anorthositic bodies in the Stillwater Complex have also been attributed to volatile fluids becoming undersaturated in the mafic component as they rise into hotter rocks and remove the pyroxene component by incongruent reaction, producing olivine as an intermediate reaction product (Meurer et al., 1997). Applied to the IRUP problem, the

model of Boudreau (2019) simply suggests that, while the scale is different in the Bushveld case, the IRUP is simply the mafic component lost from the host anorthosite.

While the above look at the role of fluids, it is also possible that fluid interaction can be mediated by melt produced by hydration melting of the host rock. For example, Keller and Katz, (2016) and Keller et al. (2017) summarize the ways in which volatiles are important in lowering the mantle solidus and promoting channeled, pipe-like transport of mantle melts, despite the low concentration of volatiles in the mantle. In regards to the Bushveld system, Cawthorn et al. (2018) have suggested that IRUP mineral assemblages crystallized from a fractionating magma that has affinities with volatile-rich meimechite or ankaramite mantle magmas that are characterized by relatively high concentrations of alkalis, the REE and high CaO/Al₂O₃ wt. ratios. Green et al. (2004) have suggested that ankaramite liquids form by flux melting of a refractory lherzolitic mantle. Similarly, a reasonable hypothesis is that a Cl-rich volatile fluid containing significant Ca, alkalis, and REE could induce partial melting as it moves into hotter Bushveld rocks and produces a meimechite- or ankaramitelike liquid. This would explain the paucity of evidence for the external derivation of these magmas in the underlying country rock, but explain the local occurrence of what appear to be examples of magmatic intrusion within the Bushveld. The local formation of a volatile-rich hydration melt would explain the coarse texture of the IRUPs and the volatile- and Ca-enriched liquid would favor the crystallization of olivine and clinopyroxene over

orthopyroxene and plagioclase. As noted by Boudreau (2019), ‘Why go into the mantle when you can make everything in your back yard?’

3.4 Dunite Pipes

We appreciate the detailed work Scoon and Mitchell have done to outline the orthomagmatic model of dunite pipe formation. As referenced in Benson et al. (2020), Viljoen and Scoon (1985) noted that the dunite pipes of the eastern Bushveld are commonly located adjacent to downwarped igneous layering in the host rock. Regionally, they are commonly found in the vicinity of faults and structural upwarps in the floor rock (our Figure 3). We noted that the latter observation was consistent with a localized origin for these pipe structures (this correlation would not be expected for mantle magmas that could pop through anywhere). Scoon and Mitchell note that IRUPs and other discordant bodies are not always associated with upwarps in the floor rocks. However, our numerical model shows that channelized, pipe-like porous flow can develop spontaneously from minor porosity perturbations even when the contact with the underlying country rock is horizontal. The presence of floor diapirs only enhances fluid focusing of both country and Bushveld fluids and explains why the more impressive examples (such as the dunite pipe Scoon and Mitchell show as their Figure 2) are seen in the eastern Bushveld where floor rock diapirs are best developed.

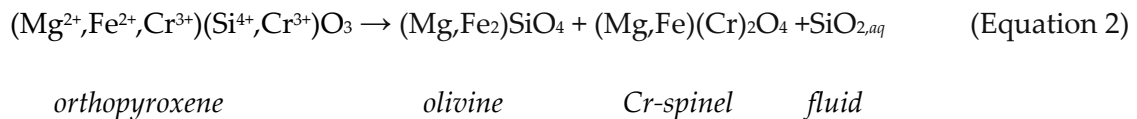
Günther et al. (2018) suggest that the oxygen isotopes of the dunite pipes are indicative of a recycled crustal component in a mantle magma, but again this could be

introduced by fluids from the underlying country rock. Roger and Scoon also discredit the work of Schiffries (1982), who proposed a high-temperature chloride solution could cause a number of metasomatic reactions. Thus, olivine can be produced via the incongruent reaction of orthopyroxene with a fluid that becomes progressively silica-undersaturated as it moves into hotter rocks:



Experimental work by Newton and Manning (2000) suggests that modest amounts of NaCl in a hydrous fluid ($X_{\text{NaCl}} \cong 0.1$) can cause a roughly 50% increase in SiO₂ solubility compared to NaCl-absent aqueous fluids at 700°C and 0.2 GPa. This and other fluid-driven reactions can produce olivine, loss of plagioclase and introduction of the PGE. This reaction would be accompanied by a 67% volume loss, which can create the collapse structures around the Driekop pipe noted by Scoon and Mitchell. They use the presence of Cr-spinel in the pipes as an argument against the hydrothermal model.

However, as noted in Boudreau (2019), pyroxenes can contain significant Cr that cannot be accommodated by the secondary olivine, and the reaction shown in Equation 1 can be generalized to produce the Cr-spinel component of the pipes:



In regard to the PGE-rich cores seen in some of these pipes, Peyerl (1982) noted that the platinum-group minerals of the UG2 chromitite have been affected by the crosscutting PGE-bearing Driekop pipe out to a distance of 1–2 km, with the PGE-base metal sulfide assemblage replaced by Pt-Fe alloy and various Pd-Pt-Ab- Sb minerals towards the pipe. Peyerl suggested this change was driven by fluids moving outward from the pipe and removing sulfur. The results of our numeric model show that the development of vertical channeled fluid flow induces a lateral flow of fluid in the host rock towards the regions of the channelized porous flow. In detail, as a porosity wave moves up, at the top of the wave fluid is pumped into the matrix on a small scale relative to the compaction length. This fluid, and any other background fluid present, is then drawn back in at the bottom of the wave on a scale comparable to the compaction length. Excluding the chromitites, the Lower Critical Zone and Upper Critical Zone rocks, average 40 and 119 ppb Pt, respectively (summary of Barnes and Maier, 2002). Assuming that as little as 5 ppb Pt was, on average, scavenged from a 1 to 2 km diameter region in the host rock and concentrated into a 10 m pipe core, the core would contain from 50 to 200 ppm Pt, well above what is seen in the PGE-bearing reefs (Boudreau, 2019).

3.5 Conclusions

Scoon and Mitchell present a number of criticisms of our paper (Benson et al., 2020a). These critiques are primarily focused on our presentation of Bushveld discordant

bodies, particularly IRUP and dunite pipes, as hydromagmatic in nature; they prefer an orthomagmatic model for the formation of these discordant bodies. We reiterate that the discussion of discordant bodies and their relationship to large-scale Bushveld fluid flow was a minor line of evidence for this hypothesis. The bulk of our paper revolved around the role of fluids as a source of contamination and called on less controversial structures such as the breccia pipe as evidence of rapid fluid transport. This idea of country fluid mixing into the Bushveld magma (and driving chromitite formation) also has been recently suggested by Veksler and Hou (2020). As we briefly attempted to suggest here, the origin of the IRUP and dunite pipes is not so clear-cut and neatly orthomagmatic as Scoon and Mitchell (2020) describe. They overlook a number of studies which present evidence contradictory to their findings and which support a hydromagmatic model for the formation of these bodies, and indeed discount evidence from other igneous and mantle settings where similar features have been attributed to reactive fluid flow. While one can appreciate the conservatism in interpretation that they espouse, we believe layered intrusions present a much richer variety of physical and chemical processes than conventionally proposed.

4. Radiogenic Isotopes at the Stillwater Complex: Sr, Nd, and Pb as Isotopic Tracers

4.1 Introduction

The Stillwater Complex is an ultramafic-mafic layered intrusion located along the northern front of the Beartooth Mountains in south-central Montana. Early studies (e.g., Hess, 1939), conducted in the 1930s to 1950s, focused primarily on the complex due to its extensive chromite deposits. However, with the discovery of rich platinum and palladium deposits in what is now known as the J-M Reef (and to some extent, the Picket Pin deposit found stratigraphically higher in the intrusion), the Stillwater Complex received increasing attention and has been extensively mapped and studied since the early 1960s. The complex is significant not just for the presence of a major Pt-Pd deposit, but also for its size and relative lack of alteration since emplacement that make it an excellent location to explore the processes that form these large layered intrusions.

Much radiogenic isotope work on Stillwater Complex samples was conducted between the 1960s and 1990s, relatively early both in exploration of the Stillwater Complex and in development of radiogenic isotope techniques. This work on Stillwater samples focused on Sm-Nd (DePaolo and Wasserburg, 1979; Lambert et al., 1994), common lead (Wooden et al., 1991; McCallum et al., 1999), Rb-Sr (Fenton and Faure, 1969; Powell et al., 1969; DePaolo and Wasserburg, 1979), and Re-Os (Martin, 1989; Marcantonio et al., 1993; Lambert et al., 1994). Since these early analyses, understanding of how both magmatic and hydrothermal processes impact isotopic signatures, as well

as precision in measuring radiogenic isotopes, have improved. As such, revisiting isotopic systems at the Stillwater Complex may contribute to refining formation models for the intrusion.

For example, recent radiogenic isotope work has proven useful in developing a better understanding of the Bushveld Complex, a 2.06 Ga layered intrusion located in South Africa (e.g., Mathez and Waight, 2003; Schannor et al., 2018; Zeh et al., 2020). The Bushveld Complex and the Stillwater Complex are analogous intrusions, hosting many similar features. Drawing on a number of studies of isotopic variability in the Bushveld Complex (e.g., Schiffries and Rye, 1990; Harris and Chaumba, 2001; Willmore et al., 2002; Mathez and Waight, 2003; Harris et al., 2005; Schannor et al., 2018; Magalhães et al., 2018; Zeh et al., 2020), Benson et al. (2020) found that the addition of 1-2 wt. % of a country fluid could produce the observed isotopic signatures that others have suggested would require large amounts (40-80%) of crustal assimilation (e.g., Maier et al., 2000; Harris et al., 2005; Zirkparvar et al., 2014). Benson et al. suggested a similar investigation to test for the influence and source of fluids involved in Stillwater Complex formation. They further suggested that layered intrusions such as the Bushveld Complex and the Stillwater Complex may act as a proxy for understanding fluid circulation in subduction zones. As such, further investigation of radiogenic isotopes in the Stillwater Complex may help to further understand how layered intrusions might function as a proxy for subduction zone fluid migration.

One unusual and little-examined feature of the Stillwater Complex are sporadic pegmatoidal bodies found primarily below the platinum- and palladium-bearing J-M Reef. These pegmatoids have been suggested to be related to fluid circulation (e.g., Braun et al., 1994; Hanley et al., 2008; Boudreau, 2016). Comparison of isotopic signatures in these pegmatoids to their nearby, more typically-textured 'host rock' can constrain how these bodies formed, specifically as to the role of country and igneous fluids. Whole rock isotope analyses were performed, as they have benefits over mineral-scale analyses in systems where later metamorphism is thought to have disturbed the isotope systematics. While analysis of whole rock samples can produce spurious 'isochrons' that are actually mixing lines, the age of the Stillwater Complex is well-constrained (DePaolo and Wasserburg, 1979; Wall et al., 2018) at ~2700 Ma. Thus, the effect of mixing, and the degree to which Rb-Sr, Sm-Nd, and Pb-Pb systems are disturbed, can be better understood. This study provides modern radiogenic isotope data for the Sm-Nd, Rb-Sr, and Pb-Pb systematics in Stillwater Complex whole rocks. Using this data, the extent to which these isotopic systems have been disturbed by later events is investigated. Finally, this radiogenic isotope data is used to investigate the formation of the pegmatoid bodies in comparison to spatially associated host rock and hornfels from the metamorphic aureole, to determine what, if any, impact fluids had in their formation.

4.2 Geology of the Stillwater Complex

4.2.1 Geologic Context and Country Rocks

The Stillwater Complex is part of the Archean core of the Beartooth Mountains and is located on the northeastern side of the range (Figure 13). The complex has a maximum exposed stratigraphic thickness of 6.5 km, and an exposed strike length of ~45 km. Geophysical evidence suggests the complex extends at depth for at least 25 km to the northeast (Kleinkopf, 1985). The complex overlies metasedimentary rocks dating to

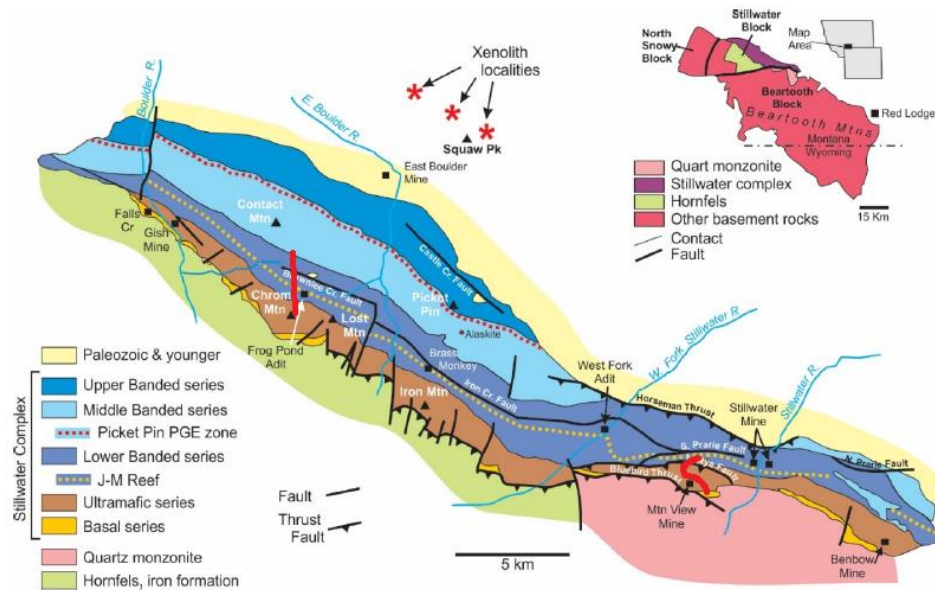


Figure 13: Geology of the Stillwater Complex, with approximate sample traverses marked in red. Redrawn after Jackson (1971) and McCallum (1996).

approximately 3300 Ma (Mueller et al., 1982, 1992) and was emplaced into a biotite schist that formed during an earlier regional metamorphic event (525-550 °C, 2 kbar; Labotka and Kath, 2001). The complex was emplaced as a subvolcanic sill at a depth of

approximately 6-7 km (Labotka, 1985; Helz, 1995; Labotka and Kath, 2001). Stillwater rocks are relatively coarse-grained for their intrusion depth; Mogk and Mueller (1990) suggest that the complex intruded into the country rocks within 50 Ma of the earlier metamorphic event, as the country rock would still be hot enough in this timeframe to allow for slow cooling. The intrusion of the complex into the country rock produced a metamorphic aureole; the exact thickness of the aureole is obscured by faulting and a lack of laterally continuous units. Labotka and Kath (2001) note a hypersthene hornfels zone 0.5-1 km from the country rock/Stillwater contact, followed by a 0.5-1.5 km-thick-cordierite-cummingtonite hornfels zone. They estimated a loss of 0.5 wt. % H₂O due to dehydration, the equivalent of a layer of water 15 m thick. After dehydration, this fluid was available to move through the Stillwater Complex. Assemblages in the iron formation record peak metamorphic temperatures at the Stillwater contact of approximately 825 °C and pressures of 3-4 kbar (Vaniman et al., 1980; Labotka et al., 1982; Vocke, 1982); McCallum (1996) suggested that the higher P recorded in the hornfels represents the additional thickness of the complex added to the intrusion depth noted above. The complex was involved in a weak, low-grade regional metamorphic event at 1600 – 1800 Ma (Page, 1977), resulting in local alteration to greenschist facies, assumed due to infiltration of fluids. However, the majority of the original igneous mineralogy is preserved in both the intrusions and in the underlying metamorphic aureole. The upper portion of the intrusion was eroded away prior to the mid-

Cambrian; it was then covered with Paleozoic and Mesozoic sediments. It was faulted and uplifted during the Laramide orogeny, leading to current tilting, typically approximately 70° NNE but locally overturned (Page, 1977).

4.2.2 Stillwater Complex Stratigraphy

The Stillwater Complex has been the subject of numerous proposed stratigraphic divisions; this report follows those based on stratigraphic variations in mineral mode described in McCallum et al. (1980) and Raedeke and McCallum (1984) (Figure 14). This stratigraphy is extensively detailed by McCallum (1996). There are generally three broad stratigraphic divisions of the complex; the Basal series, the Ultramafic series, and the Banded series. Beneath the complex are a number of Stillwater-associated mafic sills and dikes, hosted by the metasedimentary rock and thought to represent Stillwater parental magmas (Premo et al., 1990).

The Basal series is the lowermost layer of the complex; it is variable in thickness, with a typical range of 60 to 240 m and a maximum of ~400 m (Page, 1979). It is not present in all locations, having been cut out in the central part of the complex by later thrust faulting. It is defined as a laterally continuous norite with subordinate anorthosite, gabbro, and peridotite which grades upward by decreasing plagioclase mode into a bronzite. Xenoliths of hornfels are common in the lower portion of the Basal Series. The lower contact is irregular, cutting across stratigraphic units and suggestive of

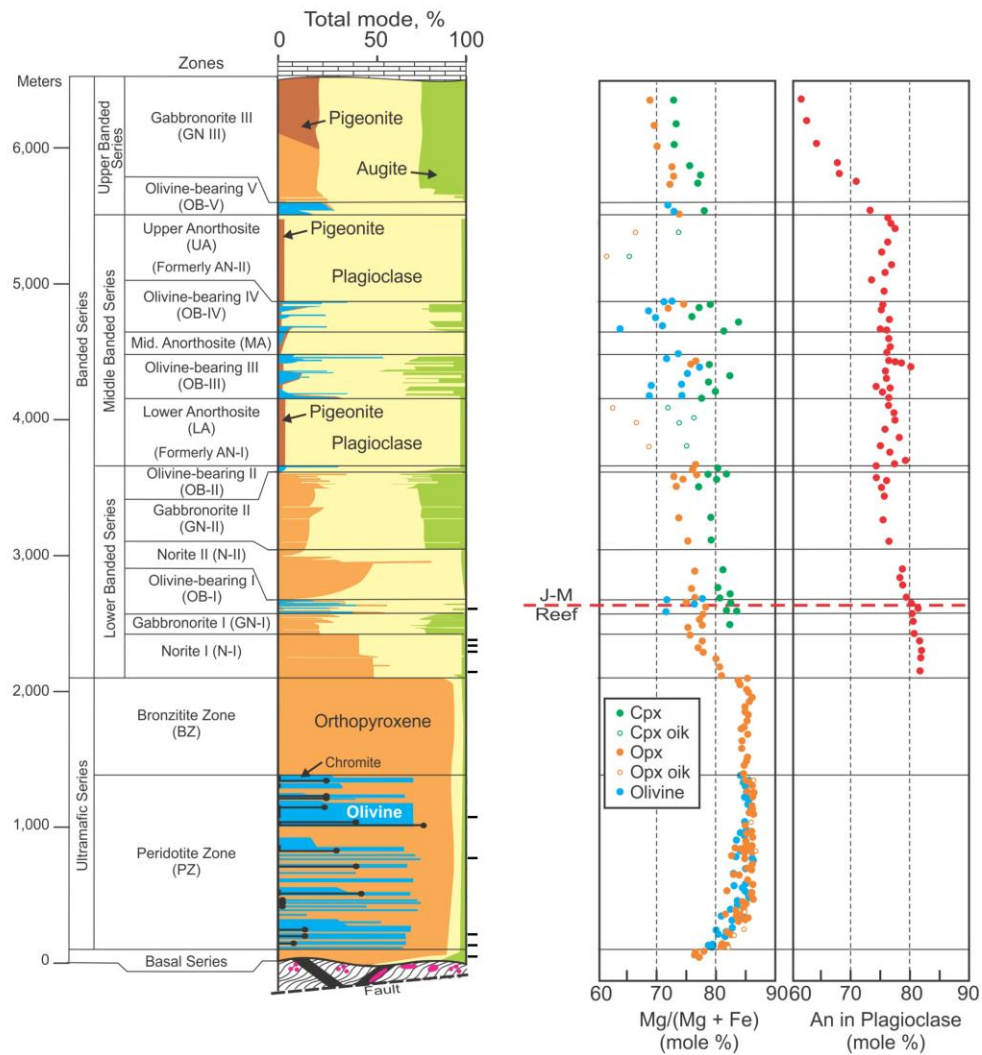


Figure 14: Stratigraphy of the Stillwater Complex with major mineral modes and major mineral compositional trends as a function of height. Modal data and stratigraphic units after McCallum et al. (1980) and Raedeke and McCallum (1984). The locations of samples analyzed as part of this study are indicated by black dashes to the right side of the modal mineralogy.

magma emplacement along an unconformity (McCallum, 1996). The upper contact is placed at the first cyclic unit of the Ultramafic series.

The Ultramafic series is subdivided into two zones; the lower Peridotite Zone and the upper Bronzite Zone. The base of the Ultramafic Series is placed at the first significant appearance of olivine, while the upper boundary is defined by the appearance of plagioclase as a major modal mineral. The Peridotite Zone consists of a sequence of cyclic units, where a complete cyclic unit is defined by a peridotite-harzburgite-bronzite sequence. There have been 21 cyclic units identified in the Peridotite Zone, 15 of which are complete. Layers of massive and disseminated chromite appear in the peridotite member of many of the cyclic units. These seams are referred to as A (lowermost) through K (uppermost). The Bronzite Zone overlying the cyclic units of the Peridotite Zone consists of a mostly uniform orthopyroxenite with interstitial plagioclase and augite, minor quartz and chromite, and rare apatite, sulfides, and phlogopite.

The Banded series is subdivided into three major units: the Lower, Middle, and Upper Banded series. These units are further subdivided into smaller zones on the basis of major rock type and the appearance/disappearance of olivine. These smaller units are thoroughly detailed by McCallum (1996). The J-M Reef, with its economic concentration of platinum-group elements, is a laterally continuous unit found in Olivine-bearing zone I (OB-I) of the Lower Banded series. The lower contact of the Lower Banded series is marked by the appearance of plagioclase as a major modal mineral; the top contact is placed at the base of the thick anorthosite unit that defines the Middle Banded series.

The Lower Banded series is dominated by 6 units: Norite-I, Gabbronorite-I, Olivine-bearing I, Norite-II, Gabbronorite-II, and Olivine-bearing II.

While the units above the Lower Banded series are not the focus of this report, we provide some detail on them here. Deeper studies into these units have been conducted by a number of investigators (*e.g.*, Boudreau and McCallum, 1986; McCallum, 1996; Meurer and Boudreau, 1996). The Middle Banded series is bounded at the top and bottom by thick anorthosite units. They differ both modally and texturally from the thin anorthosites found in other parts of the Banded series. The formation of these thick anorthosites is not well-understood and is a complication in Stillwater Complex formation models. The Upper Banded series is similar to the Lower Banded series, with a few key differences. Among these are the presence of thin troctolite and norite units at the base as well as the appearance of inverted pigeonite (Boudreau, 2016) which has caused some confusion in mapping the Upper Banded series.

4.2.3 Pegmatoids

Occurring sporadically through the Stillwater Complex are pegmatoids (*e.g.*, Figure 15); they are more common in some units than others. Pegmatoids have been noted at Stillwater since some of the earliest investigations into the complex (*e.g.*, Peoples and Howland, 1940). They have been described as commonly associated with the chromites of the Ultramafic Series (*e.g.*, Raedeke and McCallum, 1984), but are found in almost every major unit (McCallum, 1996). Despite their prevalence, few studies have

focused on understanding their composition or relationship with the more typical intrusive igneous rocks that surround them. Volborth and Housley (1984) investigated some pegmatitic samples tangentially in their study of graphite occurrence in the complex; their focus was primarily on the occurrence of graphite alongside platinum-group element mineralization. Braun et al. (1994) studied the occurrence of pegmatoids in more depth. They noted pegmatoids most commonly developed in olivine ± chromite-rich cumulate rocks in the Peridotite Zone, and sporadically in the Lower Banded Series, particularly in the Olivine-bearing subzones. Pegmatoids are mostly similar mineralogically to their host cumulates (Braun et al., 1994), but typically experienced more extensive greenschist alteration than the host rocks. Their study analyzed a relatively small number of pegmatitic samples and compared them to average host-rock composition for the section. This study found some evidence that the pegmatoids were related to fluid migration. Further investigation by McIlveen (1996) identified pegmatoids with anomalously high PGE concentrations below the J-M Reef and suggested these formed due to volatiles scavenging PGEs from lower in the intrusion, contributing to PGE enrichment both in this anomalous pegmatoidal zone of Norite-I and in the J-M Reef itself. Hanley et al. (2008) examined fluid and melt inclusions in Stillwater pegmatoids and found evidence of coexisting hydrous melts, magmatic brines, and carbonic fluids, that may have interacted during the late crystallization and early post-magmatic phases of Stillwater Complex formation. They suggest these

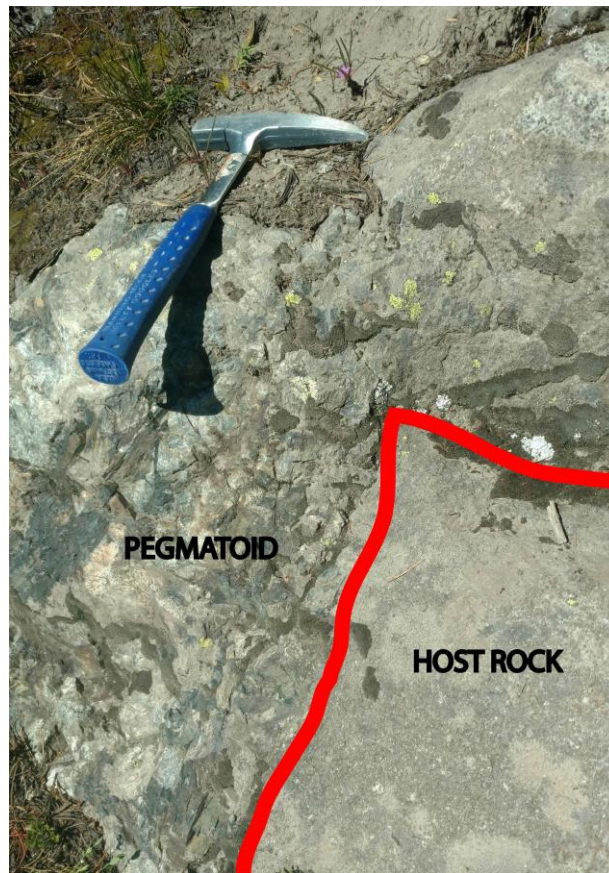


Figure 15: Outcrop showing field relationship between pegmatoid bodies and spatially associated host rock.

hydrothermal fluids may have modified J-M Reef PGE ore compositions.

4.2.4 Previous Isotopic Investigations

Radiogenic isotope studies at Stillwater have primarily focused on using radiogenic isotopes for geochronology. A number of radiogenic isotope systems were used for age dating of the complex and associated country rocks, including the Rb-Sr system (Fenton and Faure, 1969; Powell et al., 1969; Mueller and Wooden, 1976; DePaolo and Wasserburg, 1979), the Sm-Nd system (DePaolo and Wasserburg, 1979), and the Pb-

Pb system (Manhes et al., 1980). Zircon geochronology (Wall and Scoates, 2016; Wall et al., 2016, 2018) has also been conducted at the Stillwater Complex, with controversial results that nonetheless confirm the Sm-Nd age (DePaolo and Wasserburg, 1979) of 2.7 Ga.

Some isotopic studies of the Stillwater Complex have also attempted to use radiogenic isotopes as geologic tracers. In the Rb-Sr system, mineral separates from a gabbro-norite analyzed by DePaolo and Wasserburg (1979) did not fall along the expected 2.7 Ga isochron. Lambert et al. (1989) suggested whole rock Rb-Sr analysis of twenty cumulate rocks defined an isochron of 1.1 Ga, which has been taken as further evidence the Rb-Sr system was greatly disturbed and thus provides no useful information in constraining a formation model for the intrusion. For these reasons, the Rb-Sr system at Stillwater has been assumed to be disturbed and has not been explored in greater detail. This is in marked contrast to the Bushveld Complex, where extensive Sr isotopic work has been conducted (e.g., Kruger and Marsh, 1982; Harmer and Sharpe, 1985; Kruger, 1994; Yang et al., 2013; Wilson et al., 2017; Schannor et al., 2018).

The Sm-Nd system, however, has been used successfully as a tracer in a number of studies. Along with constraining a precise isochron, DePaolo and Wasserburg (1979) calculated initial Nd isotopic ratios for their samples. They found these initial values deviated from the expected CHUR evolution curve, which they suggested indicated either multiple magmatic sources or substantial crustal contamination. Later

investigations into Sm-Nd (along with Re-Os) in samples covering a greater stratigraphic range (Lambert et al., 1989, 1994) identified a greater range of initial Nd values, including many that fell off the 2.7 Ga isochron from the gabbro-norite (DePaolo and Wasserburg, 1979). Lambert et al. (1994) held that initial Nd isotopic ratio variability precluded intrusion formation from a single, isotopically homogeneous magma.

Wooden et al. (1991) analyzed Pb isotopes in plagioclase grains from the Stillwater Complex and identified a narrow range of initial isotopic compositions, which were markedly more radiogenic compared to a late Archean model mantle. However, their analysis of the Late Archean crustal suite in the region suggested that contamination by the crustal suite was not responsible for the radiogenic initial ratios of the Stillwater Complex, as the Th/U ratios of the crustal suite are highly variable (2-26), in contrast with the relatively uniform Th/U ratio of about 4 in Stillwater Complex rocks. They suggested the Stillwater Complex and the Late Archean crustal suite were derived from the same source system, during a crust-forming episode, from a reservoir with an unusual isotopic composition. McCallum et al. (1999) also examined Pb isotopes in plagioclase, as well as in sulfide minerals from the J-M Reef, and confirmed the presence of highly radiogenic initial Pb ratios at 2.7 Ga, although they also found that the sulfides and plagioclase grains were in isotopic disequilibrium. They argued this was the result of fluid infiltration during greenschist-facies metamorphism at 1.7 Ga, the result of which was enrichment of sulfide grains in radiogenic Pb.

4.3 Methods

Sampling of pegmatoids, host rock, and country rock from the metamorphic aureole (hornfels) was conducted from locations on Chrome Mountain and at Mountain View (Figure 13, Appendix A), approximately following the traverses of McCallum et al. (1980) and Raedeke and McCallum (1984). Samples with little to no alteration, as well as samples that were collected *in-situ* were prioritized for analysis. Host rock samples were selected on the basis of spatial association with pegmatoids. To ensure bulk rock geochemistry was representative of the sample as a whole, particularly in the case of pegmatoids, a large amount of material was cut from each sample and crushed in a tungsten carbide shatterbox to powder to ensure sample homogenization.

To obtain concentrations of relevant elements in the radiogenic isotope systems (Rb, Sr, Sm, Nd, Pb, U, Th), dissolved sample powder was analyzed by inductively coupled plasma mass spectrometry (ICP-MS) at Duke University. Sample powder was first dissolved in a 1:3 solution of HF:HNO₃. Samples were left for a minimum period of 24 hours at ~100 °C. Samples were dried and redissolved for a period of four hours at 160 °C in an aqua regia solution. After drying for a second time, samples were completely dissolved; two samples (GCP-03 and GCP-05) with high amounts of chromite left a very small amount of material undissolved, but this amount of undissolved material in a small number of samples is not thought to have altered trace element compositions appreciably. Samples were redissolved into a 1:5 solution of

HNO₃:H₂O over a period of 24 hours at ~90 °C. 0.5 mL of sample solution was combined with 10 mL of a nitric acid ICP-MS solution along with 5 mL of H₂O. ICP-MS analysis utilized the same set of standards as DCP-AES analysis: basalts BIR, W2a, and K1919 as well as anorthosite AN-G. Geochemical data for all analyzed pegmatoids and host rock are given in Appendices B and C, respectively.

Radiogenic isotope analyses were conducted at the University of North Carolina at Chapel Hill. Whole-rock powder was dissolved in high-pressure Teflon (Parr) vessels with HF + HNO₃ at 180°C for 72 hours. The solution was dried down, then fluxed in 6M HCl for 4-6 hours at 180°C on a hot plate. This solution was then dried down and the samples fluxed again in 6M HCl up to twice more, depending on abundance of refractory minerals in a particular sample. The sample solution was aliquoted for Sr, Nd, and Pb separation. Strontium separation followed the method of Lundblad (1994), using Sr-spec cation exchange resin. Samples were dried onto single Re filaments with a TaF₅ activator and analyzed on a VG Sector 54 thermal ionization mass spectrometer (TIMS). Strontium analyses used a dynamic multi-collector method. Mass fraction was corrected using an exponential law and normalization to $^{86}\text{Sr}/^{84}\text{Sr} = 0.1194$. Replicate analyses of NBS-987 during the period of sample analysis yielded $^{87}\text{Sr}/^{86}\text{Sr} = 0.710268 \pm 0.000020$ (2σ , $n = 97$). All data are normalized to NBS-987 $^{87}\text{Sr}/^{86}\text{Sr} = 0.710250$. Neodymium was separated by a three-stage column method, modified after Harvey and Baxter (2009). Neodymium was analyzed in dynamic multi-collector mode on a Phoenix TIMS. All

analyses were corrected for fractionation using $^{146}\text{Nd}/^{144}\text{Nd} = 0.7219$. Replicate analyses of JNdi through the period of sample analysis yielded $^{143}\text{Nd}/^{144}\text{Nd} = 0.512104 \pm 0.000012$ (2σ , $n = 12$). All data are referenced to standard JNdi $^{143}\text{Nd}/^{144}\text{Nd} = 0.512115$. Lead was separated following an HBr-based technique modified after Parrish and Krogh (1987), in which sample aliquots were purified by double-passing through anion exchange column chemistry. Purified Pb was loaded onto Re filaments with Si-gel and analyzed as a metal in static multi-collector mode on a Phoenix TIMS. Replicate analyses of the NBS-981 standard were used to correct lead analyses for mass fractionation (0.14%/amu) assuming linear fractionation behavior.

4.4 Results

Abundances of Rb and Sr, and measured isotopic ratios are presented in Table 2. Included in Table 2 are calculated $^{87}\text{Sr}/^{86}\text{Sr}_{\text{initial}}$ values for Stillwater Complex samples, using an age of 2700 Ma (DePaolo and Wasserburg, 1979). Stillwater Complex samples have very low Rb/Sr ratios (commonly <0.1), due to low Rb concentrations, whereas the hornfels samples have higher Rb concentrations, and thus higher Rb/Sr ratios (This study; Powell et al., 1969; Mueller and Wooden, 1976). Data for all Stillwater Complex samples (Figure 16a) and hornfels samples (Figure 16b; this study; Powell et al., 1969; Mueller and Wooden, 1976) are shown on $^{87}\text{Rb}/^{86}\text{Sr}$ vs. $^{87}\text{Sr}/^{86}\text{Sr}$ plots, alongside calculated isochrons and reference 2700 Ma isochrons. The initial $^{87}\text{Sr}/^{86}\text{Sr}$ for the

reference isochrons is determined using the initial value for the Stillwater Complex sample (Figure 16a) and hornfels sample (Figure 16b) with the lowest Rb/Sr ratio. Stillwater samples are grouped by unit; pegmatoids and their host rocks are differentiated. The nominal age calculated with the isochron is generally accurate, but sample scatter results in poor precision (2757.4 ± 632.5 Ma; M.S.W.D. = 688.681). The isochron generated using hornfels samples provides an age of 2726.6 ± 54.3 Ma (M.S.W.D. = 1368.383). Four hornfels samples were excluded from the isochron, as the calculated $^{87}\text{Sr}/^{86}\text{Sr}_{\text{initial}}$ for these (~ 0.693) was below what would be expected of the bulk earth. Two of these samples were previously excluded from isochron calculations by Mueller and Wooden (1976), on the basis that they fell off the isochron by more than analytical error.

Samarium and neodymium abundances and isotopic ratios, along with calculated $^{143}\text{Nd}/^{144}\text{Nd}_{\text{initial}}$ and ϵ_{Nd} (relative to CHUR; $^{143}\text{Nd}/^{144}\text{Nd}_{\text{present}} = 0.512638$; $^{147}\text{Sm}/^{144}\text{Nd} = 0.1967$) values, are listed in Table 3. Sm/Nd ratios for Stillwater samples are in the range of 0.2 to 0.4; hornfels Sm/Nd is typically < 0.2 due to higher Nd concentrations. Data for all Stillwater Complex samples (Figure 17a) and hornfels samples (Figure 17b; this study; Lambert et al., 1994) are shown alongside calculated isochrons and reference 2700 Ma isochrons on $^{147}\text{Sm}/^{144}\text{Nd}$ vs. $^{143}\text{Nd}/^{144}\text{Nd}$ plots. The initial $^{143}\text{Nd}/^{144}\text{Nd}$ for the reference isochrons is determined using the initial value for the Stillwater Complex sample (Figure 17a) or hornfels sample (Figure 17b) with the

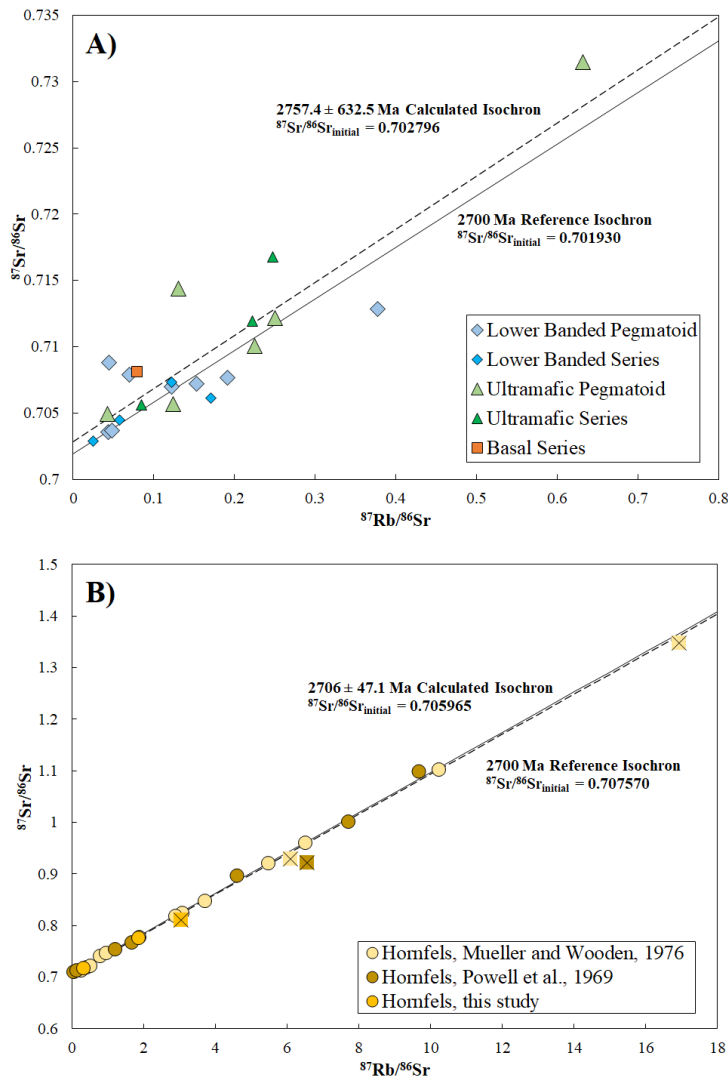


Figure 16: Results of Rb-Sr isotopic analysis, for both Stillwater and hornfels samples. Solid lines are 2700 Ma reference isochrons, while dashed lines are calculated isochrons using sample analyses. Larger, lighter-colored symbols indicate pegmatoid analyses; smaller, dark-colored symbols indicate host rock analyses. A) Stillwater Complex samples. Samples are grouped by series and divided into categories of host rock and pegmatoid. B) Hornfels samples. Samples with X through the point indicate samples that were excluded from the isochron calculation (see text for further discussion). Includes data from this study, Powell et al. (1969), and Mueller and Wooden (1976).

Table 2: Rb-Sr isotope analyses

Sample	Zone	Subzone	Type	Rb (ppm)	Sr (ppm)	Rb/Sr	⁸⁷ Sr/ ⁸⁶ Sr	⁸⁷ Rb/ ⁸⁶ Sr	⁸⁷ Sr/ ⁸⁶ Sr _{initial}
18MZ21	Hornfels	-	C	74.294	116.107	0.6399	0.776246	1.863414	0.703698
18MZ18	Hornfels	-	C	77.413	74.560	1.0383	0.811660	3.033986	0.693538
S18-81	Hornfels	-	C	20.634	180.604	0.1143	0.717913	0.330835	0.705033
M17-776	Basal	-	H	2.480	90.832	0.0273	0.708129	0.078984	0.705054
S18-76	Ultramafic	PZ	H	1.050	13.660	0.0769	0.711928	0.222421	0.703268
S18-66	Ultramafic	PZ	H	0.540	18.408	0.0293	0.705602	0.084877	0.702297
S18-60	Ultramafic	PZ	H	0.768	8.977	0.0856	0.716798	0.247733	0.707153
S18-77	Ultramafic	PZ	P	0.355	7.889	0.0450	0.714397	0.130174	0.709329
S18-65	Ultramafic	PZ	P	0.277	18.981	0.0146	0.704914	0.042248	0.703269
S18-57	Ultramafic	PZ	P	1.419	16.428	0.0864	0.712152	0.250009	0.702418
S18-59	Ultramafic	PZ	P	6.772	31.061	0.2180	0.731458	0.632148	0.706847
GCP-03	Ultramafic	PZ	P	3.368	43.254	0.0779	0.710080	0.225279	0.701309
GCP-05	Ultramafic	PZ	P	1.008	23.505	0.0429	0.705663	0.124063	0.700833
S18-18B	Lower Banded	N-I	H	1.670	39.543	0.0422	0.707338	0.122188	0.702581
S18-23	Lower Banded	N-I	H	8.400	142.542	0.0589	0.706115	0.170450	0.699479
S18-03	Lower Banded	OB-I	H	0.462	53.699	0.0086	0.702898	0.024866	0.701930
S18-ANC	Lower Banded	OB-I	H	3.107	155.327	0.0200	0.704497	0.057847	0.702272
S18-55	Lower Banded	N-I	P	2.259	34.160	0.0661	0.707679	0.191303	0.700231
S18-58	Lower Banded	N-I	P	12.351	94.783	0.1303	0.712847	0.377151	0.698163
S18-20	Lower Banded	N-I	P	1.488	35.137	0.0423	0.706978	0.122492	0.702209
S18-24	Lower Banded	N-I	P	0.761	49.458	0.0154	0.708803	0.044517	0.707070
S18-25	Lower Banded	N-I	P	1.275	52.722	0.0242	0.707895	0.069981	0.705170
S18-02	Lower Banded	OB-I	P	1.065	70.714	0.0151	0.703551	0.043538	0.701856
S18-04	Lower Banded	OB-I	P	2.119	126.898	0.0167	0.703660	0.048288	0.701780
S18-PEGC	Lower Banded	OB-I	P	7.850	148.245	0.0530	0.707184	0.153167	0.701292

lowest Sm/Nd ratio. As with the Rb-Sr system, scatter in whole rock isotopic compositions has resulted in increased error on Sm-Nd ages. The isochron generated using Stillwater samples provides an age of 2563.6 ± 383.6 Ma (M.S.W.D. = 7.164); sample S18-03 is excluded from the isochron, as it is an obvious outlier. Very few studies have analyzed Sm-Nd isotopes in the hornfels; as a result, the isochron generated for the hornfels is strongly controlled by the single point from Lambert et al. (1994). The Sm-Nd hornfels age is 2759.4 ± 288.8 Ma (M.S.W.D. = 0.735).

Lead isotopic ratios, along with elemental abundances of Pb, U, and Th, are presented in Table 4. U/Pb (0.004 – 0.18) and Th/Pb (0.015 – 1.1) ratios for Stillwater Complex samples and hornfels samples fall within the same range, although hornfels samples tend to contain higher concentrations of U, Pb, and Th. Data for Stillwater Complex samples (Figure 18a) and hornfels samples (Figure 18b; this study; Wooden et al., 1991) are shown on $^{206}\text{Pb}/^{204}\text{Pb}$ vs. $^{207}\text{Pb}/^{204}\text{Pb}$ plots. Also shown in Figure 18 are the calculated isochron and the reference 2700 Ma isochron. The slope of the reference 2700 Ma isochron is the expected $(^{207}\text{Pb}/^{206}\text{Pb})^*$ ratio at 2700 Ma, and the isochron is constrained so as to pass through the sample containing the least radiogenic Pb. The $^{207}\text{Pb}/^{206}\text{Pb}$ age calculated for the hornfels samples (this study; Wooden et al., 1991) is 2782.5 ± 125.1 Ma (M.S.W.D. = 79.982). The $^{207}\text{Pb}/^{206}\text{Pb}$ age calculated for the Stillwater Complex samples is 2701.1 ± 125.6 Ma (M.S.W.D. = 136.085).

Table 3: Sm-Nd isotopic analyses

Sample	Zone	Subzone	Type	Sm (ppm)	Nd (ppm)	Sm/Nd	$^{147}\text{Sm}/^{144}\text{Nd}$	$^{143}\text{Nd}/^{144}\text{Nd}$	$^{143}\text{Nd}/^{144}\text{Nd}_i$	ϵ_{Nd}
18MZ21	HNFL	-	C	2.304	12.651	0.1821	0.110003	0.510820	0.508860	-2.7818
18MZ18	HNFL	-	C	1.915	9.835	0.1947	0.117644	0.511088	0.508992	-5.3720
S18-81	HNFL	-	C	1.516	8.575	0.1768	0.106820	0.510806	0.508903	-4.5334
M17-776	BAS	-	H	0.598	2.296	0.2604	0.157321	0.511814	0.509011	-2.4053
S18-76	UMS	PZ	H	0.204	0.681	0.2999	0.181249	0.512057	0.508828	-3.8402
S18-66	UMS	PZ	H	0.136	0.419	0.3237	0.195623	0.512451	0.508966	-2.6212
S18-60	UMS	PZ	H	0.120	0.423	0.2837	0.171397	0.511867	0.508814	3.8418
S18-77	UMS	PZ	P	0.147	0.439	0.3338	0.201717	0.512266	0.508672	0.1650
S18-65	UMS	PZ	P	0.107	0.347	0.3084	0.186350	0.512391	0.509071	0.2006
S18-57	UMS	PZ	P	0.281	0.855	0.3287	0.198615	0.512385	0.508847	-2.3099
S18-59	UMS	PZ	P	0.208	0.624	0.3342	0.201943	0.512470	0.508872	-4.0663
GCP-03	UMS	PZ	P	0.257	1.061	0.2420	0.146178	0.511202	0.508598	-5.6394
GCP-05	UMS	PZ	P	0.174	0.551	0.3162	0.191060	0.512342	0.508938	-3.3231
S18-53	LBS	N-I	H	0.102	0.377	0.2698	0.163054	0.511921	0.509016	1.1922
S18-18B	LBS	N-I	H	0.197	0.631	0.3120	0.188557	0.512394	0.509035	1.1922
S18-23	LBS	N-I	H	0.150	0.761	0.1966	0.118810	0.511443	0.509326	-1.9433
S18-03	LBS	OB-I	H	0.173	0.659	0.2619	0.158315	0.513216	0.510396	24.7836
S18-ANC	LBS	OB-I	H	0.138	0.744	0.1857	0.112205	0.511216	0.509217	0.3612
S18-55	LBS	N-I	P	0.259	0.773	0.3354	0.202708	0.512538	0.508927	-5.1344
S18-58	LBS	N-I	P	0.167	0.642	0.2598	0.156968	0.511761	0.508965	-6.2896
S18-20	LBS	N-I	P	0.210	0.671	0.3125	0.188872	0.512663	0.509298	3.2302
S18-24	LBS	N-I	P	0.820	1.939	0.4229	0.255617	0.513696	0.509142	-3.2959
S18-25	LBS	N-I	P	0.886	2.107	0.4206	0.254224	0.513673	0.509144	-6.0051
S18-02	LBS	OB-I	P	0.323	1.060	0.3048	0.184205	0.512611	0.509329	-9.0621
S18-04	LBS	OB-I	P	0.412	1.575	0.2615	0.157985	0.512009	0.509195	1.6355
S18-PEGC	LBS	OB-I	P	1.021	4.781	0.2135	0.128984	0.511534	0.509236	2.0101

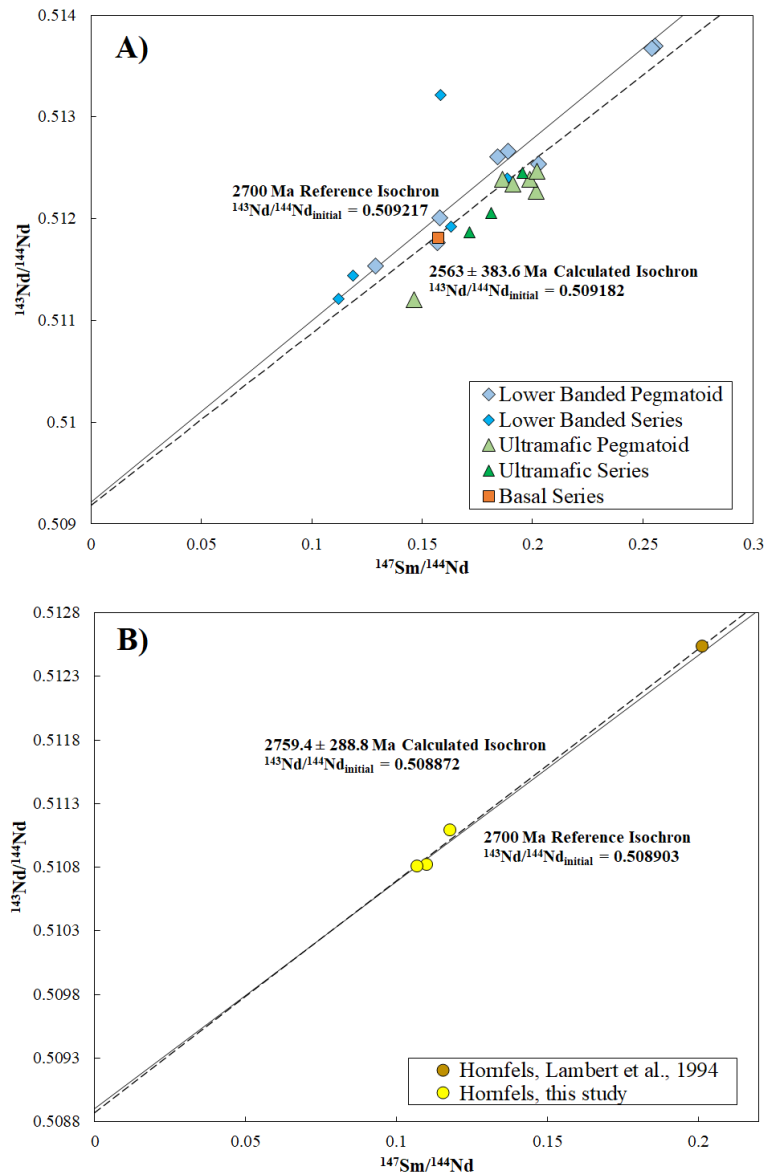


Figure 17: Results of Sm-Nd isotopic analysis, for both Stillwater Complex and hornfels samples. Solid lines are 2700 Ma reference isochrons, while dashed lines are calculated isochrons using sample analyses. Larger, lighter-colored symbols indicate pegmatoid analyses; smaller, dark-colored symbols indicate host rock analyses. A) Stillwater Complex samples. Samples are grouped by series and divided into categories of host rock and pegmatoid. B) Hornfels samples. Includes data from this study and Lambert et al. (1994).

Stratigraphic variations in $^{87}\text{Sr}/^{86}\text{Sr}_{\text{initial}}$, ϵ_{Nd} , and $^{206}\text{Pb}/^{204}\text{Pb}_{\text{initial}}$ are shown in Figure 19. In all three isotopic systems, initial isotopic ratios have been calculated to an assumed 2700 Ma age. Measured hornfels initial ratios are very similar to initial isotopic ratios from the Stillwater Complex itself, in all three isotopic systems. One hornfels sample (18MZ18) was found to have an unusually low $^{87}\text{Sr}/^{86}\text{Sr}_{\text{initial}}$ ratio. This is in line with some findings of Mueller and Wooden (1976), who identified two samples which fell off the isochron by more than analytical error. Calculation of initial values for these samples yields similar $^{87}\text{Sr}/^{86}\text{Sr}_{\text{initial}}$ ratios to that found in sample 18MZ18. These samples experienced some Sr loss or other disturbance. Comparison of Stillwater Complex pegmatoid isotopic ratios to their spatially associated host rocks shows no consistent pattern of change in isotopic ratio of pegmatoids relative to host rock or hornfels samples. Hornfels samples commonly have similar isotopic ratios when compared with Stillwater Complex sample. Pegmatoids sometimes possess higher initial ratios than their spatially associated host rock, and sometimes lower. Pegmatoid/host rock differences are inconsistent across different isotopic systems. Isotopic ratios are generally more variable in the Lower Banded series than in the Ultramafic and Basal series, particularly in the Sm-Nd and Pb-Pb systems. One sample (S18-03, a gabbro-norite from OB-I in the Lower Banded series) was found to have unusually high ϵ_{Nd} . Comparatively, Rb-Sr and Pb isotopes in this sample are not unusual.

Table 4: Pb-Pb isotopic analyses

Sample	Zone	Subzone	Type	U (ppm)	Th (ppm)	Pb (ppm)	U/Pb	Th/Pb	²⁰⁶ Pb/ ²⁰⁴ Pb	²⁰⁷ Pb/ ²⁰⁴ Pb	²⁰⁸ Pb/ ²⁰⁴ Pb
18MZ21	HNFL	-	C	1.835	7.712	17.404	0.1054	0.4431	19.7819	16.1911	38.4119
18MZ18	HNFL	-	C	1.431	4.797	11.345	0.1262	0.4228	19.1388	16.0052	37.6089
S18-81	HNFL	-	C	0.266	0.828	4.006	0.0664	0.2065	16.0450	15.4104	35.5447
M17-776	BAS	-	H	0.143	0.478	3.244	0.0439	0.1473	15.5417	15.4114	35.3497
S18-76	UMS	PZ	H	0.031	0.128	0.450	0.0695	0.2850	16.8438	15.5372	36.6559
S18-66	UMS	PZ	H	0.010	0.060	0.240	0.0420	0.2514	16.5152	15.4842	37.0192
S18-60	UMS	PZ	H	0.026	0.112	0.246	0.1074	0.4571	18.8444	15.8721	39.4316
S18-77	UMS	PZ	P	0.040	0.127	3.954	0.0102	0.0321	14.5574	15.1318	34.2829
S18-65	UMS	PZ	P	0.006	0.039	0.190	0.0301	0.2029	16.9882	15.5832	37.4089
S18-57	UMS	PZ	P	0.028	0.130	0.297	0.0931	0.4380	18.9973	15.9677	39.6389
S18-59	UMS	PZ	P	0.020	0.090	1.499	0.0133	0.0601	15.5203	15.4615	34.9421
GCP-03	UMS	PZ	P	0.093	0.374	0.533	0.1751	0.7016	20.8320	16.2526	41.2905
GCP-05	UMS	PZ	P	0.062	0.068	0.343	0.1813	0.1983	16.9017	15.5562	37.0483
S18-53	LBS	N-I	H	0.007	0.042	0.217	0.0325	0.1960	16.6593	15.4784	36.4151
S18-18B	LBS	N-I	H	0.048	0.092	2.058	0.0233	0.0449	14.6675	15.1701	34.2877
S18-23	LBS	N-I	H	0.005	0.033	0.682	0.0071	0.0486	14.8558	15.1918	34.6410
S18-03	LBS	OB-I	H	0.004	0.017	0.134	0.0279	0.1285	15.6614	15.3207	35.5278
S18-ANC	LBS	OB-I	H	0.010	0.055	0.568	0.0180	0.0968	15.8804	15.3570	35.6465
S18-55	LBS	N-I	P	0.019	0.114	1.157	0.0163	0.0985	19.4533	16.1331	39.1893
S18-58	LBS	N-I	P	0.015	0.056	3.832	0.0040	0.0146	23.2638	16.8012	44.3712
S18-20	LBS	N-I	P	0.016	0.051	1.660	0.0099	0.0306	14.6199	15.1860	34.2461
S18-24	LBS	N-I	P	0.053	0.082	0.758	0.0703	0.1080	18.4522	15.9997	37.6137
S18-25	LBS	N-I	P	0.065	0.109	1.376	0.0469	0.0795	18.1588	15.8838	38.4294
S18-02	LBS	OB-I	P	0.011	0.045	0.483	0.0217	0.0934	15.4512	15.3266	35.4084
S18-04	LBS	OB-I	P	0.087	0.376	0.664	0.1316	0.5654	17.3539	15.5780	37.4026
S18-PEGC	LBS	OB-I	P	0.197	1.637	1.496	0.1315	1.0943	16.9639	15.4325	37.5456

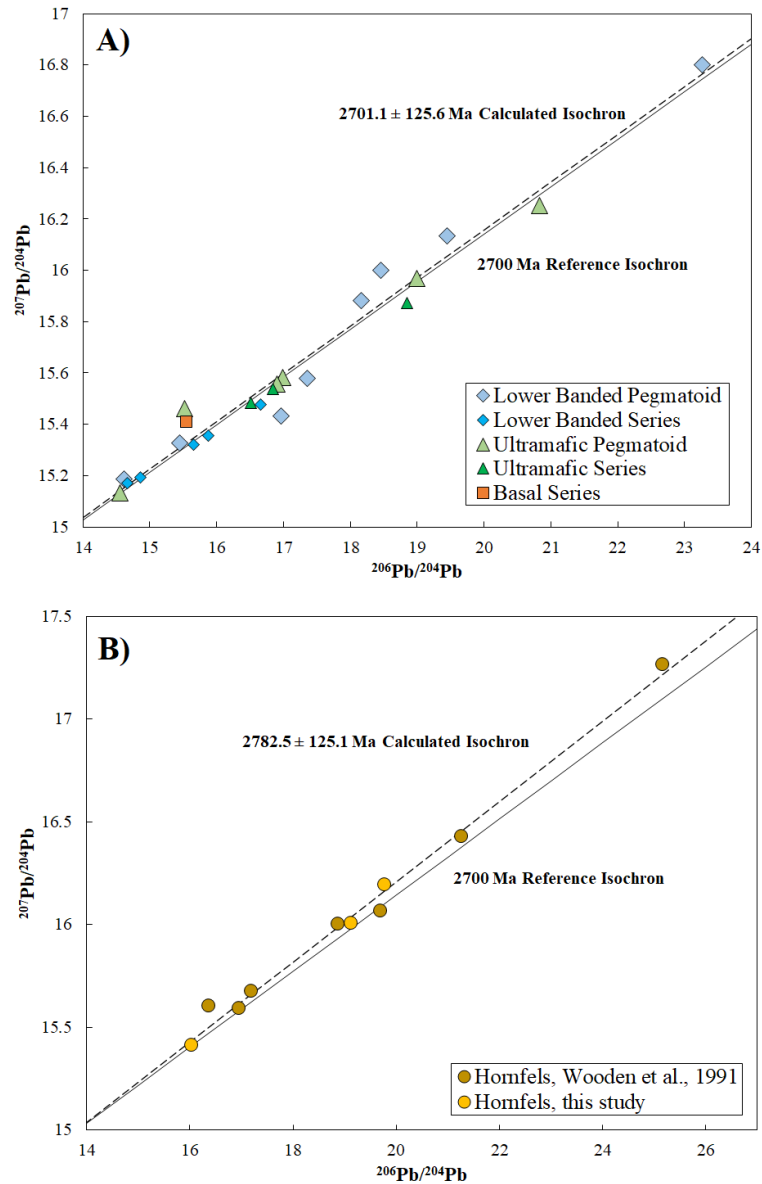


Figure 18: Results of Pb-Pb isotopic analysis, for both Stillwater Complex and hornfels samples. Solid lines are 2700 Ma reference isochrons, calculated as described in the text. Dashed lines are calculated isochrons defined by the sample analyses. Larger, lighter-colored symbols indicate pegmatoid analyses; smaller, dark-colored symbols indicate host rock analyses. A) Stillwater Complex samples. Samples are grouped by series and divided into categories of host rock and pegmatoid. B) Hornfels samples. Includes data from this study and Wooden et al. (1991).

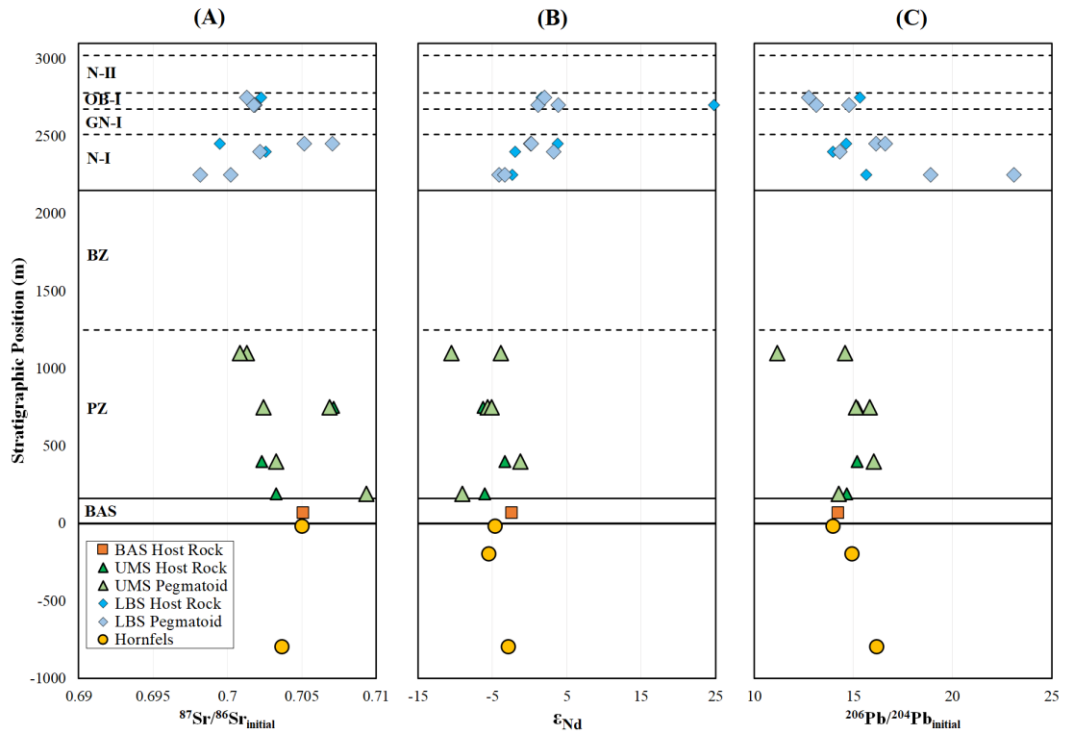


Figure 19: Stratigraphic section of radiogenic isotopes from Stillwater Complex and hornfels samples analyzed in this study. BAS – Basal series; PZ – Peridotite zone of the Ultramafic series; BZ – Bronzitite zone of the Ultramafic series; N-I – Norite zone I of the Lower Banded series; GN-I – Gabbronorite zone I of the Lower Banded series; OB-I – Olivine-bearing zone I of the Lower Banded series; N-II – Norite zone II of the Lower Banded series. A) $^{87}\text{Sr}/^{86}\text{Sr}_{\text{initial}}$, calculated using an age of 2700 Ma. B) ϵ_{Nd} , calculated using an age of 2700 Ma and $^{143}\text{Nd}/^{144}\text{Nd}_{\text{CHUR}}$ of 0.509134. C) $^{206}\text{Pb}/^{204}\text{Pb}_{\text{initial}}$, calculated using an age of 2700 Ma.

4.5 Discussion

4.5.1 Disturbance of Stillwater Complex Isotope Systematics

Rb-Sr isotopes in the hornfels define a reasonably well-constrained isochron that corresponds to the age of the Stillwater Complex. This suggests that Rb-Sr isotopes in the country rock were reset during contact metamorphism when the complex was emplaced. However, there is no evidence in the hornfels samples that a later disturbance

to the system, such as by the 1600-1700 Ma regional metamorphic event (e.g., Giletti, 1966), has affected the country rock Rb-Sr system. While the calculated whole rock Pb-Pb age of hornfels samples is within error of the intrusion of the Stillwater Complex, the calculated and reference isochrons for hornfels samples (Figure 18b) calculated using the Pb-Pb system suggest the hornfels are ~80 million years older than the Stillwater Complex. Mogk and Mueller (1990) suggested that the Stillwater Complex had intruded into the country rock while it was still warm from an earlier regional metamorphic event, ~50 million years prior to the Stillwater Complex intrusion. The older Pb-Pb ages in the hornfels may reflect this earlier regional metamorphic event. Very little work has been conducted previously to understand Sm-Nd systematics in the hornfels. As a result, the Sm-Nd isochron defined by hornfels samples is imprecise. Despite this, as with the Pb-Pb isochron, the Sm-Nd isochron suggests the hornfels samples are ~60 million years older than the Stillwater Complex. Sm-Nd isotopes may have also been impacted by the regional metamorphic event that metamorphosed the country rock to a biotite schist, and were then left unaltered by the intrusion of the Stillwater Complex and metamorphism in the aureole. This could also apply to the Sr isotopic system, although it would be more unusual for Rb-Sr isotopes to remain undisturbed through even low-grade metamorphic events.

Previous work on Rb-Sr isotopes within the Stillwater Complex suggested that the Rb-Sr system had been reset by the 1.7 Ga regional metamorphic event (DePaolo and

Wasserburg, 1979). This was based on an internal mineral isochron for a single gabbro. However, complete resetting of the Rb-Sr system would require intrusion-scale re-equilibration of Rb and Sr. Outcrop-scale work on Rb and Sr systematics has demonstrated that even during high-grade metamorphism, Rb-Sr isotopes only re-equilibrate over limited volumes of rock (Krogh and Davis, 1973); diffusion of Sr isotopes in the mantle may be limited to only tens to hundreds of meters (Hofmann, 1975). At the mineral scale, metamorphic activity such as that experienced by the Stillwater Complex may certainly reset Rb-Sr isotopic systematics. However, due to the limited diffusion of Rb and Sr, at larger scales, Rb-Sr isotopes remain relatively unaffected (e.g., Roddick and Compston, 1977). The scatter observed on the whole rock isochron (Figure 16a) suggests that Rb-Sr re-equilibration may have been at a scale larger than the individual samples. By averaging measured $^{87}\text{Sr}/^{86}\text{Sr}$ ratios and Rb and Sr concentrations in samples from the same outcrop, an average outcrop-scale ratio (Roddick and Compston, 1977) was determined for each spatially-associated set of host rock and pegmatoids. Some samples were collected from the float, and were excluded from the outcrop averaging technique on this basis.

The Rb-Sr age determined using the outcrop averaging technique (2779.9 ± 219.2 ; M.S.W.D = 20.877) is better constrained than the age determined using individual sample analyses (2757.4 ± 632.5). Remaining error may be related to the low number of samples used in averaging (two to three samples per outcrop), or the inclusion of

pegmatoids in the averaging, although the 1.7 Ga event should have impacted both pegmatoids and host rock, regardless of early differences in their formation.

Alternatively, error remaining in the age might be explained by re-equilibration during metamorphism occurring on a greater scale than a few meters. The Stillwater Complex may provide an interesting location for future investigation into the scale of Rb-Sr isotope re-equilibration during relatively low-grade regional metamorphism, or may, in the future, help to constrain the timeframe during which regional metamorphic activity was ongoing.

The observed scatter in Sm-Nd isotope systematics is unusual. It does not match the earlier findings of DePaolo and Wasserburg (1979), who analyzed six whole rock samples and found that all samples fit the internal mineral isochron of 2701 Ga. The samples analyzed as part of the present study do not define a precise isochron. However, the results of the present study are consistent with the findings of Lambert et al. (1994); their Sm-Nd whole rock isotope analyses have a similar degree of scatter (Figure 20). Samples analyzed in the present study and by Lambert et al. (1994) cover a more spatially significant section of the Stillwater Complex and include more samples; samples analyzed by DePaolo and Wasserburg (1979) may have been somehow anomalous. The degree of scatter in Sm-Nd isotopes is doubly unusual, as the Sm-Nd system tends to be relatively resilient to regional metamorphic activity, especially weak, low-grade metamorphic activity. The possible involvement of fluids in regional

metamorphism could have resulted in alteration of Sm-Nd isotope systematics, as REE mobile during interaction with open system fluids, even at greenschist facies (e.g., Li et al., 1990; Brewer and Menuge, 1998). However, even in systems involving fluid infiltration, Sm-Nd mobility is not a guarantee (e.g., Su and Fullagar, 1995). Other explanations for Sm-Nd scatter in Stillwater samples must be considered. Variability in ϵ_{Nd} does not vary systematically based on sample location. If variability in Sm-Nd isotopes in Stillwater samples is not due to alteration during regional metamorphism, it

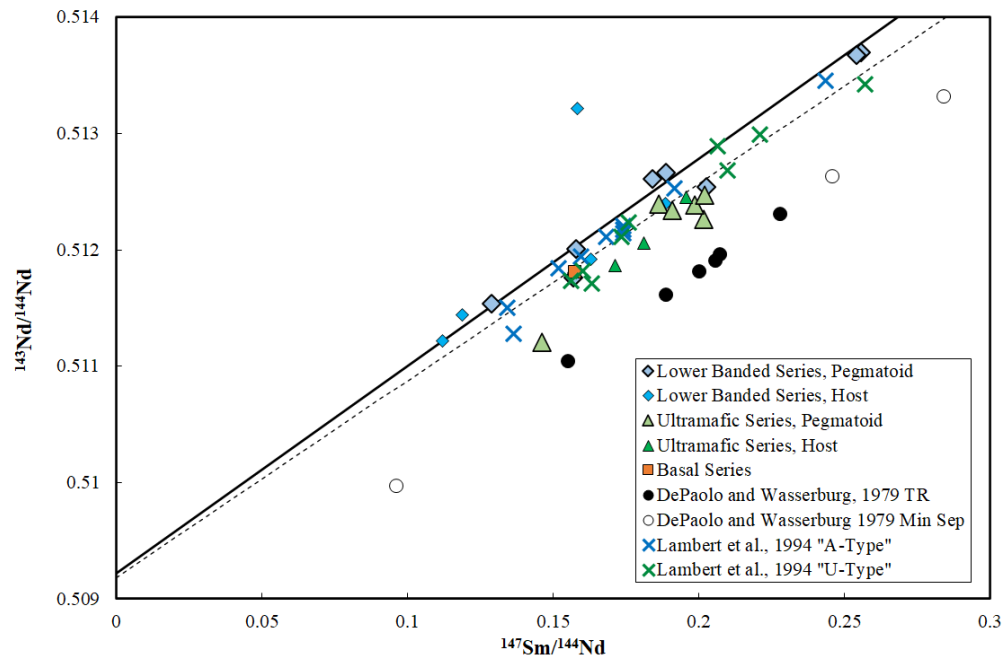


Figure 20: Sm-Nd isotopic analysis results from this study, alongside the Sm-Nd isotopic results of DePaolo and Wasserburg (1979) and Lambert et al. (1994). Lambert et al. (1994) "A-Type" samples are primarily from the Lower Banded series; "U-Type" samples are from the Ultramafic series. Isochrons are the same as in Figure 17.

may be explained by contamination or source region heterogeneity. These possibilities are explored in greater detail in the next section.

The Pb-Pb isochron, while still showing some scatter, is much better constrained than Sm-Nd or Rb-Sr. Previous work analyzing Pb isotopes at the mineral scale showed evidence of disturbance to Pb isotope systematics. McCallum et al. (1999) analyzed sulfide and plagioclase grains. Minerals from samples with little to no greenschist-facies alteration preserved 2700 Ma isotope ratios, while samples with more alteration had altered isotopic ratios. Similarly, U-Pb systematics in apatite showed evidence of lead loss during regional metamorphism (Nunes and Tilton, 1971). Leaching experiments on plagioclase (Wooden et al., 1991) also found evidence of later disturbance. The whole rock Pb-Pb isotope analyses do have some scatter about the 2700 Ma isochron. However, this scatter is substantially less than is observed in other isotopic systems. This may indicate that Pb isotopes were reset and homogenized at the mineral scale, but that original isochron relationships were largely preserved at the scale of whole rock samples.

4.5.2 Isotopic Heterogeneity in the Stillwater Complex

The previous examination of disturbance of the Rb-Sr, Sm-Nd, and Pb-Pb system suggests that, while the 1.7 Ga event did impact isotope systematics, this disturbance was primarily at the mineral scale, and can be largely avoided through use of whole rock isotopes. While whole rock isochrons are susceptible to spurious age correlations

due to mixing or other processes (e.g., Cattell et al., 1984), the ages calculated using the whole rock data from these samples yields the age of the Stillwater Complex, albeit with a low degree of precision due to scatter. Further, while isotopic ratios from Stillwater samples are highly scattered, samples from the hornfels define more precise isochrons. In particular, the Rb-Sr data from the hornfels fall along the 2700 Ma isochron. A regional metamorphic event sufficient to alter isotope systematics in the Stillwater should also have impacted the associated hornfels. This suggests that, while radiogenic isotope systematics in the hornfels were likely reset during emplacement of the Stillwater Complex, the scatter observed in Stillwater complex isotopic ratios must be explained through processes other than disturbance by the 1.7 Ga regional event.

Lambert et al. (1994) suggested that heterogeneities in ϵ_{Nd} could be explained by two parental magmas. They divided their samples into two major groups. One of these they described as possessing an 'Ultramafic' affinity (U-type). The other group was described as being of 'Anorthositic' affinity (A-type). The transition from a U-type parent, which formed the Ultramafic series and the base of the Lower Banded series, to an A-type parent, which was suggested to form the remainder of the Banded series, was described as occurring at the base of Troctolite-Anorthosite Zone I (TAZ-I), which corresponds to Olivine-bearing Zone I by the nomenclature of McCallum et al. (1980). In a comparison of the ϵ_{Nd} of this study to that of the Lambert et al. (1994) samples (Figure 21), the division between the two parental magmas was not observed. While the four

samples from OB-I and above analyzed as part of this study were found to have strongly positive ϵ_{Nd} , samples that should have an Ultramafic affinity were found in this study to fall in and above the Anorthositic affinity zone (Figure 21). In addition, the study of Lambert et al. (1994) included the total rock samples analyzed by DePaolo and Wasserburg (1979) in the U-type affinity group, as they possessed ϵ_{Nd} in between roughly -2 and -3. However, these samples were collected from a variety of locations, half of which were above OB-I of the Lower Banded series, which Lambert et al. suggested to be the point where magmatic affinities changed from U-type to A-type. Despite these samples possessing apparently U-type ϵ_{Nd} signatures, the majority of

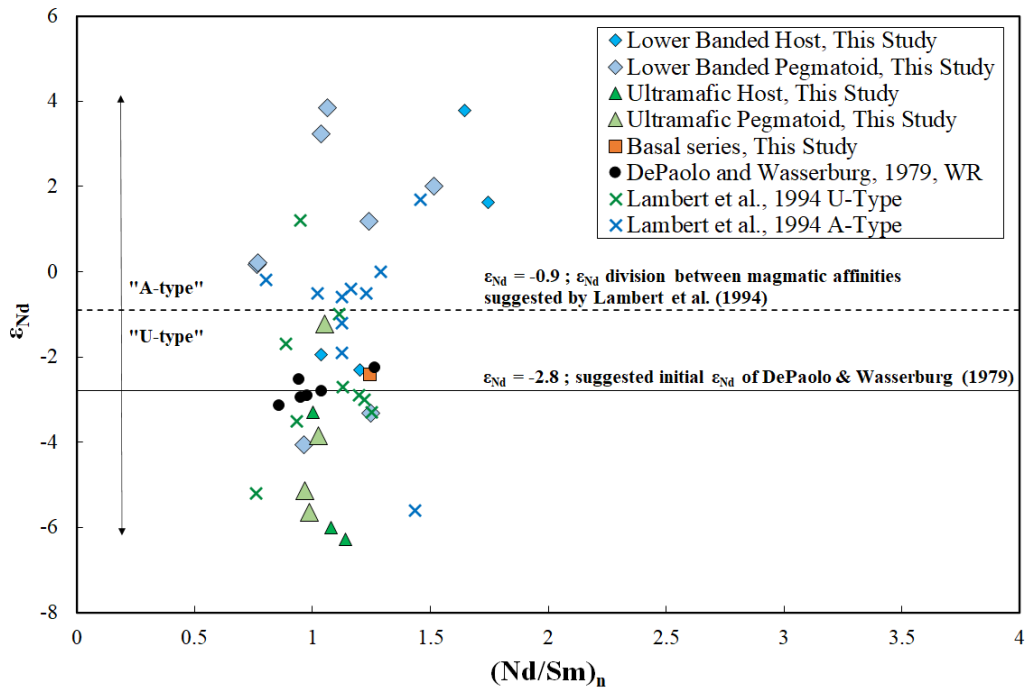


Figure 21: ϵ_{Nd} at 2700 Ma for samples from this study, DePaolo and Wasserburg (1979) and Lambert et al. (1994) plotted against their chondrite-normalized Nd/Sm ratios (chondrite normalization factors after McDonough and Sun, 1995). Lambert et al.

(1994) places the division between U-type and A-type magmas at $\epsilon_{Nd} = -0.9$. The horizontal line at $\epsilon_{Nd} = -2.8$ is the ϵ_{Nd} at 2700 Ma as proposed by DePaolo and Wasserburg (1979). Excluded from this figure is one Lower Banded series sample analyzed in this study with $\epsilon_{Nd} = 24$, which was likely due to alteration. Samples from Lambert et al. (1994) are identified as possessing A-Type or U-Type affinity based on the affinities listed for each sample in their Table 1.

samples analyzed by DePaolo and Wasserburg (1979) were not collected from the portions of the Stillwater Complex that apparently crystallized from a U-type parent, but from the portions that Lambert et al. (1994) suggested crystallized from a parent of A-type affinity. The division between A-Type and U-Type samples does not appear to be clear-cut using Nd isotopes. In addition, despite ostensibly being sourced from two separate parental magmas, all the chondrite-normalized Nd/Sm ratio for all samples falls within the same range, of ~ 0.5 to 2, with no differentiation depending on stratigraphic location. Further, Pb and Sr initial isotopic variability is does not exhibit similar stratigraphic variability.

Taken together, the radiogenic isotope data indicates that formation of the Stillwater Complex was not as simple as a single new, isotopically distinct magma entering the system at a defined stratigraphic position. The presence of six different compositional groups of Stillwater-associated dikes below the intrusion (Helz, 1985) could suggest the presence of multiple magmas, but the lack of a defined shift in radiogenic isotope geochemistry with stratigraphic height suggests that sequential emplacement of multiple distinct magmas is not the explanation for Stillwater Complex isotopic variability.

While sequential emplacement of isotopically distinct magmas does not adequately explain observed isotopic variability, a heterogeneous source region may be a better explanation. The source region for the Stillwater Complex is poorly constrained. The magma parental to the complex has variably been described as a contaminated komatiite (e.g., Jenkins and Mungall, 2018) or boninitic (e.g., Boudreau et al., 1997). However, a large source region may well have been required to support an intrusion the size of the Stillwater Complex. The scale of mantle heterogeneity is a matter of some debate; it has been explored using geophysical imaging techniques (e.g., Stixrude and Lithgow-Bertelloni, 2012) as well as by analysis of erupted material that should be drawing from roughly the same source, such as mid-ocean ridges or associated islands in volcanic chains such as Hawaii (e.g., Anderson, 2006 and references therein). These studies have suggested that mantle heterogeneity may occur at scales of tens of kilometers. Preservation of this source region heterogeneity during the formation of the Stillwater Complex could explain some of the observed variability in Stillwater Complex samples, which is not correlated to spatial variation. A challenge to this explanation of heterogeneity in the Stillwater Complex is it requires the melted mantle material to retain isotopic heterogeneity even as the magma is mixed and ascends. Some studies (e.g., Anderson, 2006) suggest melting large volumes of mantle results in homogenization of the melt, even if derived from a heterogenous source region.

Alternative explanations for isotopic heterogeneity in the Stillwater Complex rely primarily on models of contamination. Contamination could be due to assimilation of crustal material during magma ascent. Alternatively, fluids released during contact metamorphism may have acted to alter isotope systematics around the time of Stillwater Complex emplacement. The hydrothermal model of intrusion formation holds that fluids moving upward through the intrusion a) concentrated metals, forming the J-M Reef; b) left geochemical evidence in certain minerals, such as apatite (Boudreau and McCallum, 1989); and c) caused the formation of the pegmatoid bodies. Comparison of host rock to pegmatoids (Figure 19) does not yield any appreciable, consistent shifts in isotopic composition in spatially associated pegmatoid/host rock pairs. Pegmatoids and host rock commonly possess similar initial ratios, or in cases where they differ substantially, the degree of shift between host rock and pegmatoid is not consistent. In some samples, the pegmatoid has a higher initial ratio, while in others, the host rock's initial ratio is higher. The pegmatoids are likely fluid-related features, but no isotopic evidence of fluid circulation is clearly identified in this spatial comparison. One difficulty with a model involving fluid alteration of isotopic signatures is that the country rock into which the Stillwater Complex had been intruded had previously been metamorphosed to a biotite schist containing only about 0.5 wt. % H₂O released during contact metamorphism (Labotka and Kath, 2001). Unlike at the Bushveld Complex (Benson et al., 2020b), where country rock had previously been unmetamorphosed and a

great deal of fluid (as much as 6 wt. %; Connolly, 2010) could be released during contact metamorphism, relatively little fluid was available for dehydration during the emplacement of the Stillwater Complex. A lower water/rock ratio would result in less impact on Stillwater Complex rocks.

4.5.3 Crustal Contamination of Stillwater Parental Magma

The exact model of contamination – whether occurring primarily in the lower crust during melt ascent, due to contamination by the upper crustal country rock, or due to fluid released during metamorphism – is poorly constrained. One issue lies in the composition of the Stillwater Complex parent compared to the country rock into which it intruded. Samples from the hornfels possess extremely similar initial isotopic ratios when compared with samples from the Stillwater Complex itself (Figure 22). Thus, any involvement of the hornfels (or the biotite schist that was parental to the hornfels) in contamination of the Stillwater Complex would have little impact on the complex's isotopic ratios. Stillwater Complex melts were likely sourced from the mantle, regardless of what contamination occurred during ascent. The mantle at 2.7 Ga would have possessed a relatively low initial $^{87}\text{Sr}/^{86}\text{Sr}$ of 0.70123 (calculated from the modern uniform reservoir ratios of McCulloch and Wasserburg, 1978). ϵ_{Nd} of the chondritic uniform reservoir is defined at 0, but the by 2.7 Ga, the mantle would have fractionated Sm from Nd, developing a positive ϵ_{Nd} of roughly 4 (DePaolo, 1988). The Stacey-Kramers mantle evolution curve (Stacey and Kramers, 1975) places the 2.7 Ga $^{206}\text{Pb}/^{204}\text{Pb}$

ratio at 13.64 and the initial $^{207}\text{Pb}/^{204}\text{Pb}$ ratio at 14.69. Contamination of the parental melt could have occurred in the lower crust during ascent. Lower crustal granulite analyses have suggested that globally, the lower crust is a very heterogeneous Nd isotope reservoir (e.g., Vervoort et al., 2000) which tends to be a mixture of mantle-like (positive ϵ_{Nd}) and crust-like (negative ϵ_{Nd}) signatures.

The same appears to be true for Sr, although the pressure and temperature conditions of the lower crust, combined with the relatively mobility of Rb and Sr, make constraining this ratio more challenging. For this reason, Sr and Nd isotope reservoirs of the upper and lower crust are presented as a single crustal reservoir, although this may not be the case; no work to determine lower crustal isotopic signatures in the region has been conducted. Pb isotopes in the lower crust are thought to be distinctly less radiogenic than the upper crust, due to loss of U during metamorphism (Rudnick and Goldstein, 1990). The upper crust is represented by the initial isotopic ratios calculated from the hornfels isochrons. Fluid release during contact metamorphism should not fractionate Sr, Nd, or Pb isotopic ratios, such as the upper crustal endmember represents the isotopic composition of an upper crustal contamination, whether due to fluid circulation or crustal assimilation.

Most samples (Figure 22) tend to fall between the mantle and crustal end members, suggesting that variability in initial ratios is at least partially due to varying

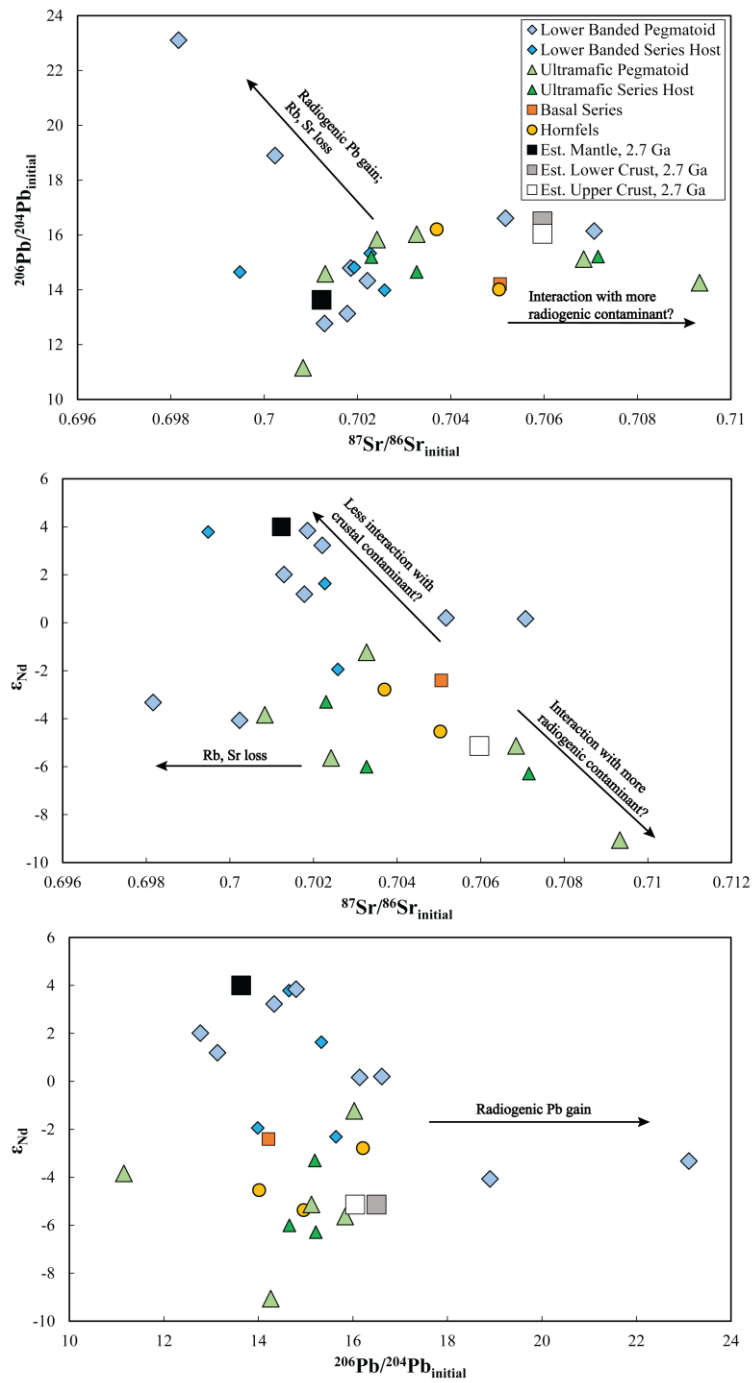


Figure 22: Three plots showing variance of initial isotopic ratios against one another. Large squares represent mantle and lower crustal compositions as described in the text. Labeled arrows indicate possible influence of various processes on observed isotopic ratios.

amounts of contamination. Some variability outside of this mixing trend is likely due to alteration during later greenschist facies metamorphism. Loss of Rb and radiogenic Sr results in calculation of unusually low $^{87}\text{Sr}/^{86}\text{Sr}_{\text{initial}}$. McCallum et al. (1999), found that alteration had produced radiogenic Pb gain in altered samples during Pb leaching experiments. Four samples (Figure 22) have more radiogenic initial Sr ratios than the estimated crustal reservoirs. This could be due to interaction with more radiogenic crust. The remaining samples, which fall between estimated mantle and crustal reservoirs, likely represent variable degrees of crustal contamination. Conversely, variability in ϵ_{Nd} does not appear correlated with either Rb and Sr loss or radiogenic Pb gain. However, there is a slight correlation between ϵ_{Nd} and stratigraphic position. Samples with more radiogenic ϵ_{Nd} , closer to 2.7 Ga mantle values, tend to occur stratigraphically higher in the complex, while more negative ϵ_{Nd} tends to occur stratigraphically lower. Thus, Nd isotopes suggest a higher degree of crustal contamination lower in the complex, with less crustal signatures higher in the complex. This is a trend that is not observed using Sr or Pb isotopes. A possible explanation for the difference could be if the contaminant was a fluid. Benson et al. (2020) describe a fluid contaminant of the Bushveld Complex which was hypothesized to contain high concentrations of Pb (1.03 wt. %) and Sr (4400 ppm), but significantly lower concentrations of Nd (10-30 ppm), as Nd is more difficult to remobilize in a fluid. A fluid front originating by dehydration of the crust and migrating upward through the Stillwater Complex would alter the isotopic signatures of the

complex rocks. However, the fluid might also undergo Nd isotopic exchange, altering the Nd isotopic composition of the fluid towards primary mantle values while leaving Sr and Pb isotopic signatures closer to crustal due to differences in concentration. At higher C_{fluid}/C_{rock} ratios, the fluid would hardly be impacted by interaction with the rock, while the rock would undergo more intense isotopic exchange. At lower C_{fluid}/C_{rock} ratios, such as would have been experienced by Nd, the fluid and the rock would both be altered, with the fluid reaching mantle-like isotopic compositions higher in the intrusion.

4.6 Conclusions

Early studies of radiogenic isotopes at the Stillwater Complex suggested isotopic systematics, particularly Sr and Pb, had largely been disturbed by at 1.7 Ga regional greenschist-facies metamorphic event, resulting in alteration of isotopic signatures past the point of usefulness. This disturbance was observed primarily at the mineral scale. Radiogenic isotopes have limited diffusion ranges during regional metamorphism, and analysis of bulk rock samples circumvents some issues of isotopic resetting. Thus, bulk rock analyses of Stillwater Complex samples allow calculated initial radiogenic isotopic ratios to be used as tracers for understanding intrusion formation.

Further analysis of Rb-Sr, Sm-Nd, and Pb-Pb isotope systematics reveals variability in initial ratios beyond what is explainable by previous models of magmatic mixing. Stillwater Complex rocks cannot be subdivided into magmatic affinities on the basis of isotopic ratio. However, variability in initial ratios may suggest a heterogeneous

source region, although this requires the parental magma to remain heterogeneous during magma ascent. Conversely, most Stillwater samples fall between estimated mantle and crustal reservoirs, suggesting variable crustal contamination may be partly responsible for the observed isotopic scatter. Spatial variability in ϵ_{Nd} , but not in initial Sr or Pb values, suggests the contaminant may have been a fluid migrating upward through the intrusion, corresponding to hydromagmatic models of complex formation. While pegmatoids and spatially associated host rock were analyzed to better understand the formation of the pegmatoidal bodies, isotopic signatures were ultimately too similar to determine a pegmatoid formation model. However, our findings suggest that radiogenic isotopes at Stillwater should be further investigated using modern techniques and understanding to better constrain Stillwater Complex source regions and formation models.

5. Stable Isotope Constraints on the Formation of Stillwater Complex Pegmatoids

5.1 Introduction

The formation of large layered intrusions remains a heavily debated topic. Various formation models have been proposed to explain these intrusions, including mixing of multiple magmas (e.g., Todd et al., 1982; Irvine et al., 1983), out-of-order emplacement as a series of sills (Mungall et al., 2016; Wall et al., 2018), variable contamination of the parental magma (Jenkins and Mungall, 2018; Jenkins et al., 2021), and circulation of fluids through the intrusion during its formation (e.g., Boudreau et al., 1997; Boudreau, 2016). These processes have been investigated at various large layered intrusions worldwide, including the Stillwater Complex, Montana and the Bushveld Complex, South Africa. These two layered intrusions are often compared, as they have a number of similar mineralogical and geochemical features.

Stable isotopes have been heavily investigated at the Bushveld Complex. It has been suggested that oxygen isotopes in the Platreef (the Platinum-Group-Element reef-type deposit of the Bushveld Complex) were mostly magmatic, although some interaction between magmatic fluids and the footwall rocks may have resulted in the alteration of the footwall oxygen isotope signatures (Harris and Chaumba, 2001). Ireland and Penniston-Dorland (2015) investigated both oxygen and lithium isotopes and determined that the diffusion of oxygen isotopes occurred at a much more limited spatial scale (~4 m) than diffusion of lithium isotopes (~ 60 m), indicating that Li may

provide a more accurate record of fluid contamination. Harris et al. (2005) investigated oxygen and hydrogen isotopes to determine if there was any change with stratigraphic height, and suggested that large amounts of crustal contamination were needed to explain the observed isotopic signatures. Isotopes of carbon and hydrogen (Schiffries and Rye, 1990), chlorine (Willmore et al., 2002), and sulfur (Penniston-Dorland et al., 2012b; Magalhães et al., 2019) have also been used to investigate crustal contamination at Bushveld. Benson et al. (2020) proposed that fluid derived from the country rock during contact metamorphic dehydration could also explain the variations observed in stable (and radiogenic) isotopes at Bushveld.

Despite the useful information provided by stable isotope analyses, very little stable isotope work has been conducted at the Stillwater Complex. Dunn (1986) investigated oxygen isotopes, and suggested that O isotope geothermometry was indicative of two temperature series at different stratigraphic heights, suggesting that this may have been the result of two parental magmas. However, his temperatures were calculated using a largely outdated geothermometer (Kyser et al., 1981). Further investigation of oxygen isotopes, as well an initial survey of lithium isotopes at Stillwater was conducted by Su et al. (2020), who focused on the lower portions of the intrusion. Their results suggested that variability in oxygen isotopes in the Ultramafic Zone were the result of re-equilibration with interstitial liquid, and that the interstitial liquid varied due to injection of fresh primitive magma. Sulfur is the most well-studied

stable isotope at the Stillwater Complex, with results suggesting crustal contamination was present in the lower portions of the complex (Zientek and Ripley, 1990), but not necessarily in at the level of the platinum- and palladium-rich J-M Reef (Ripley et al., 2017). These results, coupled with an investigation of secondary pyrite (Wernette et al., 2018) suggests S isotopes may indicate fluid circulation, whether lower-temperature fluid infiltration or high-temperature fluid flow. Finally, a single study of chlorine isotopes (Boudreau et al., 1997) suggested a crustal fluid contaminant was involved in formation of the Stillwater Complex.

This study presents new results of whole rock $\delta^7\text{Li}$, as well as plagioclase and pyroxene $\delta^{18}\text{O}$, and biotite and pyroxene hydrogen isotopes, with a particular focus on pegmatoidal bodies present throughout the Ultramafic series and Lower Banded series which have previously been suggested to have formed due to fluid circulation (e.g., Braun et al., 1994). Comparison of the pegmatoids to nearby host rocks, as well as country rock (hornfels) samples from the metamorphosed base of the intrusion to provide insight into the formation of the pegmatoidal bodies. Further, models of crustal contamination are explored.

5.2 Pegmatoid Petrography

The sporadically-occurring pegmatoid bodies at the Stillwater Complex are a major focus of this study. Pegmatoids are mineralogically similar to their host rocks (Braun et al., 1994). Both are primarily composed of plagioclase and pyroxene, although

some pegmatoid/host rock pairs, particularly from the Ultramafic series, also contain olivine. Low-temperature alteration to greenschist assemblages tends to be more extensive in pegmatoids than in the host rock (Braun et al., 1994). Pegmatoids analyzed in the present study form irregular, ~1-4 m podiform bodies (Figure 15)

The textural differences between host rock and pegmatoids are shown in thin section (Figure 23 and Figure 24). Typical Ultramafic series samples are dominantly orthopyroxene (Figure 23). Olivine may occur in Peridotite Zone samples. Plagioclase occurs interstitially in both host rock and pegmatoid. Ultramafic series orthopyroxene is typically less altered to hornblende. In comparison, plagioclase is dominant in Lower Banded series samples (Figure 24). Orthopyroxene occurs as well, but is commonly more altered to hornblende than orthopyroxene in the Ultramafic series. Clinopyroxene may also form as a major modal mineral. More heavily altered pegmatoids are found in both the Ultramafic series and the Lower Banded series (Figure 25). In these samples, pyroxenes and olivine appear more altered than plagioclase.

5.3 Methods

Sampling of pegmatoids, host rock, and country rock from the metamorphic aureole (hornfels) was conducted from locations on Chrome Mountain and at Mountain View (Figure 13), approximately following the traverses of McCallum et al. (1980) and Raedeke and McCallum (1984). Some hornfels samples were also supplied by Dr.

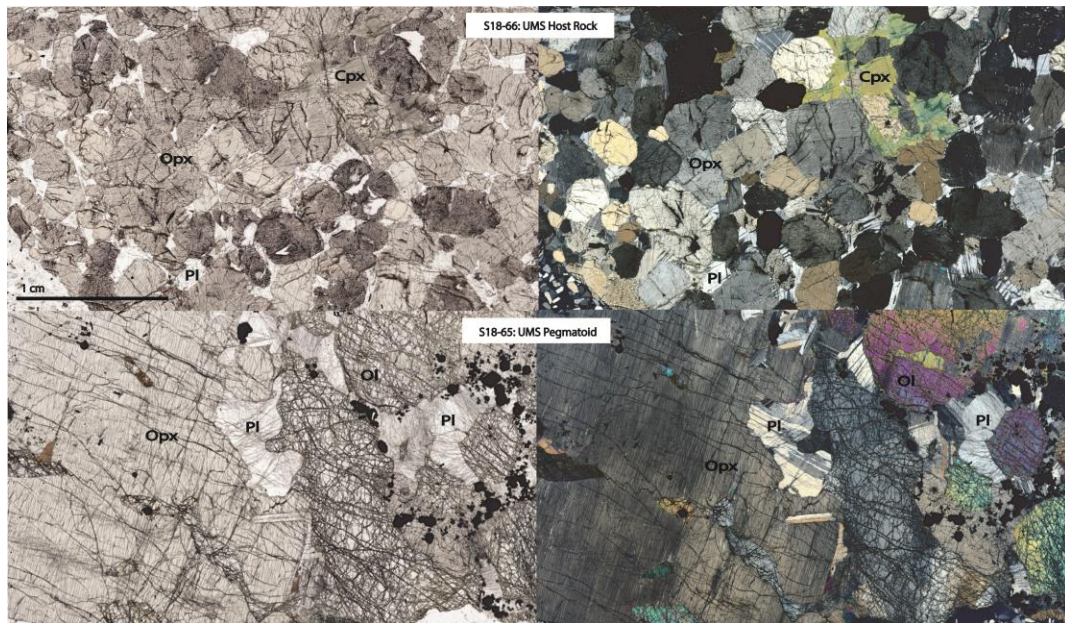


Figure 23: Thin sections of Ultramafic series host rock and pegmatoid. Left – PP Light; Right – XP Light. Top – host rock sample S18-66; Bottom – pegmatoid sample S18-65. OI – Olivine; Pl – Plagioclase; Opx – Orthopyroxene; Cpx - Clinopyroxene

Michael Zientek of the U.S. Geological Survey. Host rock samples were selected on the basis of spatial association with pegmatoids. Samples were crushed and separated into size fractions for mineral separation. In addition, samples selected for whole rock analysis were crushed in a tungsten carbide shatterbox to powder to ensure sample homogenization. The oxygen isotope composition of pyroxene from 5 samples, plagioclase from 16 samples, and whole rock powder from 3 samples was determined by laser fluorination in the Stable Isotope Laboratory at the University of Oregon (Bindeman, 2008). From each crushed rock sample, phenocrysts from the 500-1000 μm or 250-500 μm size fractions were handpicked under the microscope for clean phenocrysts with no or minimal inclusions, surface alteration, or irregular shapes. For one

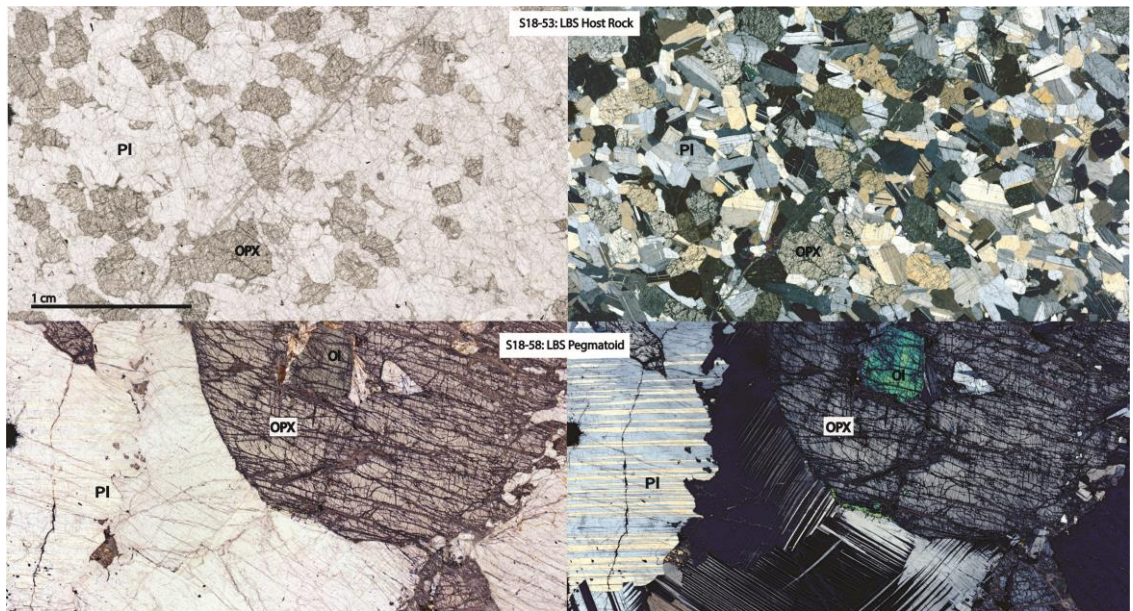


Figure 24: Thin sections of Lower Banded series host rock and pegmatoid. Left – PP Light; Right – XP Light. Top – host rock sample S18-53; Bottom – pegmatoid sample S18-58. Ol – Olivine; Pl – Plagioclase; Opx – Orthopyroxene; Hbl – Hornblende; Cpx – Clinopyroxene.

analysis, 1–2 mg is needed, which corresponds to 1–10 (most commonly 1–4) individual crystals, depending on crystal size. After laser extraction using pre-distilled BrF₅ as reagent, the oxygen was purified by being passed through a series of cryogenic traps, and boiling mercury (to remove traces of F gas that does not freeze cryogenically), and then converted to CO₂ gas using custom-made small carbon-rod-platinum converter.

Conversion times were 45–120 sec, conversion to CO₂ (rather than running gas as O₂) is preferred due to 5–10 times greater ionization efficiency of CO₂ compared to O₂ with respect to O₂ in a source of a mass spectrometer. The O-isotope ratios were then analyzed with a Finnigan MAT 253 mass spectrometer integrated with a laser fluorination line, and

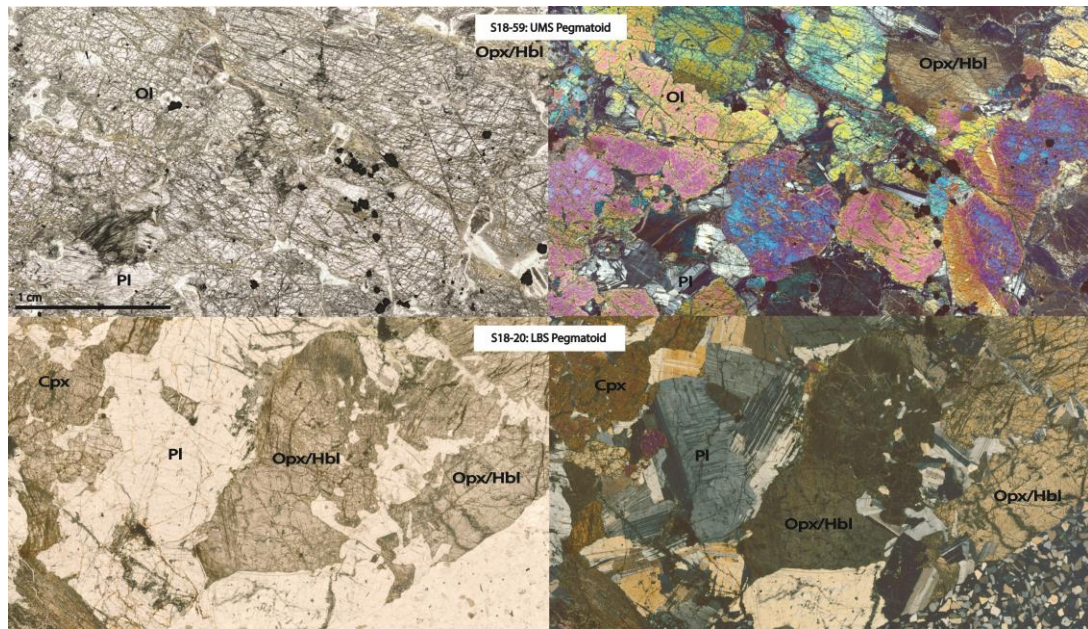


Figure 25: Thin sections of altered pegmatoid samples. Left – PP Light; Right – XP Light. Top – pegmatoid sample S18-59; Bottom – pegmatoid sample S18-20. Ol – Olivine; Pl – Plagioclase; Opx – Orthopyroxene; Hbl – Hornblende; Cpx - Clinopyroxene

normalized to the intercalibrated lab standards, which include the San Carlos olivine ($\delta^{18}\text{O} = +5.25\text{‰}$), Gore Mt. Garnet UWG ($\delta^{18}\text{O} = +5.8\text{‰}$) and the University of Oregon Garnet; $\delta^{18}\text{O} = +6.52\text{‰}$). Day-to-day $\delta^{18}\text{O}$ deviation of standards ranged from 0.1 to 0.3‰ lighter than their reference values, and measurements of unknowns were appropriately adjusted to correct for this variability. The average external (intra-day and between days) precision on standards and duplicates of individual analyses are better than 0.09‰.

Hydrogen isotope ratios of bulk rock, biotite, and pyroxene were analyzed at the University of Texas at Austin following the methods outline in Sharp et al. (2001). Pyroxene and biotite were examined optically under a binocular microscope to ensure

sample homogeneity. Mineral grains were rinsed in DI water. Samples were weighed (variable amounts of material was loaded ranging from ~4 to ~20 mg) into silver capsules, dried in a vacuum oven at 70°C for 24 hours, and then transferred to a ThermoElectron TC/EA (high temperature con-version elemental analyzer) with a Costech zero-blank autosampler flushed with helium for analysis. Samples were analyzed with a ThermoElectron MAT 253 isotope ratio mass spectrometer coupled to the TC/EA. Samples were analyzed along with certified international standards (IAEA-CH7, NBS-22, USGS-57, USGS-58) and one in-house working glass standard. Corrected δD values were calculated using the certified reference standards and reported in standard per mil notation versus SMOW. Water contents were calculated from the sample peak area and weight using the standards USGS-57 and USGS-58. All samples were analyzed in triplicate. While all replicate analyses are reported in Appendix D, all discussion of data and data in plots and Table 5 are based on the average of triplicate analyses. Reproducibility of in-run standards is $< \pm 2\%$ (1SD); reproducibility of samples is $\leq \pm 3\%$ (1SD).

Lithium isotopes were analyzed at Rutgers University using a ThermoScientific Neptune Plus MC-ICPMS. Samples were dissolved with mineral acids (Aristar Ultra grade HF, HNO₃ and HCl) and Li was isolated using a two-step two cation exchange (7 mL resin bed filled with an AGW50 × 12 200–400 mesh followed by 0.4 mL resin bed of MP50 to remove any remaining Na). Originally both ion exchange columns used 0.5 N

HCl as eluant, but the final solution of Li was found to also contain Cr and or Ni. These two elements probably occur as a complex anion (oxyanion or chloride) and while they do not stick to cation resin, the poor binding of Li meant that the tail of these elements overlapped with the leading edge of Li. Consequently, the range of the collection of Li on the first column was expanded, and the second column was recalibrated using 0.23M HCl which retarded the elution of Li allowing Cr-Ni to be removed. A standard, commonly seawater or JB-2, as well as other rock standards such as BHVO-2 or AGV-2 are routinely included with all sample batches and separated using different column pairs to ensure yields were quantitative. The total procedural was measured on the Neptune using ^7Li beam intensity of 26 pg. Based on the amount of sample used and its concentration, the blank represents $< 0.1\%$ of the total Li analyzed. Lithium solutions of 15 ppb concentration were analyzed utilizing a Teledyne Cetac Aridus II and X-type Ni skimmer cone, which yielded a signal exceeding 18 V on ^7Li with an acid blank of < 150 mV. The high sensitivity of the instrument allows small samples to be processed through ion chromatography, which enables column calibrations to be stable. Standard-sample-standard (L-SVEC) bracketing was used, and signals matched to within 5%. A solution of IRMM-016 was included in each batch of analyses, and the long-term $\delta^7\text{Li}$ average of that and seawater were $0.1\text{‰} \pm 0.07$ (2, $n = 25$) and $+30.6\text{‰} \pm 0.12$ (2, $n = 18$), respectively. $\delta^7\text{Li}$ for JB-2 yielded an average of $+4.6\text{‰} \pm 0.4\text{‰}$, $n=3$, and BHVO-2 $+5.1\text{‰} \pm 0.4\text{‰}$, $n=3$ which compares well with published estimates (Li et al., 2019).

5.4 Results

Measured O isotope compositions for Stillwater Complex pyroxene and plagioclase, as well as hornfels bulk rock, are presented in Table 5. $\delta^{18}\text{O}$ in the hornfels is highly variable, ranging from 2.05‰ to 7.99‰ in the three samples analyzed. $\delta^{18}\text{O}$ in plagioclase grains from pegmatoid samples ranges from 4.88‰ to 6.49‰. Three $\delta^{18}\text{O}$ analyses of plagioclase grains from host rock samples fall into a comparatively more limited range of 5.15‰ to 5.71‰. $\delta^{18}\text{O}$ in pyroxene grains, all of which were taken from pegmatoid samples, range from 5.13‰ to 5.84‰. Stratigraphic variability in oxygen isotopes analyzed in this study, compared to those analyzed as part of other studies (Dunn, 1986; Su et al., 2020) is shown in Figure 26.

Measured hydrogen isotope compositions and H₂O contents for Stillwater Complex biotite and pyroxene, as well as hornfels bulk rock, are presented in Table 5. Biotite was collected from only a select number of Ultramafic series pegmatoid samples, primarily from the G-Chromite seam. δD in biotite ranges from -80‰ to -48‰, with H₂O contents in the range of 3.0 wt. % to 4.3 wt. %. Host rock pyroxene δD ranges from -76‰ to -68‰, while pegmatoid pyroxene δD is more scattered at -102‰ to -60‰. Pyroxene water contents are fairly low; typically below 1 wt. % (0.3 wt. % to 2.5 wt. %). Pyroxene with higher water contents (greater than 1 wt. %) occur more commonly in Lower Banded series samples. Pyroxene is a nominally anhydrous mineral, to contain some structural water (Bell and Rossman, 1992). Alternatively, it has been suggested that

pyroxene might contain submicroscopic biotite lamellae (at the Bushveld Complex; Mathez et al., 1994; Harris et al., 2005). δD in the hornfels falls into a narrow range of -50‰ to -46‰, with water contents of 2.0 wt. % to 6.5 wt. %. Stratigraphic variability in δD is shown in Figure 27.

Lithium isotopes were analyzed in whole rock samples only (Table 5). Samples from the hornfels have higher concentrations of Li (22.6 ppm to 49.7 ppm) compared to samples from the Stillwater Complex (1.79 ppm to 7.8 ppm). δ^7Li in the hornfels ranges from -0.16‰ to 2.32‰. Host rock δ^7Li falls into a slightly wider range of -0.47‰ to 7.46‰. Pegmatoid δ^7Li is the most variable, from -1.13‰ to 8.69‰. Stratigraphic variability in δ^7Li is shown in Figure 28.

5.5 Discussion

5.5.1 Oxygen Isotope Geothermometry and Re-Equilibration

Early temperature estimates using O isotopes were calculated at Stillwater by Dunn (1986) using the geothermometer of Kyser et al. (1981). These temperatures have been recalculating using a better-calibrated geothermometer (Chiba et al., 1989). The temperatures of the pegmatoid pyroxene-plagioclase oxygen isotope pairs are also calculated (Table 6). Temperatures were calculated using assumed plagioclase compositions matching those measured from stratigraphically associated minerals (Raedeke, 1979; Figure 14). In most cases, this recalculation reduces the estimated temperature of the sample by ~200°C. In the case of four samples analyzed by Dunn

Table 5: Stable isotope analyses of mineral separates and bulk rock

Sample	Zone	Type	$\delta^{18}\text{O}_{\text{plag}}$	$\delta^{18}\text{O}_{\text{pyx}}$	$\delta^{18}\text{O}_{\text{WR}}$	$\delta\text{D}_{\text{bi}}$	$\text{H}_2\text{O}_{\text{bi}}$	$\delta\text{D}_{\text{pyx}}$	$\text{H}_2\text{O}_{\text{pyx}}$	$\delta\text{D}_{\text{WR}}$	$\text{H}_2\text{O}_{\text{WR}}$	$\delta^7\text{Li}_{\text{WR}}$	Li (ppm)
18MZ21	HNFL	C			5.75					-46	2.3	-0.16	49.7
18MZ19	HNFL	C										2.32	34.9
18MZ18	HNFL	C			7.99					-50	2.0	1.64	31.8
S18-81	HNFL	C			2.05					-48	6.5	1.94	22.6
M17-776	BAS	H										7.46	7.80
S18-65	UM	P	5.46					-87	0.3			-0.75	2.54
S18-66	UM	H	5.15					-68	0.4			-0.47	2.41
S18-59	UM	P	6.19	5.13				-80	1.5			8.69	4.5
Biotite-1	UM	P	6.16			-69	4.3	-82	0.5				
Biotite-2	UM	P	6.49			-64	3.9	-102	0.6				
Biotite-3	UM	P	6.10			-48	3.0	-90	0.5				
Biotite-4	UM	P	6.02			-80	3.9	-77	0.3				
GCP-03	UM	P	6.19					-85	0.5			-1.13	2.06
GCP-05	UM	P	6.17	5.79				-71	0.4				
S11-036A	UM	P	6.15	5.54		-64	3.3	-80	0.4				
S18-53	LB	H	5.71					-71	1.1				
S18-58	LB	P	6.10	5.84				-66	1.4			5.00	3.74
S18-18A	LB	H										3.38	5.79
S18-20	LB	P	6.15					-68	1.2			0.41	4.81
S18-24	LB	P										3.30	2.98
S18-25	LB	P	4.88					-60	2.5			3.66	5.25
S18-02	LB	P	6.15	5.44				-67	1			1.80	2.83
S18-03	LB	H	5.54					-76	0.6			4.32	1.79

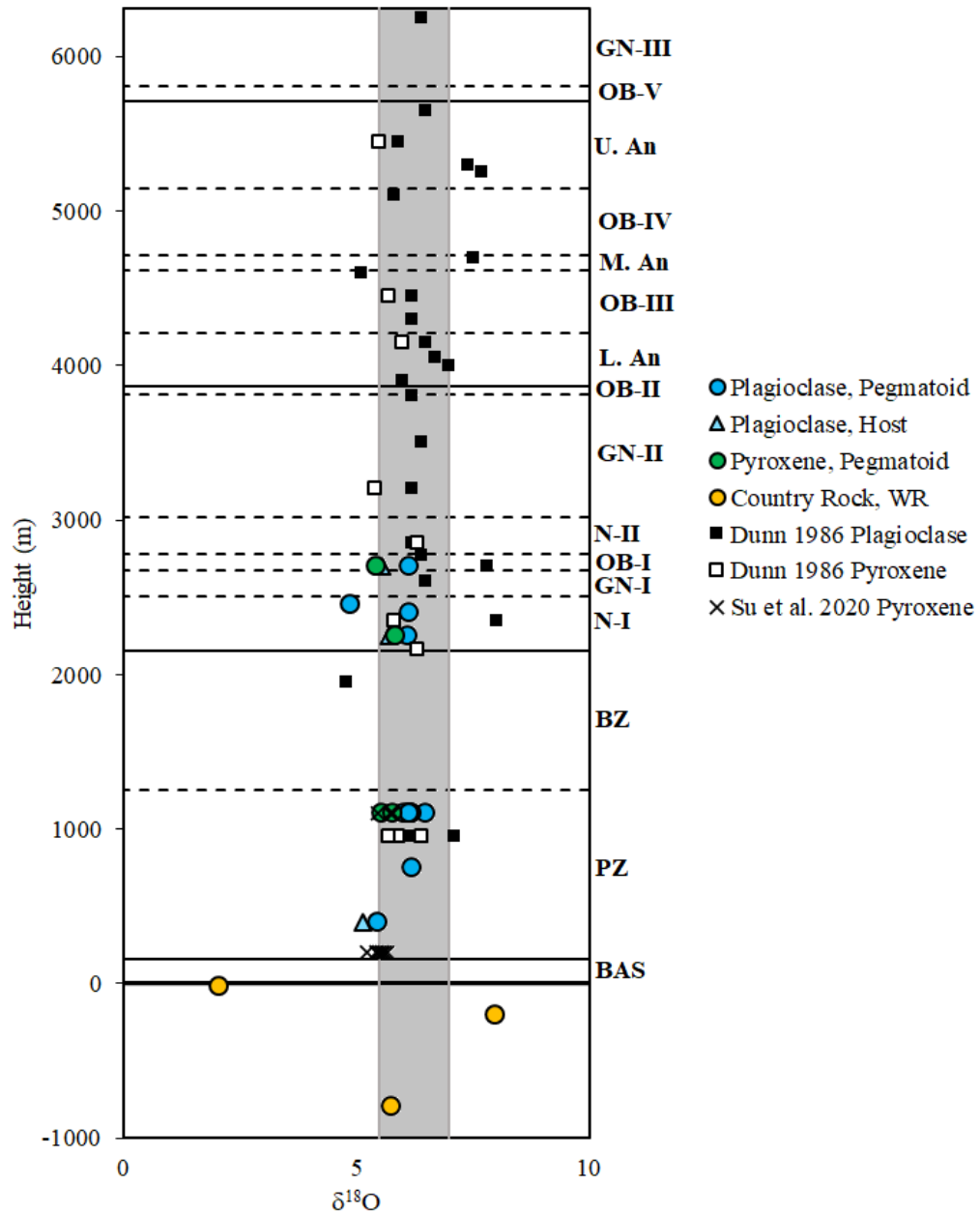


Figure 26: Oxygen isotope analyses varying by stratigraphic height. Sample analyses shown in color were analyzed as part of this study; samples in black and white are from Dunn (1986) and Su et al. (2020). The grey box ranging from 5.5‰ to 7‰ is the typical range for magmatic $\delta^{18}\text{O}$ (Taylor, 1978).

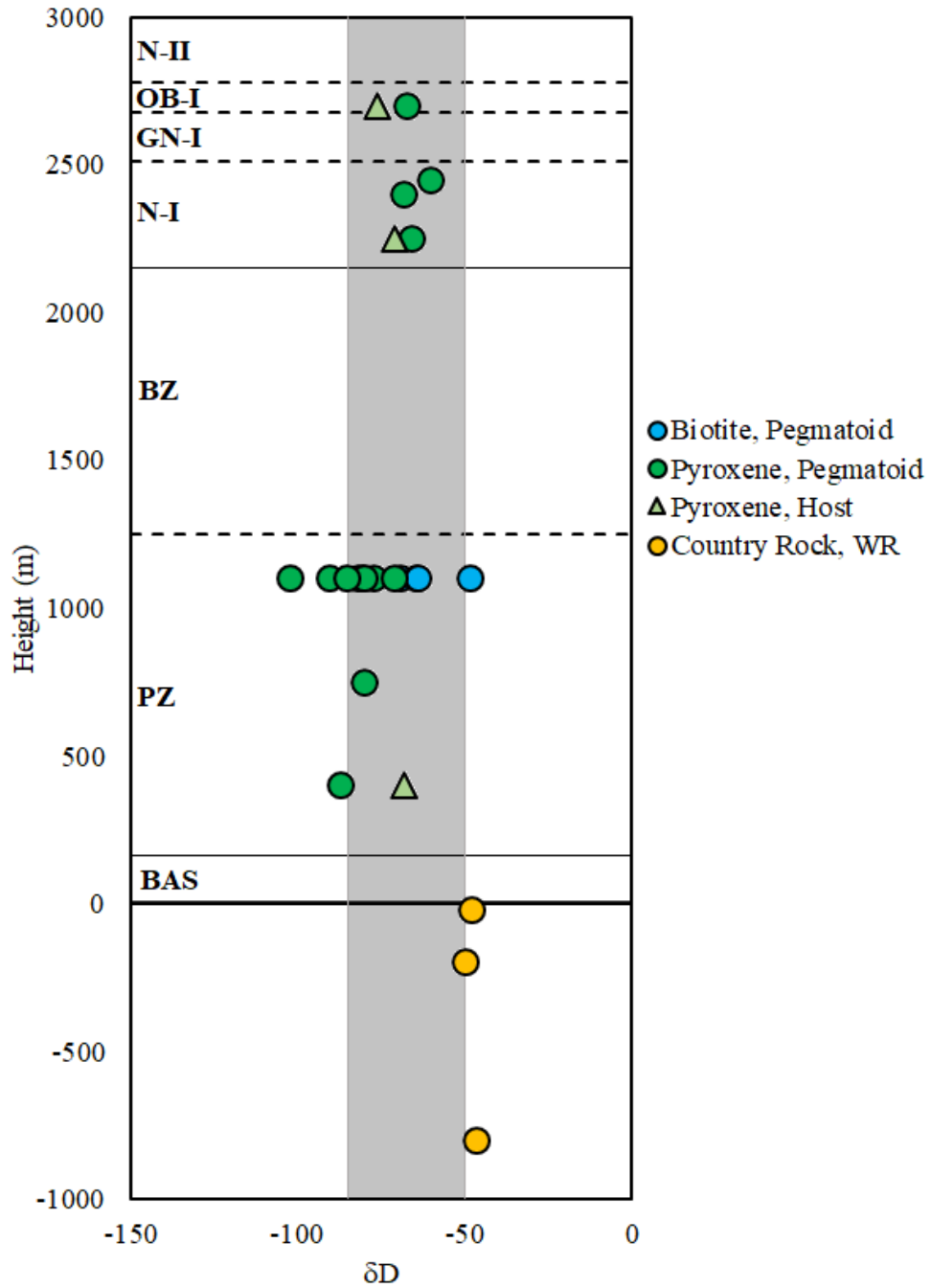


Figure 27: Stratigraphic variation in hydrogen isotopes with height. The grey box highlights the typical magmatic range in δD (-85‰ to -50‰; Taylor, 1986).

(1986) with $\Delta_{\text{pl-pyx}} = 0$, temperatures could not be calculated using this geothermometer. Pegmatoid plagioclase-pyroxene pairs analyzed as part of the present study occur lower in the Stillwater Complex than most of the mineral pairs analyzed by Dunn (1986). However, three pegmatoid samples have calculated temperatures of less than 1000°C, suggesting they formed later in the cooling history or underwent re-equilibration from initial magmatic crystallization temperatures. One pegmatoid sample (GCP-05) from the G-chromite seam, yields a magmatic temperature of 1284°C. This may suggest G-chromite pegmatoids formed at higher temperatures due to reinjection of parental magma, a process which has been proposed to explain the cyclical layers of the Peridotite Zone as well as the constant composition of pyroxenes in the Bronzite Zone. In addition, one Lower Banded series pegmatoid (S18-58) yields an abnormally high temperature of 1642°C. This abnormally high temperature estimate suggests the sample may not be suitable for geothermometry. This could be the result of plagioclase-pyroxene disequilibrium or alteration of O isotopes in the sample due to later weathering. Dunn (1986) suggests samples that have experienced weathering alteration should have plagioclase $\delta^{18}\text{O} > 7\text{‰}$, which is not observed in this sample. One sample analyzed by Dunn (1986) does have $\delta^{18}\text{O} = 8\text{‰}$, but the sample was noted to be fresh. However, the calculated temperature and unusual isotopic composition of the sample suggests either weathering not observed in thin section, or alteration of isotopic signature by some other method (e.g., crustal contamination). A clear trend in

temperature with stratigraphic position is difficult to establish given the lack of host rock mineral pairs in the Lower Banded series and below.

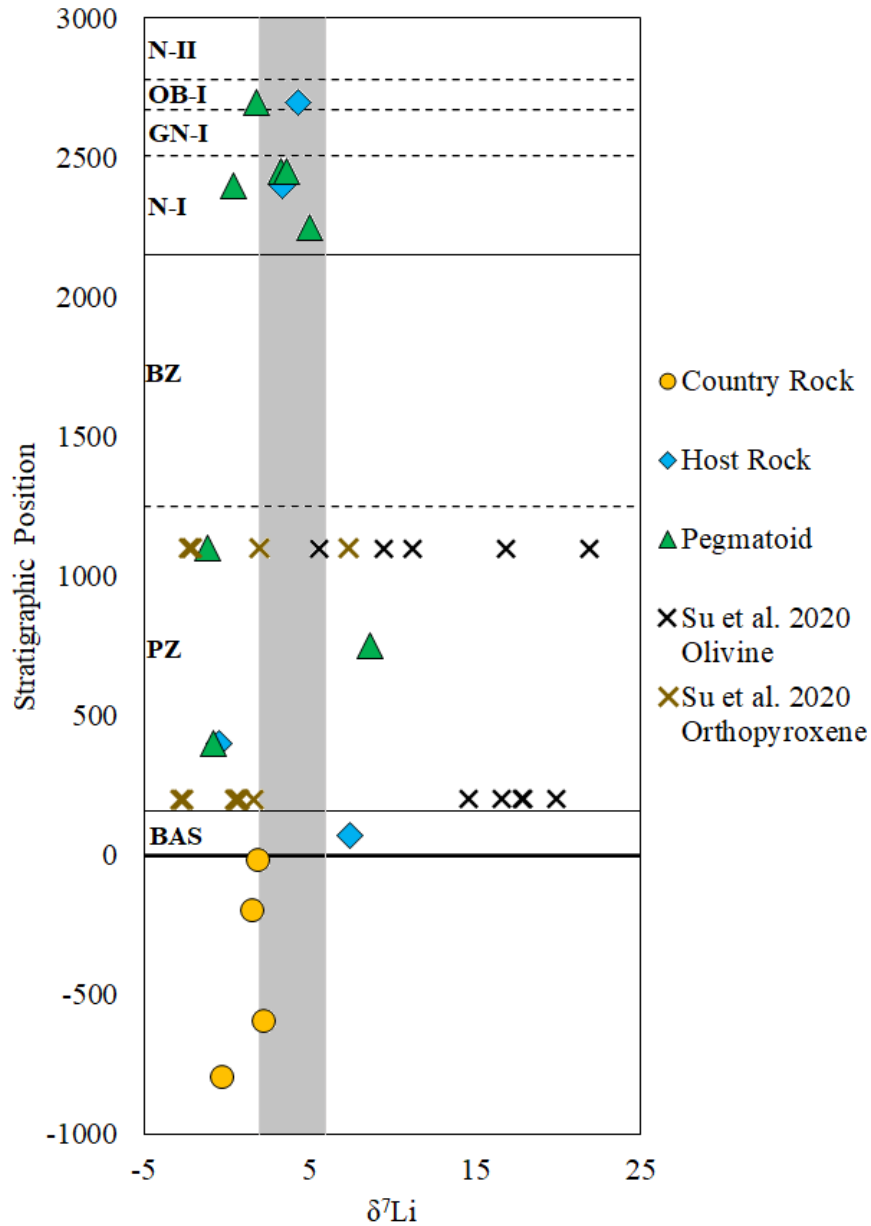


Figure 28: Stratigraphic variability in bulk rock lithium isotopes with height. The grey box highlights the typical magmatic range of $\delta^7\text{Li}$ (Tomascak, 2004; Elliott et al., 2004). Mineral data from Su et al. (2020) are also included.

Table 6: Oxygen isotope geothermometry

Sample	Source	Position	Unit	Δ_{Pl-Pyx} (‰)	Est. Pl An ¹	T (°C) ²
GCP-05	This Study	1100	PZ	0.38	85	1284.3
S11-036A	This Study	1100	PZ	0.61	85	955.8
S18-02	This Study	2700	OB-I	0.71	80	898.1
S18-58	This Study	2250	N-I	0.26	82	1642.0
S18-59	This Study	750	PZ	1.06	85	658.8
Dunn						
619	(1986) ³	950	PZ	0	85	-
622	Dunn (1986)	950	PZ	0	85	-
625	Dunn (1986)	950	PZ	0.5	85	1084.5
713	Dunn (1986)	2160	N-I	0	82	-
16	Dunn (1986)	2350	N-I	2.2	82	384.9
217	Dunn (1986)	2850	N-II	-0.1	78	-
178	Dunn (1986)	3200	GN-II	0.8	75	859.7
493A	Dunn (1986)	4150	OB-III	0.5	85	1084.7
517	Dunn (1986)	4450	OB-IV	0.5	85	1084.5
148	Dunn (1986)	5450	GN-III	0.4	70	1369.9

¹Estimated plagioclase composition based on analyzed minerals (**Figure 2**)

²Temperature calculated using the calibration of Chiba et al. (1989)

³Temperatures recalculated using data of Dunn (1986)

In estimating temperature from $\delta^{18}\text{O}$, the effects of post-crystallization alteration of oxygen isotopes, such as by hydrothermal activity, can be investigated by evaluating the degree of oxygen isotope equilibrium between existing minerals using δ - δ plots (Gregory and Criss, 1986; Gregory et al., 1989). Plagioclase/pyroxene pairs should be ideal for this type of plot as plagioclase exchanges oxygen rapidly, while pyroxene exchanges more slowly. Minerals in equilibrium in a suite of rocks fall along a line of constant per mil difference between the minerals (the $\Delta_{\text{plag-pyx}}$ of the sample). The δ - δ plot presented in Figure 29 includes equilibrium lines at temperatures of 1150°C, the crystallization temperature of a typical gabbro, and 550°C, the closure temperature of

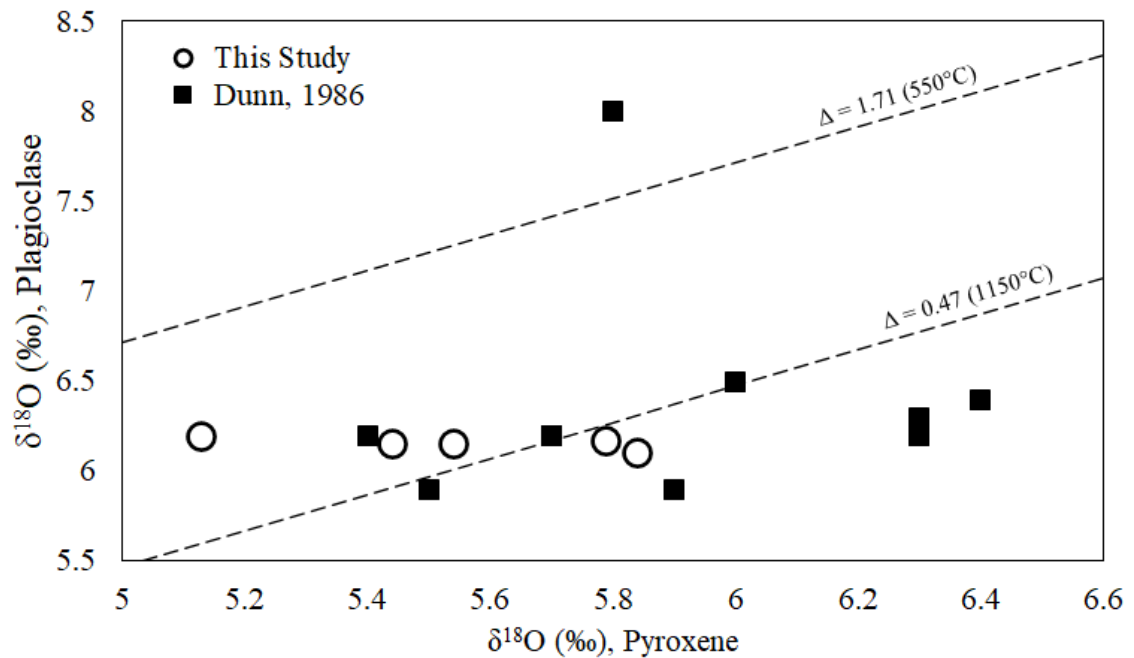


Figure 29: Plot of the $\delta^{18}\text{O}$ value of plagioclase vs the $\delta^{18}\text{O}$ value of pyroxene for pegmatoid (this study) and host rock (Dunn, 1986) pairs. Plagioclase-pyroxene isotherms are shown for 550°C and 1150°C, based on the calibrations of Chiba et al. (1989) and a constant plagioclase composition of An_{75} .

plagioclase to oxygen diffusion, at a constant plagioclase composition of An_{75} . Most samples with analyzed plagioclase-pyroxene pairs have unusually constant plagioclase $\delta^{18}\text{O}$ (this study: 6.1‰ to 6.19‰; Dunn, 1986: 5.9‰ to 6.5‰), compared with more variable pyroxene $\delta^{18}\text{O}$ (this study: 5.13‰ to 5.84‰; Dunn, 1986: 5.4‰ to 6.4‰). This result is unusual, as the faster oxygen exchange rate of plagioclase should result in more variable plagioclase $\delta^{18}\text{O}$ when compared to pyroxene. However, plagioclase separates in other samples are more isotopically variable, with an overall range of 4.88‰ to 6.49‰ (this study) and 4.8‰ to 6.7‰ (Dunn, 1986; excluding plagioclase with $\delta^{18}\text{O} > 7$ ‰).

Perhaps analysis of a wider range of pyroxene grains would yield different results; further investigation is required.

While the range $\delta^{18}\text{O}$ in pyroxene compared to plagioclase is unusual, most samples fall within or above the range of $\Delta_{\text{plag-pyx}}$ from crystallization of a gabbro to closure of plagioclase to oxygen diffusion (1150°C to 550°C). Samples with $\Delta_{\text{plag-pyx}}$ that is smaller than expected for crystallization at 1150°C ($\Delta_{\text{plag-pyx}} = 0.4713$) may have equilibrated at higher temperatures and not undergone further exchange. Alternatively, these samples may have plagioclase more anorthitic than An_{75} ; fractionation between anorthite and orthopyroxene is less than between albite and orthopyroxene (Chiba et al., 1989). Samples that fall between the two temperature curves may be the result of re-equilibration and oxygen exchange between plagioclase and pyroxene, although, again, pyroxene $\delta^{18}\text{O}$ should theoretically be altered much less than plagioclase $\delta^{18}\text{O}$ in this case, which is not observed. Alternatively, this variability could result from lower cooling temperatures; three of the samples that fall in this range are pegmatoids, which would be expected to equilibrate at lower temperatures. Another alternative would be that the plagioclase in these samples is more albitic than An_{75} , although measured variability in plagioclase compositions (Figure 14) suggests this should not be the case for the samples in question. Finally, as the samples for the most part do not fall along a single equilibrium line, variability could be the result of isotopic disequilibrium at the mineral scale. This would most likely be the result of hydrothermal alteration, as there is

a very slight positive slope to the line formed by the samples (Gregory and Criss, 1986). However, analysis of additional plagioclase-pyroxene pairs is required to distinguish among these possibilities.

5.5.2 Models for Pegmatoid Formation

The process for formation of the pegmatoidal bodies at the Stillwater Complex has not previously been clear. Studies that have examined the pegmatoids (Braun et al., 1994; McIlveen, 1996; Hanley et al., 2008) have suggested that pegmatoids are likely fluid-related features. Although they are typically mineralogically similar to their host cumulates, fluid and melt inclusions and PGE contents have suggested they may have formed by interaction with hydrothermal fluids.

Oxygen isotopes appear to be primarily magmatic in both host rock and pegmatoid samples. Dunn (1986) calculated a parental melt $\delta^{18}\text{O}$ of 5.9‰, which is extremely close to the primary magmatic MORB value of 5.7‰ (Ito et al., 1987). The shaded region on Figure 26 indicates the typical range of observed magmatic $\delta^{18}\text{O}$ (Taylor, 1978). Dunn (1986) suggested noted depletions in mineral $\delta^{18}\text{O}$ near the top of the Ultramafic series and near the tops of Olivine-bearing Zones of the Banded series. He suggested these depletions might be the result of magmatic fluid circulation, although he did not rule out meteoric water as a possibility. Similar depletions in mineral ^{18}O are observed in some pegmatoid samples, but they are not limited to the regions noted by Dunn (1986). One pegmatoid sample with $\delta^{18}\text{O}_{\text{plag}} = 4.88\text{‰}$ is found in

Norite-I, and some pegmatoid plagioclase separates from the lower parts of the Ultramafic series are also slightly depleted. This may indicate that fluids were involved in forming not just Olivine-bearing Zones of the complex, but also the pegmatoid bodies. However, not all pegmatoids exhibit a similar ^{18}O depletion.

Some analyzed mineral separates also contain elevated $\delta^{18}\text{O}$. While plagioclase above 7‰ is suggestive of later alteration, plagioclase with elevated $\delta^{18}\text{O}$ between ~6 and 7‰ may be suggestive of some crustal contamination. Analyzed hornfels samples were inconclusive with respect to country rock $\delta^{18}\text{O}$ signature; one hornfels sample was relatively depleted in ^{18}O , while another is enriched. A third sample (collected furthest from the base of the Stillwater Complex) appears to contain roughly magmatic $\delta^{18}\text{O}$. One possibility is that the country rock is isotopically heterogeneous, resulting in high variability in analyzed samples. Alternatively, hornfels may have exchanged oxygen isotopes with magmatic fluids during complex emplacement, or may have experienced later alteration from meteoric water. Further investigation of the country rock may help to distinguish these possibilities. Any crustal contamination had minimal impact on $\delta^{18}\text{O}$ in Stillwater rocks, as $\delta^{18}\text{O}$ for most samples is broadly magmatic.

Hydrogen isotopes tend to fall within the expected range of magmatic δD (-85‰ to -50‰, Taylor, 1978). Some pyroxene grains are more depleted in hydrogen isotopes than primary magmatic values; these pyroxene grains tend to originate from sample with high biotite proportions. Although little work has been done to constrain biotite-

pyroxene H isotope fractionation, depletion in D observed in these grains may be the result of fractionation from biotite formation, assuming that the H₂O in pyroxene is structural water and not submicroscopic biotite lamellae (Mathez et al., 1994). Country rock hornfels samples are enriched in D relative to the Stillwater Complex, falling just outside the expected magmatic range. A single biotite grain (Biotite-3) was found to have $\delta D = -48\text{‰}$, slightly enriched in D than expected from magmatic biotite.

The H₂O contents of most pyroxene, both pegmatoid and host rock, from the Ultramafic series are relatively low, besides one pyroxene with >1 wt. % H₂O (Figure 30).

Comparatively, all pyroxene from pegmatoid samples from the Lower Banded series have elevated H₂O contents, with H₂O increasing with increasing δD . Analysis of nominally anhydrous minerals in the mantle, such as pyroxene (Bell and Rossman, 1992) suggests the amount of H₂O in these grains is unusually high; mantle pyroxenes typically contain 200-500 ppm H₂O. This is likely the result of partial alteration of pyroxene to hornblende. Braun et al. (1994) notes partial replacement of pyroxene by hornblende in some Ultramafic series and Lower Banded series pegmatoids; replacement of pyroxene by hornblende is also observed in thin sections in the samples in this study (e.g., Figure XX). In the pyroxene grains from Lower Banded series pegmatoids which have been partially altered to hornblende, the hydrogen isotope composition approaches that of the country rock. This may suggest that the alteration to hornblende is the result of alteration by country fluids released during dehydration. In

the Ultramafic series, where biotite is more common, biotite tends to retain the majority of the H₂O, leading to less alteration of the Ultramafic series pyroxene and increased δD in biotite samples from interaction with country fluids. Hornfels δD , while slightly elevated compared to the Stillwater Complex, is similar enough that interaction with country-derived fluids could still have resulted in Stillwater δD within the magmatic range. Alternatively, it is possible that variations in Stillwater δD are due to interaction with magmatic fluids, rather than country rock hydrothermal fluids derived by contact metamorphism. However, the trend of the Lower Banded series samples and the similarity of biotite, especially the $\delta D = -48\%$ biotite-rich sample to analyzed whole rock hornfels compositions suggests that the fluid was country-rock-derived.

The isotopic range for primary mantle lithium is placed at $4 \pm 2\%$ (Tomascak, 2004; Elliott et al., 2004). The analyzed hornfels sample farthest from the contact with Stillwater possesses the least magmatic δ^7Li signature; hornfels δ^7Li approaches the lower end of the magmatic range closer to the base of the complex. This could be suggestive of interaction between the hornfels and the Stillwater Complex, resulting in alteration of country rock δ^7Li toward a more magmatic composition closer to the complex. Alternatively, while the hornfels is high in Li compared with the Stillwater Complex (Figure 31), lithium contents of the hornfels decline slightly with increasing δ^7Li . Combined with high fluid mobility of lithium (Richter et al., 1999), this may suggest that Li was mobilized during dehydration and migrated upward into the

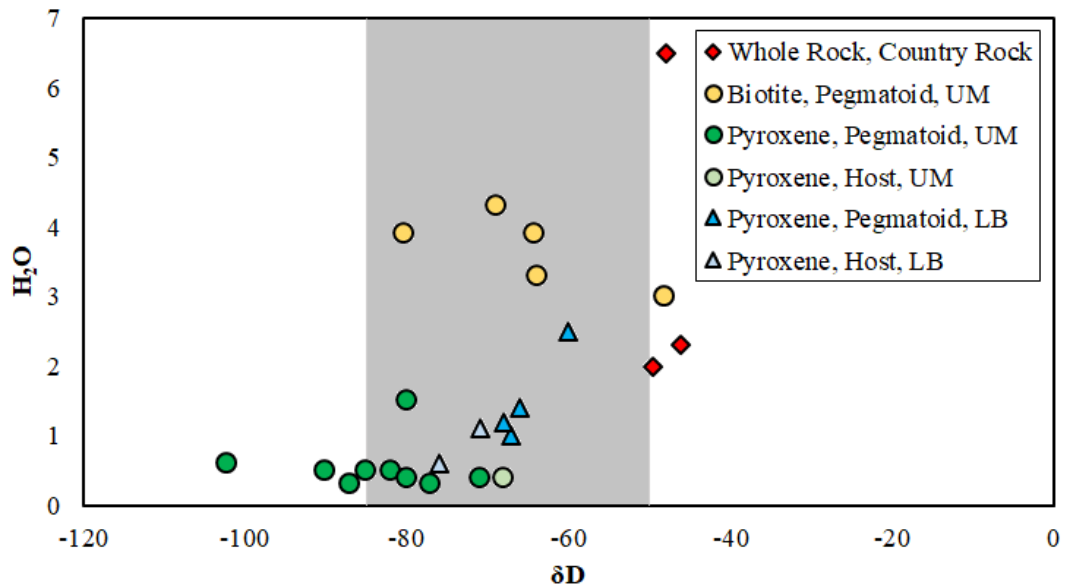


Figure 30: Hydrogen isotope composition vs H₂O contents for analyzed whole rock and mineral separates, by unit and rock type.

intrusion, resulting in fractionation of the lithium isotopes in the country rock. Studies of the effect of subduction zone dehydration on lithium isotopes (Elliott et al., 2006) have indicated that oceanic crust becomes isotopically light (lower $\delta^7\text{Li}$) as a result of dehydration preferentially removing isotopically heavy ^7Li . Dehydration of the metamorphic aureole could have similarly impacted the hornfels, suggesting that the lithium isotope composition of the country rock may have originally been more magmatic. As the Stillwater country rock was originally volcanoclastic, this is a possibility.

Lithium isotopes in the Basal and Ultramafic series are consistently outside the mantle range. Some of this variability can be explained by the mineralogy of the sample. For instance, the Peridotite Zone sample with unusually high $\delta^7\text{Li}$ (S18-59; $\delta^7\text{Li} = 8.69\%$)

contains a comparatively large amount of olivine (Figure 25). A study of lithium isotopes at Stillwater by Su et al. (2020) suggested that olivine tends to fractionate lithium isotopes, as it tends to very isotopically heavy compared to other minerals (Figure 28). However, the Basal series sample with high $\delta^7\text{Li}$ (M17-776; $\delta^7\text{Li} = 7.8\text{‰}$) does not have increased olivine content. The cause of high $\delta^7\text{Li}$ in this sample is unclear, but may be related to dehydration of the country rock. Conversely, two sample groups in the Peridotite Zone were found to contain $\delta^7\text{Li}$ below the typical magmatic range. The $\delta^7\text{Li}$ composition of these samples is more similar to the modern $\delta^7\text{Li}$ of the hornfels; if the lithium isotopes in the hornfels did not fractionate during dehydration, the Ultramafic series samples with low $\delta^7\text{Li}$ may be indicative of crustal contamination. Higher in the intrusion, in the Lower Banded series, most samples analyzed are in the magmatic range, although two analyzed pegmatoids are slightly below magmatic. Lithium isotopes higher in the intrusion may suggest that either a) Li contamination primarily impacted the lower parts of the complex (e.g., Ireland and Penniston-Dorland, 2015), or that b) Li isotopic compositions were altered by exchange with a fluid, which exchanged with the intrusion and became more magmatic in character higher in the intrusion. In the case of all spatially associated pegmatoid-host rock pairs, the pegmatoid and host rock have very similar $\delta^7\text{Li}$.

One difficulty in analyzing the impact of crustal fluids, and crustal contamination, in the Stillwater Complex is the isotopic similarity of the country rock to

the Stillwater Complex. Similar investigations at the Bushveld Complex provided more clear-cut evidence of crustal contamination because of more dramatic isotopic differences between the footwall and the intrusion. Lithium isotopes in the Bushveld Complex footwall ($\delta^7\text{Li} = 16\text{-}20\text{‰}$) differed dramatically from the intrusion ($\delta^7\text{Li} = 2\text{-}6\text{‰}$) (Ireland and Penniston-Dorland, 2015). Such distinct endmember isotopic compositions are not observed in the Stillwater Complex.

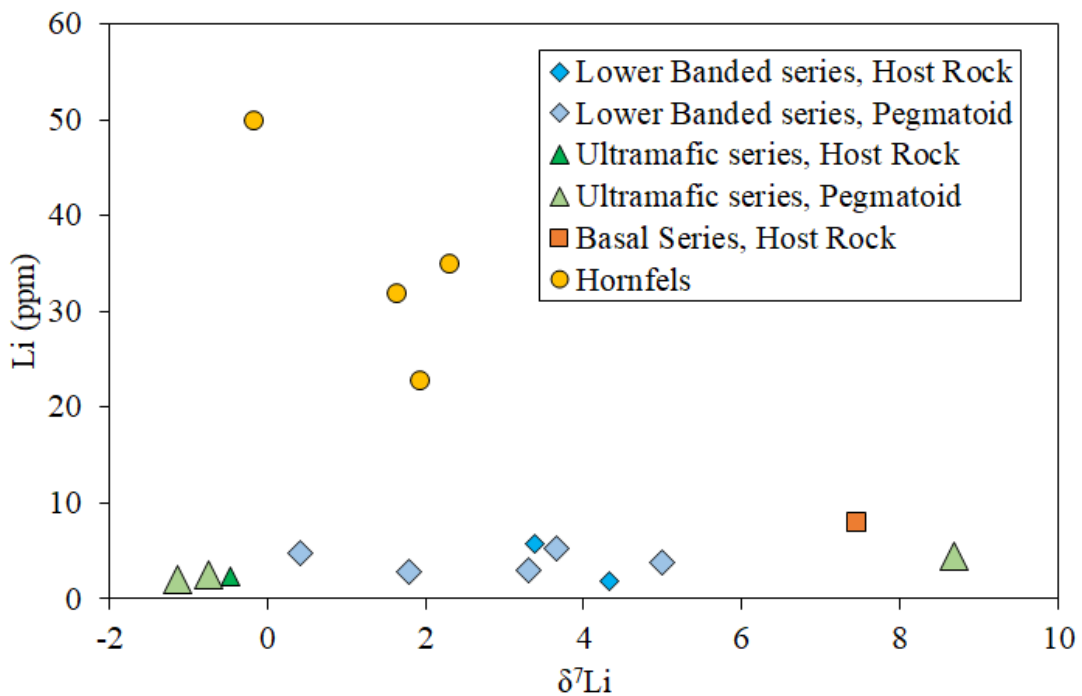


Figure 31: Lithium isotope composition vs whole rock Li contents for hornfels and Stillwater Complex samples.

5.6 Conclusions

An examination of pegmatoids of the Stillwater Complex using stable isotopes are indicative of several potential formation models, for both the pegmatoids and the

complex as a whole. Geothermometry using oxygen isotopes suggests that pegmatoids may have equilibrated at lower temperatures than the host rock, although some oxygen isotope pyroxene-plagioclase pairs may be indicative of disequilibrium. When using stable isotopes to trace contamination in Stillwater Complex samples, most stable isotopes fall into a normal magmatic range. However, some samples with unusual isotopic compositions are suggestive of contamination. Hydrogen isotopes in the Lower Banded series are particularly suggestive of a fluid formation model for the pegmatoids, with the fluid tentatively originating in the country rock and partially altering pyroxene to hornblende. Lithium isotope results may also be indicative of a country fluid, although Li evidence of fluid circulation is most clear in the lower parts of the complex, rather than in the Lower Banded series. This difference could be the result of faster diffusion of lithium compared with hydrogen (e.g., Ireland and Penniston-Dorland, 2015). Further analysis of stable isotopes at Stillwater, with particular focus on pegmatoids, may provide additional evidence for fluid contamination of the complex.

6. Using Synthetic Remelting to Identify Evolving Magma Compositions in Layered Intrusions I: Theory and Formation Models at the Stillwater Complex, Montana

6.1 Introduction

Layered intrusions (e.g., the Stillwater Complex, Montana, U.S.A; the Skaergaard intrusion, East Greenland; the Bushveld Complex, South Africa) have long been viewed as useful windows into the understanding processes of magma differentiation and crystallization. Despite extensive work on these intrusions, a general problem with interpreting rocks of layered intrusions is linked to the effect of trapped liquid. Mineral compositions can be used to model parental liquid compositions or liquid evolution (e.g., Tegner, 1997; Tegner and Cawthorn, 2010), and the evolution of the cumulus phases should record their igneous history (e.g., Papike et al., 1995). However, the crystallization of interstitial liquid can modify original mineral compositions, which can affect the accuracy of parental liquid estimates, the modeling of liquid evolution, and the overall understanding of an intrusion's history. In addition, loss of trapped liquid (e.g., Meurer and Meurer, 2006) can complicate interpretations of geochemical analyses and present difficulties in developing accurate formation models for an intrusion.

The possible effect of the crystallization of the interstitial liquid in modifying the original mineral compositions has been discussed previously (Barnes, 1986; Bédard, 1994). The crystallization of residual liquid can yield overgrowths on the original

minerals, and growth of new mineral phases enriched in less compatible elements. The final composition of the original liquidus minerals can be affected as well by what has been termed the “trapped liquid shift effect” (Barnes, 1986). Pyroxenes, for instance, will re-equilibrate readily with interstitial liquid. Studies of orthopyroxene geothermometry have found that orthopyroxene grains could be reset in Fe-Mg ratio, and that the Fe-Mg compositions of orthopyroxene grains do not necessarily record peak temperatures because of this (Pattison and Bégin, 1994). Olivine re-equilibrates even more readily. Plagioclase cores tend to remain robust absent recrystallization owing to slow diffusion, with crystallization of late liquids instead crystallizing sodic rims (Toplis et al., 2008). Identifying the effect of the trapped liquid shift for a particular sample requires determination of the composition of the trapped liquid, which can present challenges. Models for calculating the composition of the trapped liquid (e.g., Barnes, 1986; Bédard, 1994) assume that the final rock can be considered a two-component system: 1) the originally precipitated minerals and 2) the initial silicate liquid that precipitated those minerals. To the extent that one can determine the original proportions of liquid and solids, the remelting of a rock should retrieve the original liquid that was in equilibrium with the original solid. This approach recovers more than just the trace element composition of the evolving liquid as done by Bédard (1994); it should also provide the major element content of the liquid. Concurrent equilibration of the solids with the

liquid composition then can estimate the effect of the trapped liquid shift on the originally mineral assemblage.

Despite a long history of investigation, the 2.7 Ga Stillwater Complex, located in south-central Montana, has remained at the center of debate about its formation. Various features of Stillwater stratigraphy are explained by processes ranging from purely magmatic to hydromagmatic. Changes from gabbro-norite to anorthosites in the stratigraphy associated with the platinumiferous J-M reef, have been attributed to the mixing of a magma with an anorthitic affinity (“A” magma type) with an evolved ultramafic magma that originally crystallized much of the rocks below the J-M Reef (“U” magma type) (e.g., Irvine et al., 1983; Lambert and Simmons, 1987, 1988). Injections of fresh magma of varying compositions and saturated with varying minerals have been called upon to explain the thick anorthosite units (McCallum et al., 1980; Czamanske and Bohlen, 1990) and the crystallization sequences in the Ultramafic and Lower Banded series (Jenkins and Mungall, 2018; Jenkins et al., 2021). In contrast to orthomagmatic models of Stillwater formation, hydromagmatic formation models involve an upward-moving fluid front, continuously remobilizing elements upward as it migrates through the crystal pile (e.g., Boudreau, 1988, 1999, 2016). Proponents of the hydromagmatic model have pointed to pegmatoidal rocks and hydrous minerals consistent with volatiles (Boudreau, 2016), halogen concentrations, particularly Cl, in apatite (e.g., Boudreau et al., 1997), and metal contents in fluid inclusions (Hanley et al., 2008).

Identifying the impact of trapped liquid (or loss of trapped liquid through compaction, e.g., Meurer and Meurer, 2006) may be helpful in differentiating formation models at the Stillwater Complex. Remelting of physical rock samples, however, can be challenging, and it is difficult to impossible to monitor changes in liquid composition over large crystallization intervals. Synthetic remelting of a rock would shortcut this process, allowing for more accessible testing of sample and parent melt evolution models. This study tests the hypothesis that one can define the initial liquid and solids by synthetic remelting of a rock using the MELTS program. By modeling the mineral phases present and using bulk rock major element data, back-calculate the equilibrium liquid composition, changes in the major element composition of the evolving liquid in an intrusion should be evident. Most previous studies of the Stillwater Complex studies have looked at mineral compositional variations (Meurer and Boudreau, 1996; Pagé et al., 2011; Aird et al., 2017) and major and trace element variations in local sections (McCallum et al., 1980; Barnes and Naldrett, 1986; Barnes et al., 2020), or have concentrated on ore elements (Boudreau and McCallum, 1986; Keays et al., 2012; Jenkins et al., 2020). This study provides new whole rock data for samples from the base of the intrusion through the Lower Banded series, past the point where a second parental magma is thought to have intruded. Using synthetic remelting of rock and examinations of both liquid evolution and trapped liquid compositions, we evaluate formation models and processes such as compaction which influenced Stillwater Complex geochemistry.

6.2 Synthetic Melt Modeling in a Closed System

To illustrate the method, an “ideal” cumulate is constructed using a silicate liquid and the minerals that are precipitating from that liquid using the MELTS software program. MELTS is an open-source program used to thermodynamically model phase equilibria in magmatic systems (Ghiorso and Sack, 1995; Asimow and Ghiorso, 1998). In this study, the rhyolite-MELTS v1.0.x program (Gualda et al., 2012; Ghiorso and Gualda, 2015) was used for synthetic melting of bulk rock compositions taken from the literature.

In this example, two synthetic “cumulate” rocks are produced using a calculated fractionated liquid of a proposed Stillwater parent magma (Table 7). The starting parent composition is taken to liquidus temperature allowed to crystallize in 10°C intervals, with the solid removed at each step. This produces a nominally correct fractional crystallization sequence for the Stillwater Complex: olivine → orthopyroxene → orthopyroxene + plagioclase → orthopyroxene + plagioclase + clinopyroxene. Using this modeled liquid line of descent and the modes and composition of the minerals along this fractionation trend, a ‘model orthopyroxenite’ is created, composed of 80% orthopyroxene of the composition of the orthopyroxene at 1300°C mixed with 20% of the liquid in equilibrium with that orthopyroxene. Further fractional crystallization of the parental liquid was used to produce a ‘model norite’, using the mineral compositions at 1190°C at the first appearance of plagioclase. The model norite bulk composition was

Table 7: Composition of model parent and model samples during synthetic melting

Sample	SiO ₂	TiO ₂	Al ₂ O ₃	Fe ₂ O ₃	Cr ₂ O ₃	FeO	MnO	MgO	CaO	Na ₂ O	K ₂ O	P ₂ O ₅	Mg#	%An
Parent liquid, bulk composition	49.9	0.52	13.96	0.1	0.29	9.62	0.17	15.37	7.77	1.53	0.57	0.07	74	69.3
Model orthopyroxenite, liquid component	51.06	0.61	16.13	1.4	0.08	8.31	0.18	10.62	9.05	1.8	0.67	0.08	69.5	69.1
Model orthopyroxenite, orthopyroxene component	55.5	0.05	2.74	0.73		7.85		32.03	1.09	0.02			87.9	
Model orthopyroxenite, bulk composition	54.61	0.16	5.42	0.87	0.02	7.94	0.04	27.75	2.68	0.37	0.13	0.02	86.2	
Model orthopyroxenite, 100% solid orthopyroxene	55.25	0.17	2.64	0.4		9.38		31.03	1.1	0.02			85.5	
Orthopyroxene, 5% liquid loss; bulk composition	54.61	0.11	4.69	0.87	0.02	8.14	0	28.91	2.4	0.23	0.01		86.4	85
Orthopyroxene, 5% liquid loss; 100% solid OPX	54.95	0.12	3	0.7		8.84		30.69	1.67	0.03			86.1	
Model norite, liquid component	50.65	0.77	17.35	1.58	0.03	8.78	0.23	7.48	10.04	2.11	0.86	0.1	60.3	67.5
Model norite, orthopyroxene component	54.35	0.06	3.09	0.85		10.57		29.09	1.96	0.02			83.1	
Model norite, plagioclase component	48.67		32.94						15.82	2.48	0.09			77.5
Model norite, bulk composition	51.11	0.18	19.08	0.62	0.01	5.56	0.05	11.97	9.67	1.52	0.21	0.02	79.3	76.3
Model norite, 100% solid orthopyroxene	53.86	0.2	2.86	0.55		13.61		27.62	1.28	0.02			78.3	
Model norite, 100% solid plagioclase	49.61		32.25						15.03	2.75	0.37			73.5
Norite, 5% liquid gain; bulk composition	51.28	0.22	19.08	0.63	0.01	5.49	0.07	11.67	9.6	1.6	0.31	0.03	77.5	74.6
Norite, 5% liquid gain, 100% solid orthopyroxene	53.97	0.19	2.64	0.5		13.8		27.55	1.33	0.02			77.5	
Norite, 5% liquid gain, 100% solid plagioclase	50.03		31.92						14.66	2.85	0.53			71.7

composed of 36% orthopyroxene composition, 44% plagioclase composition, and 20% evolved liquid in equilibrium with those minerals at 1190°C, matching the proportions of plagioclase and orthopyroxene crystallizing from the liquid at that temperature.

The model orthopyroxenite and norite were then synthetically remelted to liquidus temperatures and then crystallized as a closed system (constant bulk composition) in steps of -10°C. At each step, the equilibrium liquid composition and the crystallizing mineral phases were recorded. Figure 32a shows both the liquid line of descent for the original parent liquid (solid black line) as well as the evolution of the residual liquid in the solidifying model orthopyroxenite (green line) and norite (blue line) on a standard AFM diagram. The changing bulk solid composition for each model sample is also shown. As expected, the evolving sample liquid composition intersects the liquid line of descent at when the sample returns to 20% liquid, at the original temperature modeled (1300°C for orthopyroxenite, 1190°C for the norite). Not only does this retrieve the original liquid for each sample, but the retrieved liquids also define the liquid line of descent over the crystallization interval defined by the two samples. The procedure can also recover the initial temperature, although this can be sensitive to the initial liquid fraction. As shown in Figure 32b for the synthetic orthopyroxenite, small errors in the estimated liquid fraction where this variable is relatively high will result in a relatively small error in the temperature estimate, but this error increases for lower estimated initial liquid fractions.

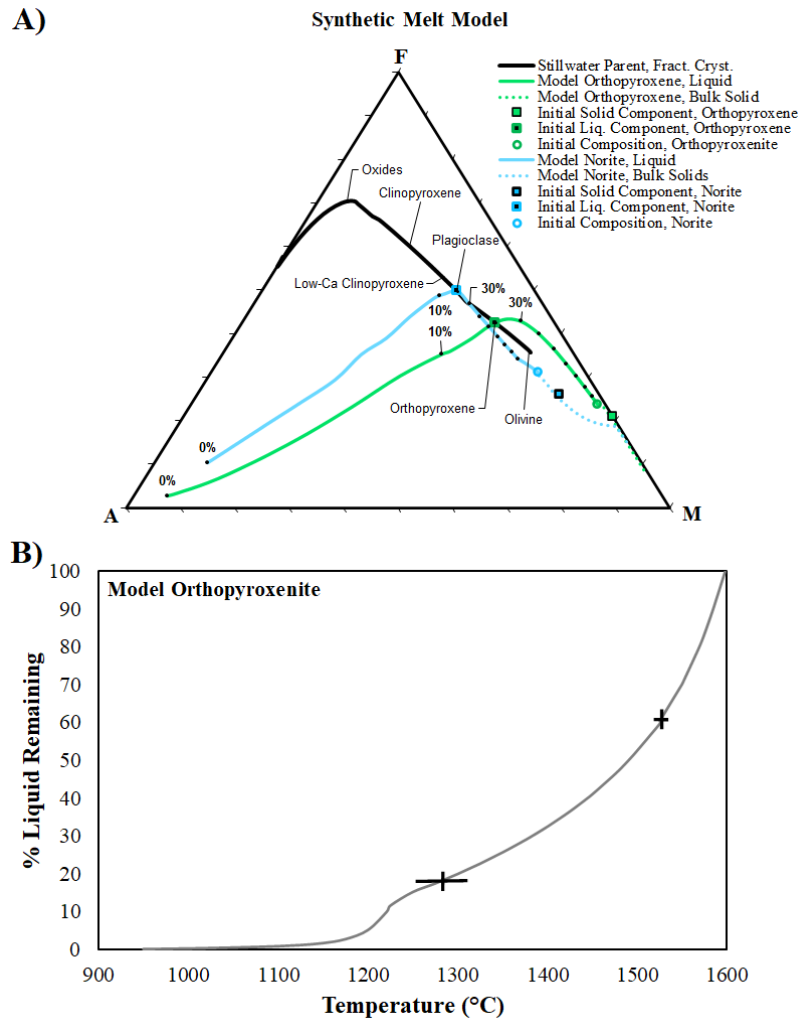


Figure 32: The synthetic melting model. A) The Stillwater Parent uses a modified version (+5 wt.% Al_2O_3 and renormalized) of the Jenkins and Mungall (2018) modeled parent composition. Mineral labels indicate the appearance of that mineral on the liquidus. The model orthopyroxenite and model norite are synthetically created from this parent as described in the text. Black circles on model samples represent intervals of 10% liquid remaining, starting at 90% liquid. Bulk solid composition trends for each model sample are indicated by the dotted lines. B) Plot of the liquid fraction as a function of temperature for the synthetic orthopyroxenite. Crosses indicate the change in temperature required to produce similar amounts of crystallization at high and low liquid proportions.

It should be noted that the above model will return the correct liquid composition regardless of variable amounts of the initial liquid (as might be produced by adcumulus overgrowth from the supernatant magma or by a period of isothermal compaction) or even non-cotectic mineral modes, provided that the liquid is in equilibrium with the solids at the time it became a closed system. Indeed, for a cotectic system, one or more minerals can even be missing, as the missing mineral will be the firsts thing to crystalize once the interstitial liquid begins to cool (or equivalently, the last minerals to disappear as temperature is increased). Ideally, however, one would use rock with roughly 'cotectic' proportions of the original minerals.

The model does require an estimate of the initial liquid fraction. Conventionally, there are two methods to this. The first, as mentioned above, uses the bulk rock incompatible element abundance to back-calculate the liquid fraction (e.g., Tegner et al., 2009). The second is the use the modal abundance of late-crystallizing minerals, which works best in rocks assumed to have precipitated from a magma initially saturated in a single mineral (e.g., dunites, orthopyroxenites, and anorthosites). Three additional methods are suggested by the analysis above that are independent of either of these techniques. The first is to model the liquid remaining along some estimate of the temperature change along the liquid line of descent. Alternatively, but similar to the latter, is to find where the liquid melting curve crosses an expected fractionation trend. As demonstrated in the model orthopyroxenite and model norite, this synthetic melting

method will return the composition and amount of the liquid associated with a sample. Yet a third method made possible by this procedure relies on the observation that plagioclase core compositions tend to resist re-equilibrate on cooling owing to very sluggish solid-state diffusion rates in the absence of wholesale recrystallization. This method simply requires adjusting the liquid fraction required to find the liquid in equilibrium with the core plagioclase composition. In practice, all of these can be used as cross-checks on the reliability of the results.

6.3 Synthetic Melting in an Open System: The Effects of Late Liquid Loss

The method outlined above assumes that the final rock is a simple two-component system of the originally precipitated minerals and the initial silicate liquid. Typically, estimates of the amount of the liquid fraction based on the concentration of strongly incompatible elements such as P that only became incorporated in very late crystallizing minerals (e.g., apatite). These methods are subject to error, as they tend to ignore the effects of concurrent compaction and crystallization. Meurer and Boudreau (1998) calculated the proportion of trapped liquid a variety of elements and found a systematic shift in calculated trapped liquid proportions for elements of different compatibility, suggesting that crystallization and compaction were occurring simultaneously in the Stillwater Complex. The effect of compaction in layered intrusions has also been suggested for the Bushveld Complex (Mathez et al., 1997) and the Skaergaard intrusion (Tegner et al., 2009), among others. Concurrent compaction and

crystallization will result in the loss of some late incompatible element-enriched liquid and can result in an underestimate of the amount of trapped liquid the rock equilibrated with. A similar problem arises for the for the loss of a volatile-rich aqueous fluid, owing to the strong effect of H₂O on lowering the liquidus and solidus as well as modifying phase relationships and modifying $f(\text{O}_2)$. This is expected to become more serious for rocks that initially formed with high proportions of trapped liquid, for which the calculated liquid abundance will be underestimated. Finally, a related probability is the possibility of a gain of a late liquid, such as can occur during compaction where liquids can collect beneath low permeability zones or rocks undergoing dilation (e.g., Meurer and Boudreau, 1996; Boudreau and Philpotts, 2002).

This problem of continuous loss of silicate liquid during crystallization is most readily observed in rocks assumed to have precipitated from a magma saturated in a single mineral. An example of this is presented by Boudreau (2019), who calculated the percent of residual liquid in an orthopyroxenite from the Bushveld Complex, South Africa. Estimates based on interstitial minerals that might be expected to crystallize early during solidification (e.g., plagioclase) and their constituent elements (e.g., Na₂O, Al₂O₃) tend to produce higher estimates of trapped liquid (20-34%) than do elements such as P and Zr that are mainly held in later crystallizing minerals such as apatite and zircon (11-14%).

To illustrate the effect of late loss of liquid on the model melting curves shown in Figure 32a, the model orthopyroxenite produced as described above (with 20% initially liquid) was synthetically melted to 5% liquid remaining and 95% solid. This residual 5% liquid was then removed, producing a new bulk rock composition of just the remaining bulk solid that is itself composed of the original solid plus some crystallized fraction of the original liquid. The late liquid that was removed from the model orthopyroxenite (5 wt. %) was then added to the bulk composition of the model norite (100 wt. %) and the composition renormalized. This makes the assumption that late liquid lost from the system due to compaction or other processes is mixed back into the fractionally crystallizing parent, as opposed to a process such as *in situ* crystallization (as suggested by Langmuir, 1989). The remelting of these “open system” bulk orthopyroxenite and norite results in two new trends (Figure 33, “Model OPX, 5% Liq Loss” and “Model Norite, 5% Liq Gain”). Owing to the loss of the alkali-rich late liquid from the model orthopyroxenite (Figure 33a), the evolving interstitial liquid from the open system orthopyroxenite moves the solidus to a lower “A” fraction and overall, the crystallization range is much more restricted as compared with the closed system melting run in Figure 32a. Also, the maximum Fe-enrichment in the melt is slightly higher than the closed system. Note, however, that the trend for the closed and open system formation of the original bulk rock still crosses the liquid line of descent at about the same point, though at different liquid fraction: without late-stage liquid loss, the

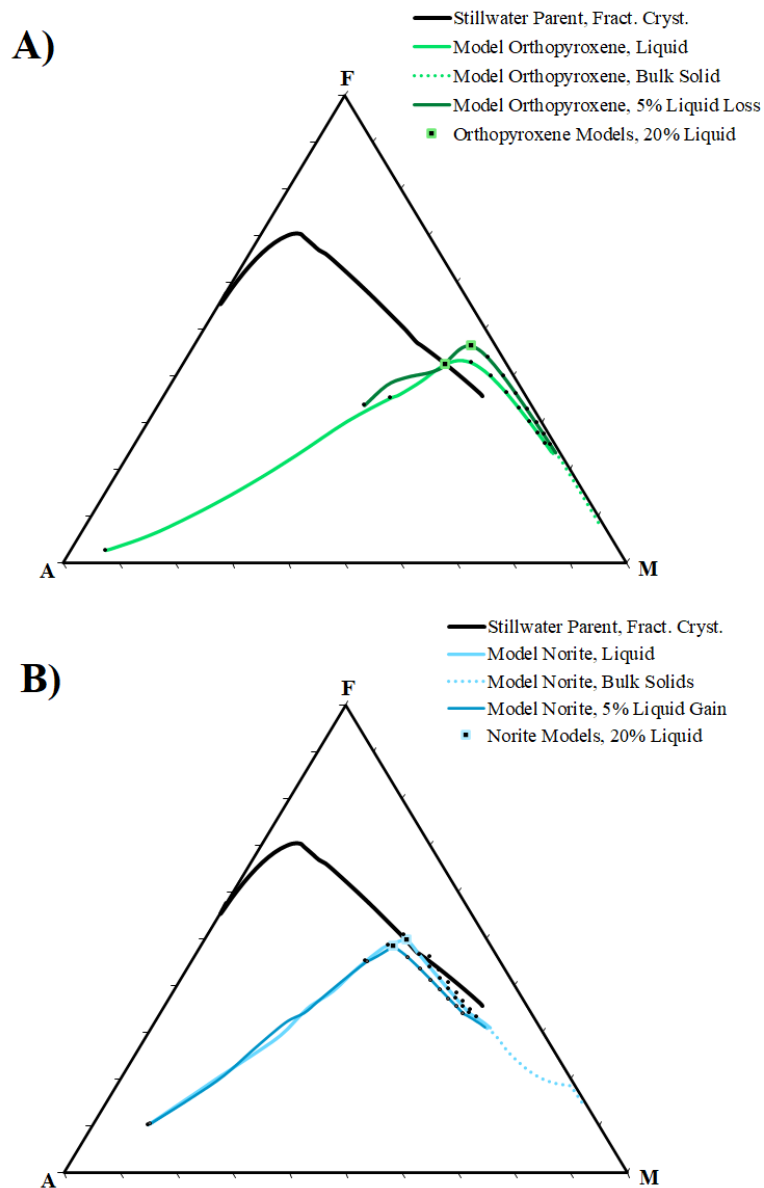


Figure 33: Synthetic melting model for rocks with open-system behavior, as described in the text. Squares highlighted in green and blue indicate the liquid composition at 20% liquid for the orthopyroxene and the norite respectively. A) Model of late-stage liquid loss in the model orthopyroxene. B) Model of late-stage liquid gain in the model norite.

sample crosses the fractionation line at 20% liquid. With the loss of the last 5% of liquid, the point where the melt crosses the original liquid line of descent is reduced to roughly 10% liquid. As expected, late liquid loss produces more magnesian orthopyroxene, and more anorthitic plagioclase (Table 7). Conversely, the gain of 5% liquid to the model norite (Figure 33b) results in a less magnesian starting composition, as well as in markedly less iron enrichment. As a result, the now slightly more evolved model norite composition does not cross the liquid line of descent for the parent, instead falling entirely below the curve and evolving to a similarly alkali-rich end liquid composition. The late liquid gain results in a less magnesian orthopyroxene and a less anorthitic plagioclase composition, due to the addition of evolved liquid to the bulk melt (Table 7).

Modeling the effects of open-system behavior on individual samples obscures the effect of open-system behavior on the evolution of the parent melt. We model two possible open-system behaviors in the parental liquid: injection of fresh pulses of primitive parent, and addition of evolved liquid into the fractionating parent. Injection of parental magma has been proposed at the Stillwater Complex to explain several geochemical features, including the consistency of the Mg# of pyroxene in the Bronzite Zone of the Ultramafic series. Reinjection of parental melt is here modeled in MELTS (Figure 34a). At every 10% interval of parent crystallization, 5% or 10% of the original parent composition is injected into the fractionating melt. This is modeled as a mixture of 5% or 10% parent composition added to 95% or 90% of the fractionated liquid

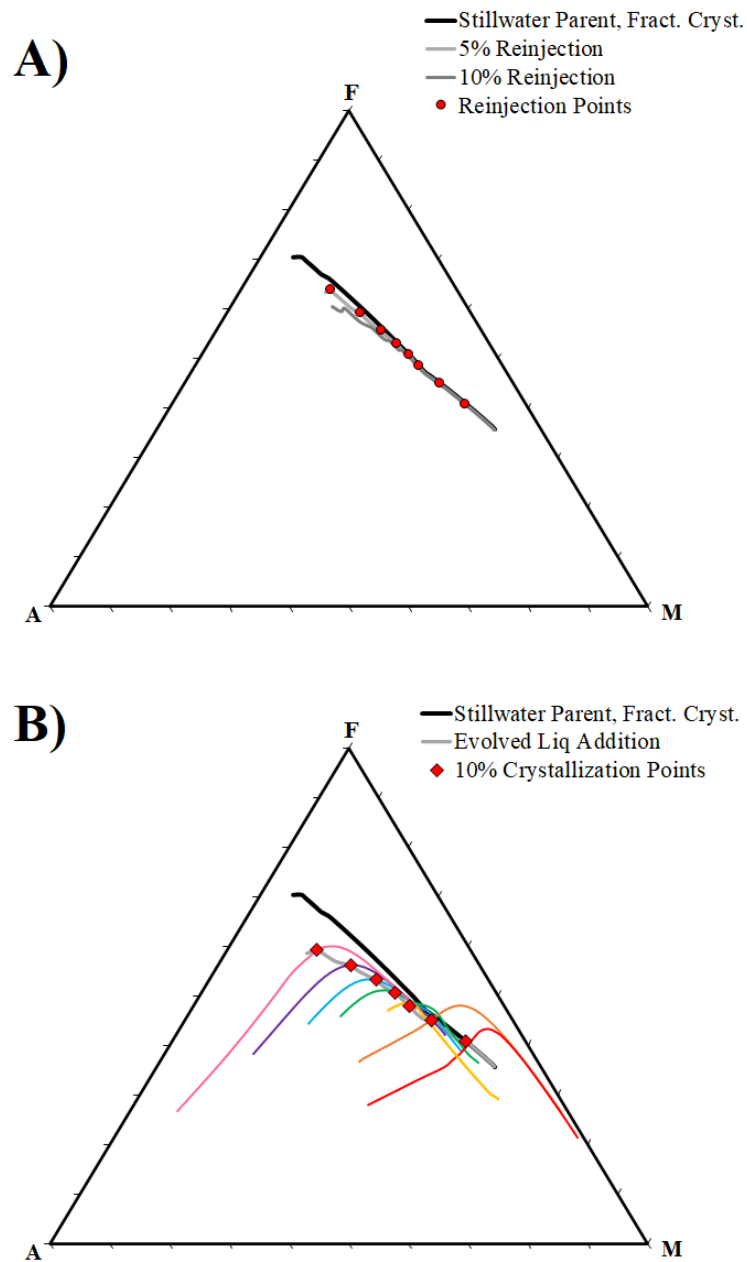


Figure 34: The effect of open-system behavior on parental liquid evolution during fractional crystallization, as described in the text. A) Reinjection of 5% and 10% parental liquid composition at 10% crystallization intervals of the parent. B) Addition of 5% evolved liquid from model sample compositions at 10% crystallization intervals of the parent.

composition at the injection point. Because the evolution of the modeled Stillwater parent is roughly a straight line of decreasing MgO and increasing FeO_t until the appearance of oxides late in the parent evolution trend, the result of injection of parental magma on the overall fractionation trend is minimal (Figure 34a). However, there is an impact of parent reinjection on orthopyroxene composition; injection of parental magma results in increased Mg#, and Mg# remains relatively constant after an injection of fresh parent (Figure 35), simulating the actual pyroxene compositions of the Bronzite Zone.

To simulate the effects of compaction and migration of late, evolved liquid into the fractionating melt, the impact of evolved liquid addition on the fractionation trend was also modeled (Figure 34b). At 10% crystallization intervals, model samples were constructed using a mixture of 20% of the liquid at each interval and 80% the modal mineralogy and modeled mineral compositions. These model samples were then synthetically crystallized to 5% remaining liquid, and this liquid was added to the fractionating parent using the same procedure as reinjection of parental melt. The result of this addition of evolved liquid is a fractionation trend that increasingly deviates from the closed system fractionation trend originally modeled. The evolved liquid addition trend falls below the closed system trend, with increased alkali contents and reduced FeO_t. In addition, the evolution of the model sample liquids at each crystallization interval are shown; model sample liquids increasingly fall below the closed system fractionation trend.

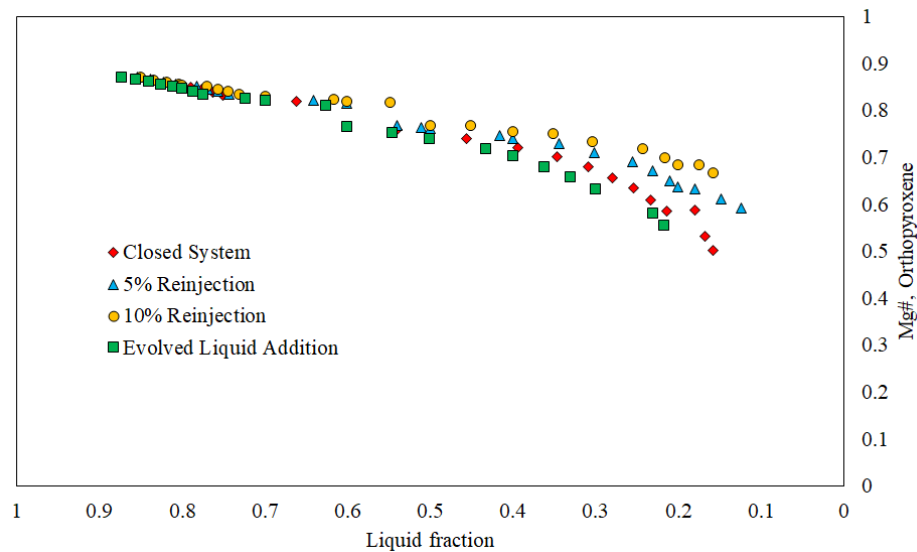


Figure 35: The effect of open-system behavior on crystallized pyroxene composition. Reinjection of parental melt to the system helps to stabilize pyroxene Mg#, as observed in the Bronzite Zone.

6.4 Application to the Stillwater Complex

6.4.1 Stillwater Complex Geochemical Analyses

Twenty-seven samples, of typical cumulate textures observed throughout most of the Stillwater Complex, were selected for geochemical analysis (Figure 36). This included three Basal Series samples, collected by U.S. Geological Survey workers, and nine Ultramafic series samples and fifteen Lower Banded series samples, collected from locations on Chrome Mountain and at Mountain View (Figure 13), approximately following traverses made by McCallum et al. (1980) and Raedeke and McCallum (1984). To ensure bulk rock geochemistry was representative of the sample as a whole, particularly in the case of pegmatoids, a large amount of material was cut from each sample and crushed in a tungsten carbide shatterbox to powder to ensure sample

homogenization. There are some concerns of contamination from tungsten carbide; previous studies show that the most problematic elements are Co and W (~150 ppm added contamination) as well as Ta (~0.5 ppm added contamination) (Thompson and Bankston, 1970; Hickson and Juras, 1986; ten Bruggencate et al., 2014).

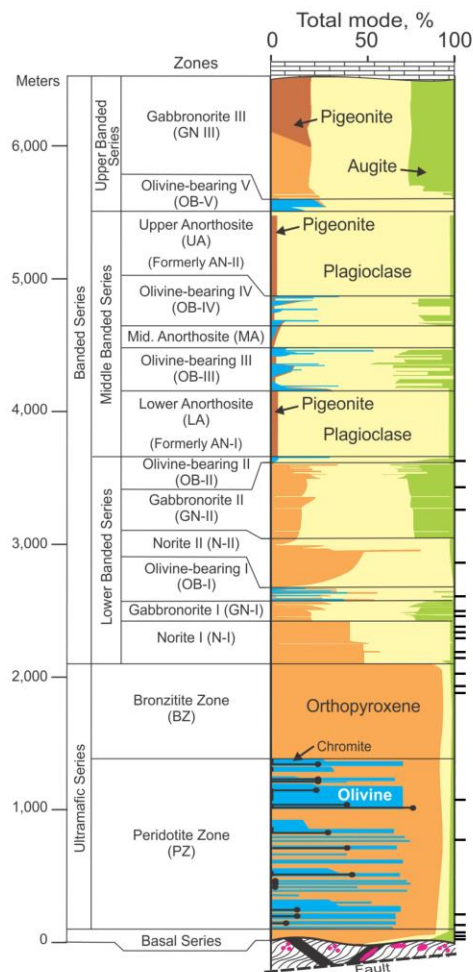


Figure 36: Stratigraphy of the Stillwater Complex with major mineral modes as a function of height. Modal data and stratigraphic units after McCallum et al. (1980) and Raedeke and McCallum (1984). The locations of samples collected as part of this study are indicated by black bars to the right side of the figure.

Sample dissolution for major element analysis was conducted following the modified methods of Braun et al. (1994). Solutions were analyzed using a Fisons SpecterSpan 7 Direct Current Plasma Emission Spectrometer (DCP) at Duke University following the methods of Klein et al. (1991). Basalts BIR, W2a, and K1919 along with anorthosite AN-G were used as standards. DCP-AES analysis provided major element analysis along with transition metals, Ba, and Sr. Ba and Sr were analyzed in both major element and minor element solutions to ensure precision of analysis. A comparison of these results suggests major and trace element analyses are within an average of 5% difference and a median of 1.5% difference of one another. A full suite of trace elements was analyzed using a Thermo-Fisher VG PlasmaQuad 3 Inductively Coupled Plasma Mass Spectrometer (ICP-MS) at Duke University following a two acid digestion procedure modified after Cheatham et al. (1993), followed by a second dissolution for a period of four hours at 160°C in an aqua regia solution. ICP-MS analysis utilized the same set of standards as DCP-AES analysis: basalts BIR, W2a, and K1919 as well as anorthosite AN-G. Major element geochemistry, along with selected trace elements, is given in Table 8. The full suite of geochemical analyses for these samples can be found in Appendix C.

6.4.2 Trapped Liquid Estimates

External estimates of trapped liquid in Stillwater samples were derived in following two methods. First, trapped liquid was calculated from the measured

concentrations of three incompatible trace elements (P, Zr, Nd). Trapped liquid estimates are commonly calculated using incompatible trace elements that typically partition into one late phase. In a study of the Skaergaard intrusion (Tegner et al., 2009), trapped liquid was estimated based on Rb, U, and P. Rb and U are fluid-mobile and may not have been preserved over the 2.7 Ga history of the Stillwater Complex. As a result, the trapped liquid calculated from P concentrations is used in the majority of calculation in this paper. P (and, to a lesser extent, Nd) partition primarily into apatite, and Zr into zircon, both of which are late-phase minerals in the Stillwater Complex. These trace elements should thus reflect the trapped liquid in each sample available to crystallize late-stage minerals. Trapped liquid is calculated from trace element contents by dividing the bulk rock trace element concentration by a calculated liquid concentration. The liquid concentration is based on the evolution of an assumed single parent magma (in this case, the modeled parent of Jenkins and Mungall, 2018). As the trace elements are assumed to be perfectly incompatible, the trace element concentration in the parent is multiplied by the amount of liquid remaining in the system, estimated from a total complex thickness, assumed to be 8000 m. While the known thickness of the Stillwater Complex is only 6500 m, the top portion of the complex has been lost to erosion. We estimate that loss to be 1500 m. Trapped liquid for Basal and Ultramafic series samples was also estimated using the modal plagioclase calculated from CIPW norms. In the Basal and Ultramafic series, plagioclase is an intercumulus mineral. Thus, the CIPW-

normative abundance of plagioclase provides an upper bound on the amount of trapped liquid in a sample. Trapped liquid estimates based on all three trace elements (P, Nd, Zr), as well as CIPW norms, are given in Table 9.

6.5 Synthetic Melting Results

Analyzed whole rock samples were synthetically remelted using the MELTS program to determine the composition of the trapped liquid in the samples. A small amount of H₂O (0.01 wt. %) was added to the bulk composition of each sample. Samples were synthetically remelted to find the composition of the trapped liquid, based on the trapped liquid fraction calculated using CIPW norms and P concentration. Modeling was conducted at 2500 bars of pressure and an oxygen fugacity at the quartz-fayalite-magnetite (QFM) buffer. The full synthetic remelting curve of each sample, in comparison to the fractional crystallization curve of the Jenkins and Mungall (2018) corrected parent composition and the open-system parent evolution curves is shown in Figure 37.

The composition of the mineral compositions calculated at those trapped liquid fractions is compared with measured mineral compositions from the Stillwater Complex (Figure 38). In the Ultramafic series, plagioclase occurs only rarely as an interstitial mineral; the trapped liquid fraction suggested by P contents is too high for the modeled liquid evolution to have crystallized plagioclase. As a result, plagioclase compositions are not recorded for most Ultramafic series samples. In the upper parts of the Lower

Table 8: Major and selected trace element concentrations of host rock samples

Sample	M17-868	M17-776	M17-363	S18-76	S18-71	S18-66	S18-64	S18-60
Position (m)	40	70	130	190	250	400	450	750
Unit	BAS	BAS	BAS	UM	UM	UM	UM	UM
Subzone	N/A	N/A	N/A	PZ	PZ	PZ	PZ	PZ
SiO₂ (wt. %)	49.07	47.63	45.05	52.42	49.15	54.92	55.45	42.00
TiO₂	0.27	0.25	0.25	0.14	0.13	0.10	0.11	0.09
Al₂O₃	6.96	8.12	8.94	2.77	6.16	4.30	3.43	1.59
Cr₂O₃	0.15	0.22	0.26	0.45	0.32	0.45	0.53	0.28
FeO	17.36	12.71	12.96	10.75	10.70	8.31	8.83	13.81
MnO	0.22	0.20	0.29	0.20	0.18	0.17	0.19	0.19
MgO	19.50	18.95	21.29	30.50	27.00	27.77	28.67	41.15
CaO	5.51	5.26	5.85	2.60	3.97	3.34	3.21	0.90
Na₂O	0.23	0.37	0.19	0.17	0.52	0.30	0.20	0.16
K₂O	0.08	0.04	0.07	0.01	0.45	0.01	0.13	0.02
Th (ppm)	0.277	0.478	0.188	0.128	0.106	0.060	0.055	0.112
Nb	0.460	0.525	0.116	0.114	0.147	0.090	0.097	0.198
Zr	11.73	11.16	7.54	6.77	6.09	4.52	4.55	5.58
Ti	1594.3	1482.0	1477.5	858.6	776.1	621.3	669.3	545.6
Y	5.40	5.00	6.87	2.61	2.95	2.29	2.39	1.514
La	1.650	1.975	2.803	0.571	0.694	0.332	0.293	0.442
Ce	3.48	4.17	5.32	1.24	1.43	0.71	0.63	0.86
Pr	0.474	0.543	0.671	0.170	0.192	0.099	0.091	0.107
Nd	2.000	2.296	2.866	0.681	0.800	0.419	0.399	0.423
Sm	0.569	0.598	0.768	0.204	0.242	0.136	0.133	0.120
Eu	0.327	0.266	0.357	0.079	0.128	0.061	0.061	0.053
Gd	0.741	0.725	0.987	0.303	0.331	0.225	0.221	0.182
Tb	0.134	0.133	0.177	0.059	0.065	0.044	0.048	0.033
Dy	0.856	0.804	1.111	0.358	0.406	0.289	0.308	0.183
Ho	0.192	0.178	0.252	0.086	0.099	0.073	0.079	0.046
Er	0.550	0.511	0.718	0.249	0.291	0.219	0.228	0.124
Yb	0.611	0.530	0.795	0.310	0.353	0.310	0.314	0.175
Lu	0.098	0.085	0.131	0.053	0.061	0.055	0.054	0.031

Table 8, cont.

Sample	S18-41	S18-17	S18-44	S18-50	S18-52	S18-53	S18-12	S18-13
Position (m)	1100	1900	1950	2050	2200	2250	2350	2350
Unit	UM	UM	UM	UM	LB	LB	LB	LB
Subzone	PZ	BZ	BZ	BZ	N-I	N-I	N-I	N-I
SiO₂ (wt. %)	44.81	53.49	55.04	55.13	48.65	49.49	49.92	49.26
TiO₂	0.06	0.10	0.24	0.20	0.07	0.07	0.14	0.12
Al₂O₃	2.89	5.11	3.47	2.78	23.98	22.56	19.71	20.07
Cr₂O₃	0.23	0.44	0.44	0.42	0.12	0.16	0.17	0.17
FeO	11.08	8.84	9.68	9.81	3.21	3.94	5.03	4.63
MnO	0.18	0.19	0.20	0.20	0.05	0.08	0.11	0.10
MgO	37.59	25.66	27.22	28.08	8.50	10.04	11.29	10.54
CaO	2.30	4.04	2.81	2.83	11.96	11.70	11.55	11.94
Na₂O	0.19	0.30	0.41	0.26	1.54	1.24	0.98	0.99
K₂O	0.17	0.29	0.23	0.01	0.02	0.15	0.35	0.03
Th (ppm)	0.015	0.022	0.519	0.197	0.043	0.042	0.174	0.170
Nb	0.035	0.037	0.299	0.145	0.079	0.072	0.250	0.219
Zr	3.12	3.85	10.05	7.04	3.75	3.57	8.53	8.05
Ti	330.4	586.6	1440.2	1189.8	409.4	389.8	827.2	730.8
Y	1.362	2.63	5.21	4.14	1.54	1.46	3.50	3.59
La	0.148	0.262	1.204	0.474	0.406	0.360	0.841	0.889
Ce	0.34	0.52	2.49	1.11	0.82	0.73	1.80	1.86
Pr	0.048	0.076	0.310	0.163	0.109	0.097	0.242	0.251
Nd	0.216	0.318	1.280	0.762	0.442	0.377	0.999	1.101
Sm	0.060	0.117	0.365	0.263	0.124	0.102	0.284	0.296
Eu	0.041	0.067	0.134	0.097	0.142	0.127	0.163	0.181
Gd	0.115	0.195	0.537	0.428	0.186	0.177	0.402	0.425
Tb	0.022	0.041	0.106	0.086	0.035	0.032	0.074	0.080
Dy	0.131	0.299	0.758	0.597	0.191	0.180	0.490	0.514
Ho	0.039	0.080	0.182	0.145	0.047	0.043	0.119	0.122
Er	0.097	0.237	0.541	0.446	0.121	0.118	0.326	0.330
Yb	0.142	0.350	0.637	0.514	0.163	0.168	0.386	0.371
Lu	0.025	0.063	0.106	0.090	0.027	0.027	0.064	0.061

Table 8, cont.

Sample	S18-18A	S18-18B	S18-23	S18-11	S18-08	S18-03	S18-06	S18-07
Position (m)	2400	2400	2450	2550	2600	2700	2700	2875
Unit	LB	LB	LB	LB	LB	LB	LB	LB
Subzone	N-I	N-I	N-I	GN-I	GN-I	OB-I	OB-I	N-II
SiO₂ (wt. %)	49.52	51.79	48.02	48.52	48.20	50.27	48.44	50.87
TiO₂	0.13	0.14	0.07	0.09	0.09	0.08	0.12	0.15
Al₂O₃	16.83	8.31	28.47	22.61	26.42	16.07	21.55	17.17
Cr₂O₃	0.10	0.17	0.02	0.14	0.08	0.26	0.01	0.11
FeO	7.90	11.20	2.60	3.84	2.82	4.79	6.24	6.51
MnO	0.16	0.21	0.04	0.07	0.06	0.09	0.11	0.13
MgO	12.75	19.86	3.52	8.11	5.02	12.76	8.40	13.25
CaO	8.91	5.67	14.19	13.38	14.63	14.24	12.55	9.95
Na₂O	1.01	0.48	1.80	1.11	1.34	0.73	1.29	1.09
K₂O	0.17	0.29	0.11	0.08	0.36	0.33	0.02	0.18
Th (ppm)	0.073	0.092	0.033	0.072	0.095	0.017	0.037	0.125
Nb	0.077	0.103	0.056	0.082	0.121	0.030	0.049	0.171
Zr	4.58	8.99	3.73	5.47	5.51	3.48	4.16	7.44
Ti	782.4	866.1	432.9	543.4	512.1	502.3	697.1	916.2
Y	2.96	3.50	1.77	2.61	2.23	2.52	2.54	3.36
La	0.966	0.489	0.805	0.527	0.633	0.214	0.650	0.823
Ce	1.83	1.04	1.53	1.17	1.32	0.54	1.23	1.76
Pr	0.226	0.147	0.186	0.159	0.167	0.084	0.162	0.229
Nd	0.854	0.631	0.761	0.697	0.749	0.426	0.659	0.975
Sm	0.215	0.197	0.150	0.219	0.207	0.155	0.173	0.267
Eu	0.262	0.129	0.287	0.146	0.161	0.084	0.205	0.192
Gd	0.292	0.308	0.236	0.302	0.302	0.250	0.244	0.363
Tb	0.053	0.067	0.036	0.059	0.051	0.053	0.050	0.071
Dy	0.380	0.460	0.180	0.363	0.313	0.342	0.316	0.457
Ho	0.097	0.117	0.044	0.085	0.078	0.090	0.081	0.114
Er	0.292	0.371	0.102	0.236	0.195	0.229	0.229	0.334
Yb	0.369	0.470	0.146	0.260	0.204	0.254	0.306	0.389
Lu	0.065	0.086	0.022	0.041	0.033	0.041	0.051	0.066

Table 8, cont.

Sample	S18-30	S18-32	S18-28
Position (m)	3300	3600	3820
Unit	LB	LB	LB
Subzone	GN-II	GN-II	OB-II
SiO₂ (wt. %)	50.99	50.89	51.42
TiO₂	0.13	0.16	0.17
Al₂O₃	17.90	13.85	17.59
Cr₂O₃	0.06	0.08	0.09
FeO	4.98	5.90	4.63
MnO	0.11	0.13	0.11
MgO	10.31	12.43	9.62
CaO	13.97	14.44	16.88
Na₂O	1.38	1.03	1.30
K₂O	0.05	0.32	0.18
Th (ppm)	0.040	0.077	0.026
Nb	0.088	0.143	0.050
Zr	5.14	6.35	6.19
Ti	799.6	973.9	1006.5
Y	4.06	5.44	5.77
La	0.538	0.540	0.620
Ce	1.16	1.32	1.54
Pr	0.182	0.215	0.249
Nd	0.910	1.133	1.267
Sm	0.323	0.407	0.448
Eu	0.214	0.218	0.262
Gd	0.464	0.628	0.690
Tb	0.094	0.126	0.135
Dy	0.617	0.845	0.907
Ho	0.145	0.188	0.205
Er	0.404	0.541	0.599
Yb	0.400	0.548	0.589
Lu	0.065	0.091	0.090

Banded series (Gabbronorite-II and above), synthetic remelting of the samples suggests low-Ca clinopyroxene crystallizes instead of orthopyroxene. The Mg# for these low-Ca clinopyroxene minerals is systematically lower than in orthopyroxene. In addition, the physical properties of the system at the appropriate liquid fractions, such as temperature and liquid and solid density can be found in Figure 39.

The trace element composition of the trapped liquid was calculated using the modeling results of MELTS. Synthetic remelting of samples in MELTS provides the equilibrium mineral modes in addition to the trapped liquid composition. These equilibrium mineral modes, in combination with the bulk rock trace element data obtained by ICP-MS, can be used to calculate the trace element composition of the trapped melt. Partition coefficients for relevant minerals (olivine, orthopyroxene, clinopyroxene, and plagioclase) were collected by Bédard (1994). A bulk partition coefficient for the sample was then calculated using the modal mineralogy, such that:

$$K_d^{bulk} = \phi^{opx} K_d^{opx} + \phi^{cpx} K_d^{cpx} + \phi^{pl} K_d^{pl} + \phi^{ol} K_d^{ol} \quad (\text{Equation 3})$$

where K_d is the mineral or bulk partition coefficient and ϕ is the proportion of a specific mineral. Using the bulk partition coefficient and the concentration of the trace element in the whole rock, the concentration of the trace element in the liquid can be calculated:

$$C_L = \frac{C_{WR}}{F + (1 - K_D^{bulk}) + K_D^{bulk}} \quad (\text{Equation 4})$$

Table 9: Trapped Melt Fraction (TMF) estimates for Stillwater

Sample	Position (m)	Unit	TMF from P	TMF from Nd	TMF from Zr	TMF from CIPW
M17-868	40	BAS	48.9	18.1	20.3	33.6
M17-776	70	BAS	54.2	20.7	19.2	39.6
M17-363	130	BAS	55.6	25.6	12.9	42.3
S18-76	190	UM	22.3	6.0	11.5	13.8
S18-71	250	UM	25.1	7.0	10.3	33.7
S18-66	400	UM	12.9	3.6	7.5	21.6
S18-64	450	UM	11.1	3.4	7.5	17.6
S18-60	750	UM	26.6	3.5	8.8	8.4
S18-41	1100	UM	13.6	1.7	4.7	15.7
S18-17	1900	UM	13.0	2.2	5.1	26.7
S18-44	1950	UM	20.9	8.8	13.2	18.9
S18-50	2050	UM	13.7	5.2	9.1	14.4
S18-52	2200	LB	11.8	2.9	4.7	
S18-53	2250	LB	10.2	2.5	4.5	
S18-12	2350	LB	26.9	6.4	10.5	
S18-13	2350	LB	24.9	7.1	9.9	
S18-18A	2400	LB	13.3	5.4	5.6	
S18-18B	2400	LB	10.4	4.0	10.9	
S18-23	2450	LB	15.0	4.8	4.5	
S18-11	2550	LB	14.1	4.3	6.5	
S18-08	2600	LB	14.9	4.6	6.5	
S18-03	2700	LB	3.8	2.6	4.0	
S18-06	2700	LB	12.9	4.0	4.8	
S18-07	2875	LB	17.9	5.7	8.3	
S18-30	3300	LB	7.4	4.9	5.2	
S18-32	3600	LB	12.8	5.7	6.1	
S18-28	3820	LB	7.0	6.0	5.6	

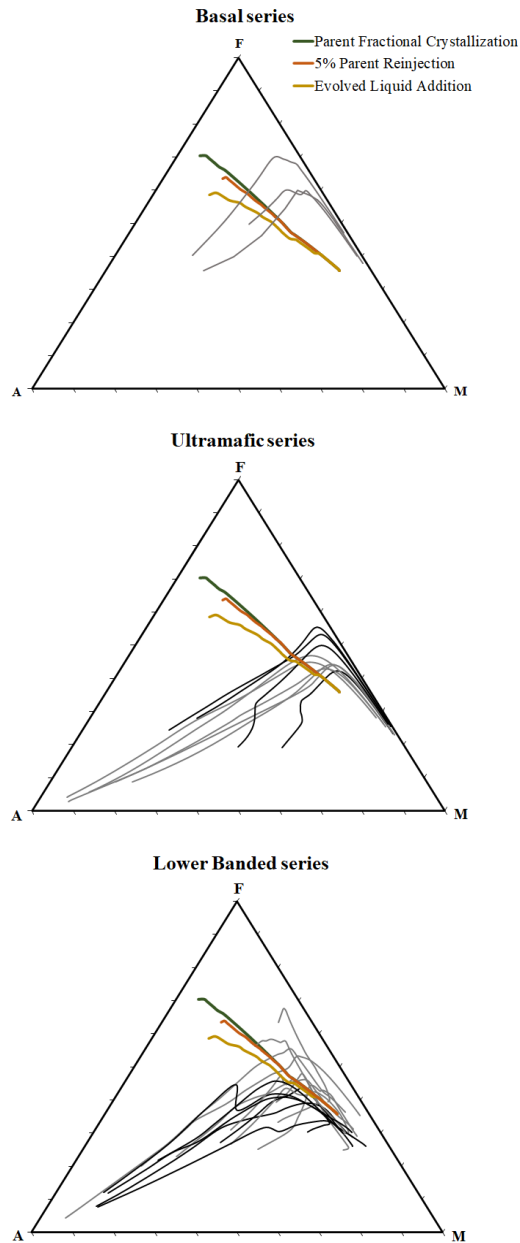


Figure 37: Synthetic melting curves for analyzed Stillwater samples in each of the three major units explored. Ultramafic series and Lower Banded series sample evolution curves in grey are nominally closed-system samples; curves in black are nominally open-system samples, as described in the text. Also shown are parent fractionation curves for closed system behavior (dark green), 5% parental melt re-injection (dark orange), and evolved liquid addition (dark yellow).

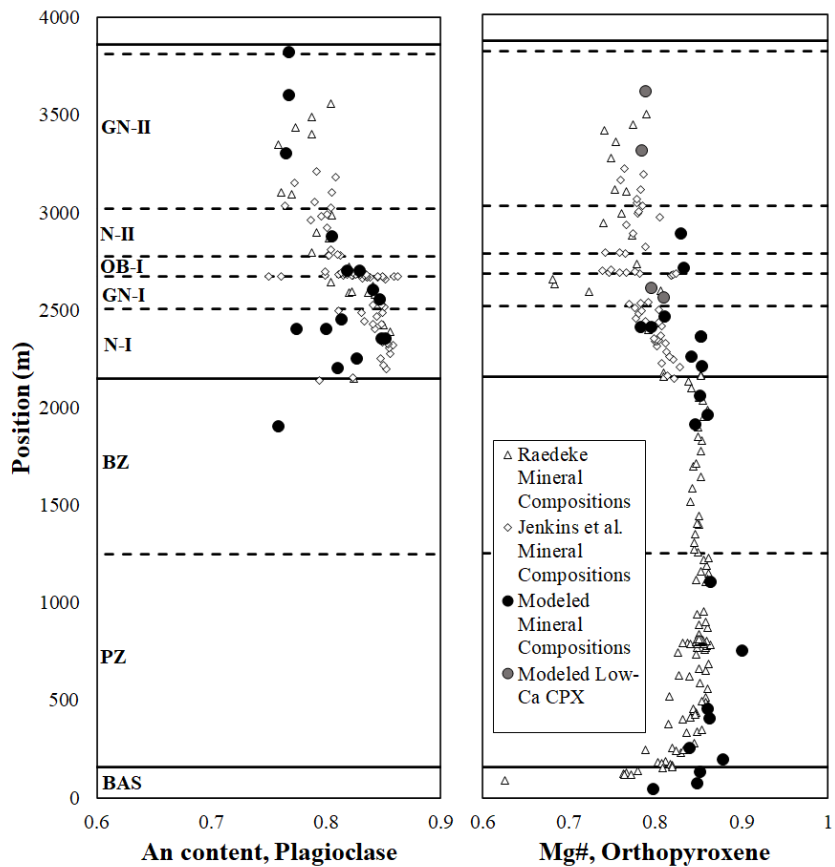


Figure 38: Variability in compositions of plagioclase and orthopyroxene moving up-section. Measured mineral compositions (open symbols) analyzed by Raedeke (1979) and Jenkins et al. (2021). Modeled mineral compositions (closed circles) are mineral compositions in equilibrium with trapped liquid proportion estimated by P content of the bulk rock. Closed circles in grey are modeled low-Ca clinopyroxenes that crystallized instead of orthopyroxene. They have a generally lower Mg#.

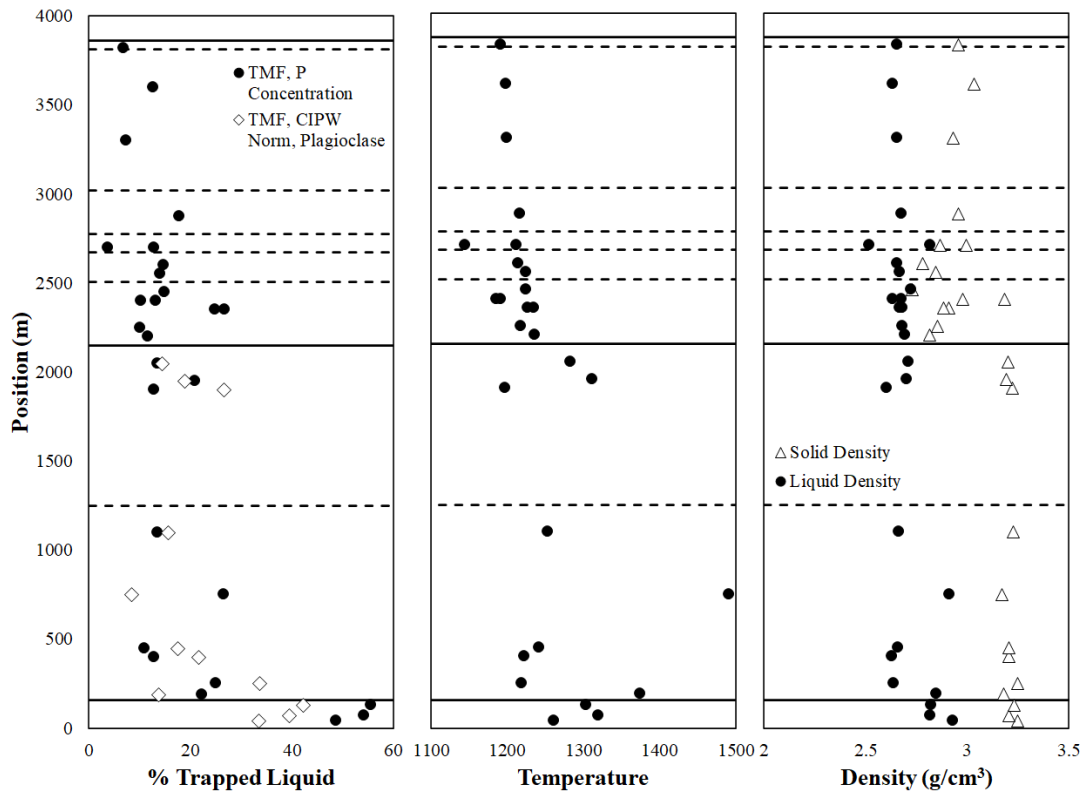


Figure 39: Physical properties of the modeled Stillwater trapped liquid fraction moving up-section. A) Amount of trapped liquid, as estimated by P content of the bulk rock and the CIPW normative plagioclase. B) Modeled temperature of the system at the appropriate trapped liquid fraction. C) Density of the trapped liquid component and bulk solid component.

This equation is identical to the equation for equilibrium crystallization and represents equilibrium melting of the bulk rock. Using Equation 2 for each trace element allows the concentration of the trace element in the modeled liquid to be calculated, providing a full modeled liquid trace element suite. Variation in the trapped liquid composition moving up-section for selected trace elements is shown in Figure 40.

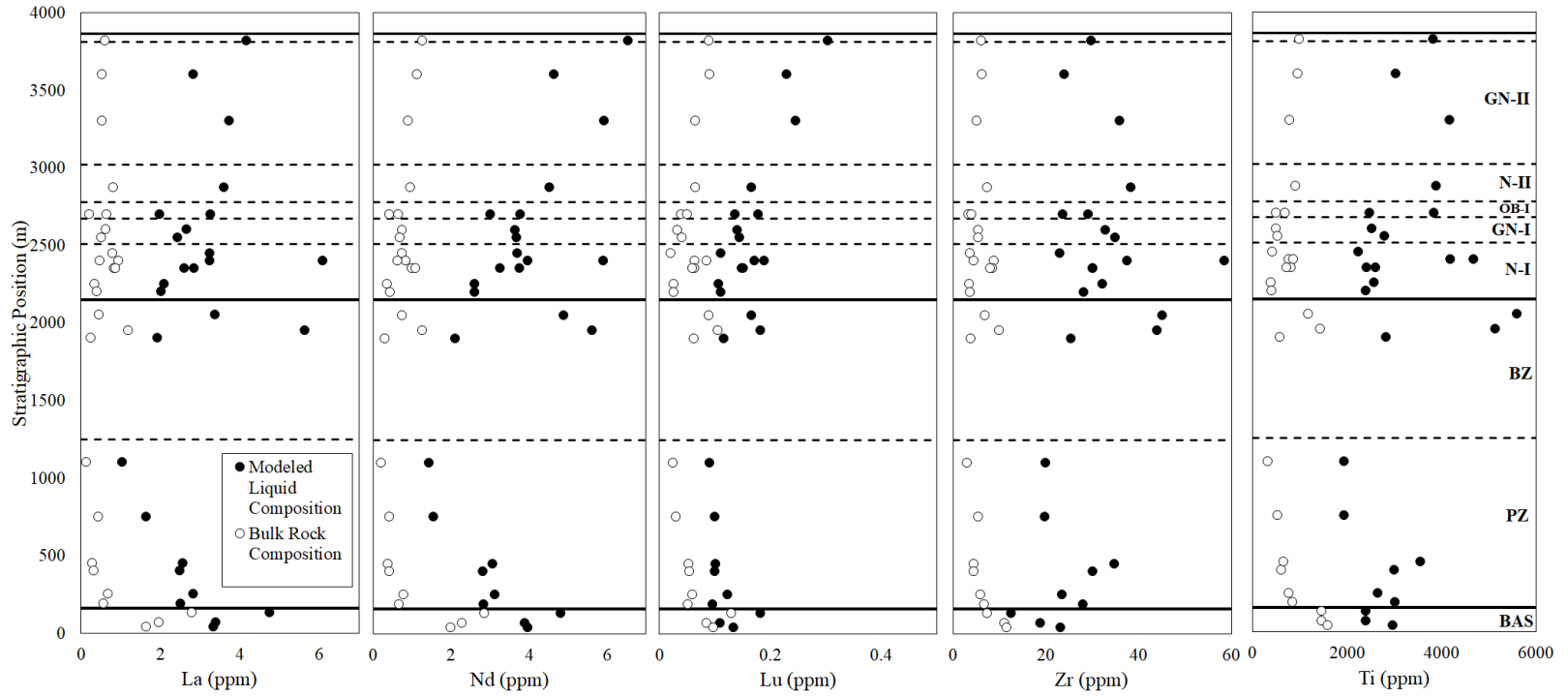


Figure 40: Modeled evolution of trapped liquid trace element concentrations as compared to measured bulk rock trace element composition for five incompatible elements (La, Nd, Lu, Zr, Ti).

6.6 Discussion

6.6.1 The Effect of Trapped Liquid on Stillwater Mineral Compositions

A comparison of the modeled plagioclase and orthopyroxene compositions to those previously measured (Raedeke, 1979; Jenkins et al., 2021; Figure 38) provides evidence for some processes that may have occurred during Stillwater Complex formation. In the Lower Banded series, where plagioclase occurs as a major modal mineral, the modeled mineral compositions are a good match for the measured mineral compositions (Raedeke, 1979; Jenkins et al., 2021). Conversely, measured orthopyroxene compositions in the Ultramafic series fit well with the modeled composition, while in the Lower Banded series the modeled orthopyroxene Mg# is higher than the measured orthopyroxene Mg#, for those samples that were modeled to contain orthopyroxene. Differences between modeled and measured orthopyroxene in the Lower Banded series is likely due to the 'trapped liquid shift' (Barnes, 1986). Orthopyroxene readily re-equilibrates with residual or interstitial liquid. Modeling of the orthopyroxene before the liquid has fully crystallized therefore results in a higher Mg# than the final Mg# recorded by the rock. The similarity between modeled and measured orthopyroxene in the Ultramafic series, but not in the Lower Banded series, is likely due to the amount of orthopyroxene present. Barnes (1986) suggests that the trapped liquid shift depends in part on the amount of a mineral present; a higher proportion of the mineral in the sample results in less re-equilibration overall. In the Ultramafic series, particularly in the

Bronzite Zone, many samples are almost entirely composed of orthopyroxene. As a result, any trapped liquid that has not been lost to open-system behavior would have less impact on the final composition of the orthopyroxene. When plagioclase (and clinopyroxene) become major modal minerals in the Lower Banded series, the proportion of orthopyroxene in the sample decreases, and orthopyroxene is more impacted by the trapped liquid shift. Conversely, the similarity of measured and modeled plagioclase is expected, as plagioclase cores typically remain robust during interstitial melt migration, rather than re-equilibrating – interstitial liquid instead forms plagioclase rims (Toplis et al., 2008). Thus, the measured An content of the plagioclase should reflect the composition of the original liquid that formed it, rather than the interstitial liquid passing through the system at a later time.

6.6.2 Models for Stillwater Complex Formation

A number of models have been proposed for the formation of the Stillwater Complex. Mixing of multiple parental magmas has commonly been called upon to explain geochemical variability in Stillwater samples, as well as the formation of the J-M Reef (Todd et al., 1982; Irvine et al., 1983; Lambert et al., 1994; Godel and Barnes, 2008). Lambert et al. (1994) proposed that the transition between parental magmas occurred just below the J-M Reef (OB-I), with magma mixing explaining the Platinum Group Element-rich nature of the Reef. Intrusion of a second magma and turbulent mixing of the two should result in changes to the geochemistry of the intrusion, which should be

evident both in mineral composition and in the trace element composition of the trapped liquid. A more recent model for the formation of large layered intrusions, including the Stillwater Complex (Wall et al., 2018) and the Bushveld Complex (Mungall et al., 2016) has been that of out-of-order emplacement. In this model, the layers intrude as sills, with intrusions occurring on ~1 Myr intervals. This model of out-of-order emplacement should be similarly observable in both mineral composition and trace element composition of the trapped liquid, as well as in the physical properties. The results of this study find no evidence of the involvement of multiple magmas or out-of-order emplacement in forming the intrusion, based on the physical properties and trace element evolution of the trapped liquid.

The physical properties of the liquid vary systematically moving up-section. The amount of trapped liquid present in the system based on P contents is highest in the Basal series (~50%, Figure 39a). This would be expected in a layered intrusion such as the Stillwater Complex. The Basal series is the base of the intrusion. When the complex formed, the Basal series would have cooled the fastest due to contact with the cold country rock. As a result, interstitial liquid would have had less time to be lost to processes such as compaction, and would instead have crystallized in place, without being lost. This results in a substantially higher trapped melt fraction. The trapped melt fraction estimated by the CIPW normative amount of plagioclase in the Basal and Ultramafic series is similar to that estimated by P. In the Ultramafic series and Lower

Banded series, the trapped liquid estimate decreases slightly moving upward. The temperature (Figure 39b) corresponds well to what would be expected for fractionation of a single magma; the modeled temperature at the appropriate trapped melt fraction decreases steadily moving upward through the intrusion. The single point with a high T estimate is a harzburgite sample that is not representative of the Bronzite Zone as a whole. Similarly, the liquid density (Figure 39c) shows a smooth trend of slightly decreasing density moving up-section, with no abrupt changes that would be expected in the event of multiple parental magmas. The solid density decreases at the Ultramafic series/Lower Banded series contact, but this is due to the appearance of less-dense plagioclase as a major modal mineral. Overall, the physical properties of the trapped liquid are suggestive of the evolution of a single parental magma, rather than multiple magmas.

The evolution of trace elements in the modeled trapped liquid and measured bulk rock samples (Figure 40) are suggestive of a single parental magma evolving in an open system. In Basal series samples, trace element concentrations in the bulk rock are elevated, as are the trace element concentrations in the modeled liquid. As the Basal series would have cooled quickly, freezing trapped liquid within the rock, this corresponds to expected trace element patterns. In the Ultramafic series, modeled (as well as bulk rock) trace element contents are low. Trace element contents increase through the Lower Banded series, and there is a greater divergence between the bulk

rock and modeled liquid trace element concentrations, as the modeled liquid becomes more enriched in trace elements relative to the bulk rock and to the modeled liquids lower in the intrusion. In part, this pattern can be explained through a simple fractional crystallization model. A single fractionating liquid would be expected to become more enriched in incompatible elements such as REEs, as well as Zr and Ti, as it evolves. Additionally, some of the differences in trace element enrichment in the modeled liquids of the Ultramafic series and Lower Banded series may be due to lower trapped melt fraction estimates higher in the intrusion. At low melt fractions, incompatible elements simply become more concentrated in the melt. Since the liquid trace element model only includes the crystallization of major phases (olivine, plagioclase, pyroxenes), late phases into which incompatible elements such as REE partition are excluded from consideration. Thus, at low trapped melt fractions (~5% in the Lower Banded series), the remaining liquid is enriched in trace elements relative to the measured bulk rock. An examination of trace element ratios helps to demonstrate this (Figure 41). The increasing divergence in modeled liquid and measured bulk rock trace element concentrations observed in individual trace elements largely disappears when analyzing trace element ratios. Further, trace element ratios in both the modeled liquid and the bulk rock samples tend to remain relatively constant or increase slightly moving up-section, as would be expected in a single evolving magma.

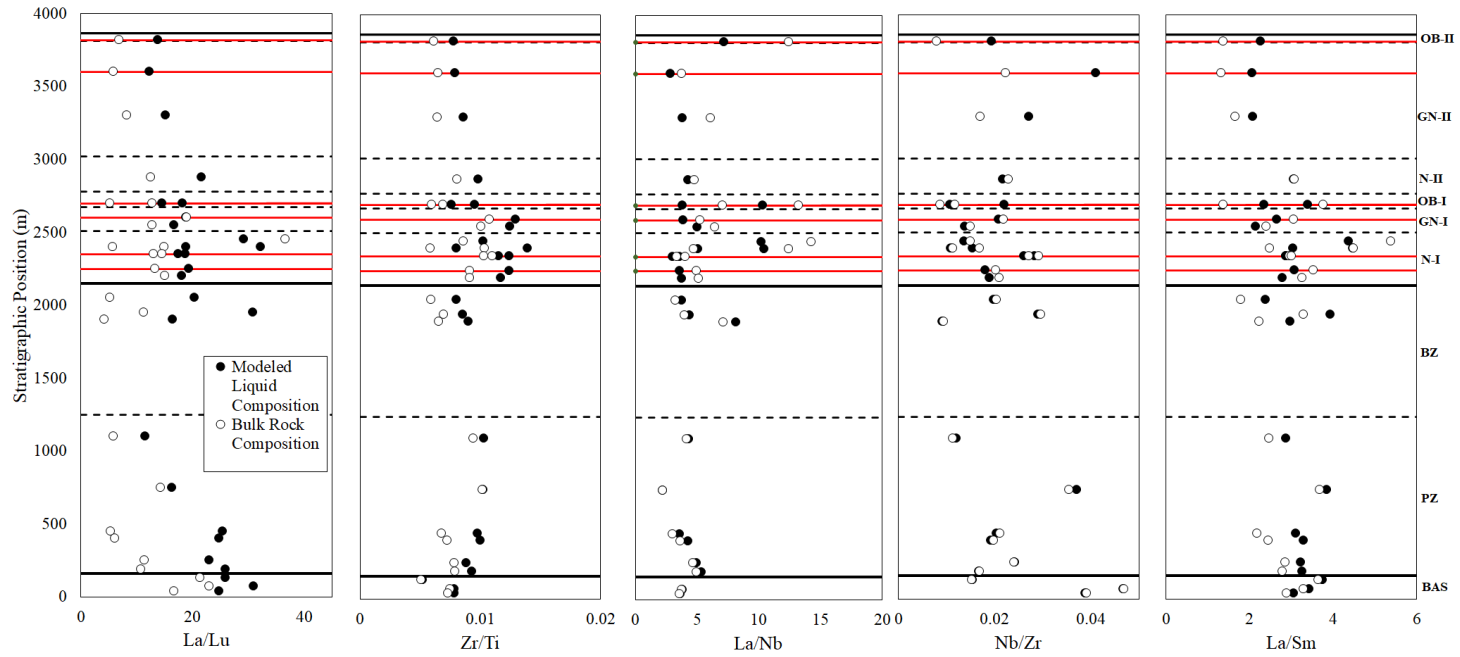


Figure 41: Trace element ratios in the modeled liquid and bulk rock. Red lines in the Lower Banded series indicate the stratigraphic position of samples suggested to reflect evolved liquid addition in Figure 37.

In a large layered intrusion such as the Stillwater Complex, ongoing, conflicting processes such as fractional crystallization of the evolving melt, compaction and resultant late-stage liquid loss from certain rocks, and possible late-stage liquid gain result in complex geochemical evidence left in Stillwater samples. Separating the influence of the processes at play in the system presents many challenges. By synthetically remelting each sample and tracking the full evolution of the liquid, it may be possible to identify certain samples that appear to have been involved in open-system behavior. A comparison of liquid evolution curves to idealized models of open-system behavior in individual samples (Figure 33) and in the melt fractionation trend as a whole (Figure 35) may provide this insight. Sample evolution curves in Ultramafic series samples in black (Figure 37) show evidence of late-stage liquid loss. They fail to evolve to an alkali-rich late liquid, as would be expected if that late liquid had been lost. Three Ultramafic series samples also show a higher maximum Fe enrichment, as would be expected in samples with late-stage liquid loss. This late-stage liquid loss is suggestive of compaction processes occurring in the lower portions of the Stillwater Complex.

A number of Lower Banded series samples (also indicated by black evolution curves) evolve below the parental evolution curves. This behavior bears some similarity to models of late-stage liquid gain in individual samples (Figure 33b) and to the evolution of model samples created from a parental melt to which evolved liquid was progressively added (Figure 34b). If evolved liquid is lost through compaction in the

Ultramafic series, some could be added back into the evolving parental melt. There are a few irregularities in the modeled sample evolution curves that do not correspond to the idealized late liquid gain model, however. Lower Banded series samples for which the sample evolution curve falls below the fractionation curve also fail to intersect the modeled fractionation curve for evolved liquid addition. This may suggest that the modeled 5% evolved liquid addition in 10% crystallization intervals is less evolved liquid than was added into the evolving melt. It may also indicate that current parental melt models for the Stillwater Complex are not a precise match for the actual parental melt.

A further issue with the evolved liquid gain model is the trace element compositions of both the measured bulk rock and modeled liquid. It would be expected that, in the case of evolved liquid gain, incompatible trace element concentrations in samples with evidence of evolved liquid gain (those falling below parental melt fractionation curves) would be elevated. The red lines in Figure 41 indicate the stratigraphic positions of those samples suggested to indicate evolved liquid gain. These samples do not have increased bulk rock incompatible trace element concentrations, nor is there consistent increased deviation between bulk rock and modeled liquid. There are two possibilities to explain the observed trace element trends. First, addition of evolved liquid may not be the process by which sample evolution curves are pulled below the parental magma fractionation trend. Second, Figure 34 shows that deviation from the

fractionation trend in the case of evolved liquid addition is less early in melt fractionation, where more parental liquid is present in the system. It may be the case that samples in the Lower Banded series are too stratigraphically low in the complex for trace element enrichment to be clear in the bulk rock. In this case, the effect of late liquid addition would be more evident in samples collected stratigraphically higher in the complex, from the Middle Banded and Upper Banded series. Further investigation of the effect of late liquid addition on trace element geochemistry is required.

6.7 Conclusions

Using the MELTS program to evolve parent liquid compositions and to synthetically 'remelt' bulk rock samples from layered intrusions can be a powerful tool to understand magmatic processes. Applying these concepts to real samples from the Stillwater intrusion allows for examination of how Stillwater Complex samples evolved and what processes may have affected these rocks. Modeled mineral compositions, when compared to measured mineral compositions from roughly the same stratigraphic position, suggest that Lower Banded series pyroxene were impacted by a trapped liquid shift, which was avoided in the Ultramafic series. This may have been due to the high modal abundance of pyroxene in this series, or in part related to late-stage liquid loss due to compaction impacting some samples. Compaction (and, possibly, resultant migration of late, evolved liquid) clearly impacted the geochemistry of rocks in both the Ultramafic series and Lower Banded series, resulting in modern geochemical trends.

The proposed procedure of synthetic remelting of bulk samples allows for a useful first-order examination of the processes involved in the formation of large layered intrusions. Alternatives to synthetic remelting, primarily laboratory remelting experiments (e.g., McBirney and Naslund, 1990) are substantially more time-consuming and subject to experimental error. While the MELTS model presented here does simplify some of the processes of magmatic evolution, it also provides a useful tool for understanding sample evolution.

7. Using Synthetic Remelting to Identify Evolving Magma Compositions in Layered Intrusions II: Application to the Skaergaard Intrusion, East Greenland

7.1 Introduction

The previous chapter demonstrated the potential of synthetic remelting of layered intrusion samples using the thermodynamic modeling program MELTS to track the evolution of layered intrusions. As previously described, trapped liquids can have a strong effect on mineral compositions and sample evolution. The effect of the trapped liquid shift (Barnes, 1986; Bédard, 1994) on modifying mineral compositions can be strong, particularly in olivine and pyroxene. Analysis of Stillwater Complex samples demonstrated that modeled mineral compositions, when compared to measured mineral compositions, indicated trapped liquid shift in pyroxene, but not in plagioclase. Results at Stillwater were also used to demonstrate large-scale open system processes of compaction resultant migration of late, evolved liquid. However, synthetic remelting of rocks from layered intrusions has broader applications to problems of parental liquid and melt evolution.

The composition of the parent magma and its liquid line of descent is potentially valuable information that can otherwise be difficult to determine. Estimates of parent liquids at layered intrusions can vary widely. Parental magmas are typically identified by analysis of chilled margins (or contemporaneous sills and dykes) formed as the magma intruded (e.g., Hoover, 1989), as chilled margins have been assumed to represent

the earliest intruded liquid. This method relies on the chilled margins being preserved, identifiable, and unaffected by contamination (Harmer and Sharpe, 1985). Alternatively, parental magmas can be modeled using mineral compositions and partition coefficients, although this requires assumptions be made regarding compositional changes on cooling and physical conditions of the liquid at the time of emplacement.

Without strong evidence for the composition of the parent magma (or magmas, if more than one is hypothesized), it can be difficult to establish a clear and agreed-upon 'starting point' from which to model the development of various geochemical and mineralogical features of the complex. Many studies of trace elements rely on comparison between sample data and inferred parental liquid composition, from a parental chilled margin sample or other modeled source. Additionally, without a good understanding of the influence of trapped liquid (or lack thereof due to compaction or other processes), bulk rock or mineral geochemistry may lead to incorrect interpretations of the history of an intrusion.

An example where such modeling can be useful is in the otherwise-well-studied Skaergaard intrusion. The liquid evolution at Skaergaard is heavily debated, with some arguing for a Fenner trend of iron enrichment (McBirney and Naslund, 1990; Tegner, 1997; Thy et al., 2009; Tegner and Cawthorn, 2010) and others promoting a Bowen trend of Si-enrichment after the crystallization of oxides (Hunter and Sparks, 1987; Toplis and Carroll, 1995; Nielsen et al., 2009). Thus, a mechanism of remelting the rock to recover the

evolving liquid could be used to test which parental liquids, and which fractionation trends, are the most viable.

This study tests the hypothesis that one can define the initial liquid and solids by synthetic melting of a rock using the MELTS program. By modeling the mineral phases present and using bulk rock major element data, back-calculate the equilibrium liquid composition, changes in the major composition of the evolving liquid in an intrusion should be evident. This work is presented in two parts; this work applies the modeling to bulk rocks for the Skaergaard intrusion to find the liquid line of descent.

7.2 Application to the Skaergaard Intrusion

The Skaergaard intrusion is a 56.02 Ma old intrusion (Wotzlaw et al., 2012) associated with Paleogene magmatism during the breakup of the North Atlantic and the ancestral Iceland mantle plume (e.g., Brooks, 1973; Nielsen et al., 2019). The geology of the Skaergaard intrusion has been well-described (e.g., Wager and Deer, 1939). It has been interpreted to represent the crystallization of a single large magma chamber inward from the roof (Upper Border Series), walls (Marginal Border Series), and floor (Layered Series) (Figure 42). The Layered Series is divided into three major zones, which are subsequently divided into subzones. The lower portion of the Lower Zone (LZa) consists of plagioclase and olivine. In LZb, clinopyroxene appears on the liquidus,

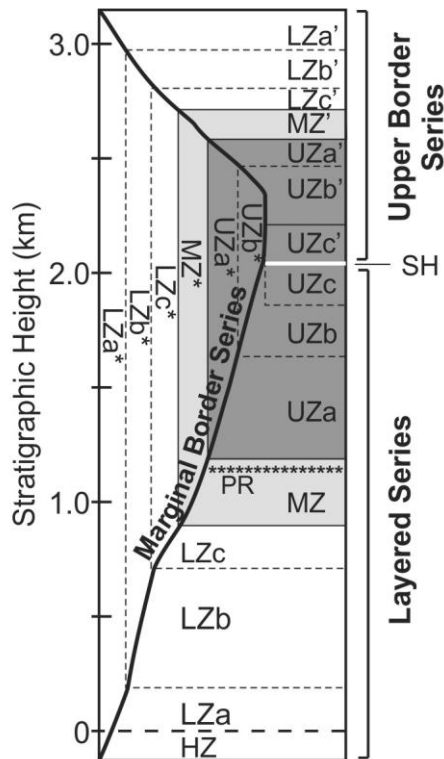


Figure 42: Stratigraphic lithological subdivisions of the Skaergaard intrusion, from Li and Boudreau (2017). HZ – Hidden Zone; LZa, LZb, LZc – subdivisions of the Lower Zone; MZ – Middle Zone; UZa, UZb, UZc – subdivisions of the Upper Zone.; SH – Sandwich Horizon; PR – Platinova Reef. Prime (') and asterisk (*) denote equivalent units in the Upper Border Series and Marginal Border Series.

followed by ilmenite and magnetite in LZc. In the Middle Zone (MZ), olivine is rare but not completely absent (a secret often kept from undergrads) and is largely replaced by pigeonite (low-Ca pyroxene) until olivine returns in the Upper Zone (UZa). This is followed by the appearance of apatite in UZb. Finally, in UZc, the wollastonite group mineral ferrobustamite begins to crystallize. The UBS and LS converge at the Sandwich Horizon. Residual granophyric melts were present in the system and are hosted in intrusive bodies in the lower part of the UBS and the upper portions of the LS,

particularly UZb and UZc (Nielsen et al., 2019). The Tinden Sill is an iron-rich granophyre thought by some to represent the residual liquid of the Skaergaard (e.g., Hunter and Sparks 1987), although others have suggested the Sandwich Horizon may be a better representation of the residual liquid (McBirney and Naslund, 1990).

While the Skaergaard intrusion in East Greenland is generally regarded as being well-understood, uncertainties linger regarding the fractionation trend the liquid experienced as it evolved (the liquid line of descent). As noted above, two major models have been put forward: a trend of iron enrichment (Fenner trend: McBirney and Naslund, 1990; Tegner, 1997; Thy et al., 2009) and a trend of silica enrichment (Bowen trend: Hunter and Sparks, 1987; Toplis and Carroll, 1995; Nielsen et al., 2009). Nielsen et al. (2019) suggested differences in the liquid line of descent depended on the proportion of granophyre included in the bulk parent composition, as well as differences in modeling paradigms and weight given to various series and zones of the intrusion.

7.3 Synthetic Melting Results

7.3.1 Modeling the Skaergaard Liquid Line of Descent

Using the bulk rock compositions reported by Tegner et al. (2009) as well as their estimates of the percent of trapped liquid, the liquid composition was found using the process of synthetic melting discussed above. A small amount of H₂O (0.1 wt.%) was added to the bulk composition to allow for apatite and other hydrous mineral crystallization. Tegner et al. (2009) estimated the trapped liquid amount associated with

each sample based on concentrations of the incompatible elements uranium, rubidium, and phosphorus, and for which the estimated trapped liquid proportion decrease as a noisy but otherwise monotonic trend upsection from ~50% in the LZa to ~1% in UZc. The equilibrium liquid composition for each sample is calculated at the trapped liquid proportion for two oxygen fugacities: $f(\text{O}_2)$ at the quartz-fayalite-magnetite (QFM) buffer (hereafter QFM+0) and two log units below the QFM buffer (hereafter QFM-2). These oxygen fugacities were selected based on previous oxygen fugacity estimates at the Skaergaard Complex. Reducing conditions (1-2 log units below QFM) have been previously suggested for the Skaergaard intrusion; Larsen et al. (1992) identified fluid inclusions trapped at between QFM-1.5 and QFM-2. Frost and Lindsley (1992) modeled a reducing trend, from near QFM+0 prior to oxide crystallization to QFM-2 at the Sandwich Horizon. Thy et al. (2009) contended that such a drop in $f(\text{O}_2)$ produces an incorrect oxide assemblage. They argued for more oxidizing conditions up to QFM+0.5 and proposed that this would result in iron enrichment and a small decline in silica.

Examples of the synthetic melting curves for typical rocks from each zone of the Layered series are shown in Figure 43 for the two different oxygen buffers. UZc is not included in the trapped liquid curve as MELTS does not include ferrobustamite that appears in UZc. A melting curve for a Sandwich Horizon sample (Wager and Brown, 1968) is also included, as no unusual phases are present.

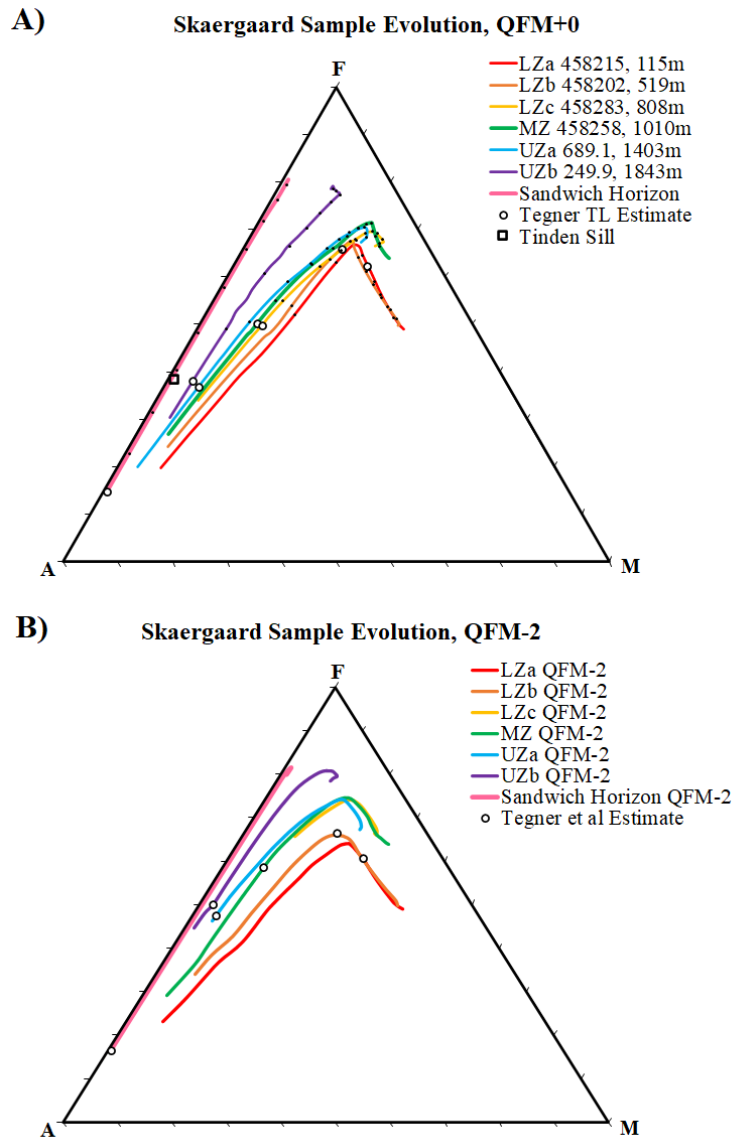


Figure 43: AFM diagram showing example Skaergaard sample synthetic remelting curves. A = Alkalis ($\text{Na}_2\text{O} + \text{K}_2\text{O}$); F = Iron ($\text{FeO} + \text{Fe}_2\text{O}_3$); M = Magnesium (MgO), all wt.%. Liquid compositions at the trapped liquid proportions estimated by Tegner et al. (2009) are shown with an open circle. A) Sample evolution at QFM+0. Liquid proportions in intervals of 10% liquid (90% to 10%) are shown with small black circles. B) Sample evolution at QFM-2.

Changing the oxygen fugacity for the samples has a number of effects on the modal mineralogy of the sample (Table 10). For the set of curves in Figure 43a (QFM+0), all the liquids tend to have a similar maximum Fe-enrichment as the bulk compositions are melted, whereas at QFM-2, the individual melting curves show a more pronounced separation of the curves, the more evolved rocks migrating towards the Fe apex. The more reducing conditions promotes ilmenite crystallization over magnetite crystallization, with magnetite disappearing from the system entirely for most samples below QFM-0.8. Low-Ca clinopyroxene (pigeonite) disappears below QFM-0.8 as well. Conversely, olivine crystallizes in higher proportions in more reducing conditions. Oxidizing conditions (QFM+1, not shown in Table 10) promotes quartz crystallization. Based on the modal mineralogy reported by Tegner et al. (2009), an adjusted $f(\text{O}_2)$ was found for each sample (Table 10), which represents the conditions the produce the nearest-matching mineralogy. This adjusted $f\text{O}_2$ suggests most of the Skaergaard intrusion is best matched to roughly QFM-0.5, while the UZb fits best to QFM-2.

Although the Sandwich Horizon is commonly considered the final crystallized rocks of the intrusion, it does not appear to be a liquid composition, its composition being at neither the end of the Bowen nor the Fenner trends. Furthermore, although enriched, its incompatible element concentrations are only about twice of that of the UZc rocks, which have some of the lowest estimated trapped liquid proportions of the

Table 10: Synthetic Melting of Skaergaard Samples, Modal Mineralogy (wt. %)

Sample	Estimate Source	Temp	fO ₂ (ΔQFM)	OI	Pl	Cpx	Low-Ca Px	Mt	Il	Ap
LZa #458215 115m	MELTS (QFM)	900	0	7.58	54.71	14.41	16.82	5.62	0.00	0.38
	MELTS (QFM-2)	910	-2	17.44	55.17	14.35	10.60	0.00	1.34	0.38
	MELTS (fO ₂ -Adj)	910	-0.5	14.35	55.09	12.33	12.56	1.74	0.92	0.38
	CIPW			15.07	58.96	10.55	10.04	1.96	2.45	0.37
	Tegner et al (2009)			5.6	56.4	10.8	22.9	1.8	2.0	0.4
LZb #458202 519m	MELTS (QFM)	875	0	1.72	48.04	29.64	15.57	2.62	1.53	0.24
	MELTS (QFM-2) ¹	900	-2	7.41	48.48	30.03	10.89	0.00	2.17	0.24
	MELTS (fO ₂ -Adj)	900	-0.6	5.57	47.90	30.43	12.72	0.38	2.02	0.24
	CIPW			5.51	52.99	22.94	12.73	2.13	2.79	0.23
	Tegner et al (2009)			3.6	51.3	28.9	13.4	0.3	2.4	0.2
LZc #458283 808m 808m	MELTS (QFM)	925	0	0.00	38.37	29.78	8.26	8.63	11.65	0.04
	MELTS (QFM-2)	1070	-2	6.19	34.14	31.04	0.00	8.26	8.48	0.00
	MELTS (fO ₂ -Adj)	955	-0.25	0.00	37.86	30.63	7.58	9.40	7.58	0.03
	CIPW			4.87	45.75	21.23	7.49	6.03	13.98	0.09
	Tegner et al (2009)			0.9	43.1	30.0	7.8	4.5	13.6	0.1
MZ #458259 1010m 1010m	MELTS (QFM)	850	0	0.00	34.33	32.22	19.00	7.49	6.48	0.13
	MELTS (QFM-2)	900	-2	15.54	34.97	33.39	7.26	0.00	7.96	0.13
	MELTS (fO ₂ -Adj)	850	-0.6	5.43	34.02	32.66	15.71	5.25	6.27	0.13
	CIPW			7.23	39.75	24.89	14.22	5.05	8.30	0.14
	Tegner et al (2009)			5.8	37.5	31.4	14.1	4.2	6.8	0.1
UZa #689.1 1403m	MELTS (QFM)	800	0	0.38	42.76	27.80	14.12	7.56	7.02	0.11
	MELTS (QFM-2)	975	-2	17.14	40.28	28.87	0.00	0.00	8.29	0.04
	MELTS (fO ₂ -Adj)	825	-0.75	8.18	42.51	28.01	8.97	4.20	8.18	0.11
	CIPW			7.67	46.92	21.50	9.59	4.81	8.53	0.12
	Tegner et al (2009)			6.2	45.5	30.8	5.9	4.0	7.4	0.1
UZb #249.9 1843m	MELTS (QFM)	875	0	0.00	41.68	19.12	8.35	18.80	2.52	3.97
	MELTS (fO ₂ -Adj)	957	-2	24.12	42.35	19.28	0.00	1.63	5.72	4.00
	CIPW			14.66	45.61	15.03	8.14	5.02	6.69	3.96
	Tegner et al (2009)			22.2	43.4	17.9	>.1	7.5	4.9	4.0

Layered Series. The result here suggests that it also formed from a liquid similar to that of the Tinden Sill, but lost all but roughly 2.5% of the liquid.

The estimates of the liquid fraction calculated by Tegner et al. (2009) of each sample are shown by the open circles on each synthetic melting curve in Figure 43. For both oxygen fugacities, the liquids show only a modest Fe-enrichment early and then move distinctly towards Si-enrichment and Fe-depletion in the more evolved liquids. This is more clearly shown in Figure 44, where it is seen that the synthetic melt liquids tend show an almost linear coupled increase in Si and decrease in total Fe, evolving to a rhyolitic composition similar to the Tinden Sill.

As discussed above, the estimates of trapped liquid by Tegner et al. (2009) are likely to be underestimates, as they are based on incompatible elements that only become incorporated into the solid assemblage late. The equilibrium liquid composition for the samples modeled was also examined at a constant 30% trapped liquid proportion, for both QFM+0 and QFM-2 (Figure 45a). At 30% trapped liquid, the equilibrium liquid modeled at QFM+0 still exhibits notable evolution towards Si enrichment and Fe depletion. At QFM-2, the trend is offset to a slightly higher Fe, but still trends to Si-enrichment is a slight trend of iron enrichment. The equilibrium liquid at 30% trapped liquid proportion at QFM-2 is similar in nature to a typical Sandwich Horizon sample (Wager and Brown, 1968). However, at lower trapped liquid

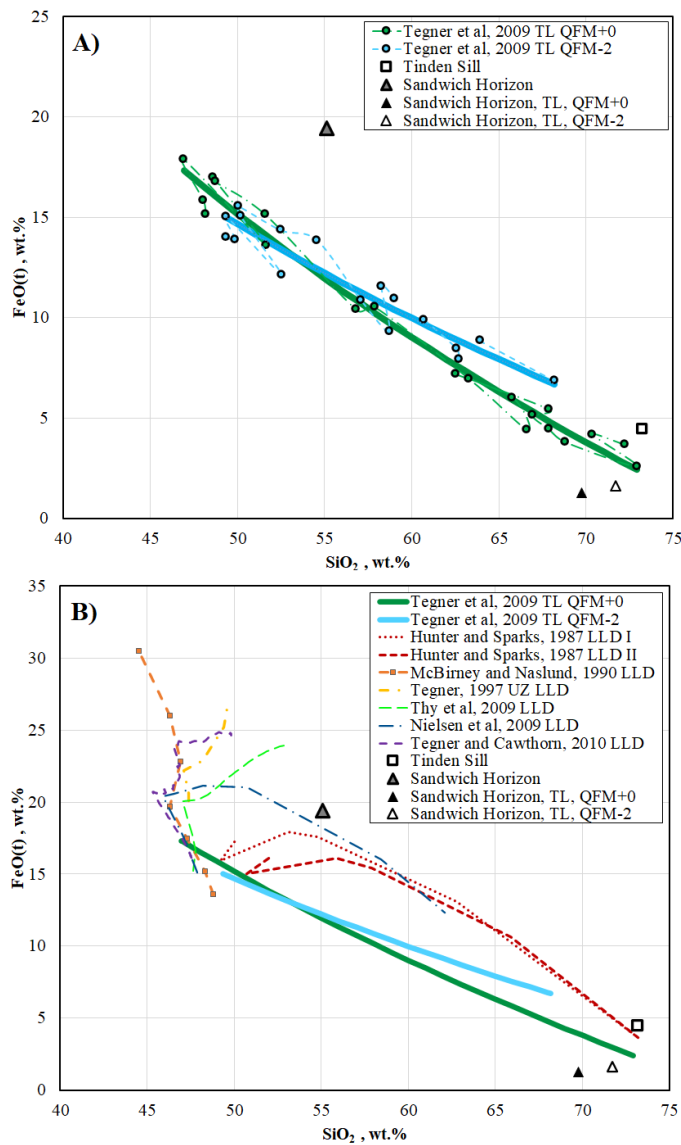


Figure 44: SiO₂/FeO(t) plot of the evolution of the modeled trapped liquid composition based on trapped liquid estimates by Tegner et al. (2009). The bulk composition of the Tinden Sill (Hunter and Sparks, 1987) is represented by the white square. The composition of a Sandwich Horizon sample (Wager and Brown, 1968) is shown by the gray triangle. A) Modeled liquid compositions of samples. Dashed line connects samples in stratigraphic order. Thick lines show fitted liquid evolution trend. B) Modeled liquid evolution trend compared to liquid lines of descent from previous studies.

proportions, the MELTS synthetic melting model still shows these samples evolving toward Si-enrichment and Fe-depletion (Figure 45b).

7.3.2 Fractional Crystallization Models

As an independent check of the synthetic melting models, the results are compared with a MELTS modeled fractional crystallization trend. Figure 46a compares previously modeled liquid lines of descent to our MELTS fractional crystallization model using two parent compositions: Nielsen et al. (2009), whose model showed Si enrichment, and Thy et al. (2009), whose model showed Fe enrichment. Fractional crystallization was modeled using methods described for the Stillwater parent; the parent composition was brought to liquidus temperatures, and crystallized in small steps, with the starting composition replaced at each step with the current liquid composition. Both bulk liquids show an initial but short iron enrichment trends to the point where magnetite appears on the liquidus in the modeled MELTS fractionation. At that point, the MELTS fractional crystallization model for both moves toward a trend of silica enrichment and iron depletion.

Using different oxygen fugacity still results in roughly similar parallel trends in the liquid line of descent (Figure 46b). Decreased fO_2 to QFM-2 buffer results in slightly higher maximum iron enrichment, and modestly higher iron content in the liquid at a given Si concentration. In contrast, at QFM+1, the liquid more quickly becomes silica-enriched, eventually resulting in the crystallization of quartz. All three trends, however,

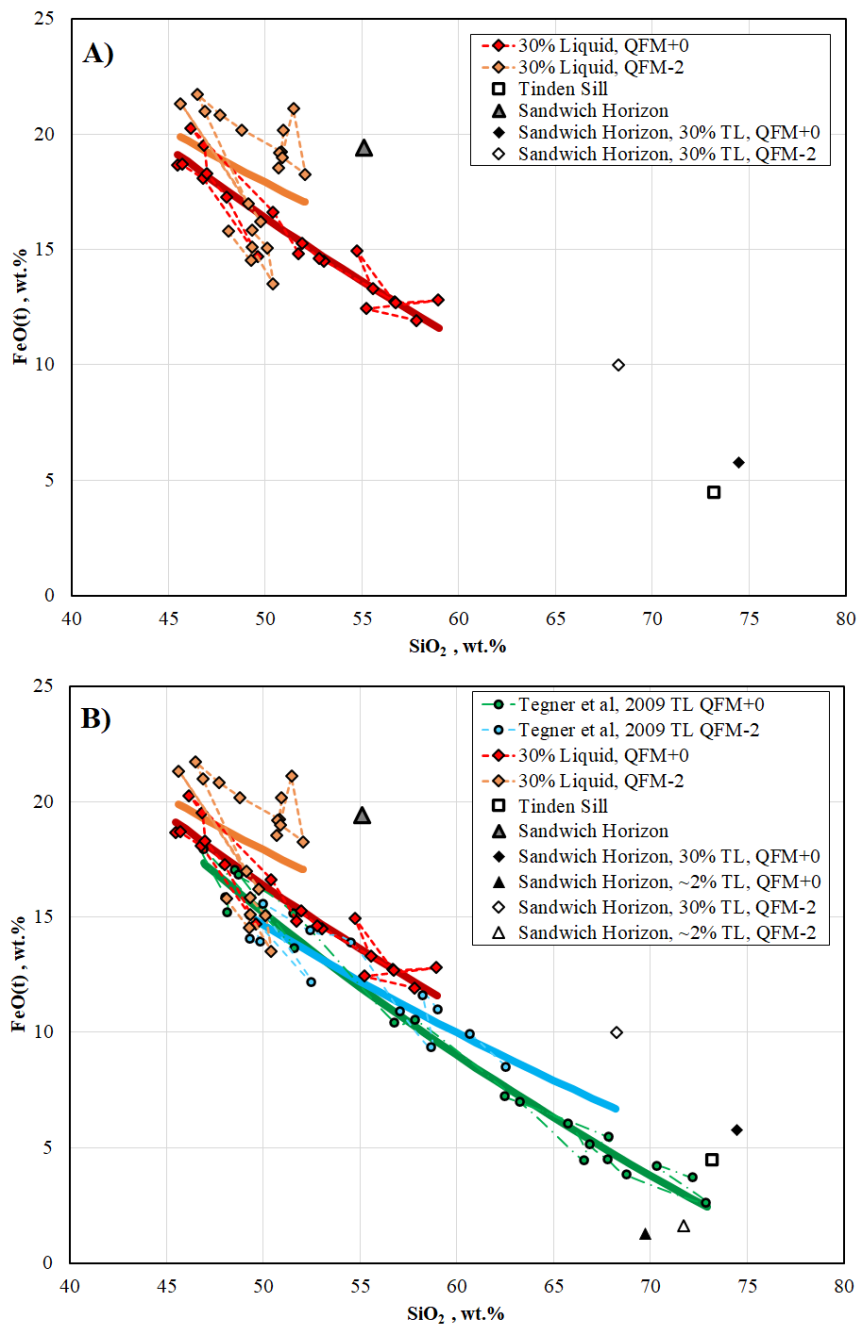


Figure 45: $\text{SiO}_2/\text{FeO}(t)$ plots of modeled trapped liquid evolutions at varying trapped liquid proportions. A) $\text{SiO}_2/\text{FeO}(t)$ plot of the evolution of the modeled trapped liquid composition at 30% trapped liquid at QFM+0 and QFM-2. B) Comparison of 30% trapped liquid to Tegner et al. (2009) trapped liquid estimate.

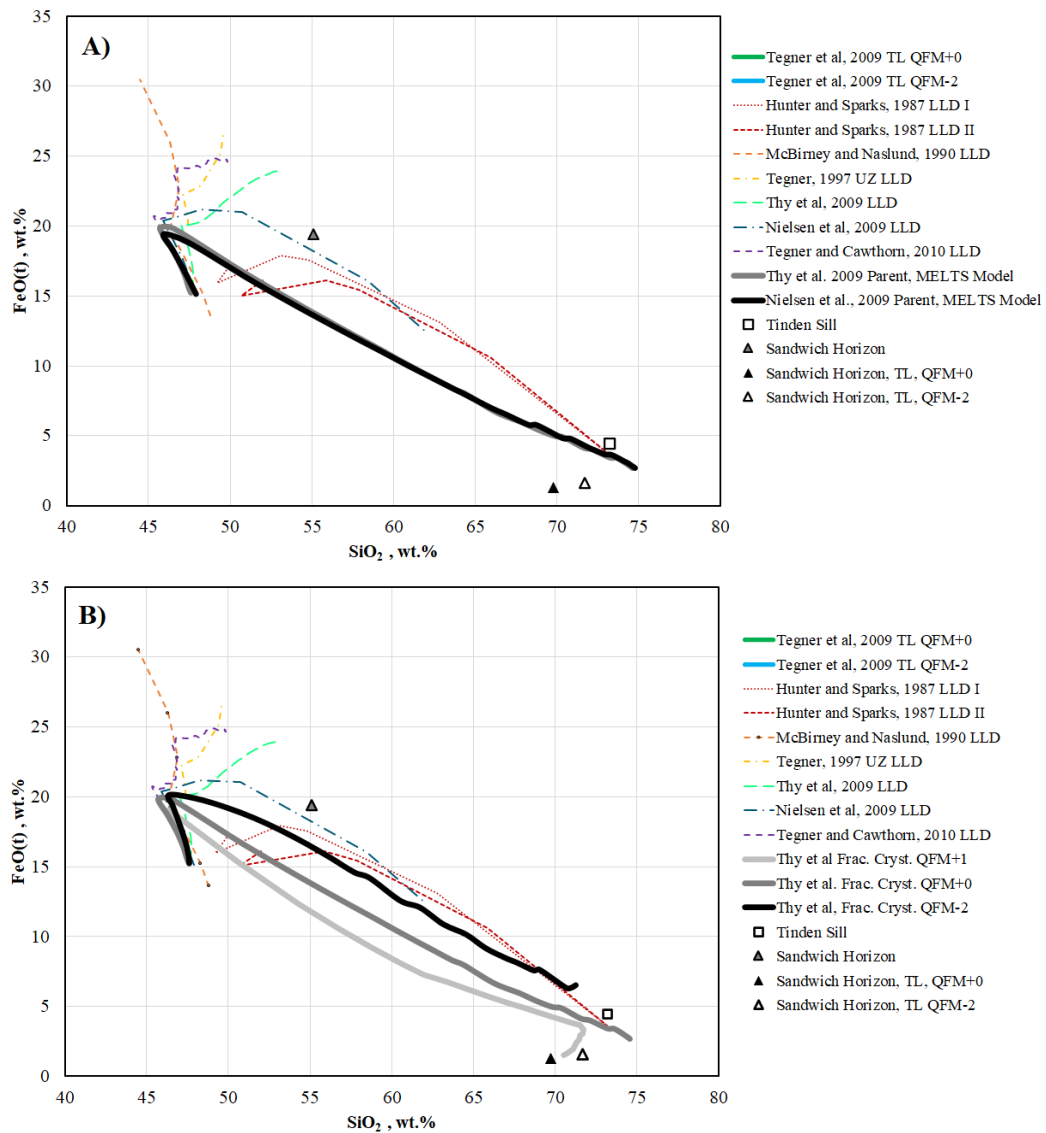


Figure 46: SiO₂/FeO(t) plots showing different parent evolution trends modeled in MELTS. A) Differences in parent evolution for two fractional crystallization trends using bulk compositions of Thy et al. (2009) and Nielsen et al. (2009) who modeled two different LLD trends (Fe-enrichment and Si-enrichment respectively). B) Differences in parent evolution based on oxygen fugacity. The parent evolved at QFM+1 crystallizes quartz, resulting in an Si-depletion near the end of the curve.

ultimately result in iron depletion and silica enrichment in the MELTS fractional crystallization model. Examining these trends on an AMF diagram (Figure 47) shows that parent liquid evolution at QFM-2 is a close match for the liquid evolution model of Nielsen et al. (2009). This result of silica enrichment regardless of oxygen fugacity is at odds with modeling by Thy et al. (2009).

7.3.3 Mineral Compositions and the Trapped Liquid Shift Effect

To estimate the amount of mineral compositional modification by reaction with the interstitial liquid, the modeled mineral compositions at Tegner et al. (2009)'s trapped liquid proportions and at 30% trapped liquid were compared with analyzed mineral compositions from Skaergaard (Thy et al., 2009; Thy, personal communication). The anorthosite component of plagioclase, clinopyroxene Mg#, and the forsterite component of olivine were examined (Figure 48).

For plagioclase, different fO_2 conditions had little impact on plagioclase composition. Because plagioclase cores are the least likely to re-equilibrate on cooling (with the later crystallizing plagioclase components precipitating as albite-enriched rims), they represent a good estimate of the original precipitated plagioclase composition. In this regard, the modeled plagioclase in equilibrium found using the trapped liquid proportions of Tegner et al. (2009) is an excellent match for measured Skaergaard plagioclase. The 30% melting runs produced plagioclase significantly more An-rich than observed, the difference becoming more pronounced with height.

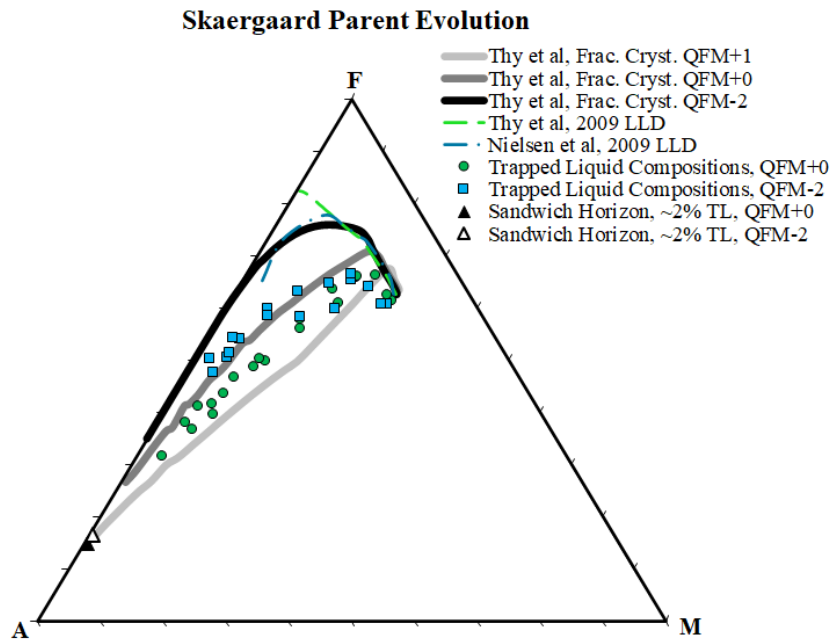


Figure 47: AFM plot showing the LLDs of Nielsen et al (2009) and Thy et al (2009) along with the MELTS modeled parent evolution at three different oxygen fugacities. Also shown are the compositions of the trapped liquid in proportions estimated by Tegner et al. (2009) at QFM+0 and QFM-2.

Unlike plagioclase, olivine and clinopyroxene can readily undergo Fe-Mg re-equilibration as the system cools and crystallizes; at higher trapped liquid proportions, calculated clinopyroxene and olivine compositions will increasingly diverge from measured compositions (e.g., Barnes, 1986). One would expect the calculated compositions of these minerals to be most offset to higher Mg# in the lower parts of the Layered Series where trapped liquid estimates are highest, and indeed that is the case. The offset is most extreme for olivine and markedly less so for clinopyroxene. Furthermore, clinopyroxene and olivine compositions were more strongly affected by changing fO_2 , and its effect on the amount and type of oxides crystallized, than was

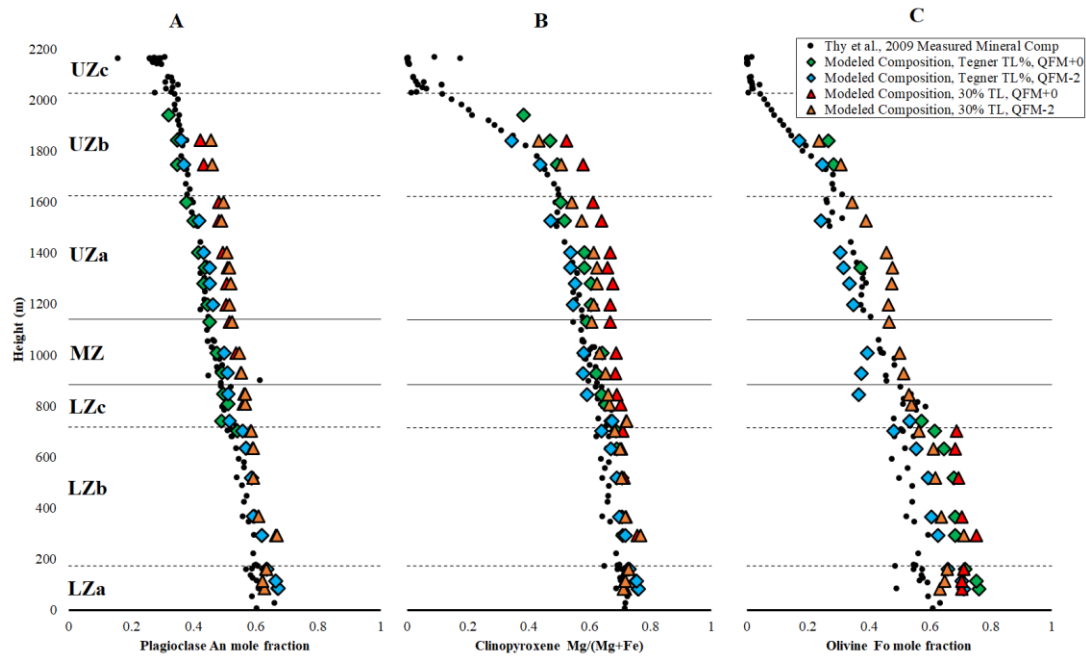


Figure 48: A comparison of modeled and measured mineral compositions for A) plagioclase, B) clinopyroxene, and C) olivine. Measured mineral compositions from Thy et al. (2009) and Thy (private communication).

plagioclase. QFM+0 crystallizes increased proportions of magnetite, whereas ilmenite crystallizes in higher proportions at QFM-2. Magnetite takes up more iron than does ilmenite, which resulting in a more magnesian liquid and thus crystallizing more magnesian olivine and clinopyroxene.

Synthetic remelting of samples in the Middle Zone at QFM+0 crystallized no olivine as should be expected, although a small amount of olivine was able to crystallize in more reducing conditions. Above the Middle Zone, synthetic remelting at QFM+0 crystallized a small amount of olivine at low liquid proportions in only three of nine modeled samples; olivine was produced more abundantly at QFM-2. Above the Middle

Zone, the low estimated liquid fractions lead the calculated Mg# to converge towards the observed mineral trends (particularly for the QFM-2 runs), whereas the modeled 30% trapped liquid runs are consistently higher but only modestly so. A combination of the low trapped liquid proportions and the low liquid concentrations of Mg and Fe (the former approaching zero in UZc) in the upper parts of the intrusion both limit the effectiveness of liquid to modify the mafic minerals during solidification of the Upper Zone. Overall, the combined effect of a decrease in the trapped liquid proportions with height (leading to a smaller shift in the mafic minerals with height) and the fractionation trend in the original mineral compositions results in much less variation in the Mg# in the final assemblage until well into the upper parts of the Layered Series.

7.3.4 Miscellaneous Results

MELTS modeling records the temperature of the liquid at the point where the synthetic melting model produces the trapped liquid proportions, as well as the density of both the liquid and the solid components (Figure 49a). The modeled temperature results at 30% trapped liquid produce a generally smooth curve of slightly decreasing temperature moving up from LZa. In contrast, the modeled temperatures at Tegner et al. (2009) trapped liquid proportions are substantially more variable. This is primarily due to the sensitivity of the model to temperature at low initial trapped liquid proportions noted previously (Figure 32b) and the effect of the uncertain minor H₂O component;

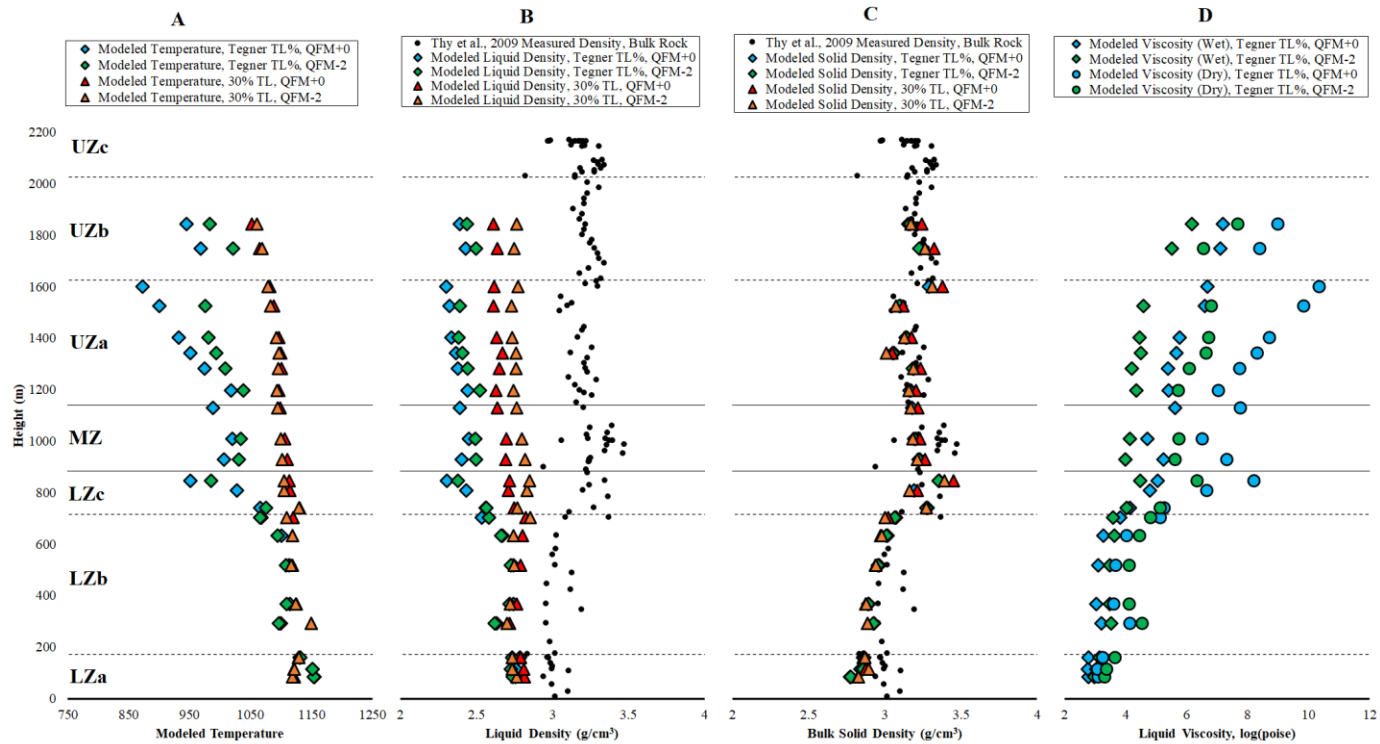


Figure 49: Modeled physical properties of the system, including A) temperature ($^{\circ}\text{C}$), B) Bulk solids density (g/cm^3), C) liquid density (g/cm^3), and D) viscosity (\log_{poise}). Modeled bulk solid and liquids densities are compared with the measured bulk solid density of Thy (unpublished data, private communication), shown as black circles. Viscosity of the equilibrium liquid (modeled in PELE; Boudreau, 1999) is determined for Tegner et al (2009) trapped liquid proportions for both 'wet' and 'dry' melts at QFM+0 and QFM-2.

modest errors in the estimate of trapped liquid proportions leads to sizable temperature errors.

The density of the modeled solid closely approximates the bulk solid density measured from samples (Figure 49b and c). There is some divergence lower in the intrusion. This is likely related to modification of mineral compositions by trapped liquid. Lower in the intrusion, greater proportions of less Fe- and Mg- depleted trapped liquid are more able to modify mafic mineral compositions, increasing the iron component, increasing the density of the bulk solid. In contrast, as the mineral compositions demonstrated, higher in the intrusion, modeled mineral compositions are more similar to measured compositions, and thus the bulk solid density is also a closer match. Conversely, the equilibrium liquid density increasingly diverges from the measured bulk solid density. Finally, the viscosity of the equilibrium liquid (Figure 49d) was also calculated using the program PELE (Boudreau, 1999b) which uses the method of Giordano et al. (2008) to calculate liquid viscosity. As added H₂O reduces liquid viscosity (Baker, 1998), liquid viscosity for each sample was recorded for both the 'wet' (with 0.1 wt. % H₂O) and 'dry' (with H₂O removed) liquids. Melt viscosity was only calculated for the Tegner et al. (2009) trapped liquid proportion. There is a generally smooth increase in liquid viscosity moving upward through the intrusion, from ~3 log_{poise} (wet and dry) in LZa to 6 log_{poise} (wet) and 10 log_{poise} (dry) in UZc. The abrupt

change in viscosity at UZb, particularly in the 'dry' liquid, is due to the onset of apatite crystallization.

7.4 Discussion

A comparison of the liquid line of descent trends produced by both modeled melting of Skaergaard rocks as well as the modeled fractional crystallization of proposed parent magmas both demonstrate that the Skaergaard magma followed a Bowen trend of decreasing Fe and increasing Si as fractional crystallization proceeded. The Tinden Sill is a reasonable approximation of the most evolved liquid produced by differentiation of the Skaergaard parent liquid.

The model of silica enrichment appears to be robust even when using much higher estimates of trapped liquid than suggested by the incompatible element concentrations. However, the melting models that assumed a higher percentage of trapped liquid in the upper part of the intrusion produces a distinctly more anorthitic plagioclase than seen in the cores and suggests that the Tegner et al. (2009) trapped liquid proportions are more realistic. This result suggests an additional benefit of synthetic melting: because core plagioclase are resistant to modification, adjusting the amount of liquid to reproduce the plagioclase core compositions is yet another mechanism that can be used to estimate the initial trapped liquid proportion.

Mineral compositions, combined with the modeled physical traits of the intrusion (density, viscosity) further imply that either that isothermal (adcumulate)

overgrowth and/or compaction became more efficient as crystallization proceeded. The increasing density difference between the calculated liquid and the bulk solid assemblage implies that the lower trapped liquid proportion seen in the upper part of the intrusion is due to increasing effectiveness of compaction. Calculated liquid viscosity for model liquids with different H₂O contents show the effect of reducing conditions in delaying silica enrichment also reduces the viscosity of the liquid (Figure 49d). All modeled conditions produce an increase in liquid viscosity of 3 or more orders of magnitude from LZa to UZb. The net effect of the increasing density difference and expected slower crystallization rates with height on enhancing compaction and the counter effect of increasing viscosity would need to be modeled to test if compaction could be effective in reducing porosity with height. Melt viscosity is a retarding factor for liquid migration (e.g., Baker, 1998 and references therein).

Modeled mineral compositions provide support for previous models of reducing conditions with the onset of oxide crystallization. Higher in the intrusion (roughly the Middle Zone and above), the Tegner et al (2009) trapped liquid proportions are ~5% or lower. At very low trapped liquid proportions, the liquid becomes less effective in further modifying mafic mineral compositions, as it is depleted in Fe and Mg. As such, modeled mineral compositions approach measured mineral compositions. This effect is particularly pronounced at QFM-2, whereas QFM+0 begins to diverge more strongly from measured mineral compositions. As the liquid should become less effective, not

more effective in modifying mineral compositions as it becomes more Fe- and Mg-depleted, this supports previous arguments (Frost and Lindsley, 1992; Larsen et al., 1992) that Skaergaard conditions become more reducing with the onset of oxide crystallization.

7.4.1 Comparison with Other Models

The finding that the Skaergaard magma followed a Bowen fractionation trend is broadly consistent with the studies of Hunter and Sparks (1987), Toplis and Carroll (1995) and Nielsen et al. (2009). The iron enrichment modeled by other workers (McBirney and Naslund, 1990; Tegner, 1997; Thy et al., 2009) is not observed using synthetic remelting of Skaergaard samples.

McBirney and Naslund (1990) developed their liquid line of descent using experimentally melted trapped liquids from Skaergaard samples. Their results are at odds with the experimental results of Toplis and Carroll (1995). McBirney and Naslund (1990)'s results also contradict the synthetically remelted trapped liquid compositions presented here. The experimental remelting experiments (McBirney and Naslund, 1990) were conducted at more reducing conditions than are estimated here. They used ~QFM+1 through the Middle Zone, ~QFM+0 in UZa, and ~QFM-1 in UZb. Differences in oxygen fugacity may have contributed to differences in results between their study and this work.

Thy et al. (2009) used forward modeling of liquidus liquid compositions of a Skaergaard parent sample to determine a liquid line of descent; their model utilized inputs of observed Fe-Ti oxide proportions, rather than experimental proportions (Thy et al. 2006). This modeling produced a Fenner trend in the liquid line of descent. However, MELTS modeling is able to closely reproduce observed oxide modes (Table 10), but still produces a trend of silica enrichment. The forward model (Thy et al., 2006, 2009) assumes simple major element exchange constants to define the evolving mineral and liquid compositions.

Tegner (1997) examined iron contents of plagioclase, and calculated liquid compositions using summation of the bulk cumulate followed by incremental subtraction starting with the youngest rocks. They note that this method of liquid calculation assumes that the summed bulk cumulate is representative of the bulk system. Hunter and Sparks (1987) had previously contested this, arguing that a late, evolved, Si-rich magma had been lost to eruption and erosion. The iron contents of plagioclase cannot be modeled with MELTS synthetic melting, iron is not a major constituent in plagioclase and is therefore not included in MELTS modeling.

7.5 Conclusions

Using the MELTS program to evolve parent liquid compositions and to synthetically 'remelt' bulk rock samples from layered intrusions can be a powerful tool to understand magmatic processes. By applying those concepts to real samples from the

Skaergaard intrusion, it becomes possible to test various models of parental liquid evolution and understand the effect of trapped liquid on modifying the original solid assemblage. MELTS modeling suggests a trend of Si-enrichment, rather than Fe-enrichment, in the Skaergaard parental liquid. This is corroborated by comparison to the modeled liquid compositions at the trapped liquid proportions suggested for the individual samples by their trace element compositions. Differences in the liquid line of descent models at the Skaergaard intrusion are most strongly associated with choice of oxygen fugacity, and whether the system is open or closed to oxygen, rather than differences in initial bulk composition.

The proposed procedure can be easily extended to other parts of the Skaergaard Intrusion. For example, a comparison of calculated liquids from marginal vs. more central sections of the Layered Series should yield similar liquid lines of descent. The same liquid line of descent should occur for a comparison of the Marginal Border Series, Upper Border Series and Layered Series if indeed all formed contemporaneously from similar liquids. In contrast, rocks that may have involved considerable metasomatic gain or loss of components would expect to produce anomalous results.

8. Conclusions

This dissertation uses geochemical analyses and thermodynamic modeling to examine a variety of processes occurring within layered intrusions. The examination of the Bushveld Complex in the second and third chapters demonstrates that fluid contamination is a viable mechanism to explain isotopic irregularities identified throughout the complex, and relaxes constraints on crustal contamination suggested by these isotopic analyses. Further, numerical modeling and examination of field evidence suggests connections between diapir formation in the Bushveld Complex and the diapir model of fluid migration in subduction zones.

The fourth and fifth chapters present new radiogenic and stable isotope analyses respectively to extend this analysis of fluid circulation in layered intrusions to the Stillwater Complex. Fluid circulation is challenging to identify in the Stillwater Complex for two reasons. First, the country rock is isotopically similar to the Stillwater Complex. This may in part be because the country rock, before metamorphism to biotite schist, was volcanoclastic. Second, the previously metamorphosed Stillwater Complex country rock contained significantly less fluid than the previously unmetamorphosed country rock at the Bushveld Complex. As a result, the isotopic impact of the fluids would be expected to be less.

Finally, the sixth and seventh chapters present MELTS modeling results at the Stillwater Complex and Skaergaard intrusion respectively. Modeling of trapped liquid

at the Stillwater Complex is suggestive of open-system behavior, such as loss of late melt due to compaction, operating at various stratigraphic positions. This has implications for interpretation of geochemical data, particularly from late phases. Synthetic remelting of Skaergaard intrusions samples to trapped liquid proportions is suggestive of a liquid line of descent following a so-called Bowen trend, ending in evolution to a Si-rich magma. In both cases, synthetic remelting using the MELTS program provides useful information on a simplified liquid/solid igneous system.

Appendix A: Sample Locations

Sample	Latitude	Longitude	Elevation	Rock Unit
GCP-03				UM
GCP-04				UM
GCP-05				UM
S18-02	45.453008	-110.131887	2849	LB
S18-03	45.453008	-110.131887	2849	LB
S18-04	45.453008	-110.131887	2849	LB
S18-06	45.454668	-110.13612	2916	LB
S18-07	45.456222	-110.137393	2904	LB
S18-08	45.452826	-110.136362	2881	LB
S18-11	45.452226	-110.137281	2854	LB
S18-12	45.451588	-110.137321	2851	LB
S18-13	45.451588	-110.137321	2851	LB
S18-17	45.449897	-110.13706	2866	UM
S18-18A	45.43464	-110.092789	2768	LB
S18-18B	45.43464	-110.092789	2768	LB
S18-20	45.43464	-110.092789	2768	LB
S18-23	45.435063	-110.093956	2775	LB
S18-24	45.435063	-110.093956	2775	LB
S18-25	45.435063	-110.093956	2775	LB
S18-28	45.47043333	-110.1449	2997	LB
S18-30	45.46943333	-110.1456	2963	LB
S18-32	45.46986667	-110.1465667	2980	LB
S18-36	45.379978	-109.89535	1928	BAS
S18-39	45.379987	-109.894703	1938	HNF
S18-41	45.38743	-109.907623	2211	UM
S18-44	45.391099	-109.903499	2123	UM
S18-50	45.391481	-109.902743	2120	UM
S18-52	45.392231	-109.901212	2103	LB
S18-53	45.392298	-109.900733	2092	LB
S18-55	45.392298	-109.900733	2092	LB
S18-57	45.385671	-109.907933	2288	UM
S18-58	45.392298	-109.900733	2092	LB
S18-59	45.385671	-109.907933	2288	UM
S18-60	45.385671	-109.907933	2288	UM
S18-64	45.383256	-109.904621	2267	UM
S18-65	45.38265	-109.904298	2245	UM
S18-66	45.38265	-109.904298	2245	UM
S18-71	45.381984	-109.900796	2178	UM
S18-76	45.381929	-109.899099	2115	UM
S18-77	45.381929	-109.899099	2115	UM
S18-81	45.380486	-109.895796	1987	HNF
S18-82	45.380527	-109.895397	1979	HNF

Appendix B: Geochemical Data, Pegmatoid

Sample	S18-77	S18-65	S18-57	S18-59	GCP-01	GCP-03	GCP-04	GCP-05
Position	190	400	750	750	1100	1100	1100	1100
Unit	UM							
Subzone	PZ							
Type	P	P	P	P	P	P	P	P
SiO₂ (wt.%)	47.60	44.41	52.42	45.21	39.13	39.44	39.83	37.39
TiO₂	0.11	0.13	0.12	0.08	0.07	0.08	0.19	0.14
Al₂O₃	1.52	6.21	4.20	3.35	4.18	7.73	7.52	7.13
Fe₂O₃	13.78	11.48	9.48	11.66	14.17	12.80	10.13	12.32
MnO	0.19	0.16	0.17	0.16	0.16	0.15	0.15	0.16
MgO	33.68	28.24	28.97	34.63	38.38	32.44	22.61	27.34
CaO	1.25	2.75	4.16	3.73	1.96	3.23	4.46	3.35
Na₂O	0.05	0.27	0.31	0.19	0.38	0.72	0.33	0.38
K₂O	0.64	0.37	0.04	0.03	0.16	0.06	0.18	0.03
Li (ppm)	4.873	2.544	2.373	4.496	3.076	1.812	2.061	2.291
Be	0.044	0.046	0.035	0.025	0.079	0.086	0.061	0.055
P	58.18	29.60	79.97	63.34	132.22	181.88	98.02	57.21
Sc	16.457	16.822	24.473	17.589	6.428	5.057	21.605	14.023
V	64.286	58.374	83.946	51.570	16.655	30.345	70.391	57.030
Cr	1670.53	4220.75	3733.31	2043.83	1471.44	4619.54	5020.26	5859.20
Co	105.85	76.98	80.30	108.23	165.10	110.39	49.55	81.94
Ni	965.39	699.21	641.85	975.33	1738.12	1194.07	503.18	999.43
Cu	23.451	16.837	18.478	2.037	16.199	17.677	28.211	25.330
Zn	62.663	62.854	61.520	61.615	22.747	59.361	62.391	0.000
As	1.379	0.189	0.189	0.346	0.348	0.503	0.199	0.214
Se	0.041	0.028	0.030	0.040	0.106	0.078	0.021	0.027
Rb	0.355	0.277	1.419	6.772	1.951	3.368	2.794	1.008
Sr	7.889	18.981	16.428	31.061	29.898	43.254	18.577	23.505
Y	2.164	1.633	3.573	2.589	1.976	1.942	4.502	2.282
Zr	4.560	3.799	8.268	5.627	5.150	12.671	11.128	5.254
Nb	0.093	0.073	0.255	0.149	0.230	0.531	0.269	0.121
Mo	0.037	0.030	0.056	0.032	0.277	0.123	0.182	0.068
Ag	0.013	0.005	0.006	0.004	0.007	0.007	0.007	0.005
Cd	0.117	0.035	0.055	0.047	0.039	0.047	0.057	0.042
Sn	0.238	0.142	0.192	0.232	0.669	0.370	0.193	0.135
Sb	0.000	0.000	0.000	0.000	0.014	0.000	0.000	0.478
Cs	0.032	0.009	0.036	0.490	0.060	0.079	0.109	0.014
Ba	9.081	7.147	10.713	33.921	20.562	24.183	13.846	8.718
La	0.334	0.261	0.614	0.433	0.588	1.044	0.921	0.408
Ce	0.739	0.579	1.365	0.994	1.199	2.147	2.224	0.906
Pr	0.107	0.083	0.193	0.141	0.156	0.278	0.333	0.131
Nd	0.439	0.347	0.855	0.624	0.637	1.061	1.491	0.551
Sm	0.147	0.107	0.281	0.208	0.137	0.257	0.420	0.174
Eu	0.050	0.056	0.102	0.118	0.092	0.139	0.155	0.090

Gd	0.225	0.180	0.410	0.311	0.231	0.326	0.580	0.266
Tb	0.044	0.033	0.079	0.062	0.036	0.054	0.110	0.052
Dy	0.276	0.201	0.531	0.371	0.198	0.276	0.701	0.321
Ho	0.069	0.051	0.126	0.088	0.050	0.062	0.165	0.078
Er	0.198	0.141	0.345	0.241	0.119	0.157	0.458	0.211
Yb	0.271	0.192	0.420	0.279	0.194	0.191	0.495	0.267
Lu	0.047	0.034	0.067	0.047	0.033	0.033	0.079	0.044
Hf	0.097	0.076	0.216	0.137	0.114	0.264	0.272	0.116
Ta	0.037	0.030	0.124	0.069	0.034	0.123	0.225	0.068
Au	0.001	0.001	0.001	0.001	0.001	0.001	0.001	0.001
Tl	0.006	0.001	0.008	0.143	0.034	0.032	0.017	0.051
Pb	3.954	0.190	0.297	1.499	0.501	0.533	0.421	0.343
Th	0.127	0.039	0.130	0.090	0.141	0.374	0.230	0.068
U	0.040	0.006	0.028	0.020	0.043	0.093	0.045	0.062

Sample Position Unit Subzone Type	S18-55	S18-58	S18-20	S18-24	S18-25	S18-02	S18-04	S18-PEG
	2250	2250	2400	2450	2450	2700	2700	2750
	LB	LB	LB	LB	LB	LB	LB	LB
	N-I	N-I	N-I	N-I	N-I	OB-I	OB-I	OB-I
	P	P	P	P	P	P	P	
SiO₂ (wt.%)	52.03	50.26	52.05	46.79	50.67	50.42	47.84	
TiO₂	0.18	0.11	0.16	3.96	0.73	0.16	0.14	
Al₂O₃	8.38	21.39	6.65	14.21	12.56	16.60	28.45	
Fe₂O₃	10.74	5.09	12.89	6.99	8.26	6.97	2.68	
MnO	0.18	0.08	0.21	0.15	0.17	0.12	0.04	
MgO	20.70	9.34	20.69	7.97	10.46	11.86	2.32	
CaO	5.97	10.48	5.70	17.95	15.05	12.29	15.93	
Na₂O	0.58	1.81	0.39	0.64	0.12	1.04	1.77	
K₂O	0.08	0.02	0.25	0.06	0.26	0.52	0.08	
Li (ppm)	1.966	3.739	4.806	2.983	5.255	2.840	4.169	2.661
Be	0.047	0.101	0.069	0.197	0.143	0.104	0.165	0.469
P	64.14	77.03	42.81	186.70	218.82	39.90	98.62	269.14
Sc	28.105	13.236	35.272	46.311	51.397	27.683	10.059	3.536
V	112.268	61.922	145.893	490.505	320.869	81.785	45.495	18.125
Cr	1685.24	654.87	1288.59	395.87	534.61	1368.24	33.87	53.77
Co	84.29	46.28	90.15	40.21	48.98	60.58	37.52	46.93
Ni	740.34	324.89	790.05	182.31	249.93	233.17	71.85	27.50
Cu	176.256	83.998	402.003	79.617	44.960	12.218	29.329	8.732
Zn	59.596	61.101	71.991	39.113	35.614	35.488	15.654	25.176
As	0.250	0.467	0.656	1.278	2.061	0.969	0.351	0.903
Se	0.116	0.057	0.135	0.084	0.026	0.002	0.033	0.080
Rb	2.259	12.351	1.488	0.761	1.275	1.065	2.119	7.850
Sr	34.160	94.783	35.137	49.458	52.722	70.714	126.898	148.245
Y	3.826	2.009	4.024	11.950	11.982	4.527	3.925	6.561
Zr	7.292	4.145	5.097	16.206	12.636	6.197	10.323	7.981
Nb	0.086	0.085	0.070	5.228	0.666	0.074	0.393	0.337

Mo	0.050	0.031	0.042	0.236	0.076	0.042	0.079	0.320
Ag	0.010	0.007	0.029	0.013	0.009	0.006	0.008	0.006
Cd	0.093	0.086	0.140	0.065	0.071	0.073	0.044	0.075
Sn	0.300	0.364	0.297	0.987	0.473	0.243	0.459	0.546
Sb	0.000	0.000	0.028	0.044	0.063	0.040	0.030	0.036
Cs	0.071	0.130	0.122	0.092	0.072	0.048	0.085	0.143
Ba	14.704	58.026	14.063	16.792	27.497	19.332	36.848	69.735
La	0.564	0.642	0.483	0.891	1.163	0.655	1.269	5.505
Ce	1.247	1.227	1.068	2.076	2.412	1.510	2.730	10.755
Pr	0.179	0.156	0.155	0.348	0.387	0.221	0.353	1.289
Nd	0.773	0.642	0.671	1.939	2.107	1.060	1.575	4.781
Sm	0.259	0.167	0.210	0.820	0.886	0.323	0.412	1.021
Eu	0.117	0.207	0.129	0.331	0.309	0.191	0.307	0.707
Gd	0.378	0.245	0.362	1.365	1.418	0.515	0.568	1.154
Tb	0.082	0.044	0.077	0.287	0.300	0.101	0.098	0.186
Dy	0.541	0.254	0.551	1.978	2.084	0.694	0.627	1.072
Ho	0.135	0.064	0.135	0.443	0.465	0.156	0.141	0.234
Er	0.394	0.180	0.415	1.260	1.319	0.438	0.381	0.648
Yb	0.501	0.224	0.527	1.237	1.265	0.480	0.365	0.660
Lu	0.082	0.039	0.091	0.192	0.191	0.079	0.056	0.105
Hf	0.195	0.094	0.144	0.621	0.484	0.194	0.280	0.222
Ta	0.096	0.059	0.019	0.447	0.081	0.057	0.143	0.270
Au	0.001	0.001	0.002	0.002	0.001	0.001	0.001	0.001
Tl	0.168	0.137	0.026	0.024	0.015	0.017	0.025	0.062
Pb	1.157	3.832	1.660	0.758	1.376	0.483	0.664	1.496
Th	0.114	0.056	0.051	0.082	0.109	0.045	0.376	1.637
U	0.019	0.015	0.016	0.053	0.065	0.011	0.087	0.197

Appendix C: Geochemical Data, Host Rock and Hornfels

Sample	18MZ21	18MZ19	18MZ17	18MZ18	S18-81	M17-868	M17-776	M17-501
Position	-800	-600	-400	-200	-20	40	70	100
Unit	CNTY	CNTY	CNTY	CNTY	CNTY	BAS	BAS	BAS
Subzone	HNF	HNF	HNF	HNF	HNF	BAS	BAS	BAS
Type	C	C	C	C	C	H	H	H
SiO₂ (wt.%)	68.27	58.90	66.74	66.75	46.83	49.07	47.63	42.86
TiO₂	0.47	0.72	0.58	0.53	1.05	0.27	0.25	0.19
Al₂O₃	13.78	18.84	12.89	13.96	21.04	6.96	8.12	1.33
Fe₂O₃	6.18	9.11	8.16	11.34	17.47	19.29	14.12	34.93
MnO	0.05	0.11	0.07	0.06	0.17	0.22	0.20	0.25
MgO	3.31	4.08	3.55	3.45	8.13	19.50	18.95	18.54
CaO	1.33	1.03	0.75	0.80	2.84	5.51	5.26	0.48
Na₂O	2.84	2.76	1.30	1.92	1.44	0.23	0.37	0.00
K₂O	1.41	2.98	1.71	2.03	0.21	0.08	0.04	0.00
Li (ppm)	49.732	34.920	42.649	31.801	22.629	5.585	7.791	2.027
Be	1.532	1.257	0.796	0.597	1.784	0.202	0.211	0.074
P	536.302	372.982	366.648	251.766	136.942	147.319	164.072	19.676
Sc	11.622	22.014	14.444	12.120	43.300	26.241	24.074	54.454
V	87.924	149.841	115.292	93.058	281.590	108.846	100.732	406.874
Cr	285.408	299.656	573.746	507.871	714.268	1009.047	1538.126	1896.980
Co	37.224	50.454	48.662	43.408	59.331	125.121	158.804	365.005
Ni	77.259	121.027	171.051	135.979	336.972	582.464	1139.058	4325.258
Cu	52.862	55.073	93.449	62.018	268.862	349.361	768.685	1355.362
Zn	67.136	33.019	94.898	22.146	58.340	78.167	76.359	156.572
As	1.345	7.506	0.974	1.388	93.581	1.107	1.161	1.533
Se	0.181	0.263	0.230	0.171	0.100	0.291	0.589	2.108
Rb	74.294	116.075	76.975	77.413	20.634	5.272	2.480	0.523
Sr	116.107	152.807	74.786	74.560	180.604	107.355	90.832	3.066
Y	9.640	6.444	8.584	3.335	9.029	5.403	4.996	6.777
Zr	27.440	58.756	43.166	36.687	40.022	11.727	11.160	4.950
Nb	5.868	8.319	5.564	4.301	7.847	0.460	0.525	0.055
Mo	0.928	1.393	1.376	0.822	2.749	0.127	0.194	6.596
Ag	0.021	0.024	0.021	0.026	0.024	0.036	0.064	0.086
Cd	0.171	0.105	0.050	0.114	2.254	0.217	0.405	0.386
Sn	1.563	2.730	1.675	1.261	0.346	0.692	0.515	0.703
Sb	0.000	0.000	0.000	0.018	0.043	0.000	0.000	0.000
Cs	3.692	7.626	5.180	4.159	2.404	0.227	0.209	0.061

Ba	339.570	481.636	275.227	238.436	106.365	38.041	26.906	2.900
La	17.356	29.844	16.011	12.566	12.923	1.650	1.975	0.175
Ce	46.301	58.989	31.669	23.990	21.417	3.485	4.169	0.422
Pr	3.712	6.673	3.662	2.753	2.393	0.474	0.543	0.063
Nd	12.651	23.921	12.969	9.835	8.575	2.000	2.296	0.316
Sm	2.304	4.489	2.526	1.915	1.516	0.569	0.598	0.170
Eu	0.555	1.042	0.681	0.597	1.488	0.327	0.266	0.028
Gd	2.185	3.572	2.329	1.695	1.608	0.741	0.725	0.369
Tb	0.306	0.413	0.334	0.205	0.231	0.134	0.133	0.101
Dy	1.694	1.643	1.759	0.834	1.389	0.856	0.804	0.894
Ho	0.361	0.260	0.341	0.133	0.323	0.192	0.178	0.257
Er	1.019	0.617	0.912	0.283	1.023	0.550	0.511	0.909
Yb	1.060	0.588	0.918	0.221	1.379	0.611	0.530	1.394
Lu	0.167	0.093	0.138	0.035	0.250	0.098	0.085	0.243
Hf	0.742	1.682	1.151	0.960	1.166	0.366	0.356	0.213
Ta	0.635	0.822	0.593	0.452	0.821	0.097	0.197	0.036
Au	0.001	0.002	0.001	0.001	0.002	0.001	0.001	0.015
Tl	0.801	1.189	0.893	0.838	0.214	0.079	0.039	0.023
Pb	17.404	20.045	10.733	11.345	4.006	2.139	3.244	1.644
Th	7.712	9.819	7.541	4.797	0.828	0.277	0.478	0.071
U	1.835	2.401	1.851	1.431	0.266	0.086	0.143	0.022

Sample	M17-363	S18-76	S18-71	S18-66	S18-64	S18-60	S18-41	S18-17
Position	130	190	250	400	450	750	1100	1900
Unit	BAS	UM						
Subzone	BAS	PZ	PZ	PZ	PZ	PZ	PZ	BZ
Type	H	H	H	H	H	H	H	H
SiO₂ (wt.%)	45.05	52.42	49.15	54.92	55.45	42.00	44.81	53.49
TiO₂	0.25	0.14	0.13	0.10	0.11	0.09	0.06	0.10
Al₂O₃	8.94	2.77	6.16	4.30	3.43	1.59	2.89	5.11
Fe₂O₃	14.41	11.95	11.89	9.24	9.81	15.34	12.32	9.83
MnO	0.29	0.20	0.18	0.17	0.19	0.19	0.18	0.19
MgO	21.29	30.50	27.00	27.77	28.67	41.15	37.59	25.66
CaO	5.85	2.60	3.97	3.34	3.21	0.90	2.30	4.04
Na₂O	0.19	0.17	0.52	0.30	0.20	0.16	0.19	0.30
K₂O	0.07	0.01	0.45	0.01	0.13	0.02	0.17	0.29
Li (ppm)	26.766	2.187	3.664	2.415	1.611	2.608	2.635	2.739
Be	0.146	0.070	0.093	0.079	0.044	0.020	0.018	0.040

P	169.563	68.679	77.585	40.833	35.332	88.213	47.415	51.090
Sc	33.664	23.178	18.544	23.731	27.262	7.444	14.218	28.888
V	150.212	116.477	83.270	90.506	107.485	27.102	33.563	81.284
Cr	1811.480	3055.665	2200.912	3068.133	3592.408	1932.065	1589.027	3037.929
Co	71.872	116.197	92.662	82.644	86.680	135.953	123.652	87.644
Ni	422.482	786.574	846.601	558.858	516.956	1266.614	1360.883	565.762
Cu	59.379	156.000	53.863	7.437	12.391	14.128	11.219	13.835
Zn	71.737	62.687	61.273	62.816	61.431	60.483	40.056	53.027
As	0.928	0.133	0.379	0.238	0.254	0.532	0.282	0.287
Se	0.209	0.065	0.052	0.043	0.032	0.087	0.074	0.049
Rb	4.363	1.050	0.907	0.540	0.274	0.768	0.153	0.937
Sr	21.513	13.660	49.090	18.408	11.324	8.977	13.228	21.837
Y	6.866	2.608	2.952	2.293	2.392	1.514	1.362	2.634
Zr	7.542	6.772	6.086	4.521	4.551	5.576	3.121	3.852
Nb	0.116	0.114	0.147	0.090	0.097	0.198	0.035	0.037
Mo	0.118	0.056	0.048	0.035	0.032	0.055	0.044	0.040
Ag	0.015	0.011	0.007	0.005	0.005	0.005	0.004	0.005
Cd	0.155	0.060	0.054	0.053	0.048	0.036	0.034	0.078
Sn	0.600	0.242	0.278	0.281	0.272	0.323	0.221	0.253
Sb	0.000	0.000	0.000	0.000	0.000	0.000	0.023	0.024
Cs	0.964	0.043	0.038	0.019	0.014	0.030	0.003	0.070
Ba	18.931	11.655	21.837	11.763	5.991	9.057	2.692	13.874
La	2.803	0.571	0.694	0.332	0.293	0.442	0.148	0.262
Ce	5.319	1.244	1.426	0.712	0.629	0.860	0.339	0.524
Pr	0.671	0.170	0.192	0.099	0.091	0.107	0.048	0.076
Nd	2.866	0.681	0.800	0.419	0.399	0.423	0.216	0.318
Sm	0.768	0.204	0.242	0.136	0.133	0.120	0.060	0.117
Eu	0.357	0.079	0.128	0.061	0.061	0.053	0.041	0.067
Gd	0.987	0.303	0.331	0.225	0.221	0.182	0.115	0.195
Tb	0.177	0.059	0.065	0.044	0.048	0.033	0.022	0.041
Dy	1.111	0.358	0.406	0.289	0.308	0.183	0.131	0.299
Ho	0.252	0.086	0.099	0.073	0.079	0.046	0.039	0.080
Er	0.718	0.249	0.291	0.219	0.228	0.124	0.097	0.237
Yb	0.795	0.310	0.353	0.310	0.314	0.175	0.142	0.350
Lu	0.131	0.053	0.061	0.055	0.054	0.031	0.025	0.063
Hf	0.232	0.166	0.154	0.103	0.105	0.130	0.071	0.101
Ta	0.035	0.104	0.057	0.074	0.079	0.048	0.020	0.049
Au	0.001	0.001	0.001	0.001	0.001	0.001	0.001	0.001
Tl	0.051	0.014	0.010	0.006	0.001	0.007	0.003	0.017
Pb	1.137	0.450	0.496	0.240	0.219	0.246	0.045	0.313

Th	0.188	0.128	0.106	0.060	0.055	0.112	0.015	0.022
U	0.057	0.031	0.024	0.010	0.011	0.026	0.003	0.004

Sample	S18-44	S18-50	S18-52	S18-53	S18-12	S18-13	S18-18A	S18-18B
Position	1950	2050	2200	2250	2350	2350	2400	2400
Unit	UM	UM	LB	LB	LB	LB	LB	LB
Subzone	BZ	BZ	N-I	N-I	N-I	N-I	N-I	N-I
Type	H	H	H	H	H	H	H	H
SiO₂ (wt.%)	55.04	55.13	48.65	49.49	49.92	49.26	49.52	51.79
TiO₂	0.24	0.20	0.07	0.07	0.14	0.12	0.13	0.14
Al₂O₃	3.47	2.78	23.98	22.56	19.71	20.07	16.83	8.31
Fe₂O₃	10.76	10.90	3.57	4.37	5.59	5.14	8.78	12.44
MnO	0.20	0.20	0.05	0.08	0.11	0.10	0.16	0.21
MgO	27.22	28.08	8.50	10.04	11.29	10.54	12.75	19.86
CaO	2.81	2.83	11.96	11.70	11.55	11.94	8.91	5.67
Na₂O	0.41	0.26	1.54	1.24	0.98	0.99	1.01	0.48
K₂O	0.23	0.01	0.02	0.15	0.35	0.03	0.17	0.29
Li (ppm)	8.686	2.389	8.737	2.266	3.654	4.957	5.789	5.017
Be	0.126	0.075	0.025	0.042	0.106	0.096	0.132	0.086
P	82.988	55.101	48.830	42.429	114.121	105.873	57.087	44.679
Sc	30.225	28.786	11.230	12.514	17.712	18.421	19.114	29.935
V	95.946	113.525	46.210	52.416	60.487	60.344	75.926	99.316
Cr	2982.580	2891.745	854.970	1067.278	1137.371	1147.733	674.036	1146.862
Co	88.227	80.967	39.566	41.699	44.490	40.187	57.167	100.044
Ni	558.268	542.506	181.555	214.599	251.468	220.343	361.373	976.478
Cu	21.973	22.622	12.125	13.914	17.979	23.012	119.177	426.707
Zn	53.117	59.242	62.622	61.884	31.056	26.938	52.824	68.069
As	0.206	0.229	0.399	0.268	1.112	0.941	1.038	0.491
Se	0.050	0.058	0.022	0.035	0.019	0.011	0.083	0.190
Rb	5.373	1.739	7.214	2.377	2.584	2.687	2.965	1.670
Sr	14.993	10.891	107.656	93.874	78.406	75.808	91.088	39.543
Y	5.210	4.139	1.540	1.456	3.500	3.593	2.960	3.495
Zr	10.054	7.044	3.753	3.567	8.526	8.046	4.581	8.994
Nb	0.299	0.145	0.079	0.072	0.250	0.219	0.077	0.103
Mo	0.103	0.049	0.035	0.034	0.053	0.057	0.037	0.041
Ag	0.006	0.005	0.004	0.005	0.012	0.007	0.028	0.038
Cd	0.067	0.060	0.033	0.042	0.057	0.086	0.116	0.138
Sn	0.247	0.178	0.257	0.189	0.301	0.343	0.241	0.299

Sb	0.029	0.000	0.000	0.000	0.050	0.057	0.027	0.029
Cs	0.179	0.061	0.321	0.057	0.154	0.193	0.199	0.134
Ba	28.304	8.105	31.240	14.675	24.422	31.389	33.579	14.403
La	1.204	0.474	0.406	0.360	0.841	0.889	0.966	0.489
Ce	2.494	1.110	0.822	0.726	1.804	1.856	1.829	1.043
Pr	0.310	0.163	0.109	0.097	0.242	0.251	0.226	0.147
Nd	1.280	0.762	0.442	0.377	0.999	1.101	0.854	0.631
Sm	0.365	0.263	0.124	0.102	0.284	0.296	0.215	0.197
Eu	0.134	0.097	0.142	0.127	0.163	0.181	0.262	0.129
Gd	0.537	0.428	0.186	0.177	0.402	0.425	0.292	0.308
Tb	0.106	0.086	0.035	0.032	0.074	0.080	0.053	0.067
Dy	0.758	0.597	0.191	0.180	0.490	0.514	0.380	0.460
Ho	0.182	0.145	0.047	0.043	0.119	0.122	0.097	0.117
Er	0.541	0.446	0.121	0.118	0.326	0.330	0.292	0.371
Yb	0.637	0.514	0.163	0.168	0.386	0.371	0.369	0.470
Lu	0.106	0.090	0.027	0.027	0.064	0.061	0.065	0.086
Hf	0.323	0.191	0.074	0.068	0.237	0.222	0.123	0.269
Ta	0.162	0.051	0.100	0.115	0.049	0.071	0.064	0.108
Au	0.001	0.001	0.001	0.001	0.001	0.001	0.001	0.003
Tl	0.068	0.019	0.023	0.005	0.039	0.036	0.040	0.026
Pb	0.660	0.317	0.292	0.217	1.046	0.794	2.574	2.058
Th	0.519	0.197	0.043	0.042	0.174	0.170	0.073	0.092
U	0.138	0.020	0.008	0.007	0.033	0.034	0.019	0.048

Sample Position	S18-23	S18-11	S18-08	S18-03	S18-06	S18-ANC	S18-07	S18-30
Unit	2450	2550	2600	2700	2700	2750	2875	3300
Subzone	LB	LB	LB	LB	LB	LB	LB	LB
Type	N-I	GN-I	GN-I	OB-I	OB-I	OB-I	N-II	GN-II
Type	H	H	H	H	H	H	H	H
SiO₂ (wt.%)	48.02	48.52	48.20	50.27	48.44		50.87	50.99
TiO₂	0.07	0.09	0.09	0.08	0.12		0.15	0.13
Al₂O₃	28.47	22.61	26.42	16.07	21.55		17.17	17.90
Fe₂O₃	2.89	4.27	3.14	5.32	6.94		7.23	5.53
MnO	0.04	0.07	0.06	0.09	0.11		0.13	0.11
MgO	3.52	8.11	5.02	12.76	8.40		13.25	10.31
CaO	14.19	13.38	14.63	14.24	12.55		9.95	13.97
Na₂O	1.80	1.11	1.34	0.73	1.29		1.09	1.38
K₂O	0.11	0.08	0.36	0.33	0.02		0.18	0.05
Li (ppm)	2.176	4.938	6.286	1.789	4.639	5.578	3.183	2.033

Be	0.156	0.050	0.046	0.006	0.101	0.129	0.089	0.079
P	64.854	62.248	66.120	17.053	58.272	193.112	84.005	37.768
Sc	5.522	16.157	11.607	29.331	14.836	0.653	20.578	31.497
V	29.641	49.442	40.644	56.463	58.373	6.168	65.206	86.949
Cr	127.725	964.454	580.538	1783.311	53.531	4.126	764.096	385.128
Co	34.143	38.616	28.720	38.648	47.829	69.982	58.041	54.399
Ni	115.859	201.375	100.065	249.480	161.720	10.722	281.690	239.964
Cu	30.168	34.818	19.141	3.205	12.947	6.019	29.734	107.532
Zn	18.992	23.701	16.252	18.272	34.494	9.588	39.015	33.938
As	0.249	0.583	0.220	0.144	3.509	0.319	0.454	0.316
Se	0.015	0.038	0.029	0.002	0.060	0.093	0.035	0.069
Rb	8.400	2.538	11.707	0.462	1.646	3.107	1.137	0.623
Sr	142.542	87.547	129.268	53.699	88.042	155.327	76.355	96.303
Y	1.772	2.612	2.227	2.523	2.540	0.712	3.356	4.059
Zr	3.733	5.465	5.510	3.479	4.156	2.426	7.440	5.136
Nb	0.056	0.082	0.121	0.030	0.049	0.063	0.171	0.088
Mo	0.191	0.038	0.044	0.027	0.043	0.181	0.047	0.047
Ag	0.006	0.009	0.006	0.005	0.005	0.005	0.007	0.010
Cd	0.058	0.054	0.034	0.043	0.038	0.040	0.051	0.069
Sn	0.626	0.326	0.393	0.314	0.321	0.359	0.326	0.287
Sb	0.017	0.030	0.032	0.026	0.035	0.060	0.025	0.030
Cs	0.401	0.147	0.978	0.018	0.121	0.147	0.043	0.017
Ba	59.517	23.910	36.676	9.280	23.414	39.816	21.383	20.049
La	0.805	0.527	0.633	0.214	0.650	0.904	0.823	0.538
Ce	1.526	1.166	1.320	0.535	1.227	1.679	1.756	1.160
Pr	0.186	0.159	0.167	0.084	0.162	0.192	0.229	0.182
Nd	0.761	0.697	0.749	0.426	0.659	0.744	0.975	0.910
Sm	0.150	0.219	0.207	0.155	0.173	0.138	0.267	0.323
Eu	0.287	0.146	0.161	0.084	0.205	0.265	0.192	0.214
Gd	0.236	0.302	0.302	0.250	0.244	0.173	0.363	0.464
Tb	0.036	0.059	0.051	0.053	0.050	0.020	0.071	0.094
Dy	0.180	0.363	0.313	0.342	0.316	0.054	0.457	0.617
Ho	0.044	0.085	0.078	0.090	0.081	0.017	0.114	0.145
Er	0.102	0.236	0.195	0.229	0.229	0.021	0.334	0.404
Yb	0.146	0.260	0.204	0.254	0.306	0.030	0.389	0.400
Lu	0.022	0.041	0.033	0.041	0.051	0.004	0.066	0.065
Hf	0.083	0.146	0.145	0.097	0.110	0.025	0.205	0.154
Ta	0.058	0.141	0.056	0.018	0.071	0.176	0.104	0.061
Au	0.001	0.001	0.001	0.001	0.001	0.001	0.001	0.001
Tl	0.087	0.034	0.059	0.012	0.025	0.015	0.019	0.009

Pb	0.682	0.502	0.332	0.134	0.305	0.568	0.342	0.281
Th	0.033	0.072	0.095	0.017	0.037	0.055	0.125	0.040
U	0.005	0.015	0.022	0.004	0.009	0.010	0.031	0.012

Sample	S18-32	S18-28
Position	3600	3820
Unit	LB	LB
Subzone	GN-II	OB-II
Type	H	H
SiO₂ (wt.%)	50.89	51.42
TiO₂	0.16	0.17
Al₂O₃	13.85	17.59
Fe₂O₃	6.56	5.15
MnO	0.13	0.11
MgO	12.43	9.62
CaO	14.44	16.88
Na₂O	1.03	1.30
K₂O	0.32	0.18
Li (ppm)	2.776	2.980
Be	0.076	0.082
P	69.807	40.173
Sc	42.828	38.015
V	147.149	103.765
Cr	577.475	621.763
Co	66.873	48.354
Ni	347.100	245.157
Cu	207.428	105.674
Zn	30.862	24.348
As	0.160	0.267
Se	0.091	0.037
Rb	0.435	0.537
Sr	70.800	86.989
Y	5.441	5.770
Zr	6.351	6.190
Nb	0.143	0.050
Mo	0.050	0.040
Ag	0.014	0.009
Cd	0.085	0.081
Sn	0.287	0.234

Sb	0.027	0.025
Cs	0.018	0.029
Ba	12.585	17.862
La	0.540	0.620
Ce	1.321	1.543
Pr	0.215	0.249
Nd	1.133	1.267
Sm	0.407	0.448
Eu	0.218	0.262
Gd	0.628	0.690
Tb	0.126	0.135
Dy	0.845	0.907
Ho	0.188	0.205
Er	0.541	0.599
Yb	0.548	0.589
Lu	0.091	0.090
Hf	0.201	0.194
Ta	0.089	0.070
Au	0.001	0.001
Tl	0.014	0.008
Pb	0.359	0.284
Th	0.077	0.026
U	0.020	0.008

Appendix D: Replicate H Isotope Analyses

Sample	Phase	δD (‰)	H ₂ O (wt%)
18MZ18	whole rock	-50	2.0
		-49	2.0
18MZ21	whole rock	-46	2.2
		-46	2.3
S18-81	whole rock	-48	6.5
Biotite-1	biotite	-70	4.3
		-69	4.3
		-69	4.3
Biotite-2	biotite	-63	3.9
		-64	3.9
		-65	3.9
Biotite-3	biotite	-49	3.0
		-48	3.0
		-48	3.0
Biotite-4	biotite	-79	3.9
		-80	3.9
		-81	3.9
S11-036A	biotite	-63	3.3
		-64	3.3
		-64	3.3
Biotite-2	pyroxene	-101	0.6
		-104	0.7
Biotite-3	pyroxene	-89	0.5
		-92	0.5
Biotite-1	pyroxene	-82	0.5
		-83	0.5
		-82	0.5
Biotite-4	pyroxene	-79	0.3
		-77	0.3
		-76	0.3
S11-036A	pyroxene	-79	0.4
		-82	0.4
		-79	0.4
GCP-03	pyroxene	-85	0.4
		-85	0.5
		-84	0.5

GCP-05	pyroxene	-71	0.3
		-74	0.4
		-68	0.5
S18-02	pyroxene	-67	1.0
		-69	1.0
		-66	1.0
S18-03	pyroxene	-76	0.6
		-74	0.6
		-79	0.7
S18-20	pyroxene	-69	1.2
		-67	1.2
		-68	1.2
S18-25	pyroxene	-59	2.5
		-60	2.5
		-59	2.5
S18-53	pyroxene	-74	1.1
		-73	1.1
		-68	1.1
S18-58	pyroxene	-66	1.4
		-65	1.4
		-65	1.4
S18-59	pyroxene	-79	1.5
		-81	1.5
		-81	1.6
S18-65	pyroxene	-88	0.3
		-86	0.3
		-88	0.3
S18-66	pyroxene	-66	0.4
		-69	0.4
		-69	0.4

References

- Aird, H.M., Ferguson, K.M., Lehrer, M.L., and Boudreau, A.E., 2017, A study of the trace sulfide mineral assemblages in the Stillwater Complex, Montana, USA: *Mineralium Deposita*, v. 52, p. 361–382, doi:10.1007/s00126-016-0664-x.
- Anderson, D.L., 2006, Speculations on the nature and cause of mantle heterogeneity: *Tectonophysics*, v. 416, p. 7–22, doi:10.1016/j.tecto.2005.07.011.
- Asimow, P.D., and Ghiorso, M.S., 1998, Algorithmic modifications extending MELTS to calculate subsolidus phase relations: *American Mineralogist*, v. 83, p. 1127–1132, doi:10.2138/am-1998-9-1022.
- Ayers, J., 1998, Trace element modeling of aqueous fluid-peridotite interaction in the mantle wedge of subduction zones: *Contributions to Mineralogy and Petrology*, v. 132, p. 390–404.
- Baker, D.R., 1998, Granitic melt viscosity and dike formation: *Journal of Structural Geology*, v. 20, p. 1395–1404, doi:10.1016/S0191-8141(98)00057-1.
- Barnes, S.J., 1989, Are Bushveld U-type parent magmas boninites or contaminated komatiites? *Contributions to Mineralogy and Petrology*, v. 101, p. 447–457, doi:10.1007/BF00372218.
- Barnes, S.J., 1986, The effect of trapped liquid crystallization on cumulus mineral compositions in layered intrusions: *Contributions to Mineralogy and Petrology*, v. 93, p. 524–531, doi:10.1007/BF00371722.
- Barnes, S.-J., and Maier, W.D., 2002, Platinum-Group Element Distributions in the Rustenburg Layered Suite of the Bushveld Complex, South Africa, *in* Cabri, L.J. ed., *The Geology, Geochemistry, Mineralogy, and Mineral Beneficiation of Platinum-Group Elements*, Canadian Institute of Mining, Metallurgy, and Petroleum, v. 54, p. 431–458.
- Barnes, S.J., and Naldrett, A.J., 1986, Geochemistry of the J-M Reef of the Stillwater Complex, Minneapolis Adit Area II. Silicate Mineral Chemistry and Petrogenesis: *Journal of Petrology*, v. 27, p. 791–825, doi:10.1093/petrology/27.4.791.
- Barnes, S.-J., Pagé, P., and Zientek, M., 2020, The Lower Banded series of the Stillwater Complex, Montana: whole-rock lithophile, chalcophile, and platinum-group

- element distributions: *Mineralium Deposita*, v. 55, p. 163–186, doi:10.1007/s00126-019-00887-3.
- Barry, T.L., Pearce, J.A., Leat, P.T., Millar, I.L., and le Roex, A.P., 2006, Hf isotope evidence for selective mobility of high-field-strength elements in a subduction setting: South Sandwich Islands: *Earth and Planetary Science Letters*, v. 252, p. 223–244, doi:10.1016/j.epsl.2006.09.034.
- Barton, E.S., and Hallbauer, D.K., 1996, Trace-element and U/Pb isotope compositions of pyrite types in the Proterozoic Black Reef, Transvaal Sequence, South Africa: Implications on genesis and age: *Chemical Geology*, v. 133, p. 173–199, doi:10.1016/S0009-2541(96)00075-7.
- Bédard, J.H., 1994, A procedure for calculating the equilibrium distribution of trace elements among minerals of cumulate rocks, and the concentration of trace elements in the coexisting liquids: *Chemical Geology*, v. 118, p. 143–153.
- Bell, D.R., and Rossman, G.R., 1992, Water in Earth's Mantle: The Role of Nominally Anhydrous Minerals: *Science*, v. 255, p. 1391–1397, doi:10.1126/science.255.5050.1391.
- Ben Othman, D., White, W.M., and Patchett, J., 1989, The geochemistry of marine sediments, island arc magma genesis, and crust-mantle recycling: *Earth and Planetary Science Letters*, v. 94, p. 1–21, doi:10.1016/0012-821X(89)90079-4.
- Benson, E., Connolly, J.A.D., and Boudreau, A.E., 2020a, Crustal fluid contamination in the Bushveld Complex, South Africa: An analogue for subduction zone fluid migration: *International Geology Review*, p. 1–25, doi:10.1080/00206814.2020.1795734.
- Benson, E.K., Ripley, E.M., Li, C., Underwood, B.W., and Mahin, R., 2020b, Multiple S Isotopes and S Isotope Heterogeneity at the East Eagle Ni-Cu-Platinum Group Element Deposit, Northern Michigan: *Economic Geology*, v. 115, p. 527–541, doi:10.5382/econgeo.4707.
- Bindeman, I., 2008, Oxygen Isotopes in Mantle and Crustal Magmas as Revealed by Single Crystal Analysis: *Reviews in Mineralogy and Geochemistry*, v. 69, p. 445–478, doi:10.2138/rmg.2008.69.12.
- Boorman, S.L., McGuire, J.B., Boudreau, A.E., and Kruger, J.F., 2003, Fluid overpressure in layered intrusions: formation of a breccia pipe in the Eastern Bushveld

- Complex, Republic of South Africa: *Mineralium Deposita*, v. 38, p. 356–369, doi:10.1007/s00126-002-0312-5.
- Boudreau, A., 1999a, Fluid Fluxing of Cumulates: the J-M Reef and Associated Rocks of the Stillwater Complex, Montana: *Journal of Petrology*, v. 40, p. 755–772.
- Boudreau, A., 2019, *Hydromagmatic Processes and Platinum-Group Element Deposits in Layered Intrusions*: Cambridge University Press.
- Boudreau, A., 1988, Investigations of the Stillwater Complex: IV. The Role of Volatiles in the Petrogenesis of the J-M Reef, Minneapolis Adit Section: *Canadian Mineralogist*, v. 26, p. 193–208.
- Boudreau, A.E., 1999b, PELE—a version of the MELTS software program for the PC platform: *Computers & Geosciences*, v. 25, p. 201–203, doi:10.1016/S0098-3004(98)00117-4.
- Boudreau, A.E., 2016, The Stillwater Complex, Montana – Overview and the significance of volatiles: *Mineralogical Magazine*, v. 80, p. 585–637, doi:10.1180/minmag.2016.080.063.
- Boudreau, A.E., and McCallum, I.S., 1986, Investigations of the Stillwater Complex; III, The Picket Pin Pt/Pd deposit: *Economic Geology*, v. 81, p. 1953–1975, doi:10.2113/gsecongeo.81.8.1953.
- Boudreau, A.E., and McCallum, I.S., 1989, Investigations of the Stillwater Complex: Part V. Apatites as indicators of evolving fluid composition: *Contributions to Mineralogy and Petrology*, v. 102, p. 138–153, doi:10.1007/BF00375336.
- Boudreau, A., and Philpotts, A.R., 2002, Quantitative modeling of compaction in the Holyoke flood basalt flow, Hartford Basin, Connecticut: *Contributions to Mineralogy and Petrology*, v. 144, p. 176–184, doi:10.1007/s00410-002-0391-4.
- Boudreau, A.E., Stewart, M.A., and Spivack, A.J., 1997, Stable Cl isotopes and origin of high-Cl magmas of the Stillwater Complex, Montana: *Geology*, v. 25, p. 791, doi:10.1130/0091-7613(1997)025<0791:SCIAOO>2.3.CO;2.
- Bouvier, A.-S., Métrich, N., and Deloule, E., 2008, Slab-Derived Fluids in the Magma Sources of St. Vincent (Lesser Antilles Arc): Volatile and Light Element Imprints: *Journal of Petrology*, v. 49, p. 1427–1448, doi:10.1093/petrology/egn031.

- Braun, K., Meurer, W., Boudreau, A.E., and McCallum, I.S., 1994, Compositions of pegmatoids beneath the J-M Reef of the Stillwater Complex, Montana, U.S.A.: *Chemical Geology*, v. 113, p. 245–257, doi:10.1016/0009-2541(94)90069-8.
- Brewer, T.S., and Menuge, J.F., 1998, Metamorphic overprinting of Sm¹⁴⁷Nd isotopic systems in volcanic rocks: the Telemark supergroup, southern Norway: *Chemical Geology*, v. 145, p. 1–16, doi:10.1016/S0009-2541(97)00114-9.
- Brooks, C.K., 1973, Rifting and Doming in Southern East Greenland: *Nature Physical Science*, v. 244, p. 23–25, doi:10.1038/physci244023a0.
- ten Bruggencate, R.E., Fayek, M., Milne, B., Park, R.W., and Stenton, D.R., 2014, Just a crush? Contamination of archaeological samples by different grinding media: *Open Journal of Archaeometry*, v. 2, doi:10.4081/arc.2014.5606.
- Buick, I.S., Gibson, R.L., Cartwright, I., Maas, R., Wallmach, T., and Uken, R., 2000, Fluid flow in metacarbonates associated with emplacement of the Bushveld Complex, South Africa: *Journal of Geochemical Exploration*, v. 69–70, p. 391–395, doi:10.1016/S0375-6742(00)00032-7.
- Buick, I.S., Maas, R., and Gibson, R., 2001, Precise U–Pb titanite age constraints on the emplacement of the Bushveld Complex, South Africa: *Journal of the Geological Society*, v. 158, p. 3–6, doi:10.1144/jgs.158.1.3.
- Cameron, E.N., 1978, The Lower Zone of the Eastern Bushveld Complex in the Olifants River Trough: *Journal of Petrology*, v. 19, p. 437–462, doi:10.1093/petrology/19.3.437.
- Campbell, I.H., and Naldrett, A.J., 1979, The influence of silicate:sulfide ratios on the geochemistry of magmatic sulfides: *Economic Geology*, v. 74, p. 1503–1506, doi:10.2113/gsecongeo.74.6.1503.
- Cartwright, I., and Buick, I.S., 2000, Fluid generation, vein formation and the degree of fluid-rock interaction during decompression of high-pressure terranes: the Schistes Lustres, Alpine Corsica, France: *Journal of Metamorphic Geology*, v. 18, p. 607–624, doi:10.1046/j.1525-1314.2000.00280.x.
- Castro, A., Gerya, T., Garcia-Casco, A., Fernandez, C., Diaz-Alvarado, J., Moreno-Ventas, I., and Low, I., 2010, Melting Relations of MORB-Sediment Melanges in Underplated Mantle Wedge Plumes; Implications for the Origin of Cordilleran-type Batholiths: *Journal of Petrology*, v. 51, p. 1267–1295, doi:10.1093/petrology/egq019.

- Cattell, A., Krogh, T.E., and Arndt, N.T., 1984, Conflicting Sm-Nd whole rock and U-Pb zircon ages for Archean lavas from Newton Township, Abitibi Belt, Ontario: *Earth and Planetary Science Letters*, v. 70, p. 280–290, doi:10.1016/0012-821X(84)90012-8.
- Cawthorn, R.G. (Ed.), 1996, *Layered Intrusions*: Elsevier.
- Cawthorn, R.G., Harris, C., and Kruger, F.J., 2000, Discordant ultramafic pegmatoidal pipes in the Bushveld Complex: *Contributions to Mineralogy and Petrology*, v. 140, p. 119–133.
- Cawthorn, R.G., Latypov, R., Klemm, R., and Vuthuza, A., 2018, Origin of discordant ultramafic pegmatites in the Bushveld Complex from externally-derived magmas: *South African Journal of Geology*, v. 121, p. 287–310, doi:10.25131/sajg.121.0027.
- Cawthorn, R.G., and Webb, S.J., 2013, Cooling of the Bushveld Complex, South Africa: Implications for paleomagnetic reversals: *Geology*, v. 41, p. 687–690, doi:10.1130/G34033.1.
- Cheatham, M.M., Sangrey, W.F., and White, W.M., 1993, Sources of error in external calibration ICP-MS analysis of geological samples and an improved non-linear drift correction procedure: *Spectrochimica Acta Part B: Atomic Spectroscopy*, v. 48, p. 487–506, doi:10.1016/0584-8547(93)80054-X.
- Chiba, H., Chacko, T., Clayton, R.N., and Goldsmith, J.R., 1989, Oxygen isotope fractionations involving diopside, forsterite, magnetite, and calcite: Application to geothermometry: *Geochimica et Cosmochimica Acta*, v. 53, p. 2985–2995, doi:10.1016/0016-7037(89)90174-9.
- Chutas, N.I., Bates, E., Prevec, S.A., Coleman, D.S., and Boudreau, A.E., 2012, Sr and Pb isotopic disequilibrium between coexisting plagioclase and orthopyroxene in the Bushveld Complex, South Africa: microdrilling and progressive leaching evidence for sub-liquidus contamination within a crystal mush: *Contributions to Mineralogy and Petrology*, v. 163, p. 653–668, doi:10.1007/s00410-011-0691-7.
- Chuvilin, E. et al., 2020, A Gas-Emission Crater in the Erkuta River Valley, Yamal Peninsula: Characteristics and Potential Formation Model: *Geosciences*, v. 10, p. 170, doi:10.3390/geosciences10050170.
- Clarke, B.M., Uken, R., Watkeys, M.K., and Reinhardt, J., 2005, Folding of the Rustenburg layered suite adjacent to the Steelpoort pericline: implications for

- syn-Bushveld tectonism in the eastern Bushveld Complex: *South African Journal of Geology*, v. 108, p. 397–412, doi:10.2113/108.3.397.
- Connolly, J.A.D., 1997a, Devolatilization-generated fluid pressure and deformation-propagated fluid flow during prograde regional metamorphism: *Journal of Geophysical Research*, v. 102, p. 18149–18173.
- Connolly, J.A.D., 1997b, Mid-Crustal Focused Fluid Movement: Thermal Consequences and Silica Transport, *in* Jamtveit, B. and Yardley, B.W.D. eds., *Fluid Flow and Transport in Rocks*, Dordrecht, Springer Netherlands, p. 235–250, doi:10.1007/978-94-009-1533-6_14.
- Connolly, J.A.D., 2010, The Mechanics of Metamorphic Fluid Expulsion: *Elements*, v. 6, p. 165–172, doi:10.2113/gselements.6.3.165.
- Connolly, J.A.D., and Podladchikov, Y.Y., 2013, A Hydromechanical Model for Lower Crustal Fluid Flow, *in* *Metasomatism and the Chemical Transformation of Rock*, Berlin, Heidelberg, Springer Berlin Heidelberg, *Lecture Notes in Earth System Sciences*, p. 599–658, doi:10.1007/978-3-642-28394-9_14.
- Connolly, J.A.D., and Podladchikov, Y.Y., 2015, An analytical solution for solitary porosity waves: dynamic permeability and fluidization of nonlinear viscous and viscoplastic rock: *Geofluids*, v. 15, p. 269–292, doi:10.1111/gfl.12110.
- Connolly, J.A.D., and Podladchikov, Y.Y., 2007, Decompaction weakening and channeling instability in ductile porous media: Implications for asthenospheric melt segregation: *Journal of Geophysical Research*, v. 112, p. B10205, doi:10.1029/2005JB004213.
- Cruz-Uribe, A.M., Marschall, H.R., Gaetani, G.A., and Le Roux, V., 2018, Generation of alkaline magmas in subduction zones by partial melting of mélange diapirs—An experimental study: *Geology*, v. 46, p. 343–346, doi:10.1130/G39956.1.
- Czamanske, G.K., and Bohlen, S.R., 1990, The Stillwater Complex and its anorthosites: An accident of magmatic underplating? *American Mineralogist*, v. 75, p. 37–45.
- DePaolo, D.J., 1988, Age dependence of the composition of continental crust: evidence from Nd isotopic variations in granitic rocks: *Earth and Planetary Science Letters*, v. 90, p. 263–271, doi:10.1016/0012-821X(88)90130-6.

- DePaolo, D.J., and Wasserburg, G.J., 1979, Sm-Nd age of the Stillwater complex and the mantle evolution curve for neodymium: *Geochimica et Cosmochimica Acta*, v. 43, p. 999–1008, doi:10.1016/0016-7037(79)90089-9.
- Dobson, P.F., and O'Neil, J.R., 1987, Stable isotope compositions and water contents of boninite series volcanic rocks from Chichi-jima, Bonin Islands, Japan: *Earth and Planetary Science Letters*, v. 82, p. 75–86, doi:10.1016/0012-821X(87)90108-7.
- Dunn, T., 1986, An Investigation of the Oxygen Isotope Geochemistry of the Stillwater Complex: *Journal of Petrology*, v. 27, p. 987–997, doi:10.1093/petrology/27.4.987.
- Eales, H.V., and Cawthorn, R.G., 1996, The Bushveld Complex, *in* Cawthorn, R.G. ed., *Layered Intrusions*, Amsterdam, Elsevier, p. 181–229.
- Eales, H.V., Field, M., de Klerk, W.J., and Scoon, R.N., 1988, Regional trends of chemical variation and thermal erosion in the Upper Critical Zone, Western Bushveld Complex: *Mineralogical Magazine*, v. 52, p. 63–79.
- Eiler, J.M., 2001, Oxygen Isotope Variations of Basaltic Lavas and Upper Mantle Rocks: *Reviews in Mineralogy and Geochemistry*, v. 43, p. 319–364.
- Elliott, T., Jeffcoate, A., and Bouman, C., 2004, The terrestrial Li isotope cycle: light-weight constraints on mantle convection: *Earth and Planetary Science Letters*, v. 220, p. 231–245, doi:10.1016/S0012-821X(04)00096-2.
- Elliott, T., Thomas, A., Jeffcoate, A., and Niu, Y., 2006, Lithium isotope evidence for subduction-enriched mantle in the source of mid-ocean-ridge basalts: *Nature*, v. 443, p. 565–568, doi:10.1038/nature05144.
- Eriksson, P.G., Hattingh, P.J., and Altermann, W., 1995, An overview of the geology of the Transvaal Sequence and Bushveld Complex, South Africa: *Mineralium Deposita*, v. 30, doi:10.1007/BF00189339.
- Eriksson, P.G., Schwitzer, J.K., Bosch, P.J.A., Schreiber, U.M., Van Deventer, J.L., and Hatton, C.J., 1993, The Transvaal Sequence: an overview: *Journal of African Earth Sciences*, v. 16, p. 25–51.
- Farquhar, J., and Wing, B.A., 2003, Multiple sulfur isotopes and the evolution of the atmosphere: *Earth and Planetary Science Letters*, v. 213, p. 1–13, doi:10.1016/S0012-821X(03)00296-6.

- Farquhar, J., Wing, B.A., McKeegan, K.D., Harris, J.W., Cartigny, P., and Thiemens, M.H., 2002, Mass-Independent Sulfur of Inclusions in Diamond and Sulfur Recycling on Early Earth: *Science*, v. 298, p. 2369–2372, doi:10.1126/science.1078617.
- Fenton, M.D., and Faure, G., 1969, The Age of the Igneous Rocks of the Stillwater Complex of Montana: *Geological Society of America Bulletin*, v. 80, p. 1599, doi:10.1130/0016-7606(1969)80[1599:TAOTIR]2.0.CO;2.
- Ferguson, J., and McCarthy, T.S., 1970, Origin of an ultramafic pegmatoid in the eastern part of the Bushveld Complex: *Geological Society of South Africa Special Publication*, v. 1, p. 74–79.
- Finn, C.A., Bedrosian, P.A., Cole, J.C., Khoza, T.D., and Webb, S.J., 2015, Mapping the 3D extent of the Northern Lobe of the Bushveld layered mafic intrusion from geophysical data: *Precambrian Research*, v. 268, p. 279–294, doi:10.1016/j.precamres.2015.07.003.
- Frost, B.R., and Lindsley, D.H., 1992, Equilibria among Fe-Ti oxides, pyroxenes, olivine, and quartz: Part II. Application: *American Mineralogist*, v. 77, p. 1004–1020.
- Gerya, T.V., Connolly, J.A.D., Yuen, D.A., Gorczyk, W., and Capel, A.M., 2006, Seismic implications of mantle wedge plumes: *Physics of the Earth and Planetary Interiors*, v. 156, p. 59–74, doi:10.1016/j.pepi.2006.02.005.
- Gerya, T.V., Uken, R., Reinhardt, J., Watkeys, M.K., Maresch, W.V., and Clarke, B.M., 2004, “Cold” diapirs triggered by intrusion of the Bushveld Complex: Insight from two-dimensional numerical modeling, *in* Special Paper 380: Gneiss Domes in Orogeny, *Geological Society of America*, v. 380, p. 117–127, doi:10.1130/0-8137-2380-9.117.
- Gerya, T.V., Uken, R., Reinhardt, J., Watkeys, M.K., Maresch, W.V., and Clarke, B.M., 2003, Cold fingers in a hot magma: Numerical modeling of country-rock diapirs in the Bushveld Complex, South Africa: *Geology*, v. 31, p. 753–756, doi:10.1130/G19566.1.
- Gerya, T.V., and Yuen, D.A., 2003, Rayleigh–Taylor instabilities from hydration and melting propel ‘cold plumes’ at subduction zones: *Earth and Planetary Science Letters*, v. 212, p. 47–62, doi:10.1016/S0012-821X(03)00265-6.

- Ghiorso, M.S., and Gualda, G.A.R., 2015, An H₂O–CO₂ mixed fluid saturation model compatible with rhyolite-MELTS: *Contributions to Mineralogy and Petrology*, v. 169, p. 53, doi:10.1007/s00410-015-1141-8.
- Ghiorso, M.S., and Sack, R.O., 1995, Chemical mass transfer in magmatic processes IV. A revised and internally consistent thermodynamic model for the interpolation and extrapolation of liquid-solid equilibria in magmatic systems at elevated temperatures and pressures: *Contributions to Mineralogy and Petrology*, v. 119, p. 197–212.
- Giletti, B.J., 1966, Isotopic ages from southwestern Montana: *Journal of Geophysical Research*, v. 71, p. 4029–4036, doi:10.1029/JZ071i016p04029.
- Gleason, J.D., Gutzmer, J., Kesler, S.E., and Zwingmann, H., 2011, 2.05-Ga Isotopic Ages for Transvaal Mississippi Valley–Type Deposits: Evidence for Large-Scale Hydrothermal Circulation around the Bushveld Igneous Complex, South Africa: *The Journal of Geology*, v. 119, p. 69–80, doi:10.1086/657301.
- Godel, B., and Barnes, S.-J., 2008, Platinum-group elements in sulfide minerals and the whole rocks of the J-M Reef (Stillwater Complex): Implication for the formation of the reef: *Chemical Geology*, v. 248, p. 272–294, doi:10.1016/j.chemgeo.2007.05.006.
- Graham, C.M., Valley, J.W., Eiler, J.M., and Wada, H., 1998, Timescales and mechanisms of fluid infiltration in a marble: an ion microprobe study: *Contributions to Mineralogy and Petrology*, v. 132, p. 371–389.
- Green, D.H., Schmidt, M.W., and Hibberson, W.O., 2004, Island-arc Ankararamites: Primitive Melts from Fluxed Refractory Lherzolitic Mantle: *Journal of Petrology*, v. 45, p. 391–403, doi:10.1093/petrology/egg101.
- Gregory, R.T., and Criss, R.E., 1986, Isotopic exchange in open and closed systems: *Reviews in Mineralogy and Geochemistry*, v. 16, p. 91–127.
- Gregory, R.T., Criss, R.E., and Taylor, H.P., 1989, Oxygen isotope exchange kinetics of mineral pairs in closed and open systems: Applications to problems of hydrothermal alteration of igneous rocks and Precambrian iron formations: *Chemical Geology*, v. 75, p. 1–42, doi:10.1016/0009-2541(89)90019-3.
- Gualda, G.A.R., Ghiorso, M.S., Lemons, R.V., and Carley, T.L., 2012, Rhyolite-MELTS: a Modified Calibration of MELTS Optimized for Silica-rich, Fluid-bearing

- Magmatic Systems: *Journal of Petrology*, v. 53, p. 875–890, doi:10.1093/petrology/egr080.
- Günther, T., Haase, K.M., Junge, M., Oberthür, T., Woelki, D., and Krumm, S., 2018, Oxygen isotope and trace element compositions of platiniferous dunite pipes of the Bushveld Complex, South Africa – Signals from a recycled mantle component? *Lithos*, v. 310–311, p. 332–341, doi:10.1016/j.lithos.2018.04.017.
- Hall, P.S., and Kincaid, C., 2001, Diapiric Flow at Subduction Zones: A Recipe for Rapid Transport: *Science*, v. 292, p. 2472–2475.
- Hanley, J.J., Mungall, J.E., Pettke, T., Spooner, E.T.C., and Bray, C.J., 2008, Fluid and Halide Melt Inclusions of Magmatic Origin in the Ultramafic and Lower Banded Series, Stillwater Complex, Montana, USA: *Journal of Petrology*, v. 49, p. 1133–1160, doi:10.1093/petrology/egn020.
- Hanley, J.J., Mungall, J.E., Pettke, T., Spooner, E.T.C., and Bray, C.J., 2005, Ore metal redistribution by hydrocarbon–brine and hydrocarbon–halide melt phases, North Range footwall of the Sudbury Igneous Complex, Ontario, Canada: *Mineralium Deposita*, v. 40, p. 237–256, doi:10.1007/s00126-005-0004-z.
- van Haren, J.L.M., Ague, J.J., and Rye, D.M., 1996, Oxygen isotope record of fluid infiltration and mass transfer during regional metamorphism of pelitic schist, Connecticut, USA: *Geochimica et Cosmochimica Acta*, v. 60, p. 3487–3504.
- Harmer, R.E., Auret, J.M., and Eglington, B.M., 1995, Lead isotope variations within the Bushveld complex, Southern Africa: a reconnaissance study: *Journal of African Earth Sciences*, v. 21, p. 595–606, doi:10.1016/0899-5362(95)00109-3.
- Harmer, R.E., and Sharpe, M.R., 1985, Field relations and strontium isotope systematics of the marginal rocks of the eastern Bushveld Complex: *Economic Geology*, v. 80, p. 813–837, doi:10.2113/gsecongeo.80.4.813.
- Harris, C., and Chaumba, J.B., 2001, Crustal Contamination and Fluid–Rock Interaction during the Formation of the Platreef, Northern Limb of the Bushveld Complex, South Africa: *Journal of Petrology*, v. 42, p. 1321–1347, doi:10.1093/petrology/42.7.1321.
- Harris, N., McMillan, A., Holness, M., Uken, R., Watkeys, M., Rogers, N., and Fallick, A., 2003, Melt Generation and Fluid Flow in the Thermal Aureole of the Bushveld Complex: *Journal of Petrology*, v. 44, p. 1031–1054, doi:10.1093/petrology/44.6.1031.

- Harris, C., Pronost, J.J.M., Ashwal, L.D., and Cawthorn, R.G., 2005, Oxygen and Hydrogen Isotope Stratigraphy of the Rustenburg Layered Suite, Bushveld Complex: Constraints on Crustal Contamination: *Journal of Petrology*, v. 46, p. 579–601, doi:10.1093/petrology/egh089.
- Harvey, J., and Baxter, E.F., 2009, An improved method for TIMS high precision neodymium isotope analysis of very small aliquots (1–10 ng): *Chemical Geology*, v. 258, p. 251–257, doi:10.1016/j.chemgeo.2008.10.024.
- Hatton, C.J., and Sharpe, M.R., 1989, Significance and origin of boninite-like rocks associated with the Bushveld Complex, *in* Crawford, A.J. ed., *Boninites and related rocks*, London, Unwin Hyman, p. 174–208.
- Hawkesworth, C.J., 1997, U-Th Isotopes in Arc Magmas: Implications for Element Transfer from the Subducted Crust: *Science*, v. 276, p. 551–555, doi:10.1126/science.276.5312.551.
- Hawkesworth, C.J., Gallagher, K., Hergt, J.M., and McDermott, F., 1993, Mantle and Slab Contributions in ARC Magmas: *Annual Review of Earth and Planetary Sciences*, v. 21, p. 175–204, doi:10.1146/annurev.earth.21.050193.001135.
- Helz, R.T., 1985, Compositions of fine-grained mafic rocks from sills and dikes associated with the Stillwater Complex, *in* Czamanske, G.K. and Zientek, M.L. eds., *Stillwater Complex*. Montana Bureau of Mines and Geology Special Publication 92, p. 97–117.
- Helz, R.T., 1995, The Stillwater Complex, Montana; a subvolcanic magma chamber? *American Mineralogist*, v. 80, p. 1343–1346, doi:10.2138/am-1995-11-1225.
- Hess, H.H., 1939, Extreme fractional crystallization of a basaltic magma: The Stillwater Igneous Complex: *Transactions, American Geophysical Union*, v. 20, p. 430, doi:10.1029/TR020i003p00430-2.
- Hickson, C.J., and Juras, S.J., 1986, Sample contamination by grinding: *Canadian Mineralogist*, v. 24, p. 585–589.
- Hildreth, W., Halliday, A.N., and Christiansen, R.L., 1991, Isotopic and Chemical Evidence Concerning the Genesis and Contamination of Basaltic and Rhyolitic Magma Beneath the Yellowstone Plateau Volcanic Field: *Journal of Petrology*, v. 32, p. 63–138, doi:10.1093/petrology/32.1.63.

- Hofmann, A.W., 1975, Diffusion of Ca and Sr in a basalt melt: Yearbook, Carnegie Institute Washington, v. 74.
- Hoover, J.D., 1989, The Chilled Marginal Gabbro and Other Contact Rocks of the Skaergaard Intrusion: *Journal of Petrology*, v. 30, p. 441–476, doi:10.1093/petrology/30.2.441.
- Hunter, R.H., and Sparks, R.S.J., 1987, The differentiation of the Skaergaard Intrusion: *Contributions to Mineralogy and Petrology*, v. 95, p. 451–461.
- Ireland, R.H.P., and Penniston-Dorland, S.C., 2015, Chemical interactions between a sedimentary diapir and surrounding magma: Evidence from the Phepane Dome and Bushveld Complex, South Africa: *American Mineralogist*, v. 100, p. 1985–2000, doi:10.2138/am-2015-5196.
- Irvine, T.N., 1977, Chromite crystallization in the join Mg_2SiO_4 - $CaMgSi_2O_6$ - $CaAl_2Si_2O_8$ - $MgCr_2O_4$ - SiO_2 ; in *Carnegie Institute of Washington Yearbook*, Washington, D. C., v. 76, p. 465–472.
- Irvine, T.N., Keith, D.W., and Todd, S.G., 1983, The J-M Platinum-Palladium Reef of the Stillwater Complex, Montana: II. Origin by Double-Diffusive Convective Magma Mixing and Implications for the Bushveld Complex: *Economic Geology*, v. 78, p. 1287–1334.
- Ito, E., Harris, D.M., and Anderson, A.T., 1983, Alteration of oceanic crust and geologic cycling of chlorine and water: *Geochimica et Cosmochimica Acta*, v. 47, p. 1613–1624, doi:10.1016/0016-7037(83)90188-6.
- Ito, E., and Stern, R.J., 1986, Oxygen- and strontium-isotopic investigations of subduction zone volcanism: the case of the Volcano Arc and the Marianas Island Arc: *Earth and Planetary Science Letters*, v. 76, p. 312–320, doi:10.1016/0012-821X(86)90082-8.
- Ito, E., White, W.M., and Goepel, C., 1987, The O, Sr, Nd, and Pb isotope geochemistry of MORB: *Chemical Geology*, v. 62, p. 157–176.
- Jackson, E.D., 1971, The origin of ultramafic rocks by cumulus processes: *Fortschritte der Mineralogie*, v. 48, p. 128–174.
- Jahn, B., Bertrand-Sarfati, J., Morin, N., and Macé, J., 1990, Direct dating of stromatolitic carbonates from the Schmidtsdrif Formation (Transvaal Dolomite), South Africa,

with implications on the age of the Ventersdorp Supergroup: *Geology*, v. 18, p. 1211, doi:10.1130/0091-7613(1990)018<1211:DDOSCF>2.3.CO;2.

Jenkins, M.C., and Mungall, J.E., 2018, Genesis of the Peridotite Zone, Stillwater Complex, Montana, USA: *Journal of Petrology*, v. 59, p. 2157–2189, doi:10.1093/petrology/egy093.

Jenkins, M.C., Mungall, J.E., Zientek, M.L., Costin, G., and Yao, Z., 2021, Origin of the J-M Reef and Lower Banded series, Stillwater Complex, Montana, USA: *Precambrian Research*, v. 367, p. 106457, doi:10.1016/j.precamres.2021.106457.

Jenkins, M.C., Mungall, J.E., Zientek, M.L., Holick, P., and Butak, K., 2020, The Nature and Composition of the J-M Reef, Stillwater Complex, Montana, USA: *Economic Geology*, v. 115, p. 1799–1826, doi:10.5382/econgeo.4777.

Johnson, T., Brown, M., Gibson, R., and Wing, B., 2004, Spinel-cordierite symplectites replacing andalusite: evidence for melt-assisted diapirism in the Bushveld Complex, South Africa: *Diapirism in t: Journal of Metamorphic Geology*, v. 22, p. 529–545, doi:10.1111/j.1525-1314.2004.00531.x.

Kanitpanyacharoen, W., and Boudreau, A.E., 2013, Sulfide-associated mineral assemblages in the Bushveld Complex, South Africa: platinum-group element enrichment by vapor refining by chloride–carbonate fluids: *Mineralium Deposita*, v. 48, p. 193–210, doi:10.1007/s00126-012-0427-2.

Keays, R.R., Lightfoot, P.C., and Hamlyn, P.R., 2012, Sulfide saturation history of the Stillwater Complex, Montana: chemostratigraphic variation in platinum group elements: *Mineralium Deposita*, v. 47, p. 151–173, doi:10.1007/s00126-011-0346-7.

Kelemen, P.B., Shimizu, N., and Salters, V.J.M., 1995, Extraction of mid-ocean-ridge basalt from the upwelling mantle by focused flow of melt in dunite channels: *Nature*, v. 375, p. 747–753, doi:10.1038/375747a0.

Keller, T., and Katz, R.F., 2016, The Role of Volatiles in Reactive Melt Transport in the Asthenosphere: *Journal of Petrology*, v. 57, p. 1073–1108, doi:10.1093/petrology/egw030.

Keller, T., Katz, R.F., and Hirschmann, M.M., 2017, Volatiles beneath mid-ocean ridges: Deep melting, channelised transport, focusing, and metasomatism: *Earth and Planetary Science Letters*, v. 464, p. 55–68, doi:10.1016/j.epsl.2017.02.006.

- Kent, A.J.R., and Elliott, T.R., 2002, Melt inclusions from Marianas arc lavas: implications for the composition and formation of island arc magmas: *Chemical Geology*, v. 183, p. 263–286, doi:10.1016/S0009-2541(01)00378-3.
- Kimura, J.-I., and Yoshida, T., 2006, Contributions of Slab Fluid, Mantle Wedge and Crust to the Origin of Quaternary Lavas in the NE Japan Arc: *Journal of Petrology*, v. 47, p. 2185–2232, doi:10.1093/petrology/egl041.
- Kinnaird, J.A., Kruger, F.J., Nex, P.A.M., and Cawthorn, R.G., 2002, Chromitite formation—a key to understanding processes of platinum enrichment: *Applied Earth Science*, v. 111, p. 23–35, doi:10.1179/aes.2002.111.1.23.
- Klein, E.M., Langmuir, C.H., and Staudigel, H., 1991, Geochemistry of basalts from the southeast Indian Ridge, 115°E–138°E: *Journal of Geophysical Research*, v. 96, p. 2089, doi:10.1029/90JB01384.
- Kleinkopf, M.D., 1985, Regional gravity and magnetic anomalies of the Stillwater Complex area, in Czamanske, G.K. and Zientek, M.L. eds., *The Stillwater Complex, Montana: Geology and Guide*, Montana Bureau of Mines and Geology Special Publication 92, p. 33–38.
- Krogh, T.E., and Davis, G.L., 1973, The effect of regional metamorphism on U-Pb systems in zircon and a comparison with Rb-Sr systems in the same whole rock and its constituent minerals: *Washington Year Book*, v. 72, p. 601–610.
- Kruger, F.J., 2005, Filling the Bushveld Complex magma chamber: lateral expansion, roof and floor interaction, magmatic unconformities, and the formation of giant chromitite, PGE and Ti-V-magnetitite deposits: *Mineralium Deposita*, v. 40, p. 451–472, doi:10.1007/s00126-005-0016-8.
- Kruger, F.J., 1994, The Sr-isotopic stratigraphy of the western Bushveld Complex: *South African Journal of Geology*, v. 97, p. 393–399.
- Kruger, F.J., 1990, The stratigraphy of the Bushveld Complex: a reappraisal and the relocation of the Main Zone boundaries: *South African Journal of Geology*, v. 93, p. 376–381.
- Kruger, F.J., and Marsh, J.S., 1982, Significance of $^{87}\text{Sr}/^{86}\text{Sr}$ ratios in the Merensky cyclic unit of the Bushveld Complex: *Nature*, v. 298, p. 53–55, doi:10.1038/298053a0.
- Kyser, T.K., Cameron, W.E., and Nisbet, E.G., 1986, Boninite petrogenesis and alteration history: constraints from stable isotope compositions of boninites from Cape

- Vogel, New Caledonia and Cyprus: Contributions to Mineralogy and Petrology, v. 93, p. 222–226, doi:10.1007/BF00371324.
- Kyser, T.K., and O'Neil, J.R., 1984, Hydrogen isotope systematics of submarine basalts: *Geochimica et Cosmochimica Acta*, v. 48, p. 2123–2133, doi:10.1016/0016-7037(84)90392-2.
- Kyser, T.K., O'Neil, J.R., and Carmichael, I.S.E., 1981, Oxygen isotope thermometry of basic lavas and mantle nodules: *Contributions to Mineralogy and Petrology*, v. 77, p. 11–23, doi:10.1007/BF01161498.
- Labidi, J., Cartigny, P., Birck, J.L., Assayag, N., and Bourrand, J.J., 2012, Determination of multiple sulfur isotopes in glasses: A reappraisal of the MORB $\delta^{34}\text{S}$: *Chemical Geology*, v. 334, p. 189–198, doi:10.1016/j.chemgeo.2012.10.028.
- Labotka, T., 1985, Petrogenesis of metamorphic rocks beneath the Stillwater Complex: Assemblages and conditions of metamorphism: Montana Bureau of Mines and Geology Special Publication, v. 92, p. 70–76.
- Labotka, T.C., and Kath, R.L., 2001, Petrogenesis of the contact-metamorphic rocks beneath the Stillwater Complex, Montana: *Geological Society of America Bulletin*, v. 113, p. 1312–1323, doi:10.1130/0016-7606(2001)113<1312:POTCMR>2.0.CO;2.
- Labotka, T.C., Vaniman, D.T., and Papike, J.J., 1982, Contact metamorphic effects of the Stillwater Complex, Montana: the concordant iron-formation: a reply to the role of buffering in metamorphism of iron-formation: *American Mineralogist*, v. 67, p. 149–152.
- Lahaye, Y., and Arndt, N., 1996, Alteration of a Komatiite Flow from Alexo, Ontario, Canada: *Journal of Petrology*, v. 37, p. 1261–1284, doi:10.1093/petrology/37.6.1261.
- Lambert, D.D., Morgan, J.W., Walker, R.J., Shirey, S.B., Carlson, R.W., Zientek, M.L., and Koski, M.S., 1989, Rhenium-Osmium and Samarium-Neodymium Isotopic Systematics of the Stillwater Complex: *Science*, v. 244, p. 1169–1174, doi:10.1126/science.244.4909.1169.
- Lambert, D.D., and Simmons, E.C., 1987, Magma evolution in the Stillwater Complex, Montana: I. Rare-Earth Element evidence for the formation of the Ultramafic Series: *American Journal of Science*, v. 287, p. 1–32.

- Lambert, D.D., and Simmons, E.C., 1988, Magma evolution in the Stillwater Complex, Montana; II, Rare earth element evidence for the formation of the J-M Reef: *Economic Geology*, v. 83, p. 1109–1126, doi:10.2113/gsecongeo.83.6.1109.
- Lambert, D.D., Walker, R.J., Morgan, J.W., Shirey, S.B., Carlson, R.W., Zientek, M.L., Lipin, B.R., Koski, M.S., and Cooper, R.L., 1994, Re–Os and Sm–Nd Isotope Geochemistry of the Stillwater Complex, Montana: Implications for the Petrogenesis of the J-M Reef: *Journal of Petrology*, v. 35, p. 1717–1753, doi:10.1093/petrology/35.6.1717.
- Langmuir, C.H., 1989, Geochemical consequences of in situ crystallization: *Nature*, v. 340, p. 199–205.
- Larsen, R.B., Brooks, C.K., and Bird, D.K., 1992, Methane-bearing, aqueous, saline solutions in the Skaergaard intrusion, east Greenland: *Contributions to Mineralogy and Petrology*, v. 112, p. 428–437, doi:10.1007/BF00310472.
- Latypov, R., and Chistyakova, S., 2021, Misinterpretation of zircon ages in layered intrusions: *South African Journal of Geology*, doi:10.25131/sajg.125.0001.
- Le Roux, V., Bodinier, J.-L., Alard, O., O'Reilly, S.Y., and Griffin, W.L., 2009, Isotopic decoupling during porous melt flow: A case-study in the Lherz peridotite: *Earth and Planetary Science Letters*, v. 279, p. 76–85, doi:10.1016/j.epsl.2008.12.033.
- Leeman, W.P., and Hawkesworth, C.J., 1986, Open magma systems: Trace element and isotopic constraints: *Journal of Geophysical Research*, v. 91, p. 5901, doi:10.1029/JB091iB06p05901.
- Letts, S., Torsvik, T.H., Webb, S.J., and Ashwal, L.D., 2009, Palaeomagnetism of the 2054 Ma Bushveld Complex (South Africa): implications for emplacement and cooling: *Geophysical Journal International*, v. 179, p. 850–872, doi:10.1111/j.1365-246X.2009.04346.x.
- Li, C., and Boudreau, A.E., 2017, The origin of high-Cu/S sulfides by shallow-level degassing in the Skaergaard intrusion, East Greenland: *Geology*, v. 45, p. 1075–1078, doi:10.1130/G39540.1.
- Li, S., Hart, S.R., and Wu, T., 1990, Rb-Sr and Sm-Nd isotopic dating of an Early Precambrian spilite-keratophyre sequence in the Wutaishan area, north China: preliminary evidence for Nd-isotopic homogenization in the mafic and felsic lavas during low-grade metamorphism: *Precambrian Research*, v. 47, p. 191–203, doi:10.1016/0301-9268(90)90038-R.

- Li, W., Liu, X., and Godfrey, L.V., 2019, Optimisation of Lithium Chromatography for Isotopic Analysis in Geological Reference Materials by MC - ICP - MS: *Geostandards and Geoanalytical Research*, v. 43, p. 261–276, doi:10.1111/ggr.12254.
- Løseth, H., Wensaas, L., Arntsen, B., Hanken, N.-M., Basire, C., and Graue, K., 2011, 1000 m long gas blow-out pipes: *Marine and Petroleum Geology*, v. 28, p. 1047–1060, doi:10.1016/j.marpetgeo.2010.10.001.
- Lundblad, S.P., 1994, Evolution of small carbonate platforms in the Umbria-Marche Apennines, Italy [Ph.D. Thesis]: University of North Carolina at Chapel Hill, 145 p.
- Magalhães, N., Farquhar, J., Bybee, G., Penniston-Dorland, S., Rumble, D., Kinnaird, J., and McCreesh, M., 2019, Multiple sulfur isotopes reveal a possible non-crustal source of sulfur for the Bushveld Province, southern Africa: *Geology*, v. 47, p. 982–986, doi:10.1130/G46282.1.
- Magalhães, N., Penniston-Dorland, S., Farquhar, J., and Mathez, E.A., 2018, Variable sulfur isotope composition of sulfides provide evidence for multiple sources of contamination in the Rustenburg Layered Suite, Bushveld Complex: *Earth and Planetary Science Letters*, v. 492, p. 163–173, doi:10.1016/j.epsl.2018.04.010.
- Maier, W.D., Arndt, N.T., and Curl, E.A., 2000, Progressive crustal contamination of the Bushveld Complex: evidence from Nd isotopic analyses of the cumulate rocks: *Contributions to Mineralogy and Petrology*, v. 140, p. 316–327, doi:10.1007/s004100000186.
- Manhes, G., Allègre, C.J., Dupré, B., and Hamelin, B., 1980, Lead isotope study of basic-ultrabasic layered complexes: Speculations about the age of the earth and primitive mantle characteristics: *Earth and Planetary Science Letters*, v. 47, p. 370–382, doi:10.1016/0012-821X(80)90024-2.
- Marcantonio, F., Zindler, A., Reisberg, L., and Mathez, E.A., 1993, Re-Os isotopic systematics in chromitites from the Stillwater Complex, Montana, USA: *Geochimica et Cosmochimica Acta*, v. 57, p. 4029–4037.
- Marschall, H.R., and Schumacher, J.C., 2012, Arc magmas sourced from mélange diapirs in subduction zones: *Nature Geoscience*, v. 5, p. 862–867, doi:10.1038/geo1634.

- Martin, C.E., 1989, Re-Os isotopic investigation of the Stillwater Complex, Montana: *Earth and Planetary Science Letters*, v. 93, p. 336–344, doi:10.1016/0012-821X(89)90033-2.
- Mathez, E.A., Agrinier, P., and Hutchinson, R., 1994, Hydrogen Isotope Composition of the Merensky Reef and Related Rocks, Atok Section, Bushveld Complex: *Economic Geology*, v. 89, p. 791–802.
- Mathez, E.A., Hunter, R.H., and Kinzler, R., 1997, Petrologic evolution of partially molten cumulate: the Atok section of the Bushveld Complex: *Contributions to Mineralogy and Petrology*, v. 129, p. 20–34, doi:10.1007/s004100050320.
- Mathez, E.A., and Kent, A.J.R., 2007, Variable initial Pb isotopic compositions of rocks associated with the UG2 chromitite, eastern Bushveld Complex: *Geochimica et Cosmochimica Acta*, v. 71, p. 5514–5527, doi:10.1016/j.gca.2007.09.014.
- Mathez, E.A., and Waight, T.E., 2003, Lead isotopic disequilibrium between sulfide and plagioclase in the Bushveld Complex and the chemical evolution of large layered intrusions: *Geochimica et Cosmochimica Acta*, v. 67, p. 1875–1888, doi:10.1016/S0016-7037(02)01294-2.
- McBirney, A.R., and Naslund, H.R., 1990, The differentiation of the Skaergaard Intrusion: *Contributions to Mineralogy and Petrology*, v. 104, p. 235–247.
- McCallum, I.S., 1996, The Stillwater Complex, *in* *Developments in Petrology*, Elsevier, v. 15, p. 441–483, doi:10.1016/S0167-2894(96)80015-7.
- McCallum, I.S., Raedeke, L.D., and Mathez, E.A., 1980, Investigations of the Stillwater Complex: Part 1. Stratigraphy and Structure of the Banded Zone: *American Journal of Science*, v. 280, p. 59–87.
- McCallum, I.S., Thurber, M.W., O'Brien, H.E., and Nelson, B.K., 1999, Lead isotopes in sulfides from the Stillwater Complex, Montana: evidence for subsolidus remobilization: *Contributions to Mineralogy and Petrology*, v. 137, p. 206–219.
- McCandless, T.E., Ruiz, J., Adair, B.I., and Freydier, C., 1999, Re-Os isotope and Pd/Ru variations in chromitites from the Critical Zone, Bushveld Complex, South Africa: *Geochimica et Cosmochimica Acta*, v. 63, p. 911–923, doi:10.1016/S0016-7037(99)00092-7.
- McCulloch, M.T., and Wasserburg, G.J., 1978, Sm-Nd and Rb-Sr Chronology of Continental Crust Formation: Times of addition to continents of chemically

fractionated mantle-derived materials are determined.: *Science*, v. 200, p. 1003–1011, doi:10.1126/science.200.4345.1003.

- McDonough, W.F., and Sun, S. -s., 1995, The composition of the Earth: *Chemical Geology*, v. 120, p. 223–253.
- McIlveen, C.L., 1996, Anomalous platinum-group element occurrence below the JM Reef Stillwater Complex Montana [M.S. Thesis]: University of Montana, 85 p.
- Meurer, W.P., and Boudreau, A.E., 1998, Compaction of Igneous Cumulates Part I: Geochemical Consequences For Cumulates and Liquid Fractionation Trends: *The Journal of Geology*, v. 106, p. 281–292, doi:10.1086/516022.
- Meurer, W.P., and Boudreau, A.E., 1996, Petrology and Mineral Compositions of the Middle Banded Series of the Stillwater Complex, Montana: *Journal of Petrology*, v. 37, p. 583–607.
- Meurer, W.P., Klaber, S., and Boudreau, A.E., 1997, Discordant bodies from olivine-bearing zones III and IV of the Stillwater Complex, Montana - evidence for postcumulus fluid migration and reaction in layered intrusions: *Contributions to Mineralogy and Petrology*, v. 130, p. 81–92.
- Meurer, W.P., and Meurer, M.E.S., 2006, Using apatite to dispel the “trapped liquid” concept and to understand the loss of interstitial liquid by compaction in mafic cumulates: an example from the Stillwater Complex, Montana: *Contributions to Mineralogy and Petrology*, v. 151, p. 187–201, doi:10.1007/s00410-005-0054-3.
- Mogk, D.K., and Mueller, P.A., 1990, Evidence ofr Archean accretionary tectonics in the northern Wyoming Province, SW Montana: *Geological Society of America Abstracts with Programs*, v. 22, p. 262.
- Mueller, P.A., and Wooden, J.L., 1976, Rb-Sr whole-rock age of the contact aureole of the Stillwater Igneous Complex, Montana: *Earth and Planetary Science Letters*, v. 29, p. 384–388, doi:10.1016/0012-821X(76)90143-6.
- Mueller, P.A., Wooden, J.L., and Bowes, D.R., 1982, Precambrian evolution of the Beartooth Mountains, Montana-Wyoming, USA: *Revista Brasileira de Geociencias*, v. 12, p. 215–222.
- Mueller, P.A., Wooden, J.L., and Nutman, A.P., 1992, 3.96 Ga zircons from an Archean quartzite, Beartooth Mountains, Montana: *Geology*, v. 20, p. 327–330.

- Mungall, J.E., Kamo, S.L., and McQuade, S., 2016, U–Pb geochronology documents out-of-sequence emplacement of ultramafic layers in the Bushveld Igneous Complex of South Africa: *Nature Communications*, v. 7, p. 13385, doi:10.1038/ncomms13385.
- Naslund, H.R., 1986, Disequilibrium partial melting and rheomorphic layer formation in the contact aureole of the Basistoppen sill, East Greenland: *Contributions to Mineralogy and Petrology*, v. 93, p. 359–367, doi:10.1007/BF00389394.
- Newton, R.C., and Manning, C.E., 2000, Quartz solubility in H₂O–NaCl and H₂O–CO₂ solutions at deep crust-upper mantle pressures and temperatures: 2–15 kbar and 500–900°C: *Geochimica et Cosmochimica Acta*, v. 64, p. 2993–3005, doi:10.1016/S0016-7037(00)00402-6.
- Nielsen, T.F.D., Brooks, C.K., and Keiding, J.K., 2019, Bulk Liquid for the Skaergaard Intrusion and Its PGE–Au Mineralization: Composition, Correlation, Liquid Line of Descent, and Timing of Sulphide Saturation and Silicate–Silicate Immiscibility: *Journal of Petrology*, v. 60, p. 1853–1880, doi:10.1093/petrology/egz055.
- Nielsen, T.F.D., Olsen, S.D., and Stensgaard, B.M., 2009, Developing a 3-D model for the Skaergaard intrusion in East Greenland: constraints on structure, mineralisation and petrogenetic models: *Geological Survey of Denmark and Greenland (GEUS) Bulletin*, v. 17, p. 61–64, doi:10.34194/geusb.v17.5015.
- Nielsen, S.G., Shimizu, N., Lee, C.-T.A., and Behn, M.D., 2014, Chalcophile behavior of thallium during MORB melting and implications for the sulfur content of the mantle: *Geochemistry, Geophysics, Geosystems*, v. 15, p. 4905–4919, doi:10.1002/2014GC005536.
- Nohda, S., and Wasserburg, G.J., 1981, Nd and Sr isotopic study of volcanic rocks from Japan: *Earth and Planetary Science Letters*, v. 52, p. 264–276, doi:10.1016/0012-821X(81)90181-3.
- Nunes, P.D., and Tilton, G.R., 1971, Uranium–Lead Ages of Minerals from the Stillwater Igneous Complex and Associated Rocks, Montana: *Geological Society of America Bulletin*, v. 82, p. 2231–2250.
- O’Driscoll, B., and VanTongeren, J.A., 2017, Layered Intrusions: From Petrological Paradigms to Precious Metal Repositories: *Elements*, v. 13, p. 383–389, doi:10.2138/gselements.13.6.383.

- Page, N.J., 1977, Stillwater Complex, Montana: Rock Succession, Metamorphism, and Structure of the Complex and Adjacent Rocks: Professional Paper Geological Survey Professional Paper 999.
- Page, N.J., 1979, Stillwater Complex, Montana: Structure, mineralogy, and petrology of the Basal Zone with emphasis on the occurrence of sulfides: Department of the Interior, Geological Survey, v. 1038.
- Pagé, P., Barnes, S.-J., and Zientek, M.L., 2011, Formation and evolution of the chromitites of the Stillwater Complex: a trace element study: , p. 3.
- Papike, J.J., Spilde, M.N., Fowler, G.W., and McCallum, I.S., 1995, SIMS studies of planetary cumulates: Orthopyroxene from the Stillwater Complex, Montana: *American Mineralogist*, v. 80, p. 1208–1221.
- Parrish, R.R., and Krogh, T.E., 1987, Synthesis and purification of ^{205}Pb for $\text{U}\text{-}\text{Pb}$ geochronology: *Chemical Geology: Isotope Geoscience section*, v. 66, p. 103–110, doi:10.1016/0168-9622(87)90033-9.
- Paterson, M.S., and Luan, F.C., 1990, Quartzite rheology under geological conditions: Geological Society, London, Special Publications, v. 54, p. 299–307, doi:10.1144/GSL.SP.1990.054.01.26.
- Pattison, D.R.M., and Bégin, N.J., 1994, Zoning patterns in orthopyroxene and garnet in granulites: implications for geothermometry: *Journal of Metamorphic Geology*, v. 12, p. 387–410, doi:10.1111/j.1525-1314.1994.tb00031.x.
- Penniston-Dorland, S.C., Mathez, E.A., Wing, B.A., Farquhar, J., and Kinnaird, J.A., 2012a, Multiple sulfur isotope evidence for surface-derived sulfur in the Bushveld Complex: *Earth and Planetary Science Letters*, v. 337–338, p. 236–242, doi:10.1016/j.epsl.2012.05.013.
- Penniston-Dorland, S.C., Mathez, E.A., Wing, B.A., Farquhar, J., and Kinnaird, J.A., 2012b, Multiple sulfur isotope evidence for surface-derived sulfur in the Bushveld Complex: *Earth and Planetary Science Letters*, v. 337–338, p. 236–242, doi:10.1016/j.epsl.2012.05.013.
- Penniston-Dorland, S.C., Wing, B.A., Nex, P.A.M., Kinnaird, J.A., Farquhar, J., Brown, M., and Sharman, E.R., 2008, Multiple sulfur isotopes reveal a magmatic origin for the Platreef platinum group element deposit, Bushveld Complex, South Africa: *Geology*, v. 36, p. 979, doi:10.1130/G25098A.1.

- Peoples, J.W., and Howland, A.L., 1940, Chromite deposits of the eastern part of the Stillwater complex, Stillwater County, Montana: US Geological Survey 922-N, doi:10.3133/b922N.
- Peyerl, W., 1982, The influence of the Driekop dunite pipe on the platinum-group mineralogy of the UG-2 chromitite in its vicinity: *Economic Geology*, v. 77, p. 1432–1438, doi:10.2113/gsecongeo.77.6.1432.
- Pokrovski, G.S., Roux, J., and Harrichoury, J.-C., 2005, Fluid density control on vapor-liquid partitioning of metals in hydrothermal systems: *Geology*, v. 33, p. 657–660.
- Powell, J.L., Skinner, W.R., and Walker, D., 1969, Whole-Rock Rb-Sr Age of Metasedimentary Rocks Below the Stillwater Complex, Montana: *Geological Society of America Bulletin*, v. 80, p. 1605, doi:10.1130/0016-7606(1969)80[1605:WRAOMR]2.0.CO;2.
- Premo, W.R., Helz, R.T., Zientek, M.L., and Langston, R.B., 1990, U-Pb and Sm-Nd ages for the Stillwater Complex and its associated sills and dikes, Beartooth Mountains, Montana: Identification of a parent magma? *Geology*, v. 18, p. 1065–1068.
- Prevec, S.A., Ashwal, L.D., and Mkaza, M.S., 2005, Mineral disequilibrium in the Merensky Reef, western Bushveld Complex, South Africa: new Sm–Nd isotopic evidence: *Contributions to Mineralogy and Petrology*, v. 149, p. 306–315, doi:10.1007/s00410-005-0650-2.
- Pronost, J., Harris, C., and Pin, C., 2008, Relationship between footwall composition, crustal contamination, and fluid–rock interaction in the Platreef, Bushveld Complex, South Africa: *Mineralium Deposita*, v. 43, p. 825–848, doi:10.1007/s00126-008-0203-5.
- Raedeke, L.D., 1979, *Stratigraphy and Petrology of the Stillwater Complex, Montana* [Unpublished M.Sc. Thesis]: University of Washington, 109 p.
- Raedeke, L.D., and McCallum, I.S., 1984, Investigations in the Stillwater Complex: Part II. Petrology and Petrogenesis of the Ultramafic Series: *Journal of Petrology*, v. 25, p. 395–420, doi:10.1093/petrology/25.2.395.
- Rapp, R.P., and Watson, E.B., 1995, Dehydration Melting of Metabasalt at 8–32 kbar: Implications for Continental Growth and Crust-Mantle Recycling: *Journal of Petrology*, v. 36, p. 891–931, doi:10.1093/petrology/36.4.891.

- Reid, D.L., and Basson, I.J., 2002, Iron-rich ultramafic pegmatite replacement bodies within the Upper Critical Zone, Rustenburg Layered Suite, Northam Platinum Mine, South Africa: *Mineralogical Magazine*, v. 66, p. 895–914, doi:10.1180/0026461026660066.
- Richter, F.M., Liang, Y., and Davis, A.M., 1999, Isotope fractionation by diffusion in molten oxides: *Geochimica et Cosmochimica Acta*, v. 63, p. 2853–2861, doi:10.1016/S0016-7037(99)00164-7.
- Ripley, E.M., Park, Y.-R., Li, C., and Naldrett, A.J., 1999, Sulfur and oxygen isotopic evidence of country rock contamination in the Voisey's Bay Ni–Cu–Co deposit, Labrador, Canada: *Lithos*, v. 47, p. 53–68.
- Ripley, E.M., Wernette, B.W., Ayre, A., Li, C., Smith, J.M., Underwood, B.S., and Keays, R.R., 2017, Multiple S isotope studies of the Stillwater Complex and country rocks: An assessment of the role of crustal S in the origin of PGE enrichment found in the J-M Reef and related rocks: *Geochimica et Cosmochimica Acta*, v. 214, p. 226–245, doi:10.1016/j.gca.2017.07.041.
- Roddick, J.C., and Compston, W., 1977, Strontium isotopic equilibration: A solution to a paradox: *Earth and Planetary Science Letters*, v. 34, p. 238–246, doi:10.1016/0012-821X(77)90008-5.
- Roelofse, F., and Ashwal, L.D., 2012, The Lower Main Zone in the Northern Limb of the Bushveld Complex – a >1.3 km Thick Sequence of Intruded and Variably Contaminated Crystal Mushes: *Journal of Petrology*, v. 53, p. 1449–1476, doi:10.1093/petrology/egs022.
- Roelofse, F., Ashwal, L.D., and Romer, R.L., 2015, Multiple, isotopically heterogeneous plagioclase populations in the Bushveld Complex suggest mush intrusion: *Geochemistry*, v. 75, p. 357–364, doi:10.1016/j.chemer.2015.07.001.
- Rudnick, R.L., and Goldstein, S.L., 1990, The Pb isotopic compositions of lower crustal xenoliths and the evolution of lower crustal Pb: *Earth and Planetary Science Letters*, v. 98, p. 192–207, doi:10.1016/0012-821X(90)90059-7.
- Rupke, L., 2004, Serpentine and the subduction zone water cycle: *Earth and Planetary Science Letters*, v. 223, p. 17–34, doi:10.1016/j.epsl.2004.04.018.
- Schannor, M., Veksler, I.V., Hecht, L., Harris, C., Romer, R.L., and Manyeruke, T.D., 2018, Small-scale Sr and O isotope variations through the UG2 in the eastern

- Bushveld Complex: The role of crustal fluids: *Chemical Geology*, v. 485, p. 100–112, doi:10.1016/j.chemgeo.2018.03.040.
- Schiffries, C.M., 1982, The petrogenesis of a platiniferous dunite pipe in the Bushveld Complex; infiltration metasomatism by a chloride solution: *Economic Geology*, v. 77, p. 1439–1453, doi:10.2113/gsecongeo.77.6.1439.
- Schiffries, C.M., and Rye, D.M., 1989, Stable isotopic systematics of the Bushveld Complex: I. Constraints of magmatic processes in layered intrusions: *American Journal of Science*, v. 289, p. 841–873.
- Schiffries, C.M., and Rye, D.M., 1990, Stable isotopic systematics of the Bushveld Complex: II. Constraints on hydrothermal processes in layered intrusions: *American Journal of Science*, v. 290, p. 209–245.
- Schiffries, C.M., and Skinner, B.J., 1987, The Bushveld Hydrothermal System: Field and Petrologic Evidence: *American Journal of Science*, v. 287, p. 566–595.
- Schmidt, M.W., and Poli, S., 1998, Experimentally based water budgets for dehydrating slabs and consequences for arc magma generation: *Earth and Planetary Science Letters*, v. 163, p. 361–379, doi:10.1016/S0012-821X(98)00142-3.
- Scoon, R.N., and Costin, G., 2018, Chemistry, Morphology and Origin of Magmatic-Reaction Chromite Stringers Associated with Anorthosite in the Upper Critical Zone at Winnaarshoek, Eastern Limb of the Bushveld Complex: *Journal of Petrology*, v. 59, p. 1551–1578, doi:10.1093/petrology/egy071.
- Scoon, R.N., and Mitchell, A.A., 2020, Discussion of “Crustal fluid contamination in the Bushveld Complex, South Africa: An analogue for subduction zone fluid migration by Benson, E., Connolly, J.A.D. and Boudreau, A.E. (2020).: *International Geology Review*, p. 1–8, doi:10.1080/00206814.2020.1830443.
- Scoon, R.N., and Mitchell, A.A., 2004, The platiniferous dunite pipes in the eastern limb of the Bushveld Complex: Review and comparison with unmineralized discordant ultramafic bodies: *South African Journal of Geology*, v. 107, p. 505–520.
- Sharman-Harris, E.R., Kinnaird, J.A., Harris, C., and Horstmann, U.E., 2005, A new look at sulphide mineralisation of the northern limb, Bushveld Complex: a stable isotope study: *Applied Earth Science*, v. 114, p. 252–263, doi:10.1179/037174505X82134.

- Sharpe, M.R., 1985, Strontium isotope evidence for preserved density stratification in the main zone of the Bushveld Complex, South Africa: *Nature*, v. 316, p. 119–126, doi:10.1038/316119a0.
- Sharpe, M.R., 1981, The chronology of magma influxes to the eastern compartment of the Bushveld Complex as exemplified by its marginal border groups: *Journal of the Geological Society*, v. 138, p. 307–326.
- Shaw, A.M., Hauri, E.H., Fischer, T.P., Hilton, D.R., and Kelley, K.A., 2008, Hydrogen isotopes in Mariana arc melt inclusions: Implications for subduction dehydration and the deep-Earth water cycle: *Earth and Planetary Science Letters*, v. 275, p. 138–145, doi:10.1016/j.epsl.2008.08.015.
- Shieh, Y.N., and Taylor, H.P., 1969, Oxygen and Carbon Isotope Studies of Contact Metamorphism of Carbonate Rocks: *Journal of Petrology*, v. 10, p. 307–331, doi:10.1093/petrology/10.2.307.
- Sobolev, A.V., and Chaussidon, M., 1996, H₂O concentrations in primary melts from supra-subduction zones and mid-ocean ridges: Implications for H₂O storage and recycling in the mantle: *Earth and Planetary Science Letters*, v. 137, p. 45–55, doi:10.1016/0012-821X(95)00203-O.
- Sonnenthal, E.L., 1992, Geochemistry of dendritic anorthosites and associated pegmatites in the Skaergaard Intrusion, East Greenland: Evidence for metasomatism by a chlorine-rich fluid: *Journal of Volcanology and Geothermal Research*, v. 52, p. 209–230, doi:10.1016/0377-0273(92)90141-Y.
- Spandler, C., and Pirard, C., 2013, Element recycling from subducting slabs to arc crust: A review: *Lithos*, v. 170–171, p. 208–223, doi:10.1016/j.lithos.2013.02.016.
- Stacey, J.S., and Kramers, J.D., 1975, Approximation of terrestrial lead isotope evolution by a two-stage model: *Earth and Planetary Science Letters*, v. 26, p. 207–221.
- Stixrude, L., and Lithgow-Bertelloni, C., 2012, Geophysics of Chemical Heterogeneity in the Mantle: *Annual Review of Earth and Planetary Sciences*, v. 40, p. 569–595, doi:10.1146/annurev.earth.36.031207.124244.
- Stone, W.E., Deloule, E., and Stone, M.S., 2003, Hydromagmatic amphibole in komatiitic, tholeiitic and ferropicritic units, Abitibi greenstone belt, Ontario and Québec: evidence for Archaean wet basic and ultrabasic melts: *Mineralogy and Petrology*, v. 77, p. 39–65, doi:10.1007/s00710-002-0194-3.

- Strauss, H., and Beukes, N.J., 1996, Carbon and sulfur isotopic compositions of organic carbon and pyrite in sediments from the Transvaal Supergroup, South Africa: *Precambrian Research*, v. 79, p. 57–71, doi:10.1016/0301-9268(95)00088-7.
- Su, B.-X., Bai, Y., Cui, M.-M., Wang, J., Xiao, Y., Lenaz, D., Sakyi, P.A., and Robinson, P.T., 2020, Petrogenesis of the Ultramafic Zone of the Stillwater Complex in North America: constraints from mineral chemistry and stable isotopes of Li and O: *Contributions to Mineralogy and Petrology*, v. 175, p. 68, doi:10.1007/s00410-020-01707-y.
- Su, Q., and Fullagar, P.D., 1995, Rb-Sr and Sm-Nd Isotopic Systematics during Greenschist Facies Metamorphism and Deformation: Examples from the Southern Appalachian Blue Ridge: *The Journal of Geology*, v. 103, p. 423–436, doi:10.1086/629761.
- Sumner, D.Y., and Bowring, S.A., 1996, U²⁰⁶Pb geochronologic constraints on deposition of the Campbellrand Subgroup, Transvaal Supergroup, South Africa: *Precambrian Research*, v. 79, p. 25–35, doi:10.1016/0301-9268(95)00086-0.
- Taylor, H.P., 1978, Oxygen and hydrogen isotope studies of plutonic granitic rocks: *Earth and Planetary Science Letters*, v. 38, p. 177–210, doi:10.1016/0012-821X(78)90131-0.
- Tegner, C., 1997, Iron in plagioclase as a monitor of the differentiation of the Skaergaard intrusion: *Contributions to Mineralogy and Petrology*, v. 128, p. 45–51, doi:10.1007/s004100050292.
- Tegner, C., and Cawthorn, R.G., 2010, Iron in plagioclase in the Bushveld and Skaergaard intrusions: implications for iron contents in evolving basic magmas: *Contributions to Mineralogy and Petrology*, v. 159, p. 719–730, doi:10.1007/s00410-009-0450-1.
- Tegner, C., Thy, P., Holness, M.B., Jakobsen, J.K., and Lesher, C.E., 2009, Differentiation and Compaction in the Skaergaard Intrusion: *Journal of Petrology*, v. 50, p. 813–840, doi:10.1093/petrology/egp020.
- Teigler, B., and Eales, H.V., 1996, The lower and critical zones of the western limb of the Bushveld Complex as intersected by the Nooitgedacht boreholes: *Council for Geoscience Bulletin* 111, 126 p.
- Thompson, A.B., 1992, Water in the Earth's upper mantle: *Nature*, v. 358, p. 295–302, doi:10.1038/358295a0.

- Thompson, G., and Bankston, D.C., 1970, Sample Contamination from Grinding and Sieving Determined by Emission Spectrometry: *Applied Spectroscopy*, v. 24, p. 210–219, doi:10.1366/000370270774371886.
- Thy, P., Leshner, C.E., Nielsen, T.F.D., and Brooks, C.K., 2006, Experimental constraints on the Skaergaard liquid line of descent: *Lithos*, v. 92, p. 154–180, doi:10.1016/j.lithos.2006.03.031.
- Thy, P., Leshner, C.E., and Tegner, C., 2009, The Skaergaard liquid line of descent revisited: *Contributions to Mineralogy and Petrology*, v. 157, p. 735–747, doi:10.1007/s00410-008-0361-6.
- Todd, S.G., Keith, D.W., Le Roy, L.W., Schissel, D.J., Mann, E.L., and Irvine, T.N., 1982, The J-M Platinum-Palladium Reef of the Stillwater Complex, Montana: I. Stratigraphy and Petrology: *Economic Geology*, v. 77, p. 1454–1480.
- Tomascak, P.B., 2004, Developments in the Understanding and Application of Lithium Isotopes in the Earth and Planetary Sciences: *Reviews in Mineralogy and Geochemistry*, v. 55, p. 153–195.
- Toplis, M.J., Brown, W.L., and Pupier, E., 2008, Plagioclase in the Skaergaard intrusion. Part 1: Core and rim compositions in the layered series: *Contributions to Mineralogy and Petrology*, v. 155, p. 329–340, doi:10.1007/s00410-007-0245-1.
- Toplis, M.J., and Carroll, M.R., 1995, An Experimental Study of the Influence of Oxygen Fugacity on Fe-Ti Oxide Stability, Phase Relations, and Mineral–Melt Equilibria in Ferro-Basaltic Systems: *Journal of Petrology*, v. 36, p. 1137–1170, doi:10.1093/petrology/36.5.1137.
- Uken, R., and Watkeys, M.K., 1997, Diapirism initiated by the Bushveld Complex, South Africa: *Geology*, v. 25, p. 723–726.
- Vaniman, D.T., Papike, J.J., and Labotka, T., 1980, Contact-metamorphic effects of the Stillwater Complex, Montana: the concordant iron formation: *American Mineralogist*, v. 65, p. 1087–1102.
- VanTongeren, J.A., 2018, Mixing and Unmixing in the Bushveld Complex Magma Chamber, *in* Processes and Ore Deposits of Ultramafic-Mafic Magmas through Space and Time, Elsevier, p. 113–138, doi:10.1016/B978-0-12-811159-8.00005-6.

- VanTongeren, J.A., Zirakparvar, N.A., and Mathez, E.A., 2016, Hf isotopic evidence for a cogenetic magma source for the Bushveld Complex and associated felsic magmas: *Lithos*, v. 248–251, p. 469–477, doi:10.1016/j.lithos.2016.02.007.
- Veksler, I.V., and Hou, T., 2020, Experimental study on the effects of H₂O upon crystallization in the Lower and Critical Zones of the Bushveld Complex with an emphasis on chromitite formation: *Contributions to Mineralogy and Petrology*, v. 175, p. 85, doi:10.1007/s00410-020-01733-w.
- Vervoort, J.D., Patchett, P.J., Albarède, F., Blichert-Toft, J., Rudnick, R., and Downes, H., 2000, Hf–Nd isotopic evolution of the lower crust: *Earth and Planetary Science Letters*, v. 181, p. 115–129, doi:10.1016/S0012-821X(00)00170-9.
- Viljoen, M.J., and Scoon, R.N., 1985, The distribution and main geologic features of discordant bodies of iron-rich ultramafic pegmatite in the Bushveld Complex: *Economic Geology*, v. 80, p. 1109–1128, doi:10.2113/gsecongeo.80.4.1109.
- Vocke, C.M., 1982, T_f O₂ conditions of the metamorphism of the Stillwater iron formation [M.S. Thesis]: State University of New York.
- Volborth, A., and Housley, R.M., 1984, A preliminary description of complex graphite, sulphide, arsenide, and platinum group element mineralization in a pegmatoid pyroxenite of the Stillwater complex, Montana, U.S.A.: *TMPM Tschermarks Mineralogische und Petrographische Mitteilungen*, v. 33, p. 213–230, doi:10.1007/BF01081382.
- Von Gruenewaldt, G., Sharpe, M.R., and Hatton, C.J., 1985, The Bushveld Complex; introduction and review: *Economic Geology*, v. 80, p. 803–812, doi:10.2113/gsecongeo.80.4.803.
- Wager, L.R., and Brown, G.M., 1968, *Layered Igneous Rocks*: San Francisco, W.H. Freeman and Company.
- Wager, L.R., and Deer, W.A., 1939, *Geological investigations in East Greenland: Part III. The petrology of the Skaergaard intrusion, Kangerdlugssuaq, East Greenland: Meddelelser om Gronland*, v. 105, p. 352.
- Wall, C.J., and Scoates, J.S., 2016, High-precision U–Pb zircon–baddeleyite dating of the J–M Reef platinum group element deposit in the Stillwater Complex, Montana (USA): *Economic Geology*, v. 111, p. 771–782, doi:10.2113/econgeo.111.3.771.

- Wall, C.J., Scoates, J.S., and Weis, D., 2016, Zircon from the Anorthosite zone II of the Stillwater Complex as a U–Pb geochronological reference material for Archean rocks: *Chemical Geology*, v. 436, p. 54–71, doi:10.1016/j.chemgeo.2016.04.027.
- Wall, C.J., Scoates, J.S., Weis, D., Friedman, R.M., Amini, M., and Meurer, W.P., 2018, The Stillwater Complex: Integrating Zircon Geochronological and Geochemical Constraints on the Age, Emplacement History and Crystallization of a Large, Open-System Layered Intrusion: *Journal of Petrology*, v. 59, p. 153–190, doi:10.1093/petrology/egy024.
- Walraven, F., 1988, Notes on the age and genetic relationships of the Makhutso Granite, Bushveld Complex, South Africa: *Chemical Geology: Isotope Geoscience section*, v. 72, p. 17–28, doi:10.1016/0168-9622(88)90033-4.
- Wernette, B.W., Ripley, E.M., Li, C., and Wintsch, R.P., 2018, Strongly negative $\delta^{34}\text{S}$ values associated with secondary pyrite above and below the J-M Reef, Stillwater Complex, Montana: *Chemical Geology*, v. 493, p. 58–66, doi:10.1016/j.chemgeo.2018.05.023.
- Willmore, C.C., Boudreau, A.E., and Kruger, F.J., 2000, The Halogen Geochemistry of the Bushveld Complex, Republic of South Africa: Implications for Chalcophile Element Distribution in the Lower and Critical Zones: *Journal of Petrology*, v. 41, p. 1517–1539, doi:10.1093/petrology/41.10.1517.
- Willmore, C.C., Boudreau, A.E., Spivack, A., and Kruger, F.J., 2002, Halogens of Bushveld Complex, South Africa: $\delta^{37}\text{Cl}$ and Cl/F evidence for hydration melting of the source region in a back-arc setting: *Chemical Geology*, v. 182, p. 503–511.
- Wilson, A.H., 2015, The Earliest Stages of Emplacement of the Eastern Bushveld Complex: Development of the Lower Zone, Marginal Zone and Basal Ultramafic Sequence: *Journal of Petrology*, v. 56, p. 347–388, doi:10.1093/petrology/egv003.
- Wilson, J., Ferré, E.C., and Lespinasse, P., 2000, Repeated tabular injection of high-level alkaline granites in the eastern Bushveld, South Africa: *Journal of the Geological Society*, v. 157, p. 1077–1088, doi:10.1144/jgs.157.5.1077.
- Wilson, A.H., Zeh, A., and Gerdes, A., 2017, In Situ Sr isotopes in Plagioclase and Trace Element Systematics in the Lowest Part of the Eastern Bushveld Complex: Dynamic Processes in an Evolving Magma Chamber: *Journal of Petrology*, v. 58, p. 327–360, doi:10.1093/petrology/egx018.

- Wooden, J.L., Czamanske, G.K., and Zientek, M.L., 1991, A lead isotopic study of the Stillwater Complex, Montana: constraints on crustal contamination and source regions: *Contributions to Mineralogy and Petrology*, v. 107, p. 80–93, doi:10.1007/BF00311186.
- Wooden, J.L., and Mueller, P.A., 1988, Pb, Sr, and Nd isotopic compositions of a suite of Late Archean, igneous rocks, eastern Beartooth Mountains: implications for crust-mantle evolution: *Earth and Planetary Science Letters*, v. 87, p. 59–72, doi:10.1016/0012-821X(88)90064-7.
- Woodhead, J., Stern, R.J., Pearce, J., Hergt, J., and Vervoort, J., 2012, Hf-Nd isotope variation in Mariana Trough basalts: The importance of “ambient mantle” in the interpretation of subduction zone magmas: *Geology*, v. 40, p. 539–542, doi:10.1130/G32963.1.
- Wotzlaw, J.-F., Bindeman, I.N., Schaltegger, U., Brooks, C.K., and Naslund, H.R., 2012, High-resolution insights into episodes of crystallization, hydrothermal alteration and remelting in the Skaergaard intrusive complex: *Earth and Planetary Science Letters*, v. 355–356, p. 199–212, doi:10.1016/j.epsl.2012.08.043.
- Yang, S.-H., Maier, W.D., Lahaye, Y., and O’Brien, H., 2013, Strontium isotope disequilibrium of plagioclase in the Upper Critical Zone of the Bushveld Complex: evidence for mixing of crystal slurries: *Contributions to Mineralogy and Petrology*, v. 166, p. 959–974, doi:10.1007/s00410-013-0903-4.
- Yardley, B.W.D., 2005, 100th Anniversary Special Paper: Metal concentrations in Crustal Fluids and Their Relationship to Ore Formation: *Economic Geology*, v. 100.
- Zeh, A., and Gerdes, A., 2014, HFSE (High Field Strength Elements)-transport and U–Pb–Hf isotope homogenization mediated by Ca-bearing aqueous fluids at 2.04Ga: Constraints from zircon, monazite, and garnet of the Venetia Klippe, Limpopo Belt, South Africa: *Geochimica et Cosmochimica Acta*, v. 138, p. 81–100, doi:10.1016/j.gca.2014.04.015.
- Zeh, A., Gerdes, A., Will, T.M., and Frimmel, H.E., 2010, Hafnium isotope homogenization during metamorphic zircon growth in amphibolite-facies rocks: Examples from the Shackleton Range (Antarctica): *Geochimica et Cosmochimica Acta*, v. 74, p. 4740–4758, doi:10.1016/j.gca.2010.05.016.
- Zeh, A., Wilson, A.H., Gudelius, D., and Gerdes, A., 2020, Hafnium Isotopic Composition of the Bushveld Complex Requires Mantle Melt–Upper Crust

Mixing: New Evidence from Zirconology of Mafic, Felsic and Metasedimentary Rocks: *Journal of Petrology*, v. 60, p. 2169–2200, doi:10.1093/petrology/egaa004.

Zhu, G., Gerya, T.V., Yuen, D.A., Honda, S., Yoshida, T., and Connolly, J.A.D., 2009, Three-dimensional dynamics of hydrous thermal-chemical plumes in oceanic subduction zones: Dynamics of 3-D hydrous thermal-chemical plumes: *Geochemistry, Geophysics, Geosystems*, v. 10, doi:10.1029/2009GC002625.

Zientek, M.I., and Ripley, E.M., 1990, Sulfur isotope studies of the Stillwater Complex and associated rocks, Montana: *Economic Geology*, v. 85, p. 376–391, doi:10.2113/gsecongeo.85.2.376.

Zirakparvar, N.A., Mathez, Edmond.A., Scoates, J.S., and Wall, C.J., 2014, Zircon Hf isotope evidence for an enriched mantle source for the Bushveld Igneous Complex: *Contributions to Mineralogy and Petrology*, v. 168, p. 1050, doi:10.1007/s00410-014-1050-2.

Biography

Erin Benson obtained a B.Sc. in Geology and a B.A. in Anthropology at Western Washington University (Bellingham, WA, 2016). She then earned an M.Sc. at Indiana University Bloomington (2018). She then moved to Duke University to pursue a Ph.D. in Earth and Climate Sciences (ECS) (Durham, NC, 2018 – 2022). At Duke, she was first supported by NSF Grant EAR 1647727 to Dr. Alan Boudreau (2018-2021), then by a Teaching Assistantship from the Division of Earth and Climate Sciences (2021-2022). She was awarded Society of Economic Geologists (SEG) Hugh McKinstry Student Grant to pursue analysis of lithium isotopes in the Stillwater Complex (2019). She earned the Dean's Award for Outstanding Student Ph.D. Student Manuscript for work published on the Bushveld Complex, South Africa.